THE UNIVERSITY OF HULL

AN INVESTIGATION INTO PHENOMENA WHICH INFLUENCE THE OPTIMISATION OF ION PLATING SYSTEMS

being a Thesis submitted for the Degree of

Doctor of Philosophy

in the University of Hull

by

Kevin Stephen Fancey, BSc(Hons), MSc

JUNE 1989

For my wife,

parents

and

belated friends

Jan and Mick

ACKNOWLEDGEMENTS

I wish to thank the following colleagues from the Department of Engineering Design and Manufacture: Dr Allan Matthews (supervisor) for his encouragement, support and expert advice; Adrian James, Adrian Leyland and Azzedine Dehbi for useful discussions; Tony Pace and Les Houghton for technical support; Tony Parry for performing the EDAX work and Gary Robinson for the scanning electron micrography. I am also indebted to Mrs Sandra Langdale for her skilful typing of the thesis.

The provision of equipment by Tecvac Ltd and Ion Coat Ltd, and also the financial support of the SERC, is gratefully acknowledged.

Finally, I would like to thank my wife, Lynne, for her devoted support and patience (which I have occasionally tried) whilst working on this thesis.

Kevin S Fancey

June 1989

SUMMARY

Ion plating involves the transportation of vapour through a low pressure glow discharge to form solid coatings on negatively biased substrates. Although the method has gained commercial acceptance, particularly for engineering applications, much of the underlying science of the process is poorly understood. This work is concerned with investigating certain mechanisms occurring within the ion plating environment, and their role in process optimisation.

The work has concentrated primarily on electron beam evaporation in thermionically enhanced discharges. Investigations have centred on various aspects of discharges used in ion plating and the influence of gas scattering mechanisms on the vapour species during deposition. This has been achieved by analysing the published literature and performing experiments involving cathode sheath thickness measurements, sputter weight loss determinations, optical emission spectroscopy and coating thickness evaluation.

The main findings are:

(i) Thermionically enhanced discharges can considerably reduce cathode sheath thickness, providing benefits in terms of bombardment uniformity and energy transportation. However, the influence of plasma bombardment is anisotropic and also falls off exponentially with distance from the thermionic emitter. This can be offset by a comparable reduction in coating flux arrival rates if the thermionic emitter is positioned close to the vapour source.

(ii) The incorporation of nitrogen in (reactive) ion plating discharges may reduce the rate of ion generation, particularly in the presence of thermionic emitters. Nitrogen dissociative charge transfer

collisions within the cathode sheath may be significant but their practical importance is questionable.

(iii) There is evidence to suggest that the metal vapour in an argon ion plating discharge transports most of the ion current to the substrate and at least some of the material arrives as atomic clusters.

(iv) A model which unifies coating thickness uniformity with source to substrate distance has been developed. This predicts the existence of a virtual source phenomenon.

CONTENTS

1. INTRODUCTION

1.1 OBJECTIVES

The ion plating process is regarded by some as a black art. Indeed, many of the papers published on ion plated coatings tend to consider the deposition process as a black box; the coating characteristics are simply correlated with one or two externally controllable deposition parameters. Some other papers, where attempts have been made to understand the process, concentrate on isolated aspects and tend to produce over-idealised models which are generally inappropriate for use in real ion plating systems. The published literature, considered as a whole, shows that the underlying science of the ion plating process is still poorly understood. The probable reasons for this are that (i) a broad interdisciplinary knowledge of many topics related to the physical sciences and engineering disciplines is required and (ii) the ion plating process is by no means idealistic and it is therefore experimentally and theoretically difficult to analyse the various mechanisms collectively. Thus a gulf exists between those who use ion plating to produce practical coatings (eg, materials technologists) and those who strive to understand fundamental mechanisms which relate to the ion plating process (eg, plasma physicists).

It is not the objective of this work to bridge the gulf by attempting to explain the science of ion plating; such a proposal would be naïve, in addition to being presumptuous. The aims are, however, to identify at least some of the potentially important mechanisms occurring within the ion plating environment and to consider them in terms of their influence on process optimisation. The work is centred on the following:

(i) Investigation of the fundamental and practical aspects of discharges used in ion plating, with particular reference to phenomena which

influence bombardment at the substrate surface.

(ii) Evaluation of the role of gas scattering mechanisms on the evaporant species and its effect on coating distribution.

As the range of ion plating techniques is considerable, it has been necessary to confine much of this work to one which is commonly used, namely electron beam evaporation in a thermionically enhanced discharge. Many of the findings though, should be applicable to other ion plating methods.

1.2 WHAT IS ION PLATING?

"Ion plating is a generic term applied to atomistic film deposition processes in which the substrate surface is subjected to a flux of high energy ions sufficient to cause sputtering before and during film formation". This was the definition given by Mattox (ref 1) some years ago. Essentially, the process involves the emission of a vapourised material through a low pressure inert gas glow discharge. The vapour arrives at a substrate that has a negative potential with respect to the discharge in which it is immersed, and forms a solid coating. Figure 1.1 (after ref 1) is a schematic of a simple ion plating system, using a resistive evaporation source.

Most of the hardware used in an ion plating system is similar to that employed in vacuum evaporation equipment (ie, pumps, deposition chamber, etc). In fact, many experimental ion plating systems have been developed from basic vacuum coating equipment, simply by the addition of an inert gas supply (usually argon), electrical feedthroughs and appropriate power supplies.

When compared with vacuum evaporation, the process offers benefits in terms of increased coating density, cohesion and adherence to the substrate. This is due to the inert gas and vapour being partially ionised.

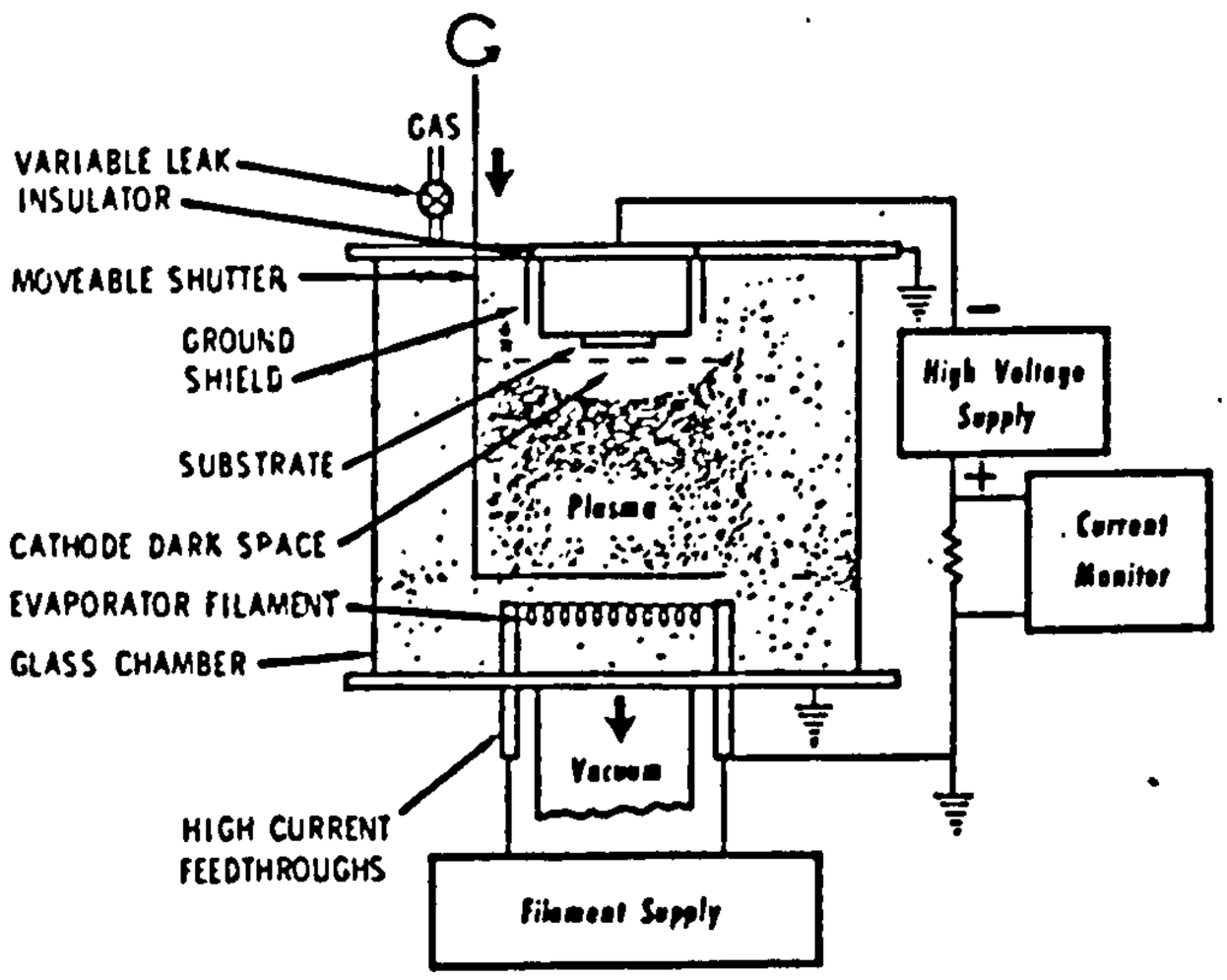

Figure 1.1 Simple DC diode ion plating system with movable shutter and resistively heated evaporation source (after ref 1).

The (positive) ions accelerate across the cathode dark space (Fig 1.1) where most of the discharge potential is dropped, and strike the substrate (cathode) with energies which are generally considerably greater than the thermal energies encountered in vacuum evaporation. The substrate is also subjected to bombardment by high energy neutrals arising from charge exchange collisions with ions in the cathode dark space. The high energy bombardment by ions and neutrals causes a number of mechanisms to occur during film growth, sputtering being one of the main effects. The growing layer is sputtered and re-sputtered and adatom mobility is increased so that coating material which might be loosely bound at one site is removed and eventually re-deposited at another site where conditions are more favourable for adhesion. The overall effect is to counteract the porous open columnar type of film growth associated with vacuum evaporation (as described in the

Movchan-Demchishin model, ref 2), to produce dense cohesive coatings at relatively low substrate bulk temperatures. Similarly, these mechanisms improve coating adhesion to the substrate by, for example, promoting atomic mixing at the film - substrate interface to produce a "pseudo-diffusion" layer (eg, refs 3,4) even when no mutual solubility exists between the two materials. Sputtering the substrate prior to coating deposition will also improve adhesion by leaving the surface atomically clean.

A further benefit which ion plating offers, is the ability to coat substrates of complex shape with reasonable thickness uniformity, without the need for rotation. This is because the evaporant flux is subjected to "soft" vacuum conditions in the deposition chamber, thus collisions causing scattering occur, making the flux less directional. Therefore, substrate surfaces remote from the vapour source can become coated.

1.3 MODERN ION PLATING PROCESSES

Although a form of film deposition through an inert gas glow discharge was described more than 50 years ago (ref 5), the concept lay dormant until the early 1960's, when results from a similar process were reported by Mattox (ref 6) who coined the term "ion plating". This early work concentrated on simple D.C. diode configurations, typical process parameters being 10 to 50 mTorr argon pressure, 2 to 5 kV DC bias and 0.5 mA cm^{-2} current density at the substrate (ref 1). Although similar systems are still sometimes used, certain benefits were found in later years, when some form of ionisation enhancement was used in the process. This could be achieved by, for example, employing an additional biased electrode, thermionic support or a magnetic field (refs 7,8). The advantages of employing some form of ionisation enhancement was probably first recognised by Baum (ref 9). Comparing a thermionically supported system to a simple

diode arrangement, it was found that improved gas discharge control was obtained and lower voltages were required, which reduced potential arcing problems and unwanted substrate heating (low substrate temperatures sometimes being preferable, depending on the nature of the substrate). It was also found that lower pressures could be used whilst still maintaining the discharge. Although a lower pressure reduces the benefits of evaporant flux scattering on coating thickness uniformity, coating densification is generally increased. This is because increasing the gas pressure tends to promote an open columnar film growth, similar to that associated with low substrate bulk temperatures in vacuum evaporation. The effect is comparable to the model proposed by Thornton (ref 10), whose findings were based on sputter deposited coatings.

The additional benefits of ionisation enhancement outlined above, has fuelled interest in ion plating techniques for industrial exploitation. One of the greatest areas of growth has been in the deposition of hard ceramic coatings such as titanium nitride, which considerably extends the life of industrial cutting tools (ref 7). Other nitrides, carbides and oxides have also been deposited by ion plating techniques to produce thin (a few μm) dense adherent coatings for wear resistance, corrosion protection and dry lubrication and these are reviewed in ref 8. Although some ceramic compounds may be evaporated directly, they are not always available in a form suitable as a source material. Also, in some cases, the gas species may be lost upon dissociating and must be replaced by admitting additional gas. Thus ceramics such as titanium nitride are normally deposited by evaporating the metal through an ionisation enhanced glow discharge comprising a reactive gas with argon; the argon acting as a buffer gas for optimum process conditions. Chemical reaction between the metal flux and gas produces the ceramic at the substrate surface. Figure 1.2 shows

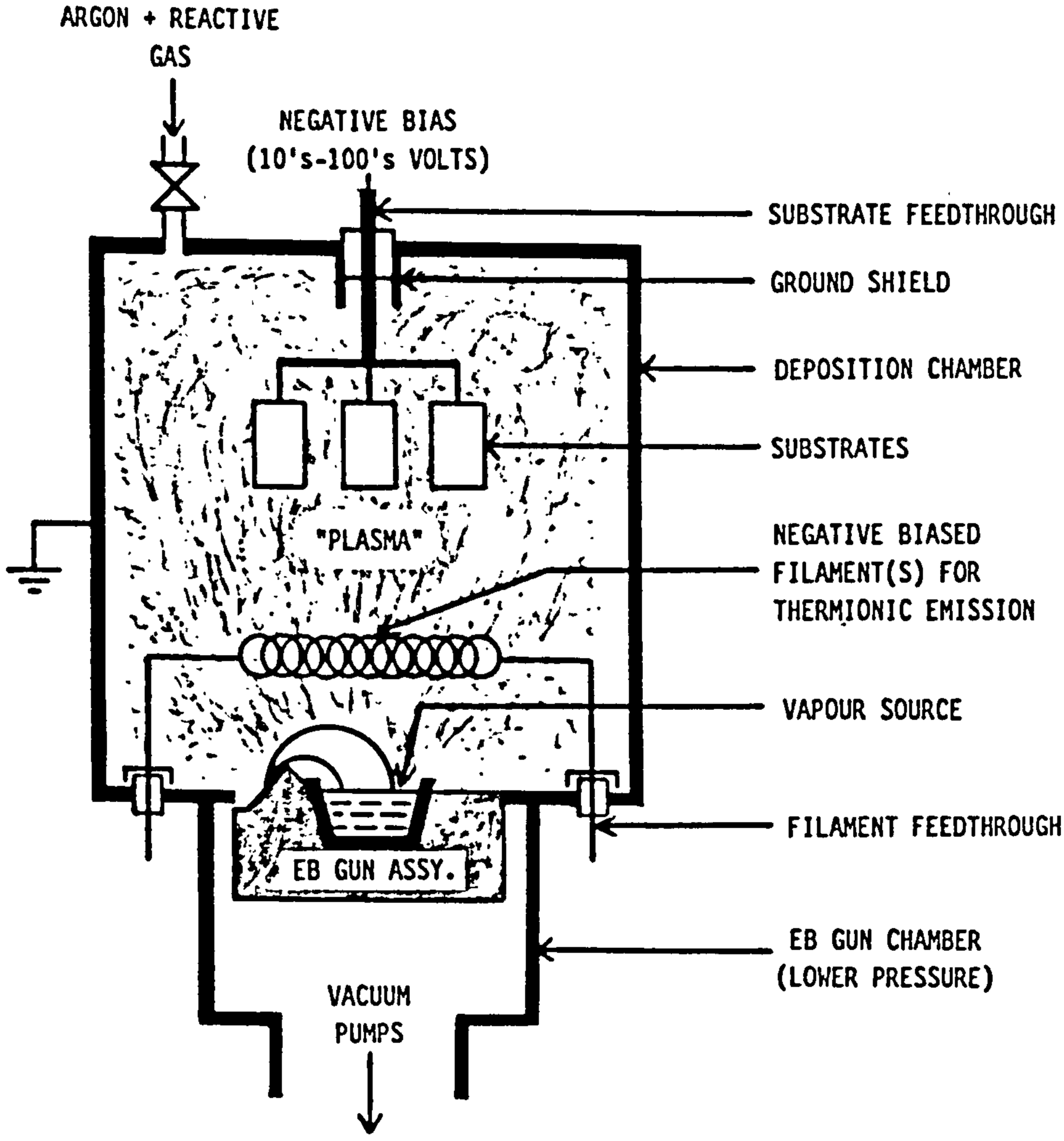

Figure 1.2 Modern ion plating process, using a thermionically enhanced discharge and EB evaporation for producing ceramic coatings.

schematically, a modern ion plating process, utilising a low pressure thermionically supported discharge and an electron beam (EB) evaporation source.

Most commercial systems using enhanced DC discharges typically operate with gas pressures of about 1 to 10 mTorr, have substrate biases of 10's to 100's of volts and substrate current densities up to a few mA cm^{-2} (ref 8). Radio frequency (RF) substrate biasing in ion plating has also been used (eg, refs 11,12) which produces a negative bias comparable to the DC case. Although RF biasing allows electrically insulating materials to be utilised (either as substrate or coating), it is not widely used at the present. Alternatives to the EB evaporation source in Figure 1.2 include resistive evaporation, arc sources and sputter sources. Their relative merits are reviewed in ref 13. However, EB evaporation offers benefits in terms of (i) flexibility (evaporant material can be readily changed or replenished and does not need to be in any specially machined form), (ii) ability to evaporate very high melting point materials and (iii) relatively high energy efficiency.

Over the years, the multiplicity of ion plating processes developed and the awareness of the term "ion plating" being something of a misnomer, has led to a proliferation of names being used in the scientific literature. Some examples are: Ionisation Assisted Physical Vapour Deposition (IAPVD); Plasma Assisted Physical Vapour Deposition (PAPVD); Activated Reactive Evaporation (ARE), and Biased Activated Reactive Evaporation (BARE).

Although there are now many forms of commercial and experimental ion plating systems in use, they all generally incorporate the principles outlined in this chapter. As a consequence, they all tend to share the same difficulties in terms of understanding the mechanisms which influence process optimisation.

2. THE ION PLATING EQUIPMENT

2.1 INTRODUCTION

This chapter describes the two ion plating systems used for the experimental work, designated rig (1) and rig (2). Rig (1) was a laboratory sized system, most of which was built in-house. Rig (2) was a commercially available system, manufactured by Tecvac Ltd., UK (model IP35L), being primarily designed for the production of titanium nitride coatings using a thermionically supported discharge. Figures 2.1 and 2.2 show the general layouts of the rigs.

2.2 RIG (1) - DESCRIPTION

2.2.1 General Details

Figure 2.3 is a schematic of rig (1). It comprised a deposition chamber constructed from 3mm thick stainless steel with two 26 cm diameter view ports. The chamber was approximately a 45 cm cube, lined with 1.5 mm thick stainless steel shielding to facilitate periodic removal of coating deposits. Access was via one of two 17 mm thick doors.

The evaporation source comprised a water cooled copper crucible with electron beam heating, and was differentially pumped with respect to the deposition chamber. Substrates were attached to a water cooled high voltage feedthrough which could be connected either to an RF or DC supply. Two electrical feedthroughs in the base of the chamber could be used to provide thermionic support.

Argon and/or nitrogen could be bled into the deposition chamber, which was supplied from standard compressed gas cylinders. The vacuum pumping system consisted of two diffusion pumps backed by a single stage rotary pump.

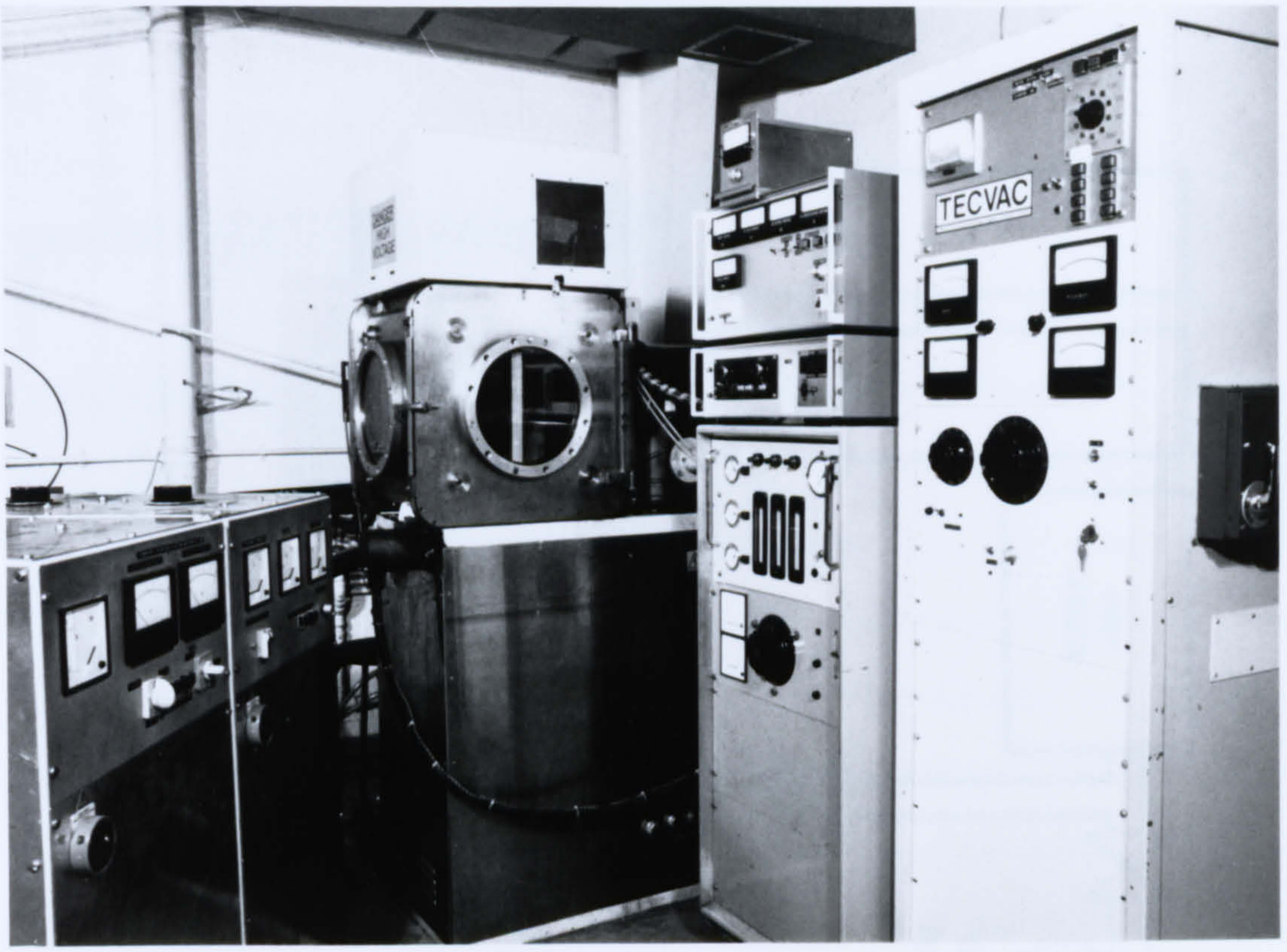

Figure 2.1 General view of rig (1)

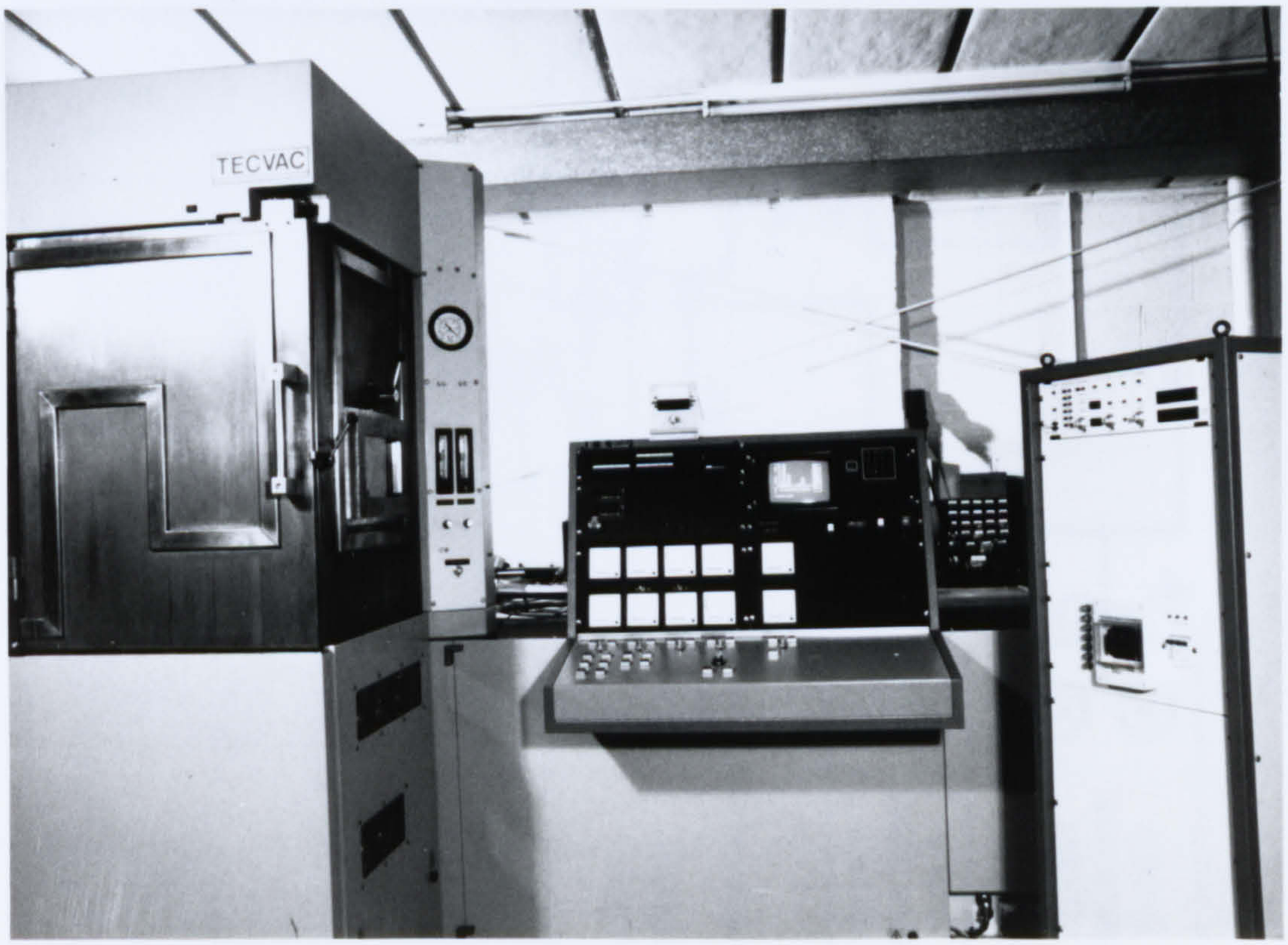

Figure 2.2 General view of rig (2)

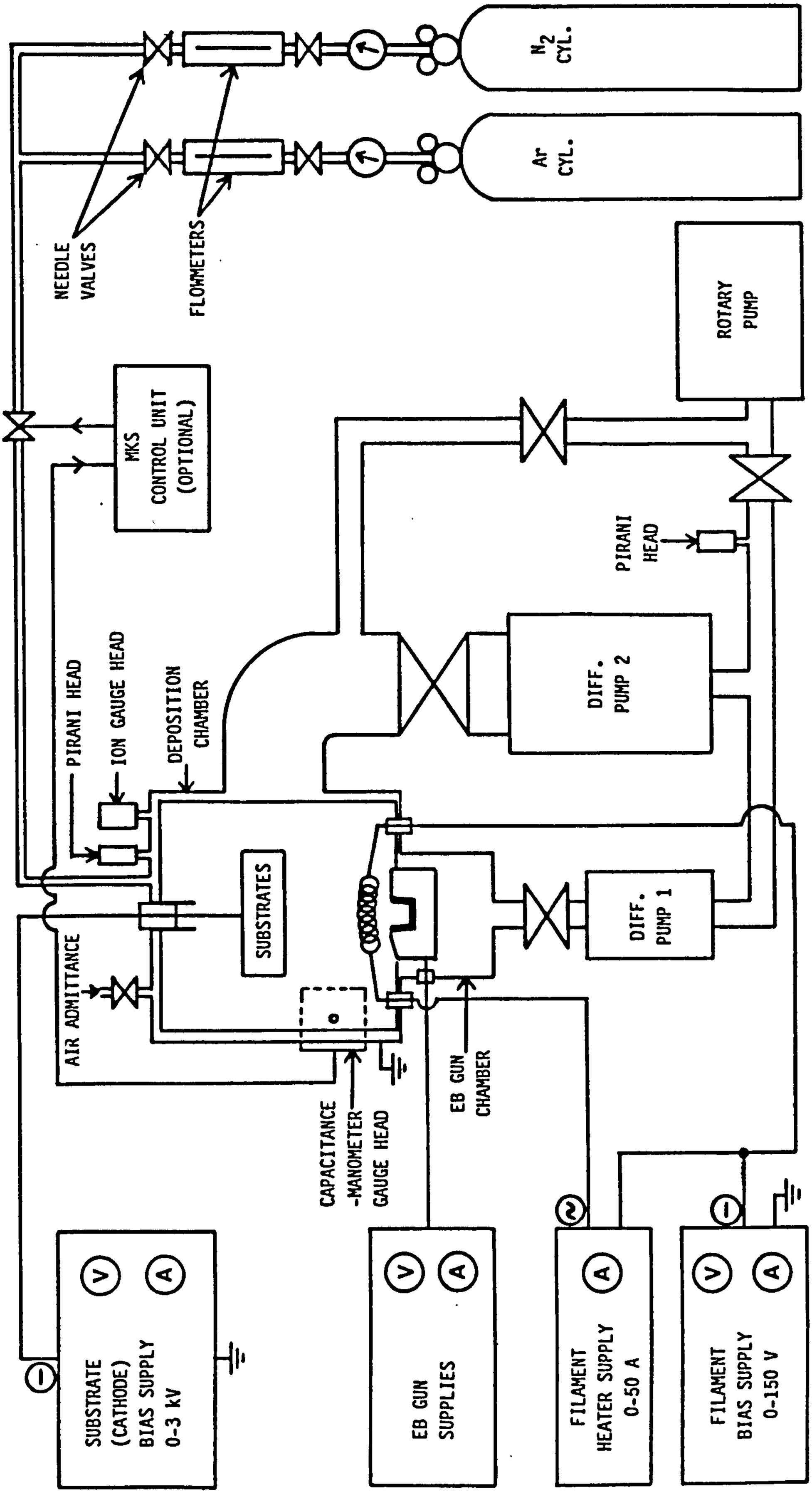

Figure 2.3 Schematic of rig (1).

2.2.2 Vacuum and Gas Supply Systems

Two Edwards diffusion pumps, one 15 cm diameter (pump 1) the other 23 cm diameter (pump 2) were both used to obtain a high vacuum (less than 10^{-5} Torr) in the deposition chamber prior to commencement of processing. During processing, valve 2 was normally closed so that only pump 1 was in use. The EB gun chamber was baffled from the deposition chamber to provide sufficient differential pumping of the former. This allowed the EB gun to operate under relatively high vacuum conditions, whilst maintaining gas pressures in the deposition chamber of up to about 15 mTorr. Chamber pressures of 100 mTorr or more could be used when the EB gun was not operated.

The pump down and venting sequences were automatically cycled by a mechanically programmed rotary switching arrangement controlled by the Pirani gauges. All valves were activated electro-pneumatically.

The gas supplies (argon and nitrogen) to the deposition chamber could be controlled manually through needle valves. In addition, an MKS type 250B controller could be used to maintain a preset total pressure in the chamber. The controller operated from the output of an MKS Baratron capacitance-manometer pressure gauge head.

Four vacuum gauge heads were fitted to the deposition chamber. These included the Pirani head used for pumping control and a Bourdon gauge for checking that the chamber had no gross leaks during initial pump down. For checking the attainment of high vacuum, an ion gauge was used. The MKS capacitance-manometer unit was used as the standard for experimental work, as it provided pressure readings which were independent of the nature of the gas species (unlike an ion gauge) and its calibration was traceable to the American National Bureau of Standards. The usable range of this unit was

from about 0.1 mTorr to 1 Torr; the lower figure being limited by noise effects. One problem encountered with the capacitance-manometer unit was a tendency for the zero offset to drift upwards slightly, during processing. This was due to a warming of the unit, arising from heating of the deposition chamber. The effect was corrected for, by periodically checking the readout under high vacuum conditions.

2.2.3 Electrical Systems

The EB gun comprised a tungsten filament heated by an AC power supply. The filament was negatively biased up to 10 kV, using a 3 kW supply. This caused the filament to emit electrons which were accelerated through an earthed anode aperture. The resultant electron beam was then deflected through 225° to impinge on the surface of the source material in the crucible, by means of a solenoid mounted immediately beneath the chamber base plate. Beam position could be adjusted by altering the solenoid supply voltage.

The substrate (cathode) bias supply was continuously adjustable up to 3 kV by means of a variac control. Using an oscilloscope with a high voltage attenuator, ripple on the supply output was found to be about 12% over the entire voltage range. As an accurate determination of cathode voltage and current was essential for this work, a digital voltmeter (Racal-Dana type 4003 or Beckman type 310) with a calibrated high voltage attenuator was used for voltage measurement, in preference to the power supply voltmeter. The ammeter in the power supply was used directly, as this had been previously calibrated against a precision digital multimeter.

Thermionic support required two power supplies, one for filament heating, the other for filament biasing. The filament AC heater supply was continuously adjustable up to 50 amps. Filament biasing was achieved by

means of a 0-150 volt variac controlled supply. Ripple on the output was measured to be about 12% for zero heater current, rising to about 20% over the range of practical heater currents used. Filament bias, emission and heating current could be monitored with the meters built into the supplies.

In addition to the DC power supplies, an RF supply was also available for substrate biasing. Details of this are given in ref 11. With the exception of some data reported in Chapter 6, the RF facility was not used in this work.

2.3 Rig (2) - DESCRIPTION

2.3.1 General Details

Figure 2.4 is a schematic of rig (2). Essentially, it was a scaled-up version of rig (1). The deposition chamber, constructed from 25 mm thick stainless steel was water cooled and had a small rectangular view port approximately 1/3 of the way up from the chamber base. The chamber was approximately a 67 cm cube, lined with 0.5 mm thick steel shielding, which was designed to be periodically disposed of and replaced. Access was via a 25 mm thick water cooled door.

The differentially pumped evaporation source and facilities for thermionic support were similar to those in rig (1). The water cooled high voltage feedthrough for supporting subtrates was rotatable and had a motor drive facility so that planetary motion of substrates mounted off axis from the evaporation source could be achieved to improve coating thickness uniformity. Two thermocouple leads mounted via the substrate feedthrough enabled sample temperatures to be monitored during processing. The thermocouples, being at the same potential as the substrates, were electrically isolated outside the chamber by means of a fibre optic link to the temperature instrumentation on the control console.

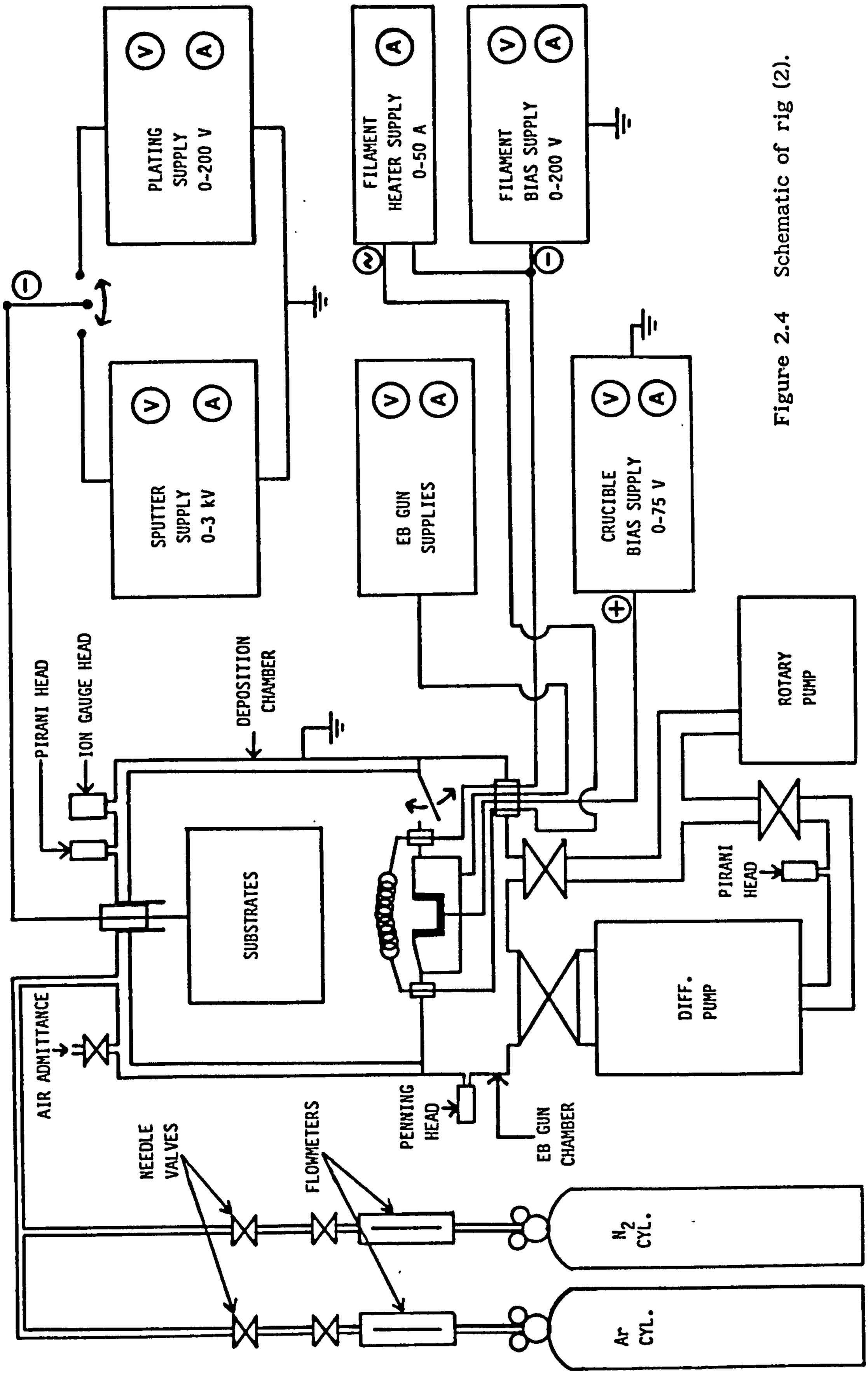

Figure 2.4 Schematic of rig (2).

The vacuum pumping system comprised a single diffusion pump with rotary pump backing.

2.3.2 Vacuum and Gas Supply Systems

The single diffusion pump (Edwards 30 cm diameter), provided both pump down to high vacuum (less than 10^{-5} Torr) and differential pumping during processing. This was achieved by the remote operation of a hinged plate in the bulkhead between the deposition chamber and the EB gun chamber (see Figure 2.4). When the gun was not operated, gas pressures in the deposition chamber of up to 50 mTorr could be used.

The pump down and venting sequences were automatically cycled by an Edwards type 2011 controller, operating from Penning and Pirani gauges. The controller also switched hot water into the chamber cooling channels during initial pump down to improve the level of vacuum which could be attained.

The argon and nitrogen gas supplies to the deposition chamber were controlled manually through needle valves.

In addition to the Penning and Pirani gauges fitted, a Bourdon gauge was available for checking gross leaks. Deposition chamber pressure monitoring was by means of an ion gauge.

2.3.3 Electrical Systems

The EB gun operating principles were identical to those of rig (1), though it was slightly larger, thus requiring a more powerful supply (5 kW). In addition, the crucible could be positively biased with a 75 volt supply.

Two substrate bias supplies were available. The first was a 3 kV low current supply, to enable high voltage diode sputter cleaning of the substrates to be performed prior to coating. The second was a 200 volt high current supply for substrate biasing during thermionic triode ion plating.

Thermionic support was provided by a 50 amp heater supply and a 200 volt filament bias supply.

Unfortunately, although this rig was capable of producing high quality titanium nitride coatings, detailed investigations of the power supply output waveforms showed that they were not generally suitable for experimental evaluation of discharge phenomena. When the biasing supplies were operated at maximum voltage (3 kV or 200 volts for the substrates and 200 volts for filament bias), the ripple was minimised. At these settings, the ripple was typically 20%. A full account of the results of these investigations and calibration work performed on the electrical instrumentation is given in ref 14.

2.4 SUMMARY

Although rig (1) had a smaller deposition chamber and lacked the advantages of chamber water cooling (which would be useful for long processing times), it offered the following benefits:

(i) Large area view ports to facilitate direct observation of discharge phenomena.

(ii) Accurate chamber pressure determination due to the capacitance-manometer gauge facility.

(iii) Power supplies which had relatively smooth output waveforms over all ranges.

The power supply characteristics of rig (2) was one of the main limitations with regards to its usefulness in this work. Consequently, most of the experimental work was performed on rig (1).

3. ION PLATING DISCHARGES - FUNDAMENTAL CONSIDERATIONS

3.1 INTRODUCTION

The obvious place to begin an investigation into ion plating discharges is to review the available published literature. Although much theoretical and experimental work has been performed on electrical discharges during this century, most of it relates to pressure ranges, voltages and geometries which are inappropriate to those used in ion plating. An example of this is given in Figure 3.1, which shows the general appearance and electrical characteristics of a DC diode glow discharge (ref

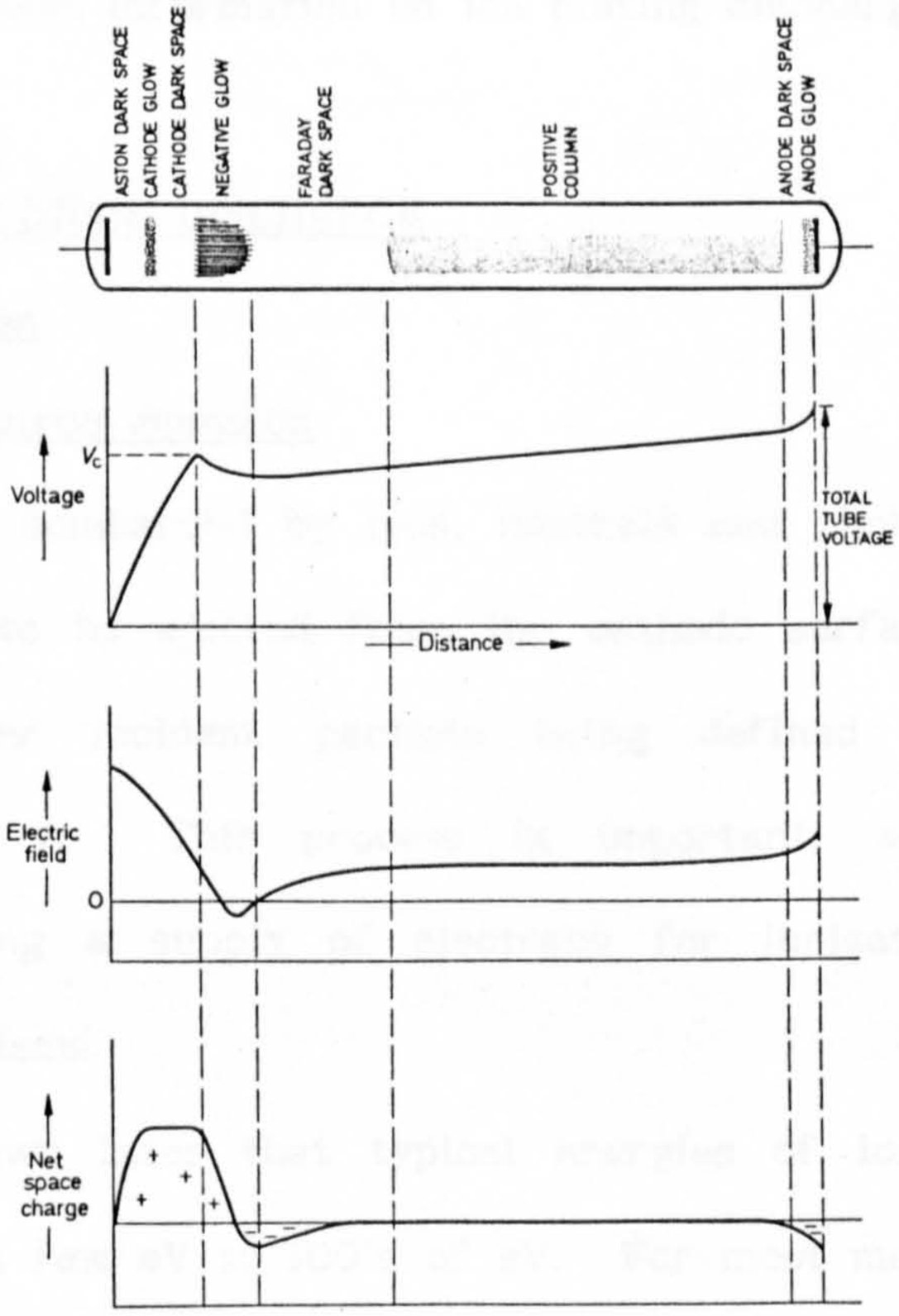

Figure 3.1 Glow discharge operating at a gas pressure of a few Torr (after ref 15).

15) and similar diagrams can be found in many of the standard texts on this subject. The long thin electrically insulating tube, equal sized electrodes and relatively high pressure (a few Torr) does not represent the situation encountered even in a simple diode ion plating system. In the latter case, most of the discharge volume would be occupied by the negative glow region, as shown in Figure 1.1 (where it is designated the "plasma").

This chapter reviews some of the more relevant aspects from the textbooks (eg, ref 16), by considering the mechanisms occurring within a low pressure argon diode discharge (operating in the "abnormal" state) as the starting point. From this, the role of the cathode sheath region is analysed in relation to practical discharge systems, primarily by attempting to pull together published information on ion plating discharges.

3.2 THE DC ARGON DIODE DISCHARGE

3.2.1 Basic Mechanisms

3.2.1.1 Secondary electron emission

The cathode is bombarded by ions, neutrals and photons. All of these can cause electrons to be ejected from the cathode surface; the number of electrons emitted per incident particle being defined as the secondary electron coefficient, γ. This process is important, as it sustains the discharge by providing a supply of electrons for ionisation to offset the recombination mechanisms.

It will be shown later that typical energies of ions arriving at the cathode range from a few eV to 100's of eV. For most metals, γ is typically 10% (ie, one electron emitted for every ten ions) for Ar^+ ions with energies below 1 keV. However, the value is heavily dependent upon the nature of the surface and can change significantly with, for example, crystallographic orientation and the amount of adsorbed gases and other impurities present.

As discussed in ref 17, secondary electron emission generally occurs via the potential emission mode, where the incident ion is neutralised very close to the cathode surface by an electron tunnelling from the Fermi sea. The ionisation energy released is then transferred to a second electron which is ejected. The probability of electron ejection is therefore not heavily dependent upon ion kinetic energy and the average ejection energy is typically only a few eV. Figure 3.2 (after refs 18,19) shows how γ for tungsten and molybdenum changes with argon ion energy; the influence of kinetic energy only becoming apparent in the keV range.

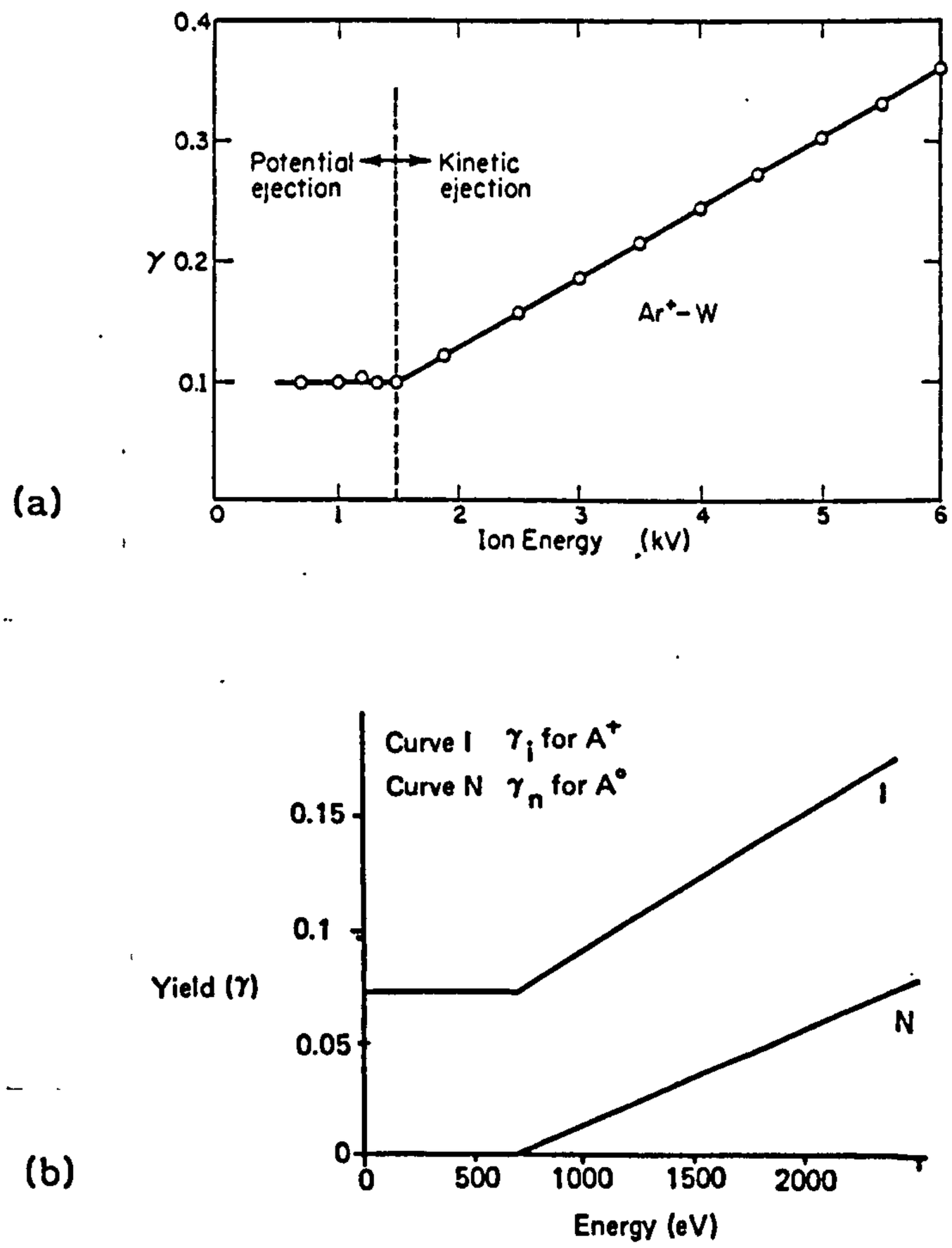

Figure 3.2 Secondary electron emission as a function of argon bombardment energy for (a) tungsten (ref 18) and (b) molybdenum (ref 19).

Figure 3.2b shows the dependence of γ for neutral bombardment on molybdenum. There appears to be no potential ejection component and if this is typical for all cathode materials then electron emission by high energy neutral bombardment (which tend to have lower kinetic energies than the ions, as discussed later) is unlikely to be significant in these discharges. However, as discussed in ref 16, long lived neutral metastables have potential energy and these may be more effective than the ground state neutrals though there is little information available on this subject.

Although electron emission by photon bombardment is well known (the photo-electric effect), its influence in glow discharges is poorly understood. γ from this mechanism is relatively low for pure metals, being typically 10^{-4} to 10^{-3} electrons per incident photon in the visible to near U.V. wavelengths. Loeb (ref 20) suggests that the photo-electric effect is small compared with positive ion impact. This is based on previously published findings comparing fine wire gauze with solid plate cathodes. No significant change was observed in the discharge characteristics, even though the gauze (which would transmit photons) reduces the photo-electric effect yet still collects ions. Therefore, it can be inferred that secondary electron emission from the cathode contributes to about 10% of the total cathode current.

In addition to electron emission by ions, neutrals and photons, electron bombardment can also produce electrons. Although this would not occur at the cathode of a DC diode discharge, it may occur at other surfaces exposed to the discharge. The yield by this mechanism is typically unity (one electron ejected per incident electron) for clean metals and incident electron energies of 100's of eV, this figure being higher for insulating materials. For surfaces other than the cathode however, the yield from lower electron energies is more important. Unfortunately, there is little

relevant data available on this subject.

3.2.1.2 Ionisation and recombination

The following ionising collisions might be expected to occur in a DC argon diode discharge:

(i) Electron-atom (or electron impact) ionisation:

$$e + Ar \longrightarrow Ar^{+} + 2e$$

$$e + Ar^{*} \longrightarrow Ar^{+} + 2e \quad (Ar^{*} = \text{metastable})$$

(ii) Ion-atom (or ion impact) ionisation:

$$Ar^{+} + Ar \longrightarrow 2Ar^{+} + e$$

(iii) Photon-atom ionisation (or photo-ionisation):

$$h\nu + Ar \longrightarrow Ar^{+} + e$$

(iv) Symmetrical charge exchange:

$$Ar^{+} + Ar \longrightarrow Ar + Ar^{+}$$

The significance of these collisions in terms of their influence on the discharge will obviously depend on their frequency of occurrence. This may be considered in terms of the number of incident particles available and the probability of the event occurring. The collision probability can be evaluated in terms of the mean free path, λ, which is a measure of the distance travelled by a particle in a background gas before a particular type of collision occurs. As λ will depend on the number density, n, of the background gas it can be more convenient to consider collision phenomena in terms of their effective cross sectional area. Thus,

$$\sigma = 1/n\lambda \tag{3.1}$$

where σ is the collision cross section for a particular mechanism. Figure 3.3 shows σ as a function of incident particle energy for the ionisation

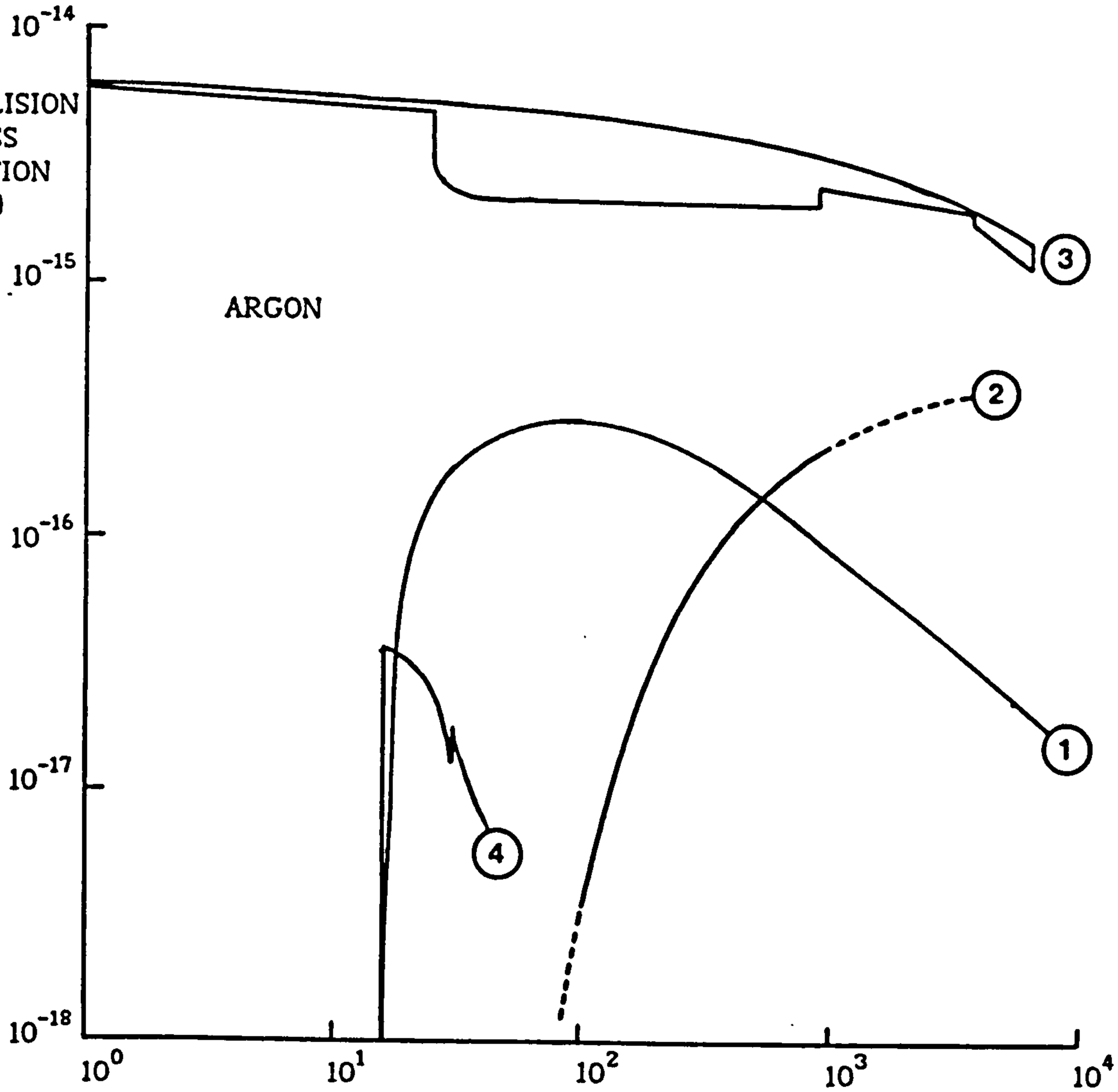

(1) ELECTRON-ATOM IONISATION

(2) ION-ATOM IONISATION

(3) $Ar^+ - Ar^\circ$ CHARGE TRANSFER (RANGE OF DATA UP TO 1964)

(4) PHOTON-ATOM IONISATION

Figure 3.3 Collision cross section data for ionisation processes expected to occur in an argon DC diode discharge (data from various sources reported in ref 16).

processes listed above.

The threshold energy for ionisation of argon atoms (ie, the ionisation potential) is 15.76 eV. Symmetrical charge exchange can occur below this threshold however, because of the potential energy of the incident argon ion. Argon ions with more than one unit charge may be created, though the ionisation potential increases. For example, the ionisation potential for Ar^{2+} is 27.63 eV.

In addition to ionisation processes, recombination also must take place for the discharge to remain in equilibrium. It can be shown (eg ref 16) that two body coalescence (electron-ion) is not possible, due to considerations of simultaneous conservation of energy and momentum. Thus other mechanisms occur such as three body recombination. Here, a third body allows energy and momentum to be conserved. The third body could be another gas atom, or, more likely, a solid surface such as an electrode; the latter being even more probable at lower gas pressures. Radiative recombination may also take place. Here, a photon is emitted, which carries away the excess energy arising from coalescence.

3.2.1.3 Non-ionising processes

In addition to ionisation phenomena, excitation also occurs. This may arise from impact with electrons or photons. Ion or atom excitation impact would require very high energies, at least a few keV to be significant (ref 21). The energy threshold for excitation (excitation potential) is lower than the ionisation potential as the bound electron is raised only to a higher energy level rather than being completely removed. For argon, the excitation potential is 11.56 eV. The excited states produced are unstable and the electron configuration will eventually return to its original ground state, emitting a photon of specific energy (de-excitation or relaxation).

The lifetimes of these excited states vary considerably, from nanoseconds to seconds. Long lived excited states are known as metastables (for argon, the designation is Ar^*). These appear to have an important role in the ion plating process, and this will be discussed in later sections.

Another potentially significant process is elastic scattering of electrons. However, the relevance of this will also be discussed later.

3.2.2 The Discharge Regions

3.2.2.1 The negative glow

As mentioned in Section 3.1, most of the discharge volume is occupied by the negative glow region. There is usually no positive column because the pressures considered (tens of mTorr) are too low and the inter-electrode separation is too small (a few tens of cms). Thus the negative glow is the "plasma" region lying between the cathode and anode sheaths.

A true plasma can be described as a partially ionised gas containing equal numbers of positive and negative charges (positive ions and electrons) which are uniformly distributed. The negative glow is often referred to as a plasma, though high energy electrons enter the glow from the cathode sheath (as described in the next section), which influence the charge distribution.

Three groups of electrons are generally considered to exist in the negative glow:

(i) Primary electrons, which are the high energy electrons from the cathode sheath and are therefore highly directional.

(ii) Secondary electrons, which have much lower energies, and consist of electrons produced by ionising collisions or primaries which have lost much of their energy.

(iii) Ultimate electrons, which have the lowest energies.

Based on data reported in ref 16, the number of ultimate electrons present is the order of 100 times the number of secondaries and there are about 10 times more secondaries than there are primaries. The secondary and ultimate groups are generally assumed to have Maxwellian energy distributions, each with a corresponding electron temperature, representing the mean energy. Knewstubb et al (ref 22) report on published data which suggests that the secondaries have electron temperatures of about 3 to 5 eV and the ultimates are in the order of 0.3 to 0.5 eV. Ball (ref 23) found from Langmuir probe measurements (3 kV, 10 mTorr argon DC diode discharge) two groups of electrons present in the glow. These had electron temperatures of 7.5 eV and 0.35 eV, concurring with the data above. The primary electrons may be considered almost monoenergetic when they enter the glow, with energies close to the maximum which could be acquired through the potential drop in the cathode sheath. This assumption is based on conclusions reported in ref 16 and comments in ref 24.

Electron temperature is regarded as an important parameter in plasma physics. The fact that there are considered to be three groups of electrons, with different average temperatures and number densities, tends to complicate the situation. Although not implicitly defined, some authors (eg, refs 16,25) consider the typical electron temperature in the negative glow to be about 2 eV. Thus, we may regard this as the "effective" electron temperature.

In addition to electrons, the temperatures of the ions and neutrals require some comment. Typical values for these (ref 16) are 300 K (neutrals) and 500 K (ions). Thus the negative glow can be regarded as a cold, quasi-neutral plasma. The density of charged particles (either ions or electrons) in this region is very low. It is usually quantified in terms of the degree of ionisation, α, which is the fraction of charged particles

relative to the total gas number density. The value for α, based on Langmuir probe data (eg ref 23), is typically in the order of 10^{-5}.

3.2.2.2 The sheath regions

For the purposes of describing the anode and cathode sheath regions, it is necessary first, to consider an electrically isolated body immersed in the negative glow. The body will be immediately struck by ions and electrons arising from their random motion. However, the average electron velocity is considerably higher than that of the ions due to the high temperature and low mass of the former. This results in the body receiving a much higher electron impingement rate initially, and then becoming negatively charged. The negative charge produces a negative potential, V_f, on the body with respect to the plasma potential, V_p (V_f and V_p are defined relative to earth). The magnitude of $V_f - V_p$ is determined by the amount of repulsion required to reduce the electron flux impingement rate to that of the ions. Thus a positive space charge sheath is set up in the vicinity of the body which ensures that no net current is received, and, from ref 16,

$$\text{Sheath potential} = V_p - V_f = (kT_e/2e)\ ln\ (m_i/2.3\ m_e) \qquad (3.2)$$

where k = Boltzmann constant, T_e = electron temperature, e = electronic charge, m_i and m_e are the ion and electron masses respectively. Equation 3.2 allows for the effects of the "Bohm Criterion", although it is beyond the scope of this work to explain the phonemenon. Assuming the only ionic species to be Ar^+ and T_e to be 2 eV, the equation predicts the sheath potential to be about 10 volts.

The anode can now be considered. The cathode current comprises a flow of electrons achieving neutralisation of bombarding ions and, to a lesser

extent, "secondary" electron emission. The anode therefore has to balance this cathode current by collecting an equal electron current. As in the case of a floating body, the anode will initially receive more electrons than ions anyway, simply due to random motion effects. However, if the anode is small, the net random electron flux collected may not be large enough to balance the cathode current and a negative space charge will accumulate in the vicinity of the anode. The space charge will produce a potential drop which is just sufficient to create additional electrons through ionisation of the gas surrounding the anode. Therefore, a small anode develops a sheath for attracting electrons. In this case then, V_p will be lower than the anode potential, though it would never be more than the ionisation potential of the gas (ref 26) ie, 15.8 volts for argon.

Usually, the anode of a diode discharge in an ion plating chamber is large. The anode is normally at earth potential and is either part of the chamber (eg, the top and bottom plates of the system in Figure 1.1) or, in the case of an all metal system, it is the chamber itself. For large anodes, the total random electron flux collected may be larger than that required to balance the cathode current. In this situation, a positive space charge will accumulate at the anode, with a corresponding sheath potential large enough to repel the excess electrons. If the anode area approached infinite size, then the sheath potential would approach the value of $(V_p - V_f)$ predicted by Equation 3.2 because the net electron current required per unit collecting area would approach zero. Thus Equation 3.2 predicts the maximum positive space charge potential which could occur. The calculation performed earlier, predicts this value to be about 10 volts. As the anode is normally earthed, V_f is zero. Therefore, it may be concluded that the plasma potential, V_p, will probably be between 0 and 10 volts above earth potential for a DC diode argon discharge set up in an ion plating

chamber. This concurs with the experimental results of Ball (ref 23) who found V_p values of 1 or 2 volts above earth in a DC diode discharge.

The cathode sheath region is also known as the cathode dark space (as in Figure 1.1), Crookes dark space, or cathode fall region. As stated in Section 1.2, most of the discharge potential is dropped across the cathode sheath. This is because the field across the negative glow is negligible, (being a quasi-neutral plasma) and the anode sheath potential is small in comparison with the bias applied to the cathode. In fact, if the negative glow is assumed to be field-free, then the cathode sheath voltage will be the applied bias, V_c, added to the plasma potential, V_p. Thus, if V_p is +5 volts and V_c (with respect to earth) is -2 kV, then the cathode sheath voltage will be -(2000 + 5) volts, ie -2.005 kV.

The cathode sheath may be considered to be a thin pre-sheath region and a much larger positive space charge region. The pre-sheath region, at the edge of the negative glow, is comparable to the anode sheath. Here, the electron density becomes rapidly negligible, leaving a positive space charge of more or less uniform ion density; this region being typically less than a few tenths of a mm thick. The negative bias applied to the cathode however, produces the main positive space charge region and here, the ion density is not uniform. This region is typically a few cms thick and dominates the behaviour of the cathode sheath. In practice, secondary electron emission from the cathode may change the nature of the main positive space charge region, though as the electrons rapidly accelerate away from the sheath and they only contribute to about 10% of the cathode current (as inferred in Section 3.2.1.1), their effect may be considered to be negligible.

Chapman (ref 16), has suggested that the cathode current density, J, in a diode discharge, is close to the space charge limited current density represented by the free fall version of the Child-Langmuir equation, ie:

$$J = (4\varepsilon_o/9)(2q/m_i)^{1/2} V_c^{3/2}/L^2 \qquad (3.3)$$

where ε_o = permittivity of free space, q = ion charge, m_i = ion mass, V_c = cathode bias (which is assumed to be equal to the cathode sheath voltage) and L = sheath thickness. Equation 3.3 will be considered in more detail in Section 3.3.2.

3.2.3 A Simple Model

Figure 3.4 is a schematic, representing the main regions and processes occurring in a low pressure DC diode argon glow discharge. The negative glow is assumed to be virtually field free and approximates to a cold plasma of very low charged particle density. As the plasma potential is only a few volts positive with respect to earth, the cathode sheath voltage is essentially the same as the bias applied to the cathode. The cathode sheath is typically a few cms thick, whereas the anode sheath is less than a few tenths of a mm.

The main processes are as follows: The cathode is bombarded by ions, high energy neutrals, thermal neutrals (ie, neutrals near to room temperature, which make up the bulk of the gas number density) and photons.. Secondary electron emission occurs at the cathode surface, primarily as a result of ion bombardment. These electrons accelerate across the cathode sheath due to the repulsive field in this region until they enter the negative glow, where they are designated as primary electrons. Most of the ionisation is believed to occur in the negative glow, the main mechanism being by electron impact (ref 16). Electrons are the most efficient ionising particles, followed by ions and, lastly, photons (ref 21). Ion impact ionisation requires relatively high ion energies (see Figure 3.3)

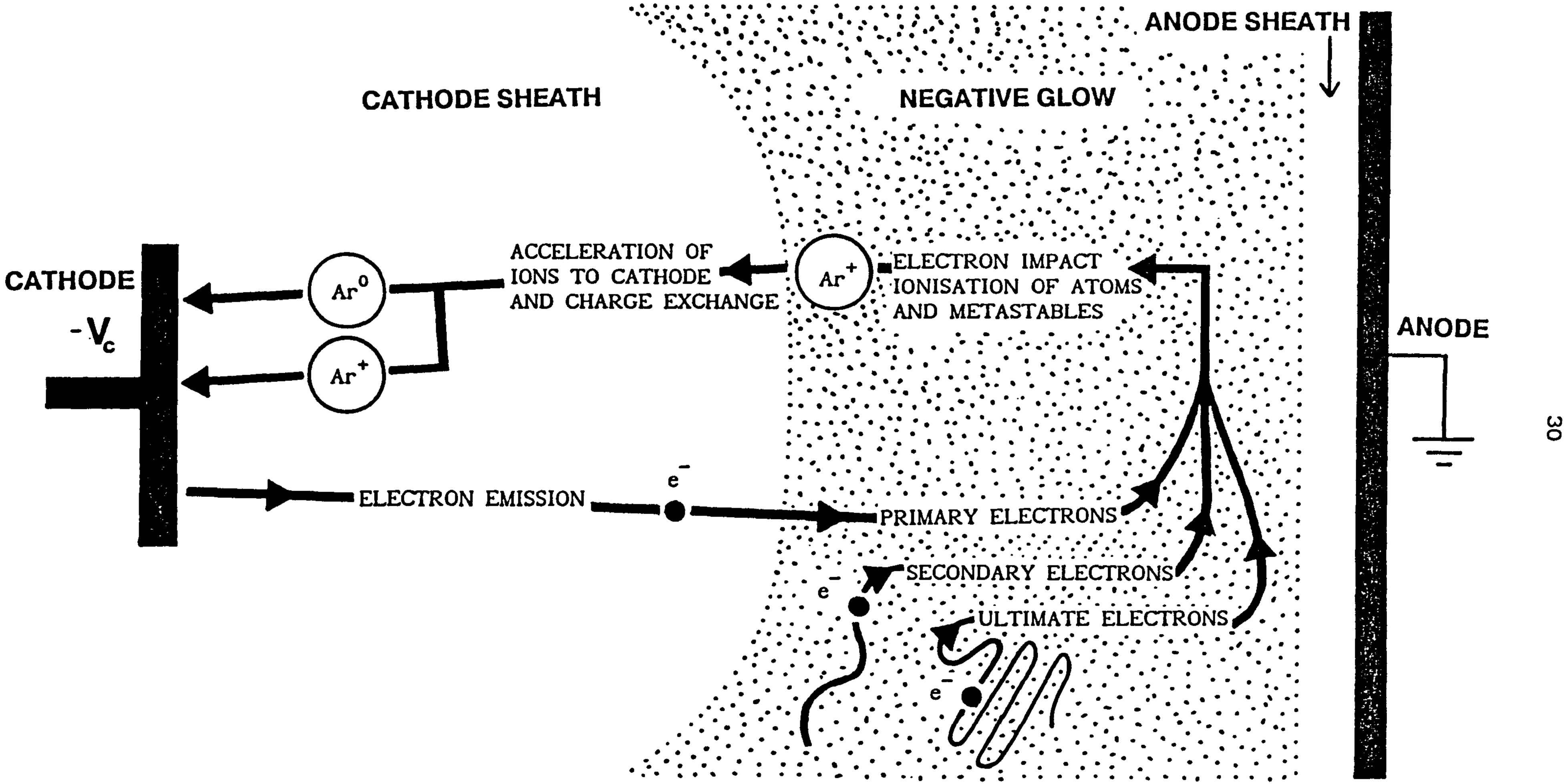

Figure 3.4 Schematic of a low pressure DC diode argon glow discharge.

which are not present in the negative glow.

The primary electrons ionise the argon atoms, though because the lower energy electron groups have a distribution of energies (assumed Maxwellian) the high energy end of their distributions will also contribute to electron impact ionisation. In addition, ionisation of the argon metastables would only require about 4.2 eV as opposed to the 15.8 eV for argon ground state atoms. Argon single charge ions (Ar^+) are the dominant ionic species; evidence of this can be seen, for example, in the ion mass spectroscopy data in ref 22.

Some of the ions will move towards the negative glow edge of the cathode sheath and accelerate across the sheath to bombard the cathode. During their traversal however, a proportion of these ions will undergo charge exchange collisions with thermal neutrals present in the sheath. The incident ion becomes a high energy neutral (as most of its original kinetic energy is retained) and the newly formed low energy ion begins to accelerate. Although the ion current density is unaffected by this process, the energy distribution of the ions (and neutrals) arriving at the cathode, is profoundly influenced. This will be investigated in Section 3.3.

The model represented by Figure 3.4 could be criticised for being too simplistic. However, it provides a good foundation for considering some of the important mechanisms which influence the ion plating process.

3.3 ION AND NEUTRAL ENERGY DISTRIBUTIONS

3.3.1 Quantification of Charge Exchange Phenomena

3.3.1.1 Theoretical background

It has been reported in ref 27 that charge exchange collisions within the cathode sheath were considered to be an influential mechanism as early

as 1931. It took another 30 years though, to develop an experimentally verified quantitative theory which relates charge exchange to the resulting ion energy distribution incident at the cathode. This was the work of Davis and Vanderslice (ref 28) which has been extensively quoted in the literature. Their model was developed with the following assumptions:

(i) All ions originate in the negative glow or the cathode pre-sheath region (as described in Section 3.2.2.2).

(ii) The dominant collision process is symmetrical charge exchange, the incident energetic ion interacting with its neutral counterpart to produce an equally energetic neutral and a new ion with initially zero energy.

(iii) The collision cross section for charge exchange is independent of energy.

(iv) The electric field decreases linearly from the cathode to the edge of the negative glow.

Rickards (ref 29) modified the model to produce a more general form which enables field distributions other than the linear case (iv) to be considered. This gives:

$$\frac{dN}{dE} = \frac{N_o}{m}\frac{L}{\lambda_c}(1-E)^{(1/m)-1}\exp\left[-\frac{L}{\lambda_c}+\frac{L}{\lambda_c}(1-E)^{1/m}\right] \qquad (3.4)$$

where E = ion energy incident at the cathode, relative to the maximum and therefore lies between zero and unity, N_o = number of ions entering the sheath from the negative glow, L = cathode sheath thickness, λ_c = mean free path for symmetrical charge exchange and m = field distribution parameter. A linear field distribution is assumed when m = 2 and Equation 3.4 is then equivalent to the original Davis and Vanderslice model.

Figure 3.5 shows the energy distributions predicted by the equation for the linear field case (after ref 28). It is clear that as the value of L/λ_c is increased, the proportion of higher energy ions diminishes. The proportion of ions which do not undergo charge exchange collisions and therefore reach the cathode with maximum energy (E=1) is given by:

$$N/N_o = \exp(-L/\lambda_c) \qquad (3.5)$$

and clearly this is independent of the field distribution. The effect of these ions has not been included in the curves of Figure 3.5, though the values of N/N_o are shown as percentages to the right of each curve.

Figure 3.6a shows predicted ion energy distributions for L/λ_c values of 0.1, 1 and 10 (after ref 29) using the linear field case (m=2), the mobility limited case (m=3/2, which is discussed in Section 3.3.2.3), and the space charge limited free fall case (m=4/3). If the free fall Child-Langmuir equation (Equation 3.3) is assumed to be representative of the cathode sheath characteristics then the most appropriate value for m would be 4/3. However, Figure 3.6a shows that the curves are not particularly sensitive to these changes in m. Figure 3.6b is a similar set of curves, predicted for the high energy neutrals generated by charge exchange. These curves were generated by Monte-Carlo calculations (ref 29) and show that the neutrals have a significantly lower high energy content than the ions at equivalent L/λ_c values.

3.3.1.2. Comparison with experimentally determined distributions

Davis and Vanderslice (ref 28) measured the ion energy distributions at the cathode of a diode discharge using various gases (including argon) and compared the results with their theory. A small orifice at the centre

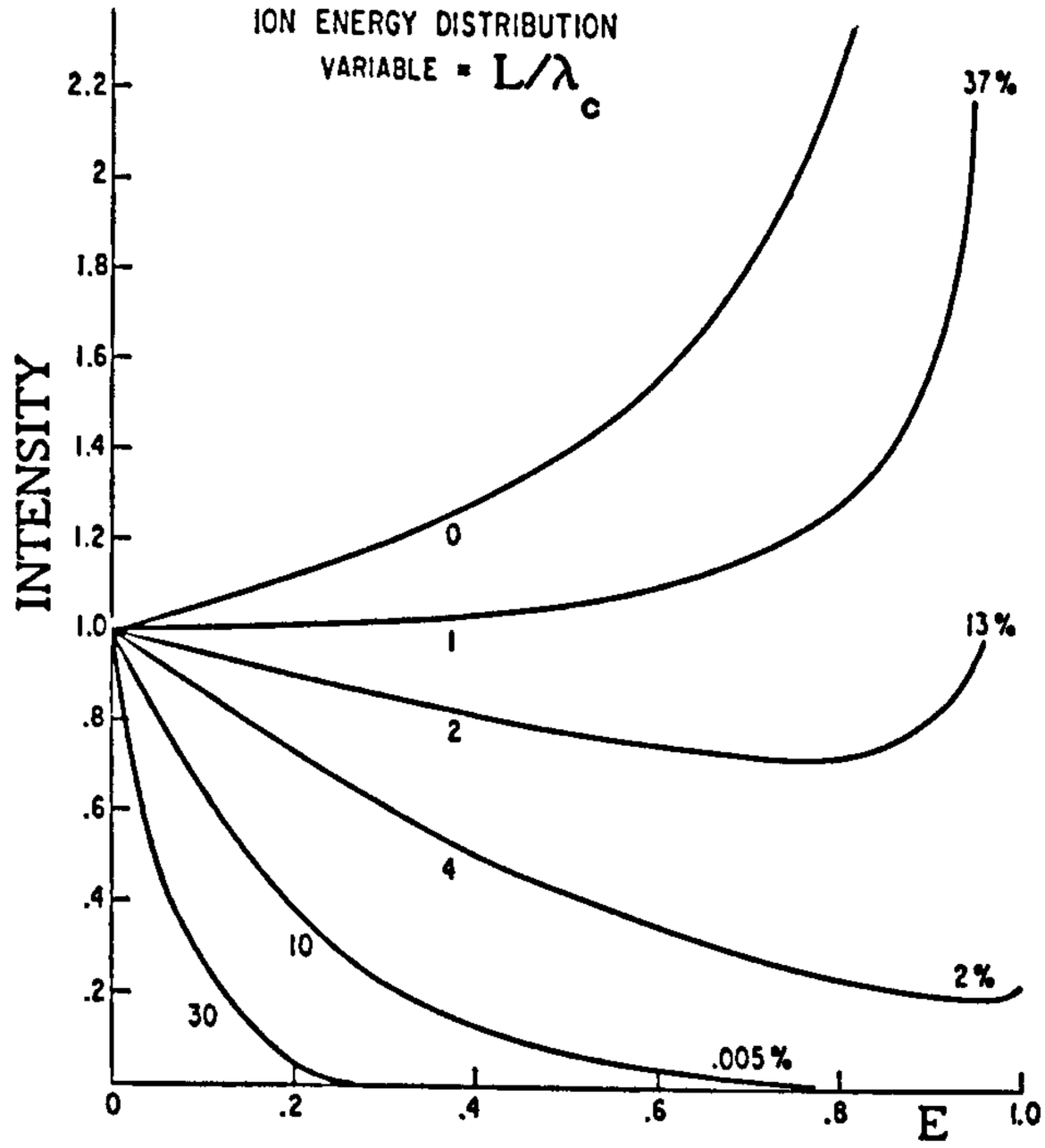

Figure 3.5 Calculated ion energy distributions for various values of L/λ_c using Equation 3.4 (m = 2, intensities normalised at E=0). Percentages to the right of each curve refer to the proportion of ions which arrive at the cathode with maximum energy (after ref 28).

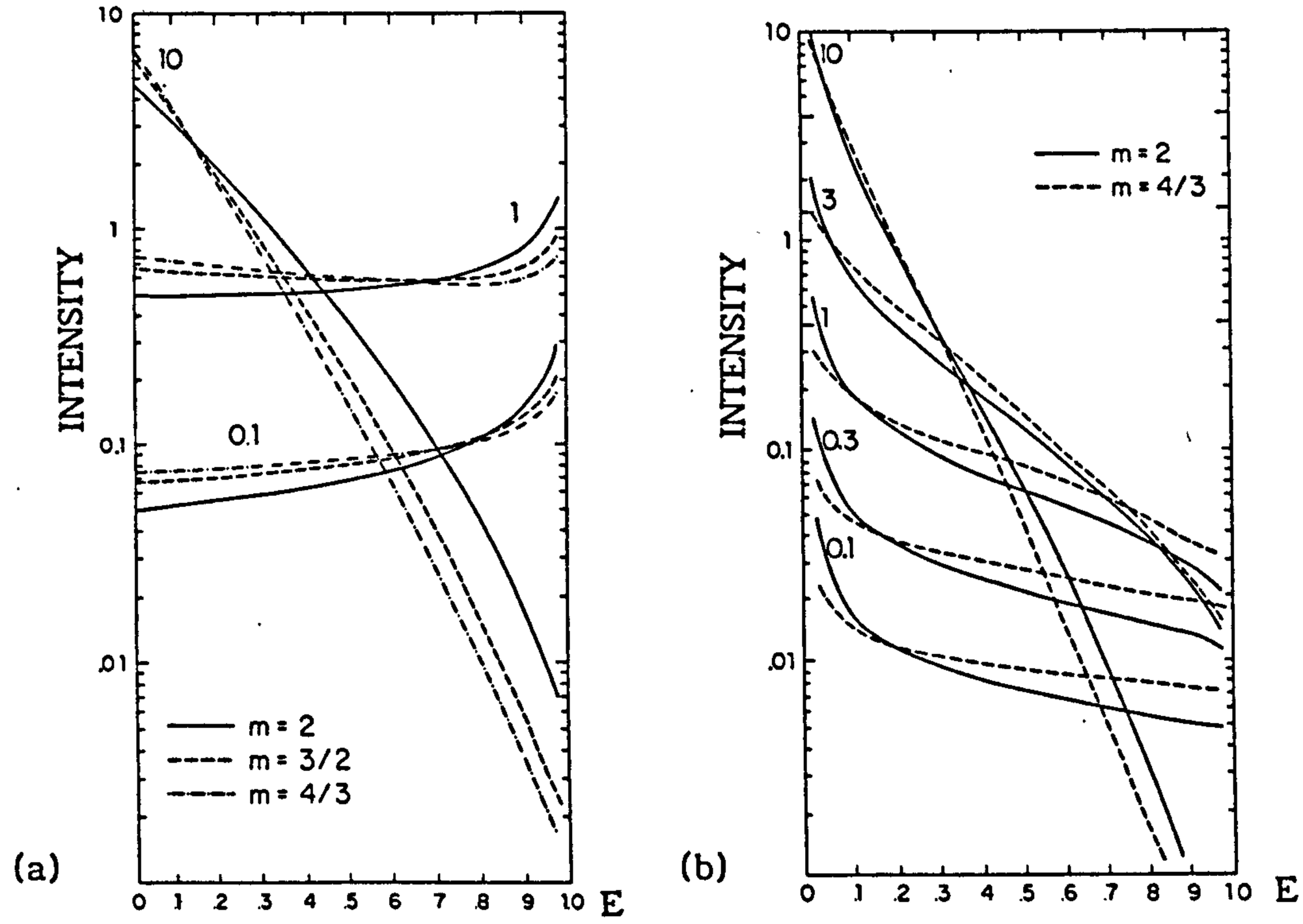

Figure 3.6 Predictions by Rickards using the Davis and Vanderslice model for different field distributions, m : (a) ions, (b) neutrals (Monte-Carlo calculation). Numbers on each group of curves refer to the L/λ_c value (after ref 29).

of the cathode was used for extracting the ions. The ion energies were analysed by a sector type electrostatic analyser and species discrimination was achieved by means of a magnetic analyser. An electron multiplier was used for detection. In general, the experimental results agreed with the theory. Figure 3.7 shows the measured Ar^+ energy distribution from a pure argon discharge, the optimum theoretical fit being when L/λ_c is 15. Ar^{2+} ions were also studied and this gave an L/λ_c result of 2.3, indicating that the Ar^{2+} collision cross section for charge exchange is significantly smaller than the value for Ar^+.

Other workers have also measured argon ion energy distributions, using similar techniques. In a number of cases, some apparent disagreement with the theory has been observed. Examples of this are shown in Figure 3.8. All the experimental curves show ions at low energies being at or near to zero intensity. As will be shown later, L/λ_c for argon DC diode discharges is typically between 10 and 15. Therefore, a result similar to the curve in Figure 3.7 might be expected. The low energy discrepancy in Figure 3.8a has been attributed to scattering effects at the sampling orifice in the cathode, which is said to increase at decreasing energies (ref 31). The discrepancy in Figure 3.8b is attributed, in ref 32, to the rapid drop in gas pressure near the relatively large cathode aperture. This would reduce the likelihood of low energy ion formation (region A) and ions formed at intermediate energies would be less liable to further collisions (region B). The high energy peak (region C) is explained in ref 32 as being due to the contribution from Ar^{2+} ions (L/λ_c being much smaller), as there was no ion species discrimination. There are also peaks at higher Ar^+ energies in Figure 3.8a, these occurring at about 1/3 of the maximum energy (cathode bias was 3 kV). Although no explanation has been proposed by the authors, the peaks might be attributed to some alternative

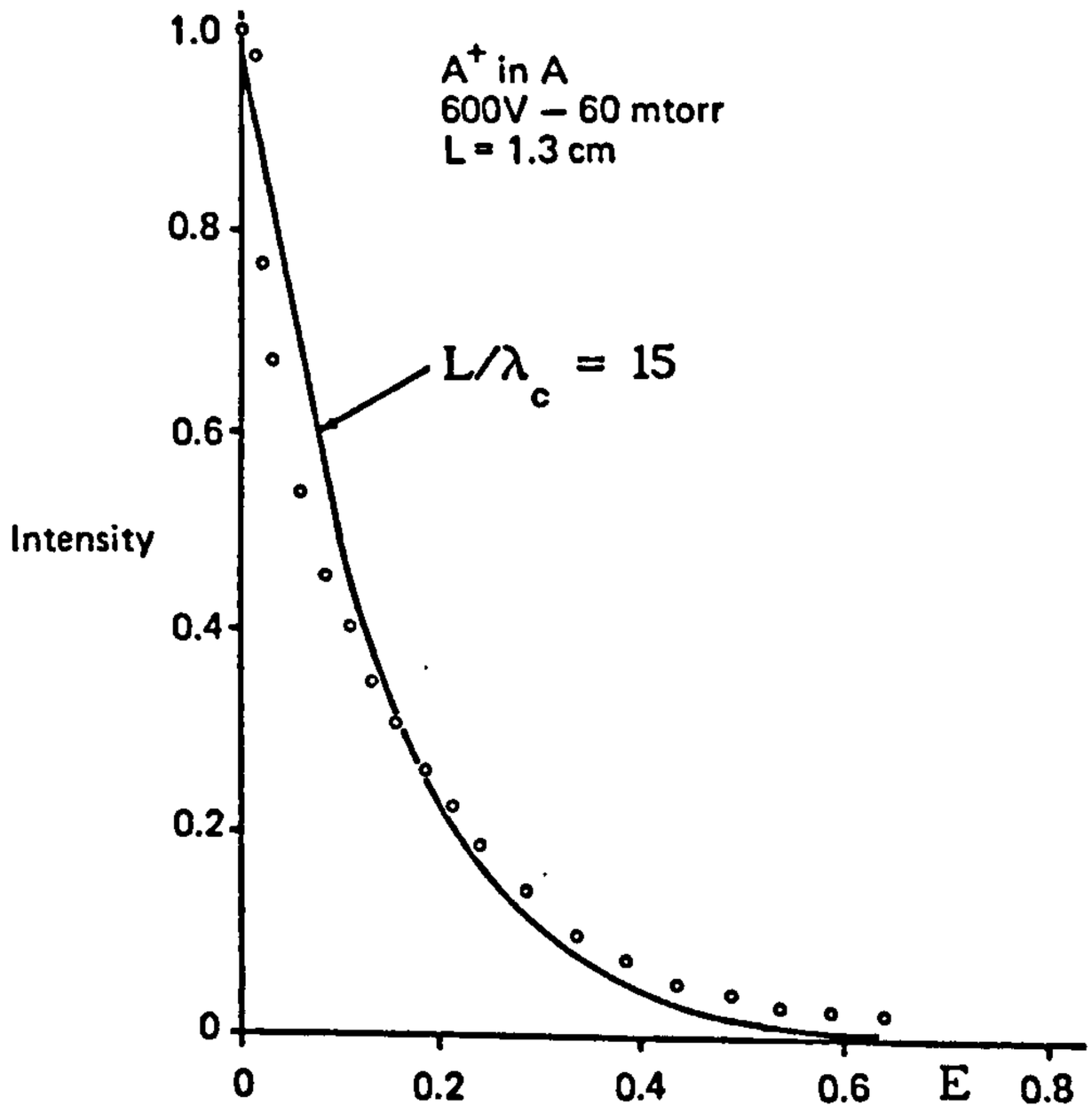

Figure 3.7 Energy distribution for Ar^+ ions at the cathode of an argon diode discharge. Solid curve represents the best theoretical fit to the experimental data (after ref 28).

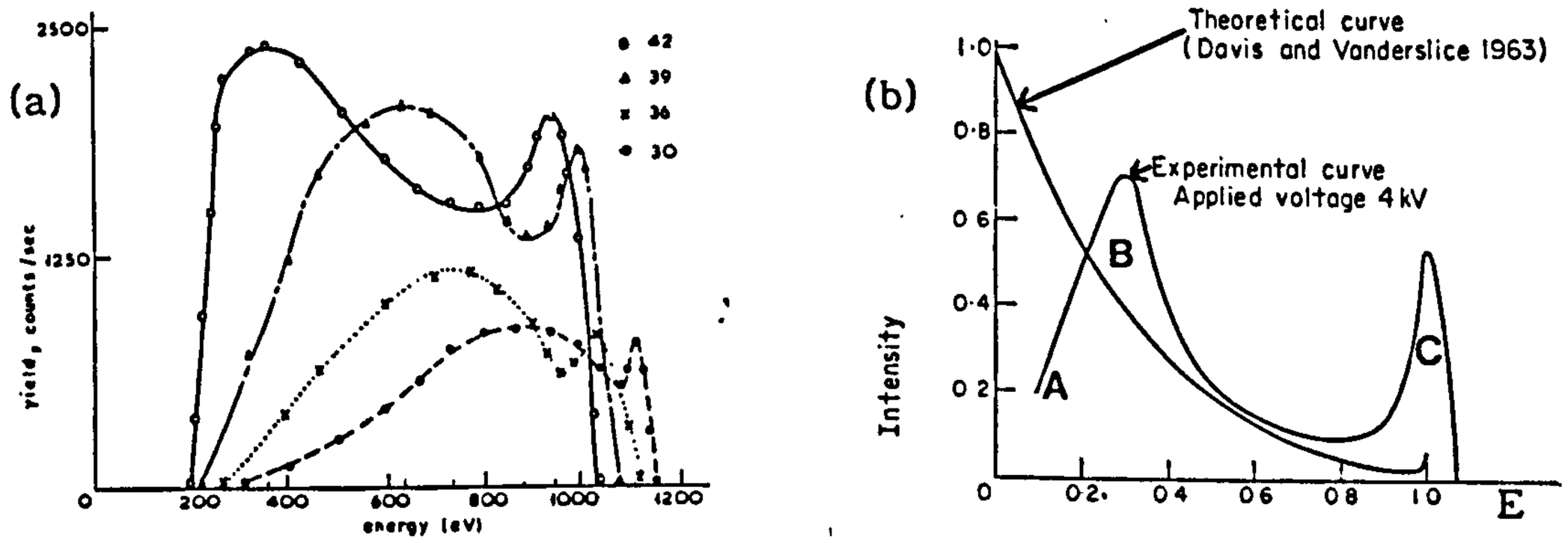

Figure 3.8 Examples of measured ion energy distributions (argon diode discharges) which show disagreement with the Davis and Vanderslice theory: (a) Ar^+ ions at different discharge pressures (key in mTorr, after refs 30, 31), (b) Argon ions (no species discrimination) sampled from a system designed as an ion beam source (after ref 32).

interaction involving Ar^+, other than symmetrical charge exchange.

The main area of disagreement with theory though, seems to be at low ion energies. The explanations put forward to explain the discrepancies, suggest that the main cause might be an experimental artefact rather than an oversight in the theory. The low energy ions may not be detected in some analyser systems because of, for example, the pressure drop caused by the samping orifice. As the analysing systems employed behind the cathode have to be operated at pressures considerably lower than those used in the discharges, a rarefication in gas density must occur around the orifice on the discharge side. This in turn would reduce the probability of ion creation near the cathode and reduce the number of low energy ions detected. Also, the orifice could distort the electric field distribution causing ions to traverse the aperture on trajectories at oblique angles to the cathode surface. Lower energy ions would tend to be influenced more by the distorted field and this would also reduce their probability of detection. Larger orifice sizes would increase the influence of pressure gradients and field distortion. Higher discharge pressures would also create larger pressure gradients. Therefore, provided that a small sampling orifice is used and the discharge pressure is sufficiently low, good agreement with the theory might be expected.

Figure 3.9 summarises the available published work on experimentally determined ion energy distributions in terms of agreement or disagreement with the theory. It is interesting to note that disagreement with the theory occurs typically when the product of discharge pressure and orifice diameter is greater than 10 mTorr.mm and this supports the suggestions made above. Table 3.1 gives the references and other information used in Figure 3.9.

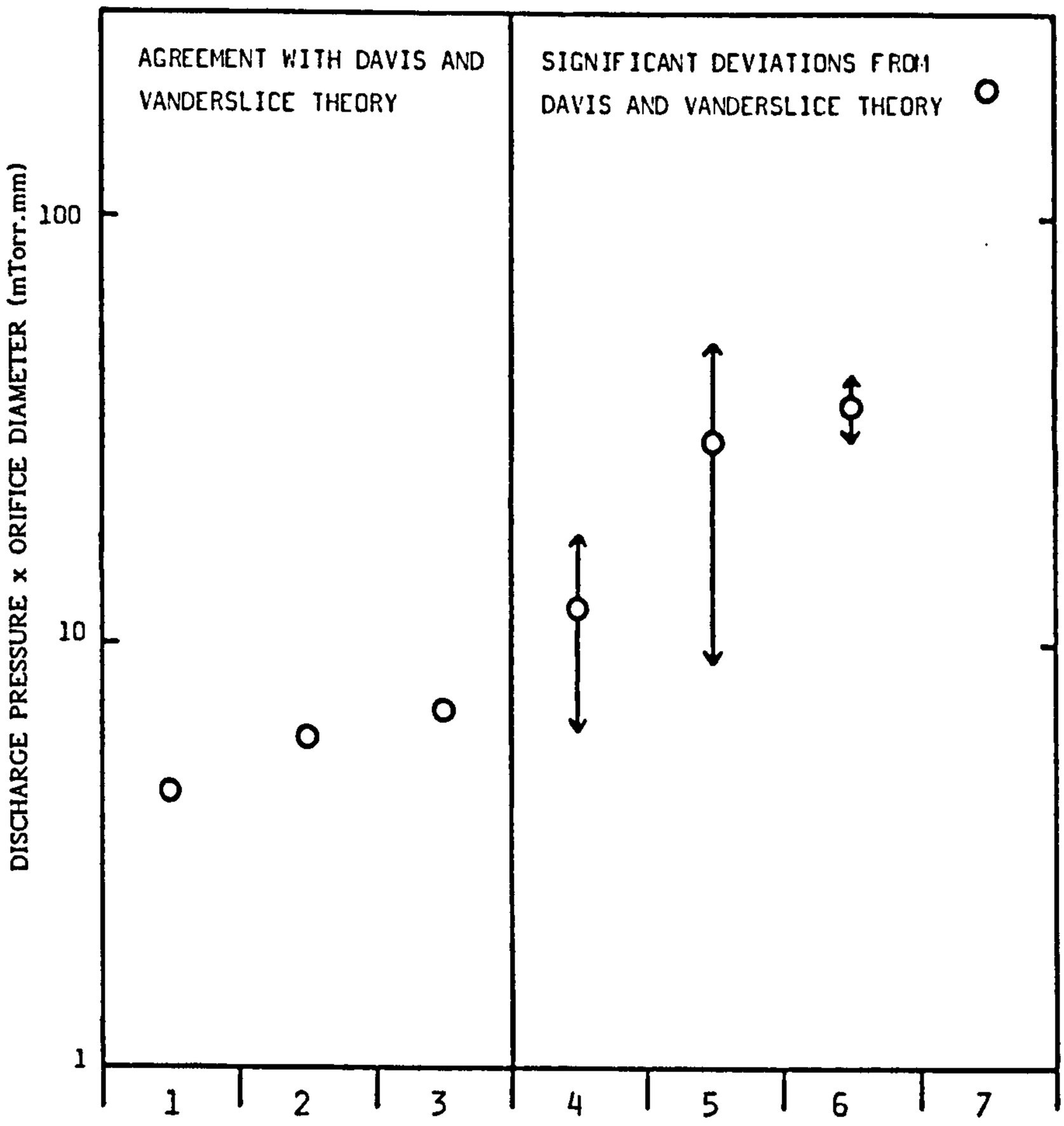

Figure 3.9 Logarithmic plot of the product of discharge pressure and cathode sampling orifice diameter for experimental equipment used to measure argon ion energy distributions in the published literature. Further information is given in Table 3.1.

Figure 3.9 Reference	Publication Reference	Cathode Orifice Diameter (mm)	Discharge Pressure (mTorr)
1	33,34	0.30	15
2	28	0.10	60
3	35	0.23	30
4	36	0.30	20 - 60
5	37	1.00	9 - 50
6	30,31	1.00	30 - 42
7	32	1.00	200*

Table 3.1 References, orifice size and pressure information used in Figure 3.9. * = estimated pressure near the cathode.

Some comment is required on the type of energy analysis systems used by workers in this field. In some systems, the sampling window (ΔE) is not constant, but increases in width linearly with relative energy, E. Thus, as the ion energy decreases, the intensity is seen to fall towards zero with this type of system, distorting the measured distribution. The work published in refs 30, 31, 33, 34, 35 and 37 used a varying sampling window and the distortion effect has been allowed for in Figure 3.9. A further complication is that cumulative energy distributions are also sometimes published, as in refs 33 and 34.

In addition to experimental ion energy distributions, the high energy neutrals also require consideration. In Section 3.3.1.1, Monte-Carlo calculations predicted that the neutral energy distributions would have less high energy content that the ions for a given L/λ_c value (see Figure 3.6). Unfortunately, there appears to be little experimental data available on neutrals, but the results shown in Figure 3.10 (after refs 30,31), even

though they are distorted as previously discussed, seem to confirm the predictions.

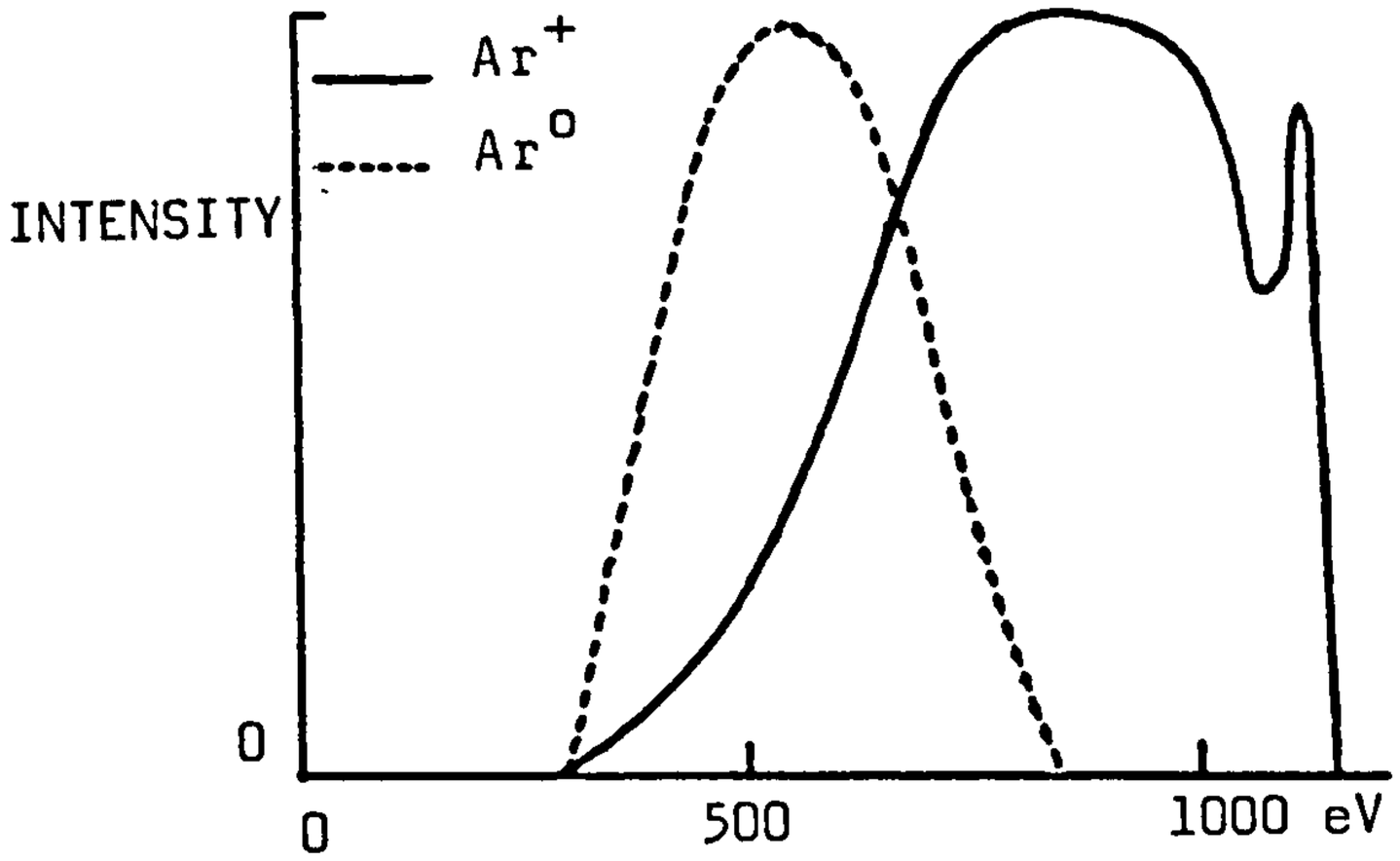

Figure 3.10 Measured energy distributions of Ar^+ and Ar neutrals from a 30 mTorr 3kV argon diode discharge (after refs 30, 31).

The work reviewed here has shown that L/λ_c is a very important parameter. It would therefore be useful to predict the value of L/λ_c for various argon discharge configurations, by evaluating L and λ_c from readily measurable system parameters.

3.3.2 Evaluation of the Cathode Sheath Thickness, L.

3.3.2.1 Background

Aston's equation (eg, ref 38) is often quoted in the literature. This shows, to a first order approximation, that the size of L is inversely proportional to the discharge pressure used in a DC diode discharge. The

relationship is empirical however, and as it can only be applied to diode configurations, its use is inappropriate for predicting L in discharges where some form of ionisation enhancement is employed. An alternative expression, based on theoretical considerations, is the free fall version of the Child-Langmuir equation, discussed in Section 3.2.2.2. By transposition of Equation 3.3, we get:

$$L = (4\varepsilon_o/9J)^{1/2} (2q/m_i)^{1/4} V_c^{3/4} \qquad (3.6)$$

Thus L may be predicted from a knowledge of V_c, J and the ion charge to mass ratio. However, Equation 3.6 is based on the following assumptions:

(i) The cathode has only one face exposed to the discharge, this being flat and infinitely large.

(ii) Only one type of charged species is present (in this case, Ar^+ ions).

(iii) The charged particles enter the sheath with zero initial energy.

Assumption (i) can be approximately achieved by taking measurements of J and V_c from a large flat cathode, with the rear face and edges shielded from exposure. The shielding may be part of the chamber wall or a separate ground shield.

Assumption (ii) cannot be achieved in practice, because of, for example, secondary electron emission from the cathode, the presence of sputtered ionic species, multiply charged ions and ionised contaminants. However, as previously discussed, this may not be highly significant. ArH^+ is likely to be one of the major contaminants (as reported in Section 3.5.2.3), though as its charge/mass ratio is very close to that of Ar^+, the influence on Equation 3.6 will be negligible.

With regard to (iii), the ions enter the sheath with finite energy. The full version of the free fall Child-Langmuir equation accounts for this

factor, though it is not often quoted in the literature:

$$L = (4\varepsilon_o/9J)^{1/2} (2q/m_i)^{1/4} V_c^{3/4} \left[1 + 2.66 (kT_i/qV_c)^{1/2}\right]^{1/2} \quad (3.7)$$

where k = Boltzmann constant and T_i = ion temperature. Equation 3.7 is based on information from refs 39 and 40. As discussed in Section 3.2.2.1, an appropriate value for the ion temperature in the negative glow would be 500 K. Using this value for T_i and V_c = 1 kV, L is predicted to be less than 1% larger using Equation 3.7 compared with Equation 3.6. Even for V_c = 100 volts, the change is less than 3%. Therefore, the effect may be regarded as negligible. There is however, another potential problem. The pre-sheath region (Section 3.2.2.2), will accelerate the ions to energies significantly greater than the 500 K value quoted above, ie up to 10 eV (if V_p is 10 volts). Substituting kT_i = 10 eV into Equation 3.7 gives a change of 13% for V_c = 1 kV and 36% for V_c = 100 volts. These predicted errors might be a little pessimistic though. In practice, there would not be a well defined boundary between the pre-sheath and main space charge regions. Therefore, at least part, if not all of the pre-sheath behaviour could be assumed to be represented by the Child-Langmuir relationship for practical purposes.

Greater accuracy might be achieved by substituting V_c in Equation 3.6 with $|V_c| + V_p$, the actual cathode sheath potential. For diodes, and triode configurations where the additional electrode is negatively biased, V_p will depend on the (earthed) anode as discussed in Section 3.2.2.2. The magnitude of V_p will therefore be small in comparison with V_c and could be ignored. This would not be the case, however, if an electrode was inserted into the system, which was positively biased with respect to the original anode. The new electrode would then become the true anode, raising V_p to a

value close to the applied anode potential. For a small anode, V_p would be slightly less than the anode potential but not by more than the gas ionisation potential, as previously discussed. Thus for a triode system with a positively biased electrode, the value for $|V_c| + V_p$ would have to be used in Equation 3.6.

Equation 3.6, based on the discussions above, may provide a convenient means of predicting L. To evaluate its performance would require measured L values to be compared with those predicted by the equation.

3.3.2.2 Experimental

A circular mild steel cathode, 24.6 cms in diameter and 0.11 cms thick was used for this work. To prevent the rear face and edges being exposed to the discharge, a ground shield, also of mild steel, was fitted. The clearance between ground shield and cathode was small enough (2.5 ± 0.5 mm) to stop any secondary discharge forming. Rig (1) was used for this work and Figure 3.11 shows the cathode in an argon diode discharge at about 40 mTorr with V_c = 2 kV; the cathode sheath being clearly visible. L was measured by direct observation, using a steel strip with notches at 1 cm intervals mounted inside the view port, and a perspex rule fitted to the exterior. The distance between the steel strip and the rule was about 3 cms, so that parallax errors were prevented. After initial pump down, argon was introduced and a diode discharge was run for about 20 minutes. The chamber was subsequently pumped down to ultimate pressure again and the process was repeated a few times to minimise contamination effects (eg, due to water vapour) and to sputter clean the cathode. This procedure was performed prior to every period when sheath thickness measurements were to be taken.

In addition to argon diode discharges, sheath thickness measurements

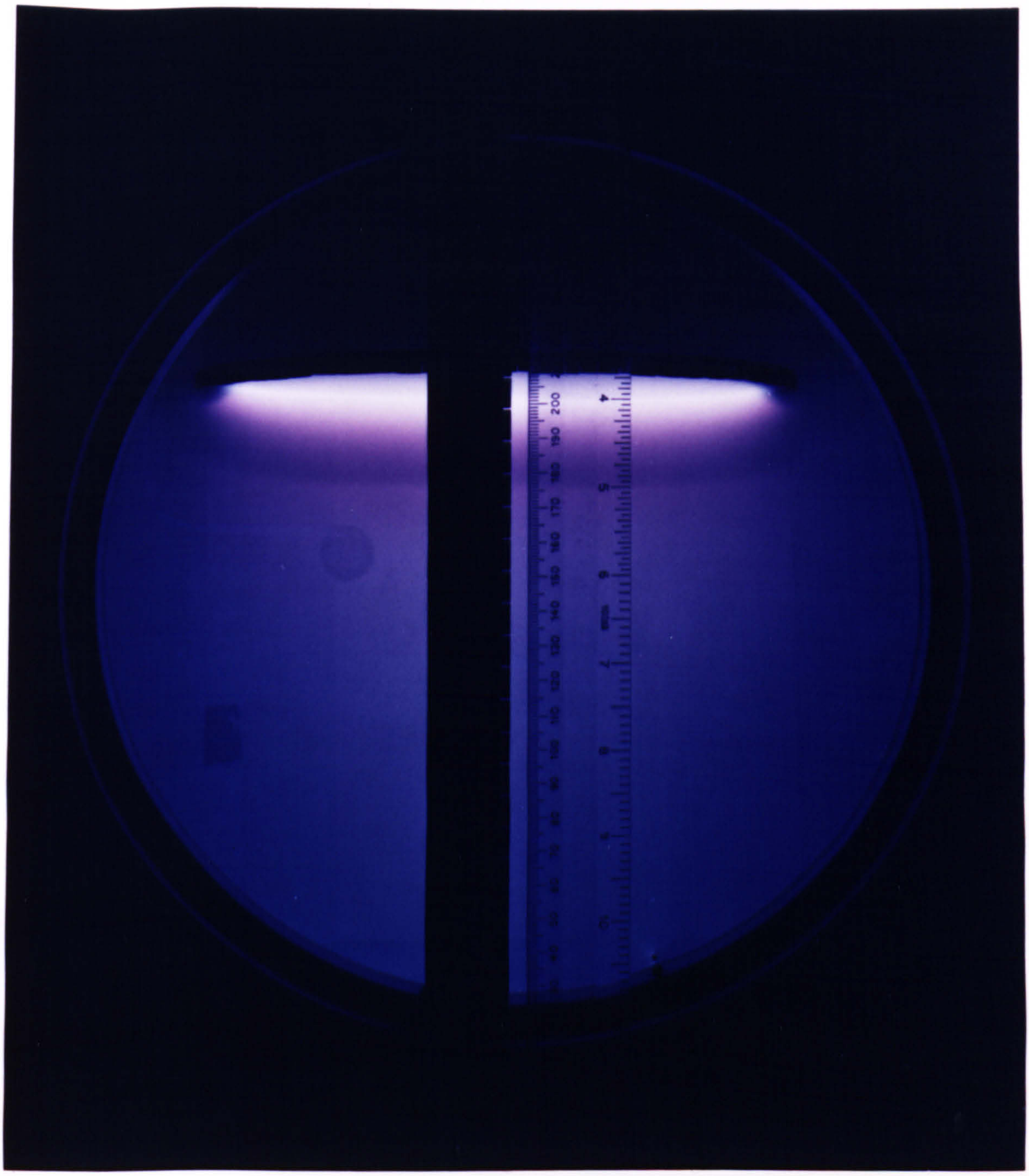

Figure 3.11 Experimental arrangement used for measuring cathode sheath thickness. The discharge shown is an argon diode at about 40 mTorr pressure.

were also performed on argon thermionic triodes and nitrogen discharges (the latter are reported later, in Section 3.5.2.2). The thermionic triode discharges utilised a filament made from 0.7 mm diameter tungsten wire, 30 cms in length. This was coiled to reduce the length to about 15 cms and fitted directly above the vapour source crucible, approximately 20 cms below the cathode face.

3.3.2.3 Results and comments (argon discharges)

In addition to data obtained from this work, results of sheath thickness measurements from published sources were also used to test Equation 3.6. Table 3.2 summarises the sources of reference and the discharge details.

REF	DISCHARGE TYPE	PRESSURE RANGE (mTorr)	CATHODE VOLTAGE RANGE (kV)	NOTES
33	TRIODE (+VE ELECTRODE)	15	3.00	(a)
36	DIODE	20-60	1.00 - 1.81	-
39	THERMIONIC TRIODE	0.8	0.25 - 0.87	(b)
41	DIODE	12-65	2.15 - 5.85	-
42	DIODE	80	1.77	-
THIS WORK	DIODE	20-100	0.80 - 2.00	-
THIS WORK	THERMIONIC TRIODE	5-50	0.50 - 2.00	(c)

Notes:

(a) Positive electrode voltage was 0 to 250 V, thus V_p = 0 to 250 V.

(b) Anode was not earthed. Measured V_p = 50 ± 10 V.

(c) Filament bias = 20 to 150 V (negative).

Table 3.2 Summary of data sources for testing cathode sheath predictions from Equation 3.6.

As discussed in Section 3.3.2.1, V_c was replaced by $|V_c| + V_p$ in Equation 3.6 for data from refs 33 and 39. Figure 3.12 is a logarithmic plot of measured versus predicted values of cathode sheath thicknesses. Although there is considerable scatter in the data, the graph shows a general agreement between measured and predicted values. Note that the thermionic triode sheath thicknesses tend to be of the order of mm, in contrast with the diode, where they are typically several cms. Discharges utilising a positively biased third electrode for enhancement (ref 33) show thicknesses similar to those obtained under diode conditions.

Table 3.3 summarises the results in terms of mean and standard deviation values of L_{MEAS} / L_{PRED} ratios for the different data groups.

DATA GROUP	NUMBER OF DATA POINTS	L_{MEAS} / L_{PRED} MEAN	L_{MEAS} / L_{PRED} STD. DEVIATION
PUBLISHED (DIODE + TRIODE)	45	1.237	0.260
THIS WORK (DIODE)	41	0.908	0.127
THIS WORK (TRIODE)	17	1.196	0.251
THIS WORK (DIODE + TRIODE)	58	0.992	0.216
ALL GROUPS	103	1.109	0.241

Table 3.3 L_{MEAS} / L_{PRED} results for data used in Figure 3.12.

The following observations can be made from Table 3.3:

(i) The standard deviation for the published data group has the largest value. This is perhaps to be expected, because of uncertainties in the methods of measurement employed by other workers and the accuracy of their results.

(ii) The standard deviation for diode data in this work is considerably

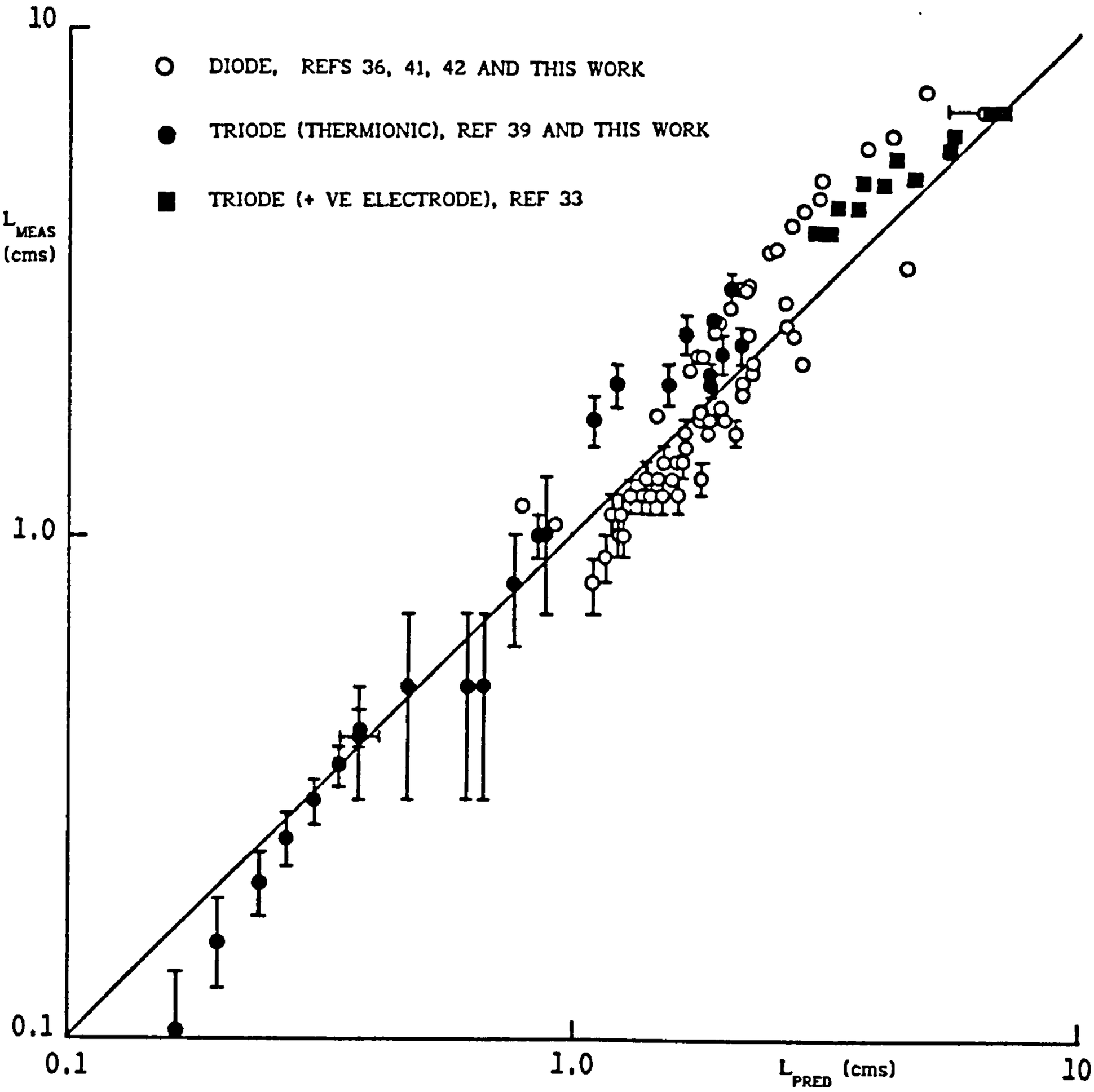

Figure 3.12 Plot of measured versus predicted cathode sheath thicknesses for argon DC discharges, utilising a flat cathode with bombardment on one face only. Data from various sources.

less than the equivalent triode result. This can be attributed to the greater difficulties incurred with sheath thickness measurements under thermionic triode conditions. Light emission from the filament tended to reduce the sheath visibility making measurements prone to larger errors.

(iii) Results from this work show that L_{MEAS} is less than L_{PRED} for the diode, yet the inverse is true for the triode data. The higher gas pressures used in the diode work may be a factor because mobility limited (rather than free fall) effects in the sheath might be expected to become more significant as gas number density is increased. The mobility limited version of the Child-Langmuir equation is (ref 16):

$$J = (9\varepsilon_o / 8)\ (V_c^2 / L^3)\mu \qquad (3.8)$$

where μ is the mobility. If mobility has any influence at higher (diode) pressures, then as pressure is increased, μ will decrease. For a given value of J and V_c, this will reduce the sheath thickness, in accordance with Equation 3.8. Thus under diode conditions, L_{MEAS} could be less than the value of L_{PRED} predicted from the free fall version of the equation due to this effect.

The relatively smaller L_{PRED} values for the triode data might also be attributed to ion temperature effects and the pre-sheath region, outlined in Section 3.3.2.1 (see Equation 3.7). The tendency to use lower cathode biases under triode conditions would increase the discrepancy between Equations 3.6 and 3.7, making the value of L_{PRED} from Equation 3.6 smaller in the absence of ion temperature considerations.

(iv) The mean value for all data groups shows that $L_{PRED} < L_{MEAS}$ by about 10%. In addition to ion temperature effects mentioned above, secondary electron emission from the cathode might also make L_{PRED} smaller. If about 10% of the measured cathode current density is due to electron emission then the value for J used in Equation 3.6 would be ~ 10% too large, making L_{PRED} about 5% smaller.

3.3.2.4 Discussion

Whether any improvements can be made in the accuracy of sheath thickness prediction for practical purposes, remains uncertain. For example, in ref 43, a (rather complex) model of the cathode sheath region has been developed. This has a form which is intermediate between the free fall and mobility limited extremes of the Child-Langmuir relationship. The authors compared their model predictions in ref 43 with measured sheath thicknesses from ref 41. Table 3.4 shows the data used and the predictions from ref 43 compared with those from Equation 3.6.

DATA FROM REF 41				L_{PRED} (cms)		L_{MEAS} / L_{PRED}	
V_c (kV)	J (mA/cm^2)	PRESSURE (mTorr)	L_{MEAS} (cms)	REF 43 MODEL	EQN 3.6	REF 43 MODEL	EQN 3.6
5.85	0.16	12	7.69	4.07	4.92	1.89	1.56
5.15	0.39	21	4.44	2.36	2.86	1.88	1.55
3.10	0.47	45	2.27	1.40	1.78	1.62	1.28
2.15	0.39	65	1.73	1.13	1.49	1.53	1.16

Table 3.4 Comparison of predicted sheath thicknesses using the model in ref 43 and Equation 3.6.

It is claimed in ref 43 that $L_{PRED} \sim 0.6\ L_{MEAS}$ using their model (ie, L_{MEAS}/L_{PRED} is about 1.7) and that this consistency is maintained. However, as Table 3.4 shows, L_{MEAS}/L_{PRED} decreases from 1.9 at lower pressure to 1.5 at higher pressure. In fact, the consistency is little better than that obtained with the free-fall equation. The predictions from Equation 3.6 are also closer to L_{MEAS} in absolute terms.

For practical purposes, the free fall Child-Langmuir equation appears to offer a suitable means of evaluating the cathode sheath thickness from readily determined discharge parameters. Although the accuracy of prediction may not be considered to be very high, this is offset by ease of use.

3.3.3 Evaluation of the Mean Free Path, λ_c

To evalate λ_c, a knowledge of σ_c, the collision cross section for argon symmetrical charge exchange, is required (see Equation 3.1). There is considerable uncertainty in the value of σ_c, as Figure 3.3 shows. The more recent results of Hegerberg et al (refs 44, 45) is probably the most accurate data available at present. Unfortunately, their measurements were performed at very high energies (1 - 10 keV, ref 44) and very low energies (below 1 eV, ref 45). There appears to be no reliable data at intermediate energies, which are of interest in this work.

Sheldon (ref 46), has developed a charge exchange cross section-energy relationship of the form:

$$E_i = K_1\ \sigma_c^{1/2} \exp\ (-K_2\ \sigma_c^{1/2}) \qquad (3.9)$$

where E_i = incident ion energy, K_1 and K_2 are constants. This equation can be fitted to the data of Hegerberg et al, by transposition into a linear

equation:

$$(\ell n\ E_1 - \ell n\ \sigma_c^{1/2}) = - K_2\ \sigma_c^{1/2} + \ell n\ K_1 \qquad (3.10)$$

Thus a linear regression of $(\ell n\ E_1 - \ell n\ \sigma_c^{1/2})$ versus $\sigma_c^{1/2}$ will yield the values of K_1 and K_2 from the resulting intercept and gradient. Figure 3.13 shows the σ_c data as a function of energy. The solid curve represents the regression fit to the Hegerberg data, yielding:

$$K_1 = 5.1985 \times 10^{16} \qquad K_2 = 2.8954 \times 10^{8}$$

for E_1 in eV and σ_c in cm^2. The excellent fit to the data (correlation coefficient = - 0.9997) and the low experimental errors claimed in refs 44 and 45, suggests that this curve could be the most accurate determination of σ_c as a function of energy to date. Other workers (refs 47, 48) have also published limited σ_c data, though with larger estimated errors. Within their stated error limits, the data from refs 47 and 48 agrees with the solid curve in Figure 3.13.

The Davis and Vanderslice energy distribution model assumes σ_c to be independent of energy (see Section 3.3.1.1). Clearly, this is not the case and therefore a suitable single value of σ_c is required which represents the typical ion energies encountered in an ion plating discharge. For argon diode discharges, the value of L/λ_c is normally greater than 10 (as will be shown later). Therefore under these conditions, we can consider a simplified version of Equation 3.4 which is appropriate when $L \gg \lambda_c$ (ref 28):

$$\frac{dN}{dE} = \frac{N_o L}{2\lambda_c} \exp\left[\frac{-EL}{2\lambda_c}\right] \qquad \text{(for } m = 2\text{)} \qquad (3.11)$$

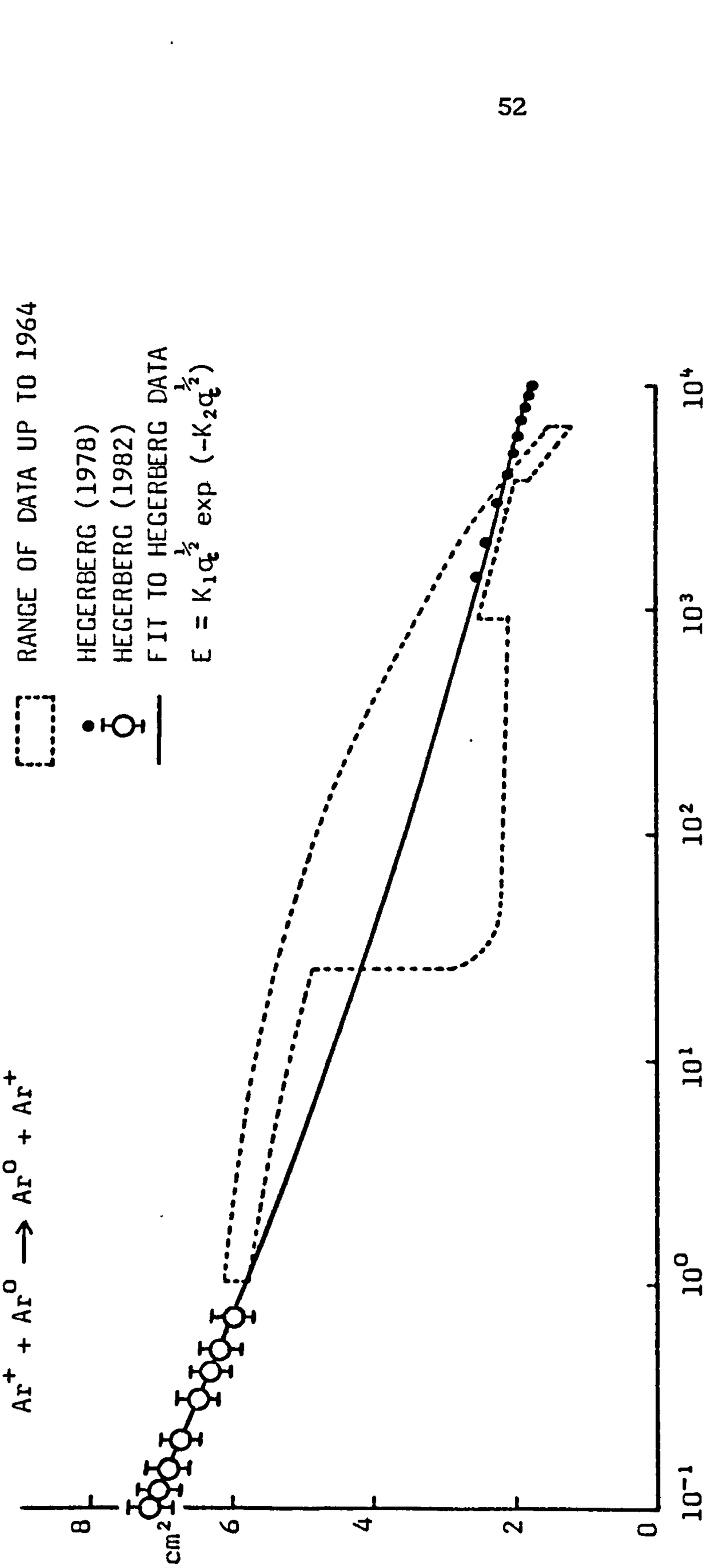

Figure 3.13 Collision cross section for $Ar^+ - Ar^o$ charge exchange as a function of ion energy. Solid curve represents Equation 3.10 fitted to the data of Hegerberg et al (refs 44, 45).

Therefore, the total ion energy arriving at the cathode will be,

$$\int_0^{N_o} E.dN \qquad (3.12)$$

Substituting Equation 3.11 into 3.12 and integrating (between the limits E=0, E=1), gives:

$$\text{Total ion energy} \sim 2\, N_o\, \lambda_c / L \qquad (3.13)$$

and in absolute terms,

$$\text{Total ion energy} \sim 2\, eV_c\, N_o\, \lambda_c / L \qquad (3.14)$$

where eV_c represents the maximum energy the ions could attain from traversing the cathode sheath. Equation 3.14 thus represents the amount of energy transported to the cathode by ions (as opposed to that carried by high energy neutrals). We need to know the average energy of an ion arriving at the cathode. Therefore, from 3.14,

$$\text{Average ion energy} \sim 2\, eV_c\, \lambda_c / L \qquad (3.15)$$

Using published data on experimentally determined L/λ_c values and knowing the cathode voltages applied, Equation 3.15 can be used to estimate the average ion energy in each case. Some results are shown in Table 3.5.

REF	V_c (kV)	L/λ_c	ESTIMATED MEAN Ar^+ ION ENERGY FROM EQN 3.15	σ_c FROM EQN 3.9 ($x10^{-15}cm^2$)	L (cms)	DISCHARGE PRESSURE (mTorr)	σ_c FROM PUBLISHED DATA ($x10^{-15}cm^2$)
28	0.6	15.0	80	3.65	1.3	60	5.97
35	1.5	12.0	250	3.16	2.6-3.5	30	3.55-4.78
33	3.0	10.4	580	2.82	7.0	15	3.11

Table 3.5 Calculated mean ion energy and σ_c data from published argon diode discharge results.

Typical average ion energies are of the order of a few hundred eV (column 4). The σ_c values calculated from the Hegerberg data fit to Equation 3.9 are given (column 5). Also shown, are σ_c results calculated from the published L/λ_c data (column 8), knowing L and the argon pressure (1 mTorr = 3.219×10^{13} atoms/cm^3 at 300 K assuming ideal gas conditions). The value for L in ref 35 is not given and the Child-Langmuir equation could not be used to predict L, as J is also unknown. So, the result in Table 3.5 has been estimated by assuming the product of pressure and sheath thickness is constant in a diode discharge (see Section 3.3.2.1); the constant of proportionality being derived from the data in refs 28 and 33.

It is interesting to note that the σ_c values in column 8 are higher than those in column 5. This can be attributed to the former being "effective" values, ie, they represent the value of σ_c for an energy range from zero to eV_c. This is because in practice, the ions in the sheath would have this spread of energies. Therefore, the results in column 8 are a more

realistic representation of the σ_c value which should be used to evaluate λ_c.

Generally, diode ion plating discharges utilise cathode bias voltages in the order of a few kV. Thus, a reasonable value for σ_c would be 4 x 10^{-15} cm^2 based on the results in column 8. For enhanced discharges, the sheath thicknesses tend to be smaller (see Figure 3.12) and pressures are lower, therefore the average ion energy will be closer to the maximum value than under diode conditions. However, this proportionally higher ion energy will be offset by the fact that lower bias voltages (100's of volts) are generally used. Therefore, σ_c = 4 x 10^{-15} cm^2 might be considered to be appropriate for all types of argon ion plating discharges. Using this value in Equation 3.1 will give λ_c for a known pressure.

3.3.4 Use of L/λ_c Values

3.3.4.1 Energy transportation characteristics

By evaluating L/λ_c using the methods previously described, various argon discharge configurations can be assessed in terms of their ion energy distributions, using Equation 3.4. However, a more convenient assessment of energy transportation characteristics can be gained by interpretation of the curves shown in Figure 3.14. The broken curve represents the fraction of ions arriving at the cathode with maximum energy, this being calculated from Equation 3.5. The solid curve represents the fraction of energy transported by ions (as opposed to high energy neutrals) and this has been derived from data given in ref 29.

The curves in Figure 3.14 show that a small L/λ_c value is favourable for two reasons. Firstly the ion energy distributions exhibit a greater proportion of high energy content than those of the neutrals (see Figures 3.6 and 3.10). Therefore, reducing L/λ_c will transfer more of the energy

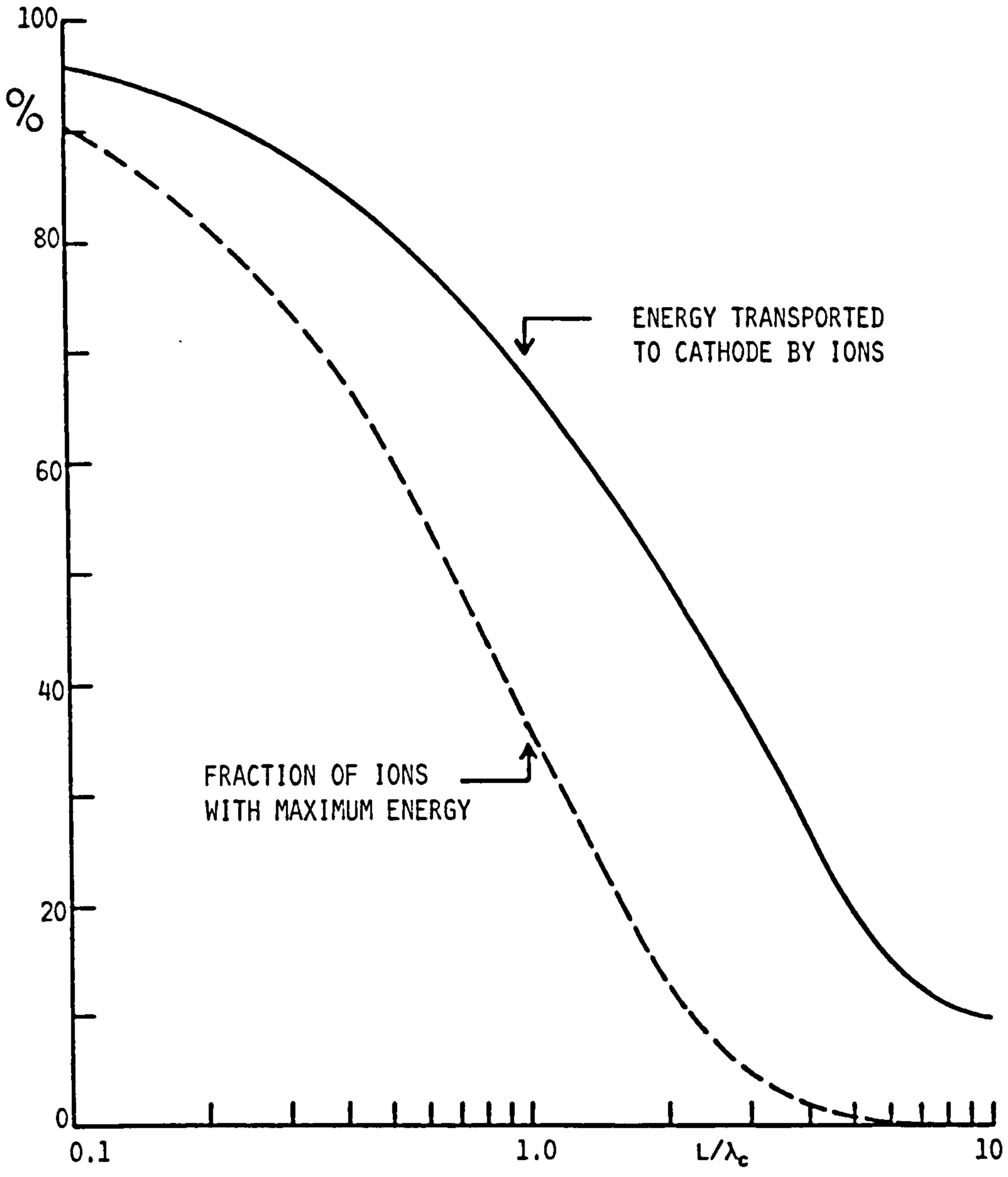

Figure 3.14 The dependence of ion energy transportation characteristics with L/λ_c. Solid curve is derived from data in ref 29, broken curve is from Equation 3.5.

transportation to the ions and increase the high energy content. Secondly, as L/λ_c is reduced, more of these ions will have maximum energy, so that the resulting distribution approaches a monoenergetic condition. These factors are important in ion plating, if it is assumed that there is a minimum energy requirement for the benefits obtained by this type of coating deposition process.

3.3.4.2 Energy requirements

The tendency towards using lower substrate bias voltages in modern enhanced ion plating systems raises the question of whether there is a minimum (or critical) energy required. Below this critical energy, the improvements in coating characteristics imparted by the process may no longer be apparent. Table 3.6 lists some phenomena which could be considered to be important in the ion plating process, together with their energy requirements.

It must be noted that the list of mechanisms in Table 3.6 is not exhaustive; only those phenomena whose energy requirements can be readily quantified are shown. Based on this information, it is not possible to define a single critical energy which must be exceeded to obtain good quality ion plated coatings. However, as a rough guide, a minimum recommended bombardment energy is likely to be in the range 40 to 70 eV. Clearly, this does not mean that bombardment by, for example, 10 eV particles would not provide any benefit. The suggestion is that greater benefits would probably be obtained from particles in the range of 40 to 70 eV and that increasing the particle energies beyond this range may not necessarily improve the situation.

The proportion of ions (and high energy neutrals) which exceed some critical energy, eV^*, will depend on the cathode (substrate) bias and L/λ_c.

MECHANISM:	DESCRIPTION:	EFFECTS:	ENERGY REQUIREMENTS:
IONISATION Figs 3.3,3.4 Refs 16, 21	Electrons emitted from substrate accelerate across substrate (cathode) sheath to gain sufficient energy for electron impact ionisation in negative glow region.	Maintains the discharge in a diode configuration; provides means of ionisation in addition to any enhancement applied to the process.	For argon and many other gases (eg nitrogen), maximum collision cross section for electron impact ionisation is typically 70 - 100 eV.
SUBSTRATE SURFACE CONTAMINATION Ref 49	Desorption of adsorbed impurities on the substrate surface prior to deposition.	Prevents, for example, contaminants reducing adhesion between coating and substrate.	Several eV.
ADATOM MOBILITY Ref 26	Removal/surface diffusion of adsorbed atoms on the growing coating surface.	Promotes coating densification.	Several eV.
ATOMIC DISPLACEMENT Refs 49,50,51	Atoms in the substrate and coating are displaced from their normal sites, creating lattice defects.	Can lead to, for example, intermixing of substrate and coating atoms. Increased defect densities promote rapid interdiffusion. Improves coating - substrate adhesion. May also increase coating densification.	Thresholds are in the region of 20 - 50 eV.
SPUTTERING Ref 16,50	Substrate and subsequent growing coating is sputtered.	Can be used to clean the substrate prior to deposition. Promotes atomic mixing which can improve coating-substrate adhesion and coating densification.	Thresholds (argon bombarding metals) are in the region of 15 - 35 eV.
ENTRAPMENT Ref 50	Support gas (argon) is incorporated in coating during deposition.	Gas atoms may cluster within the coating to form bubbles. May be detrimental to coating properties.	Argon entrapment probability is is believed to be very low, below 100 eV.

TABLE 3.6 SOME BASIC PHENOMENA WHICH ARE BELIEVED TO HAVE A SIGNIFICANT ROLE IN THE ION PLATING PROCESS.

For a given bias, reducing L/λ_c will increase the proportion of ions exceeding eV^* which in turn must provide greater benefits. Figure 3.15 illustrates this effect by showing two different ion energy distributions at the same cathode bias. Thus, for ion plating systems where L/λ_c is small, lower substrate biases may be used to obtain good quality coatings.

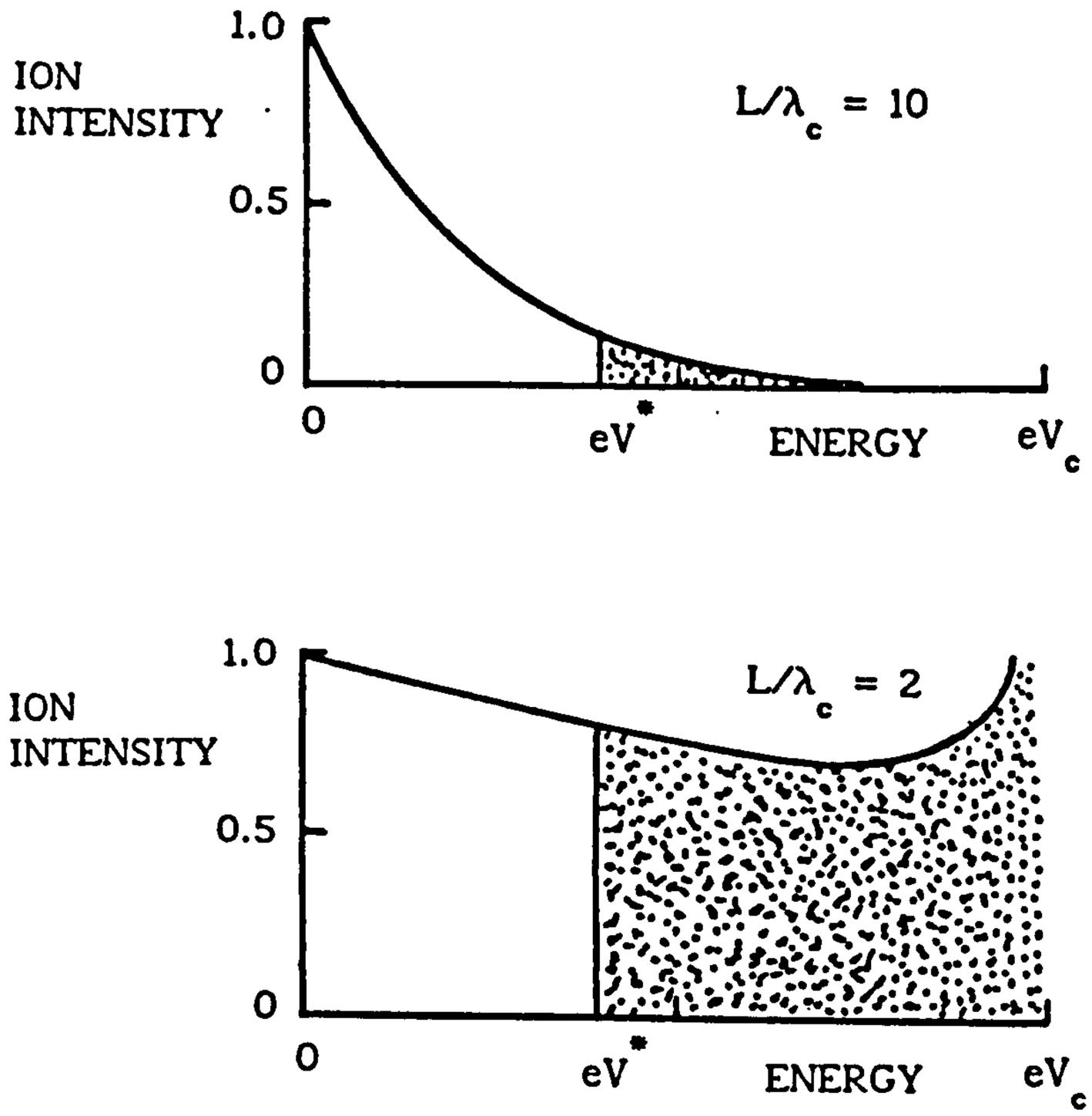

Figure 3.15 Ion energy distributions, showing how a greater proportion of ions exceed the critical energy, eV^*, as L/λ_c is decreased.

3.4 ION INTENSITY AND IONISATION EFFICIENCY

It has been proposed (ref 52), that the substrate current density is more important than substrate bias for producing high quality ion plated coatings, provided that some minimum bias is always exceeded. Essentially, the arguments in the previous section support this view. Where systems have most of the particles arriving at the substrate exceeding eV^*, the intensity of particle bombardment becomes the influential parameter for improving coating quality. As shown by the curves in Figure 3.14, most of the energetic particles are ions, rather than high energy neutrals, when L/λ_c is small. Therefore, for systems with favourable energy transportation characteristics, the ion intensity, which is represented by the measured substrate current density, becomes the dominant factor.

In practice, the non-energised (thermal) neutrals of the support gas (argon) must also be considered in ion plating discharges; these contributing to most of the measured pressure. If two discharge configurations transport a comparable number of ions to the substrate with energies greater than eV^* and operate at the same current density, we might expect coatings produced in both discharges to have similar characteristics. However, if one of the discharges requires a higher gas pressure to attain the necessary current density, the resulting coatings produced may be inferior. This is because of the tendency towards an open columnar type of film growth, associated with higher pressures, as reported in Section 1.3. Therefore, to account for both ion intensity at the substrate and the effects of thermal neutrals, a performance parameter known as the "Ionisation Efficiency" has been developed. This is defined as the percentage of particles bombarding the substrate which are ionised (ref 52) ie:

$$\text{Ionisation Efficiency} = I_{EF} = \frac{N_i \times 100\%}{N_{np}} \qquad (3.15)$$

where N_i is the ion arrival rate and N_{np} is the total bombardment rate at the substrate (both in units of cm^2/sec). Thus, in terms of achieving dense coatings, I_{EF} should be as high as possible.

Equation 3.15 can be more conveniently expressed in terms of the current density, J, and the gas pressure P, by using the standard gas equations (eg ref 16):

$$N_i = J/q \qquad (3.16)$$

$N_{np} = n\bar{c}/4$. As $\bar{c} = (8\ kT/\pi m_n)^{1/2}$ and $P = nkT$, we get:

$$N_{np} = P(1/2\pi m_n kT)^{1/2} \qquad (3.17)$$

$$\therefore \quad I_{EF} = (J/P)((2\pi m_n kT)^{1/2}/q) \times 100\% \qquad (3.18)$$

in S.I. units, where q = ionic charge, m_n = atomic mass of the arriving species and T is the gas temperature.

Previously reported values for I_{EF} in the literature (eg ref 53), have been based on measured J and P results regardless of the relative proportion of different species present (eg, argon, nitrogen, titanium). Thus, in ref 53 for example, the value for N_{np} was based on argon data only. Although this is not strictly representative, the results allowed the convenient comparison of data from different commercial ion plating systems used for the deposition of titanium nitride coatings. Since the argon atomic mass is between that of titanium and N_2, the error in m_n in Equation 3.18 would not have been large. Probably a more significant error in the

results would be the assumption that the pressure (which is proportional to impingement rate), measured at the deposition chamber walls, represents the impingement rate at the substrate surface. For example, the evaporant flux density will be lower near the chamber walls than in the vicinity of the substrate. The vapour would also have a high probability of condensing on the surfaces of an entrance port used for linking the chamber to the vacuum gauge head and not be detected. However, the error incurred by these pressure discrepancies has been estimated, and is usually small (ref 53).

For this work, there are some advantages in evaluating I_{EF} in terms of measurements obtained from pure argon discharges only. The benefits are that (i) m_n is more accurately known, (ii) there is no pressure discrepancy due to evaporant flux effects, and (iii) there is more published data available on argon-only discharges. Although the results should be more accurate, there will be some error in assuming T to be the bulk gas temperature (300 K). This is because the ions and high energy neutrals bombarding the cathode will have temperatures (energies) considerably higher than that of the thermal neutrals. However, as the proportion of high energy species will be small, the resulting error should not be large.

3.5 PRACTICAL DISCHARGE SYSTEMS

3.5.1 Systems With Argon Only

In Sections 3.3 and 3.4, it has been shown that the energy transportation characteristics and ionisation efficiency can be estimated for various argon discharge configurations, if the cathode sheath voltage, current density and pressure are known. Using, where necessary, Equation 3.6 and assuming the only ionic species to be Ar^+, L/λ_c values have been estimated from this work and published data; Figure 3.14 being used to interpret these values. Ionisation efficiencies have been calculated from

Equation 3.18. Table 3.7 shows the results for various diode and triode configurations.

Errors in some of the L/λ_c values quoted in Table 3.7 could be large. For example, the error in λ_c, by assuming σ_c to be 4×10^{-15} cm^2 might be ± 25%, based on the results in Table 3.5. The error in L by prediction from the Child-Langmuir equation might also be around ± 25%, on consideration of the standard deviation values in Table 3.3. In spite of these uncertainties, the following observations can be made from the data in Table 3.7:

(i) L/λ_c for diode systems is always greater than 10. This agrees with the findings of other workers, eg, 15 in ref 28 and 12 in ref 35. In fact, as L, like λ_c, is (approximately) inversely proportional to discharge pressure under diode conditions (see Section 3.3.2.1), L/λ_c will not change appreciably.

(ii) A triode discharge using a positively biased third electrode reduces L/λ_c (ref 33) and therefore increases the proportion of energy transported by ions compared with that of the high energy neutrals. I_{EF} is also seen to increase compared with the equivalent diode system.

(iii) Triode discharges using a thermionic emitter can give very low L/λ_c values, resulting in much of the energy being transported to the cathode by maximum energy ions. I_{EF} values of a few per cent can also be achieved.

These results show therefore, that considerable improvements in terms of energy transportation and ionisation efficiency can be gained using thermionically supported discharges, when compared with the other configurations. Although a triode system using a positively biased electrode gives some improvement when compared with diode layouts, the

DISCHARGE TYPE:	REF.	V (kV)	J (mA/cm^2)	P (mTorr)	L (cms)	L/λ_c	FRACTION OF IONS WITH MAX ENERGY (%)	FRACTION OF ENERGY TRANSPORTED BY IONS (%)	I_{EF} (%)	NOTES
DIODE	41	5.85	0.158	12.0	7.69	11.85	$< 10^{-3}$	< 10.0	0.03	(a)
	41	2.15	0.394	65.0	1.73	14.44	$< 10^{-4}$	< 10.0	0.01	(a)
	33	3.00	0.028	15.0	7.00	10.40	$< 10^{-2}$	< 10.0	< 0.01	(b)
	THIS WORK	1.00	0.202	100.0	0.90	11.56	$< 10^{-3}$	< 10.0	< 0.01	(a)
TRIODE (+VE ELECTRODE)	33	3.25	0.181	15.0	4.00	6.00	0.25	15.5	0.02	(b)
	33	3.25	0.185	15.0	3.40	5.11	0.60	20.0	0.02	(c)
TRIODE (THERMIONIC)	THIS WORK	0.20	0.603	5.0	0.20	0.13	87.84	95.0	0.24	(d)
	THIS WORK	1.00	0.427	20.0	0.80	2.06	12.81	49.0	0.04	(a)
	39	0.19	1.650	0.8	0.05	0.005	99.49	> 96.0	4.03	(a)
	39	0.92	1.650	0.8	0.41	0.042	95.86	> 96.0	4.03	(a)

Notes: V = cathode sheath voltage = $|V_c| + V_p$, as discussed in Section 3.3.2.

(a) L is measured, λ_c is calculated assuming $\sigma_c = 4 \times 10^{-15}\ cm^2$ (T = 300 K).

(b) L/λ_c from published data.

(c) L is measured; λ_c is calculated using $\sigma_c = 3.12 \times 10^{-15}\ cm^2$, estimated from other data in this reference (T = 300 K).

(d) L is calculated, λ_c is calculated, assuming $\sigma_c = 4 \times 10^{-15}\ cm^2$ (T = 300 K).

TABLE 3.7 ENERGY TRANSPORTATION AND IONISATION EFFICIENCY CALCULATIONS FOR VARIOUS ARGON DISCHARGE LAYOUTS.

mechanism of discharge enhancement is limited to increasing secondary electron emission by making all other surfaces within the chamber cathodic with respect to the electrode. However, a thermionically supported system uses an electrode which is capable of injecting a high density flux of electrons into the discharge, and this can give much greater discharge enhancement.

3.5.2 Other Considerations

So far, this chapter has been concerned primarily with argon discharge phenomena. The role of other effects occurring within ion plating discharges will now be considered.

3.5.2.1 Evaporant source and metal flux

The ionisation potential of most metals is typically in the range 5 to 8 eV. As these values are lower than the argon excitation energy (11.56 eV), long lived excited argon neutrals (metastables) are capable of ionising the metal vapour. This process is known as Penning ionisation (eg, ref 16):

$$Ar^{*} + M \longrightarrow Ar + M^{+} + e$$

where M is the metal species. Evidence of preferential ionisation of the metal species by this mechanism, has been found in sputtering discharges by Coburn and Kay (refs 54, 55, 56). Ion mass spectroscopy studies were made by sampling ions through an aperture in the earthed anode of an argon diode sputter deposition system. It was found that with a copper sputtering target, for example, the partial pressure of copper in the discharge was about 10^4 times less than the argon yet the copper ion peak was lower than the argon ion peak only by a factor of 10. Although this did not mean that

the copper was 10^3 times more likely to be ionised than the argon (because of non uniform discrimination effects in the spectroscopy equipment), this and other observations led the authors to conclude that Penning ionisation is the dominant ionising mechanism for the sputtered metal species. Therefore, it is probable that a large proportion of the metal flux in an ion plating discharge will be ionised, because of Penning ionisation, in addition to electron impact mechanisms.

It has been reported in ref 37, that the cathode (substrate) current density is reduced when a metal is evaporated, by resistive heating, into an argon diode discharge. Similar effects have also been observed with EB evaporation in triode discharges when the additional electrode has been positively biased (ref 52), as shown in Figure 3.16. A reduction in current density would seem to be anomalous, if a large proportion of the metal flux is ionised. However, there could be a number of reasons for this effect. For example, the contribution to ionisation in a pure argon discharge, by electron impact ionisation of argon metastables, does not appear to be well understood. If this mechanism is important in sustaining a pure argon discharge, then the proportion of argon which is ionised in the presence of a metal flux may be substantially reduced. This is because the argon metastables would return to ground state by Penning ionisation of the metal species, rather than becoming ions themselves. Therefore, the metal flux could become ionised in preference to the argon, resulting in most of the cathode current being transported by metal ions rather than argon ions. A reduction in cathode current density during metal evaporation might be expected to occur, if the metal ions lose more of their charge to the chamber walls than argon ions would, due to the former being more directional. The current density may also reduce, if, for a given sheath

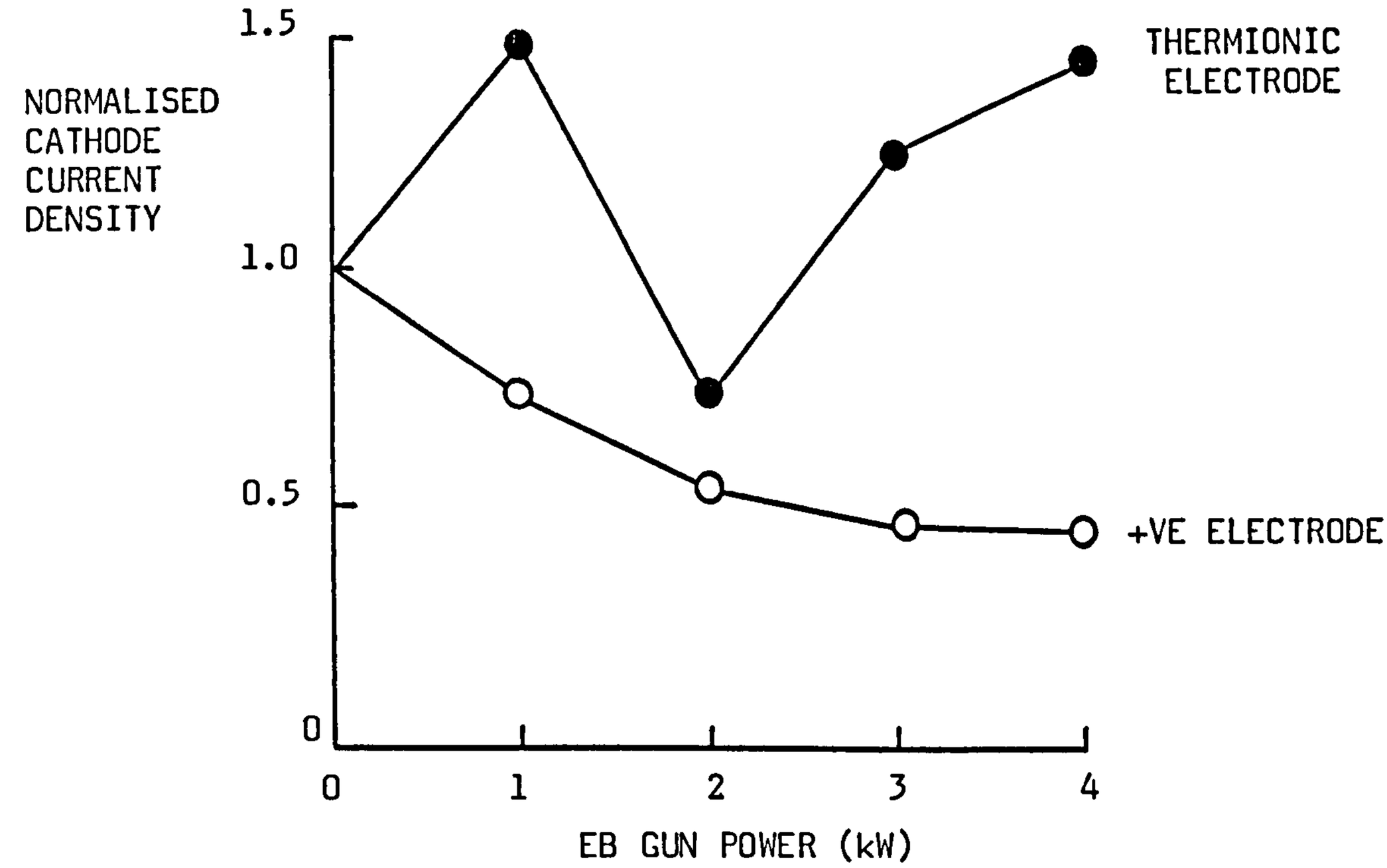

Figure 3.16 Effect of EB gun power and titanium evaporation on argon triode discharges run at 5 mTorr (ref 52).

thickness in Equation 3.6, the charge to mass ratio of the metal ions is smaller than that of the argon ions. Alternatively, the effect could be explained as being due to distortion of the discharge; interactions between the vapour source and negative glow producing an intense secondary discharge remote from the cathode. When a thermionic emitter is used in the discharge, the situation is even more complicated, as shown in Figure 3.16. Here, the current density may increase or decrease (depending on process conditions) and therefore counteracting effects must operate.

In addition to the effects of metal ionisation, the energy transportation characteristics also require consideration. Unfortunately, the data available on metal ion energy distributions in argon discharges is very limited. Table 3.8 summarises the published results obtained in various diode configurations.

REF	ARGON PRESS. (mTorr)	V_c (kV)	METAL SPECIES AND SOURCE	L/λ_c (ARGON)	L/λ_m (METAL)
33	15	3.0	SPUTTERED METAL IONS FROM CATHODE	10.4	3.0
34	14	3.0	EVAPORATED SILVER	8.2*	1.5
35	35	3.0	SPUTTERED MOLYBDENUM IONS FROM CATHODE.	>10	~4

Table 3.8 Ion energy distribution data measured at the cathode of argon diode discharges for Ar^+ ions and metal ions (* value obtained without evaporation).

As reported in Section 3.5.1, the argon L/λ_c values are greater than 10; the result from ref 34 being a little lower because the authors had not accounted for the contribution from sputtered metal species in their discharge. The equivalent values for metal ions (L/λ_m) are considerably lower, indicating that metal ions undergo fewer charge transfer collisions in the cathode sheath. Although the dominant charge transfer process is not clear, the data shows that metal energy distributions will tend to have a greater high energy content than that for Ar^+ ions. Further evidence for this is given by data in refs 30 and 31, for Cu^+ energy distributions during evaporation of copper in an argon diode discharge; the Cu^+ distributions show a shift towards the higher energies when compared with the Ar^+ results obtained without evaporation. No definite information has been found on the influence of evaporated metal ions on Ar^+ energy distributions, though it

could be inferred from the total ion energy distribution results of ref 37 (evaporation of lead) that the Ar^+ energy characteristics do not change appreciably.

3.5.2.2 Reactive gases

Although a number of different reactive gases may be employed in ion plating systems to produce ceramic coatings, nitrogen is probably the most commonly used at the present time, for example in the production of titanium nitride. Therefore, the study of reactive gases in this work has been limited to investigations with nitrogen discharges.

Using the same equipment and procedure outlined in Section 3.3.2.2, nitrogen diode and thermionic triode discharges were studied, to investigate the validity of the free fall Child-Langmuir equation (Equation 3.6) by comparing measured with predicted values of sheath thickness. Unfortunately, the visibility of the sheath under triode conditions was worse than that observed with argon, the main difficulty being poor contrast due to light emitted by the filaments. Therefore, only sheath thickness measurements under diode conditions could be taken. Figure 3.17 shows the results of the Child-Langmuir equation validity test, for nitrogen diode discharges run at 20 to 100 mTorr pressures and 1 to 2 kV cathode biases.

The results in Figure 3.17 show better agreement between measured and predicted L values when the charge to mass ratio for N^+ is used in Equation 3.6. It can be inferred from these results that N^+, rather than N_2^+ is the dominant ionic species arriving at the cathode under these conditions. This is interesting, because the dominant ionic species in the negative glow region of nitrogen diode discharges is found to be N_2^+ (eg, ref 57). Bohme and Goodings (ref 58) also found N_2^+ to be the dominant ionic species in a microwave supported nitrogen discharge (9 to 27 mTorr pressure) using ion

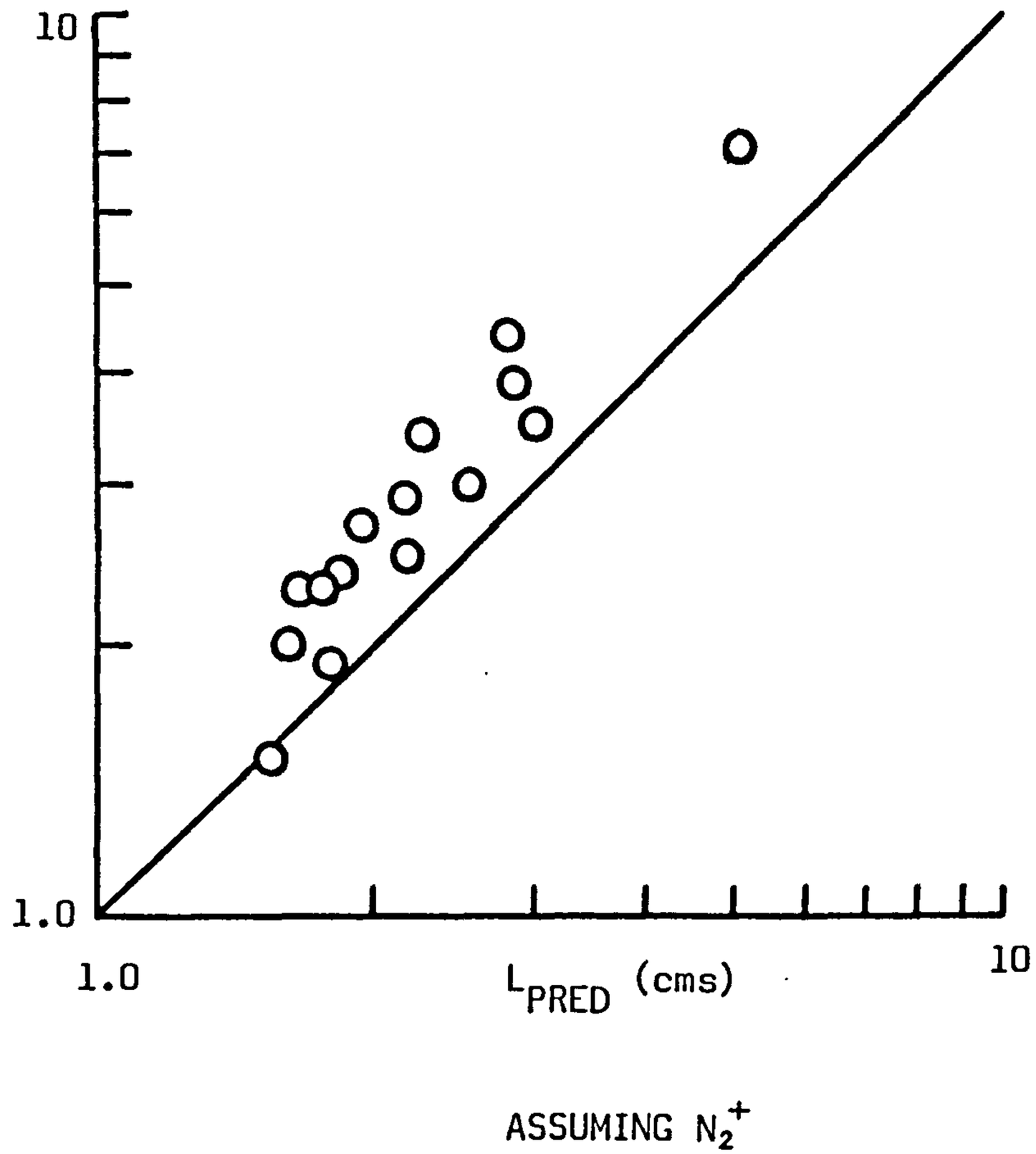

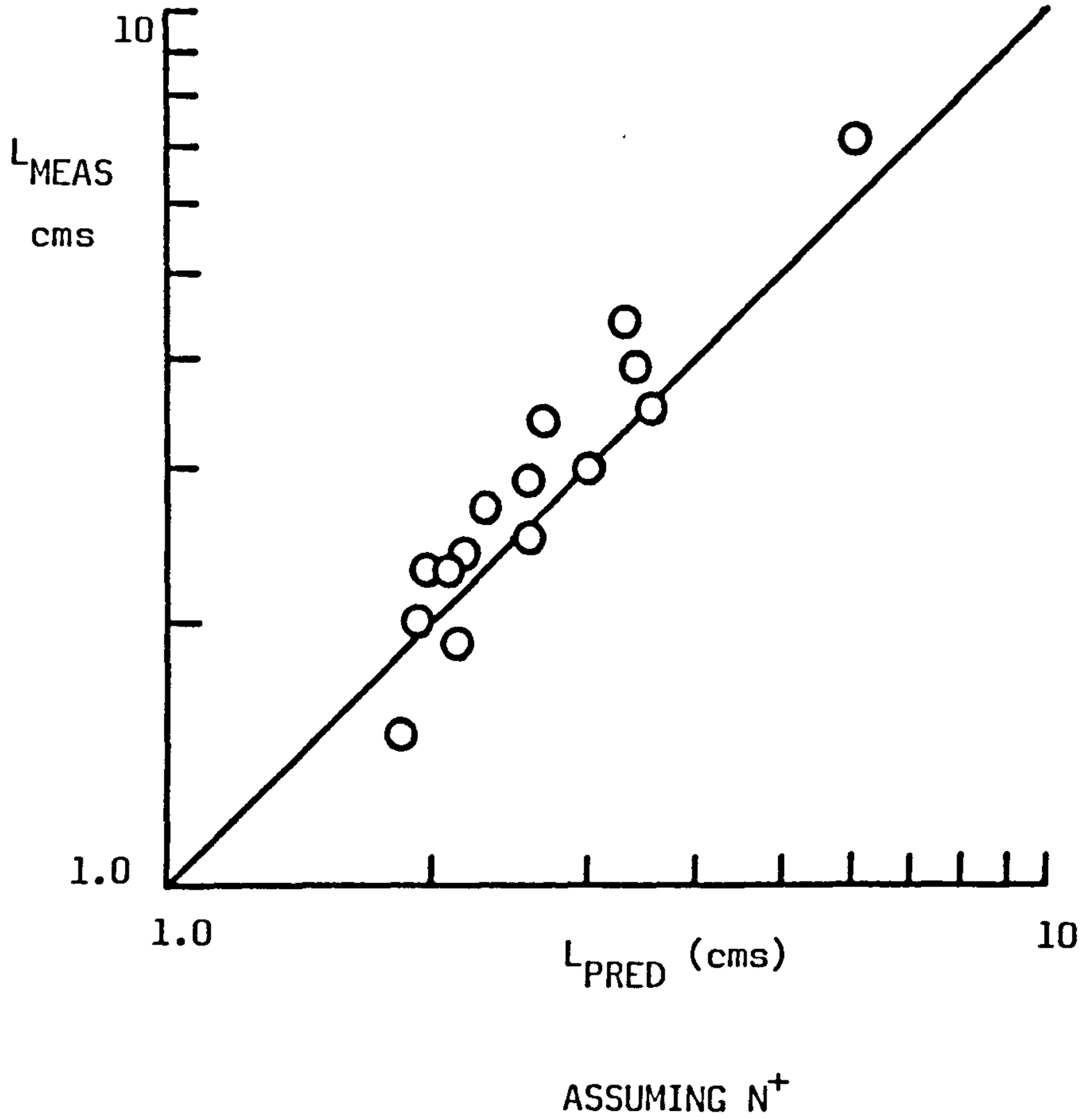

Figure 3.17 Plots of measured versus predicted cathode sheath thicknesses for nitrogen DC diode discharges. Note the improved agreement when N^+ is assumed to be the ionic species in the predicted results.

mass spectroscopy analysis. However, they also observed that sheath effects in front of the sampling orifice could significantly change the proportion of N^+ species collected. They attributed this to formation of N^+ ions in the sheath by dissociative charge transfer, suggesting the mechanism:

$$N_2 \text{ (FAST)} + N_2 \longrightarrow N_2^{+*} \text{ (SLOW)} + N_2$$

$$N_2^{+*} \longrightarrow N^+ + N$$

where * denotes vibrational excitation energy. Therefore, this mechanism is probably responsible for N^+ generation in the results of this work. Further evidence of N^+ rather than N_2^+ ions being the dominant ionic species arriving at the cathode of nitrogen diode discharges can be found in the ion mass spectroscopy data of ref 31; the N^+ peak height being more than twice that of N_2^+ for a 30 mTorr 2 kV discharge. Although N^+ may be predominant in diode configurations, this may not be the case when some form of ionisation enhancement is used. When discharges are run at very low pressures and cathode sheaths are thin (eg, thermionic triode configurations) there will be fewer ion-neutral collisions within the sheath region. This could result in N_2^+ being the dominant ionic species arriving at the cathode under these conditions.

There is little information available on the energy distribution characteristics of nitrogen discharges. However, Armour et al (ref 30) have reported that they are similar to those of argon under the same (diode) conditions. This is confirmed by the results in ref 31, where N^+ and Ar^+ energy distributions from diode discharges (1.5 to 3 kV, 30 mTorr) show comparable shapes, although the N^+ distributions are shifted to slightly higher energies.

Some comment is required on the generation of ions in nitrogen discharges. Electron impact ionisation is the main mechanism and the collision cross section for this is similar to that for argon (see, for example, ref 21). Therefore, for argon and nitrogen discharges operated at similar pressures and bias boltages, the measured cathode current densities might be expected to be comparable. Table 3.9 shows some ratios of measured current densities obtained in this work (whilst performing the sheath thickness measurements previously described) from diode and thermionic triode discharges.

DIODE		THERMIONIC TRIODE	
Ar or N_2 PRESSURE (mTorr)	J_N/J_{Ar} (%)	FILAMENT BIAS (volts)	J_N/J_{Ar} (%)
40	100	20	21
60	100	50	19
80	83	60	18
100	67	100	18

Table 3.9 Measured current density ratios (J_N/J_{Ar}) from discharges of nitrogen and argon. Cathode bias = 1 kV in all cases. The triode discharges were run at 5 mTorr, filament heating current was 16 A.

Under diode conditions, the current densities are similar though at higher pressures, the nitrogen values decrease. This might be attributed to electrons losing energy due to the very large electron impact excitation cross section of nitrogen molecules (as suggested in ref 57) which in turn

would reduce the probability of ionisation. The nitrogen current density in the triode discharges is considerably lower than that for argon. Here, the explanation is more likely to be due to some interaction between the nitrogen and the hot filament used as the thermionic emitter. This is based on the observation that the filament emission current was lower (0.5 to 1 A) in nitrogen than that obtained in argon (1 to 2.5 A) for otherwise identical process conditions.

3.5.2.3 Impurities

Although this work is not primarily concerned with the influence of background impurities in ion plating systems, their presence merits some comment. Water vapour is one of the main contaminants and the following reactions in argon discharges have been reported (ref 22):

$$Ar^{*} + H \longrightarrow ArH^{+} + e$$

$$H_2O^{*} + H_2O^{*} \longrightarrow H_3O^{+} + OH^{-}$$

where * represents metastable states. The effects of these hydrogenous impurities in ion plating systems is not clear and there appears to be little information available on the subject. They have been detected in the negative glow region (ref 22) and at the anode (refs 54 - 56) of argon diode discharges. Although no reliable information on their presence at the cathode of such discharges can be found, it must be assumed from the available data, that practical systems with even trace quantities of water vapour may produce significant hydrogenous ion populations in argon discharges.

3.5.2.4 Substrate geometry

So far, this chapter has only dealt with flat cathode geometries. In practice, many of the substrate geometries which have to be considered for ion plating are complex. Examples include drills, cutting hobs and moulding dies. The main problems associated with complex substrate geometry can be attributed to the influence of localised plasma intensification and cathode sheath distortion.

Mattox (ref 1) has reported on some of the difficulties which may be encountered; these include through holes, blind holes and re-entrant corners in substrates which can essentially trap electrons that have been emitted from the substrate surface, giving localised regions of high plasma density. A more extreme form of this is the hollow cathode effect (eg ref 59). This can occur between parallel cathodic faces (eg, in a tube) if the gap between the faces is large enough for a negative glow region to be formed. The large cathodic area in relation to the small negative glow volume results in the latter being subjected to a much larger flux of emitted electrons, causing the glow to become a very dense localised plasma. The effect of localised changes in plasma density is to alter the bombardment characteristics between different parts of the substrate. For example, the surfaces of a hole which was being bombarded from a very dense region of plasma during coating deposition would be subjected to a higher plasma bombardment/coating flux arrival ratio than elsewhere. This in turn could lead to effects such as preferential sputtering of the growing coating within the hole, which may produce a localised change in coating characteristics such as stoichiometry, reduced thickness and increased density.

In addition to the effects of localised plasma intensification, cathode sheath distortion around substrate corners, edges and narrow

protrusions can also change the bombardment characteristics. Figure 3.18a illustrates this effect. The density of bombardment will be very intense at the corner because of the electric field in the sheath converging to a point. In practice, the sheath may appear more like that represented in Figure 3.18b, as suggested in ref 60. Although no clear explanation is

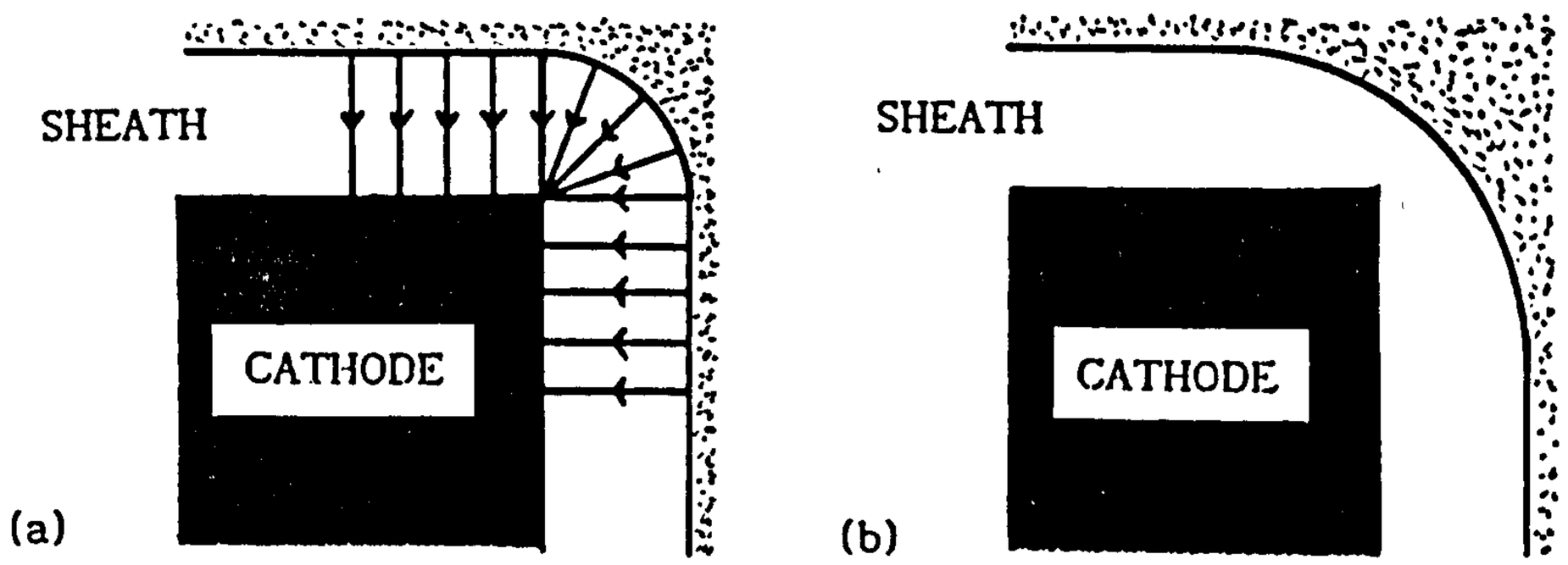

Figure 3.18 Effects of substrate geometry on the cathode sheath, (a) uniform sheath thickness, (b) "real" sheath (ref 60).

offered in ref 60, a higher current density at the corner would tend to locally reduce the sheath thickness for a given bias, in accordance with Equation 3.6. This is turn would reduce the convergence effect, although the corner region would still receive a higher bombardment density than on the flat faces. The relatively higher bombardment at the corner could increase coating density and reduce thickness in this region as previously described. The effect has been observed, for example, on the corners and edges of ion plated zirconia samples (refs 11, 12).

To minimise these potential problems, the general solution would be to perform ion plating with the cathode sheath around the substrates maintained as small as possible. For substrates of complex shape, the

simple flat plate form of the Child-Langmuir equation (Equation 3.6) cannot be expected to accurately predict average sheath thickness, even in a pure argon discharge. Other forms of the equation do exist (eg ref 40) to cover geometries such as cylinders and spheres but they are more complex and, for practical applications, may be considered to be equally idealistic. A further difficulty in predicting sheath thicknesses for real ion plating systems is that there is more than one ionic species present (eg, metal, reactive gas and argon ions) and their relative influences on thickness would be difficult to ascertain. However, the main concern is to minimise sheath thickness and Equation 3.6 will at least provide some indication of values likely to be encountered for a given substrate bias voltage and current density by assuming Ar^+ ions to be the only species present.

Finally, some comment on the influence of subtrate geometry on the energy distributions of ions (and high energy neutrals) arriving at the surfaces is required. Machet et al (ref 34) found some interesting results from measurements of ion energy spectra taken at sampling orifices in horizontally mounted, vertically mounted and hollow cathodes in argon diode discharges. Fewer high energy ions were detected from orifices positioned near cathode edges or re-entrant corners but no detailed explanation in ref 34 is offered to account for this. The effect may, however, be due to sheath distortion, causing the higher energy ions to enter the orifice at more oblique angles than the lower energy ions, the latter being formed nearer to the orifice. Therefore, the observed changes in energy distributions may have been more of an experimental artefact than a real effect. The measured ion energy distributions from their hollow cathode geometries are probably more reliable. They found that the high energy content significantly increased as the gap between the cathode walls was reduced. This can be readily explained as a reduction in sheath thickness

and hence a lower L/λ_c value, due to increased plasma intensification as the gap was decreased.

3.6 SUMMARY

Basic discharge phenomena, and their significance in glow discharges used in ion plating, have been reviewed. An appraisal of the published literature has indicated that the Davis and Vanderslice model for ion energy distributions can be applied to ion plating discharges. Using data from other workers, it has been shown that experimentally measured ion energy distributions may not agree with the model if the product of sampling orifice diameter and discharge pressure is too large. The main parameter which influences energy distributions of the bombarding species is the ratio between cathode sheath thickness (L) and mean free path for charge exchange (λ_c). Validity tests on the free fall version of the Child-Langmuir equation have shown that it can be used to predict cathode sheath thickness and an appropriate value for the argon symmetrical charge exchange cross section has been evaluated. This enables L/λ_c to be predicted for various argon discharge configurations. It is proposed that the minimum recommended bombardment energy at the substrate should be 40 - 70 eV, based on the energy requirements of mechanisms which are considered to be important in ion plating. Increasing the bombardment energies above this range may be less important than increasing the bombardment intensity or ionisation efficiency. Calculated L/λ_c and ionisation efficiency values for various argon discharge layouts have shown that thermionic triode discharges can give excellent ion intensity and energy transportation characteristics.

The behaviour of species other than argon, which are present in ion plating discharges, are not so well documented and are therefore poorly understood. The proportion of metal species in the discharge which are

ionised is probably high, due to Penning effects. Limited data available on metal ion energy distributions suggest that the metal flux arriving at the substrate has a much greater high energy content than that of argon in the same discharge. Investigations in this work with nitrogen discharges, have indicated that N^+ rather than N_2^+ ions are the dominant ionic species arriving at the cathode in diode configurations. This is probably due to dissociative charge transfer mechanisms occurring in the cathode sheath, which suggests that N_2^+ may become the main ionic species in enhanced discharges. Although the energy transportation characteristics of nitrogen are likely to be comparable to those of argon under similar conditions, ionisation of the former might be influenced by its preference for excitation and interactions with the heated filaments in thermionic triode discharges. In addition to argon, metal vapour and reactive gas, hydrogenous ions arising from water vapour contamination may have some influence on the ion plating process, but their significance is difficult to ascertain.

Finally, the effects of substrate geometry have been reviewed, the main problems being identified as localised plasma intensification and cathode sheath distortion which can cause preferential bombardment of corners, edges etc. This in turn may produce variations in coating characteristics such as thickness, structure and stoichiometry. It is suggested that in general, these problems could be minimised by making the cathode sheath thickness as small as possible, in accordance with the Child-Langmuir equation.

4. ION PLATING DISCHARGES - SPUTTER WEIGHT LOSS EXPERIMENTS

4.1 INTRODUCTION

The investigations reported in Chapter 3 have given rise to some inferences which are reasonably conclusive. It is clear that enhancing a glow discharge by thermionic means provides significant benefits in terms of ionisation efficiency and energy transportation. What is not so clear is how beneficial thermionic enhancement might be in terms of bombardment uniformity, relative to non-enhanced conditions. Also there could be potential disadvantages in using thermionic support which have not yet been considered. This chapter reports on experimental work undertaken to investigate these effects and their possible significance in the ion plating process.

The primary interest in any investigation related to ion plating is to obtain information about phenomena which influence the substrate surface rather than the properties of the discharge itself. For many decades, electrostatic or Langmuir probes have been used to investigate plasmas. Probe data can be interpreted to characterise a plasma in terms of its electron temperature and charge carrier density. Interpretation of results has been shown to be relatively straightforward when the probe is operated in the "orbital motion limited" mode (ref 61), otherwise more complex approaches have to be used such as those forwarded by Laframboise (eg, ref 62). Probe contamination in practical discharges is common and this can cause significant errors in the data (eg, ref 63). However, the main disadvantage with Langmuir probes is that they will only provide information about the body of the plasma, ie, the negative glow region. It is clear that the cathode sheath can drastically change the ionisation characteristics, the effects of which the sample is directly subjected to.

To illustrate this point, consider Figure 4.1a. This is a plot of calculated ionisation efficiency, $I_{EF,}$ (from pressure and cathode current density data) versus degree of ionisation, α, in the negative glow region (from pressure and Langmuir probe data) using argon DC diode results from various published sources. We might expect there to be a relationship between ionisation efficiency and α, as both parameters are a measurement of ion fraction. However, I_{EF} is a parameter associated with impingement rate at the sample surface and α is associated with density in the plasma volume. Therefore, α is a measurement of ion concentration in the plasma "reservoir" and I_{EF} will depend not only on α but also on a velocity component which must be a function of the potential drop across the cathode sheath. Figure 4.1b confirms this hypothesis, as the relationship between ionisation efficiency and the product of α and $V_c^{1/2}$ is less scattered. The $V_c^{1/2}$ function could be explained as follows:

Average incident ion kinetic energy at the sample surface =

$$\frac{1}{2} m_i \bar{c}^2 = q\bar{V} \qquad (4.1)$$

where m_i = ion mass, q = ion charge, $\bar{c}$ = ion mean velocity and $\bar{V}$ is the average potential through which the ions travelled after the final atomic collision in the cathode sheath. The impingement rate of particles bombarding a surface of unit area is proportional to the product of their number density and mean velocity (eg, ref 16). From Equation (4.1), the mean velocity, $\bar{c}$, is proportional to $\bar{V}^{1/2}$.

$\therefore$ Ion impingement rate per unit area = constant $n_i \bar{V}^{1/2}$

(n_i = ion number density)

$$\therefore I_{EF} = \text{constant } \alpha.\bar{V}^{1/2} \qquad (4.2)$$

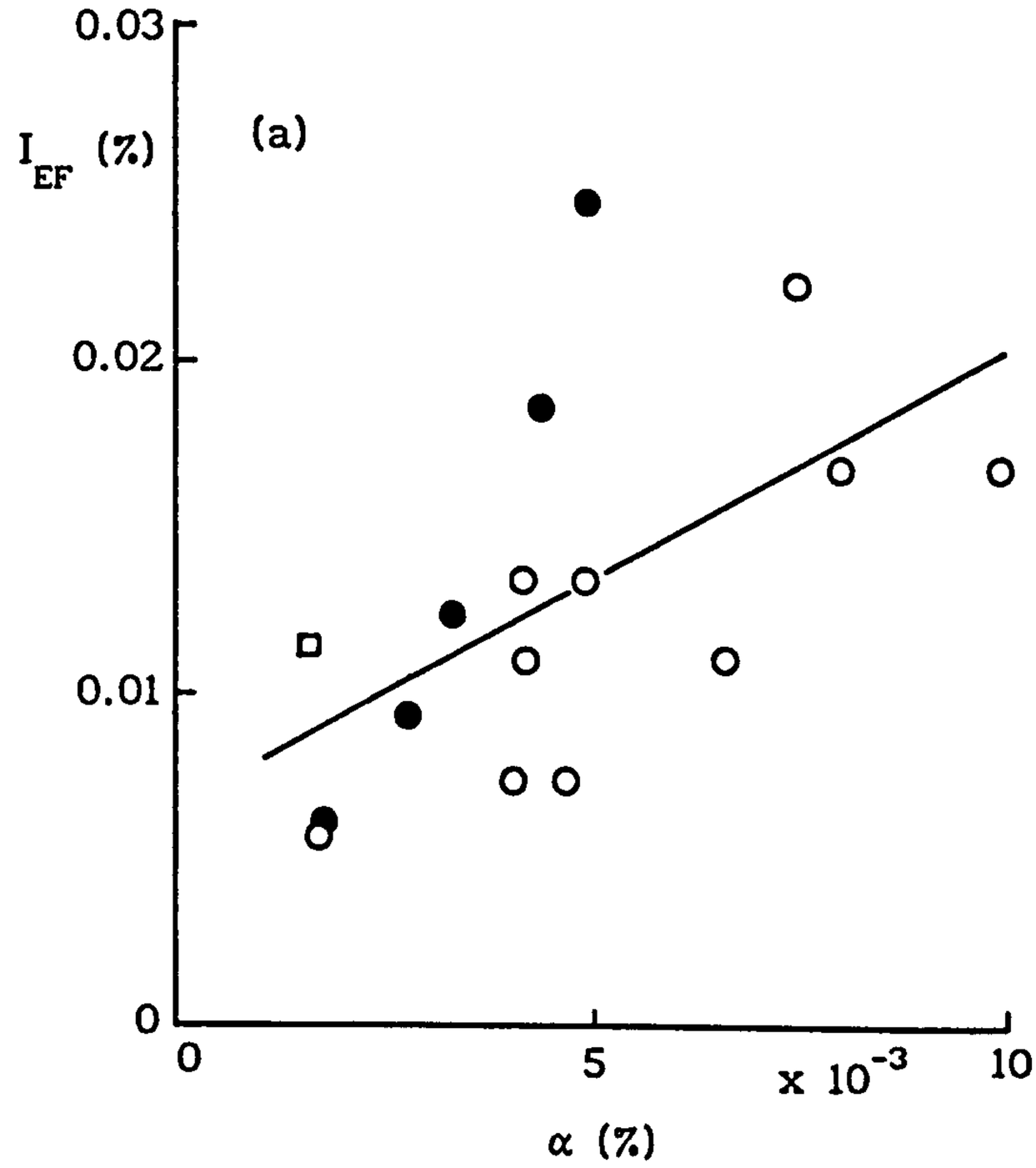

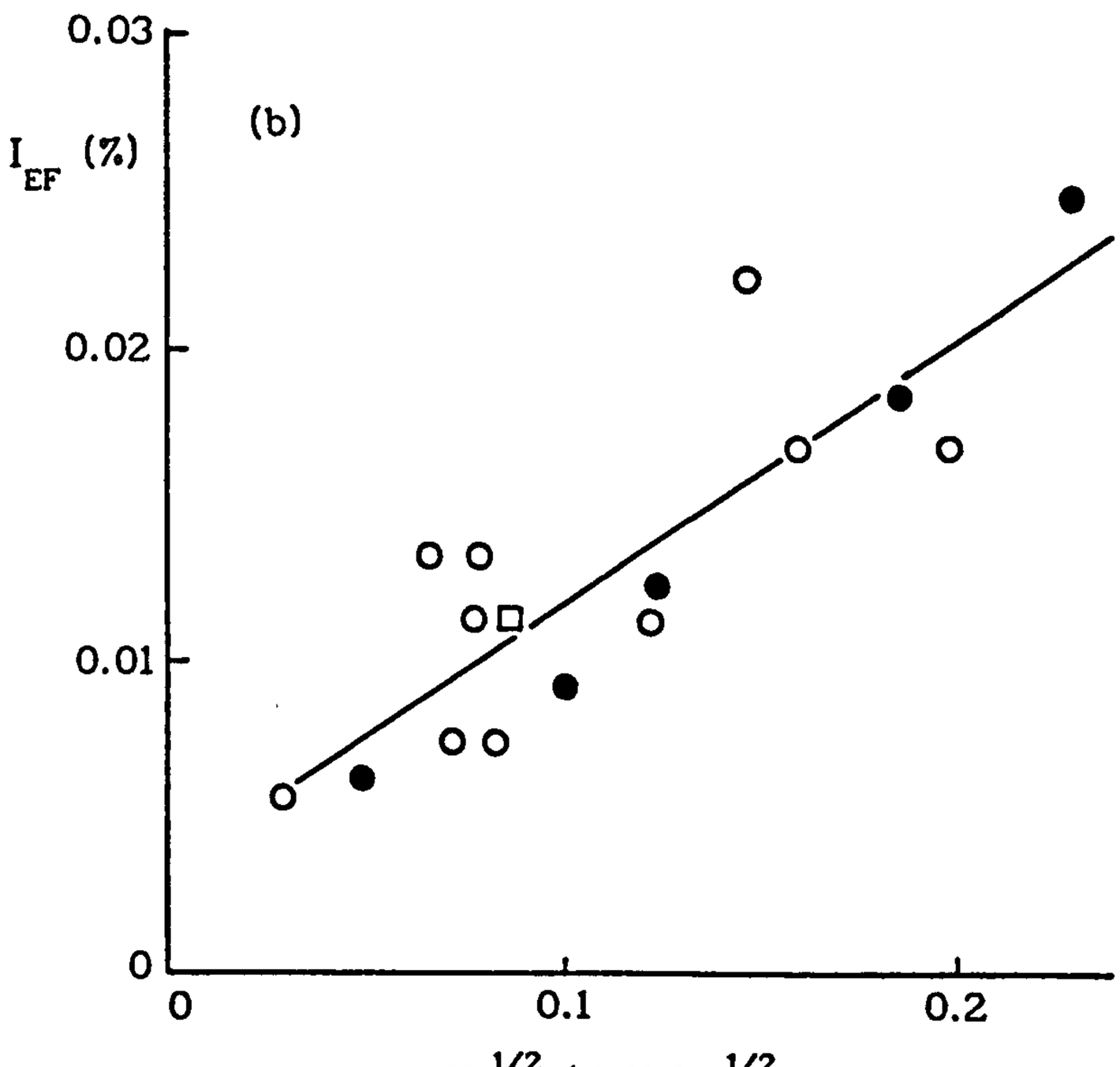

Figure 4.1 Plots of ionisation efficiency versus (a) α, and (b) $\alpha.V_c^{1/2}$. Data from published argon DC diode results; □ ref 23, ● ref 42, O ref 64. Solid curves represent linear regression fits to the data. Correlation coefficients are, (a) 0.5783, (b) 0.8618.

The value of $\overline{V}$ will depend on the applied cathode voltage and also the L/λ_c value in the cathode sheath. As shown in Chapter 3, L/λ_c for argon diodes does not change significantly with discharge parameters. Therefore V_c may be substituted for $\overline{V}$ when considering this type of discharge. Thus Figure 4.1b shows that phenomena related to the body of the plasma can be unified with effects occurring at the sample surface. Clearly though, this relationship will not be valid for enhanced discharges because L/λ_c would depend on the process conditions and the situation therefore becomes more complex.

The example given here illustrates the importance of employing experimental techniques which provide information that relates either directly to the substrate surface or to the cathode fall region which surrounds the substrate. Sputter weight loss measurements (SWL) could provide direct information on the effects of the discharge at the substrate surface. The principle of SWL is simply to sputter a sample under controlled discharge conditions for a period of time long enough to provide a measurable material weight loss. The weight loss may then be related to the discharge conditions. From a purely scientific viewpoint, this method might be criticised for its crudeness because sputtering rates depend on factors such as (i) sputter threshold, (ii) sputter yield dependence on energy, and (iii) bombarding particle angle. These effects may be difficult to de-convolute from variations in discharge phenomena. However, the principle advantage of SWL is that it provides a direct indication of particle bombardment effects at the sample surface which are representative of those that occur under ion plating conditions. SWL investigations were undertaken to study the influence of variations in uniformity of bombardment from the discharge due to (i) geometrical effects, and (ii) plasma spatial

density effects.

4.2 GEOMETRICAL PHENOMENA

4.2.1 Background

It has been reported in refs 65 and 66 that samples of different diameters will receive different plasma bombardment intensities due to sheath effects. This is because the power density at the sample surface is governed by the area of the sheath/plasma boundary rather than the sample surface area. The effect is illustrated in Figure 4.2a. As reported in Chapter 3, discharge enhancement will reduce the sheath thickness. Therefore bombardment intensities should become more comparable between large and small diameter samples under thermionic triode conditions (Figure 4.2b). The aim of this experiment was to verify the phenomenon by SWL measurements on cylindrical samples and correlate these results with values predicted from sheath thickness calculations.

It should be possible to obtain some theoretically based estimate of the change in power density arriving at two cylinders of different size, provided the sheath thickness is known. Consider a cylinder of radius R and sheath thickness L. The increase in power density, W, relative to that received by a flat plate, will depend on the ratio between the sheath circumference and the cylinder circumference. Thus,

$$W = \frac{2\pi\ (L + R)}{2\pi R} = \frac{L + R}{R} \qquad (4.3)$$

For two cylinders, of radii R_a and R_b in the same discharge, the ratio between power densities will therefore be:

$$W_a/W_b = \frac{(L + R_a)}{R_a} \Big/ \frac{(L + R_b)}{R_b} = \frac{R_b}{R_a}\left(\frac{L + R_a}{L + R_b}\right) \qquad (4.4)$$

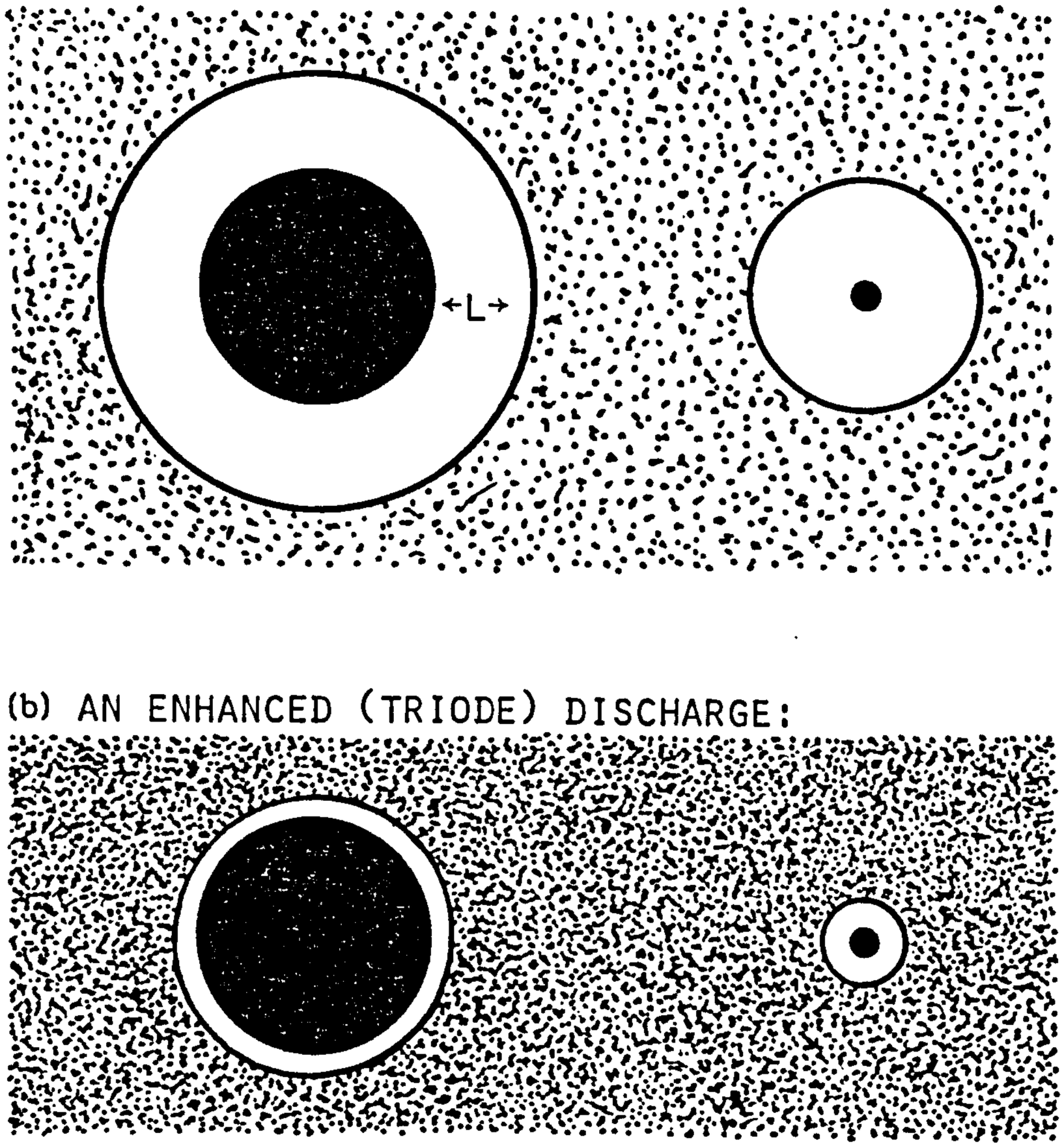

Figure 4.2 Illustration showing (a) how a large sheath under diode conditions can cause significant differences in plasma bombardment intensity between cylinders of different diameters, and (b) how enhancing the discharge reduces the sheath thickness so that bombardment intensities become more equalised.

Equation 4.4 is comparable to that given by Matthews in ref 65. Thus, knowing L, the power density ratio can be predicted and correlated with the SWL results.

4.2.2 Experimental

To evaluate the effects of sheath thickness on bombardment intensity, mild steel cylinders of two different diameters were sputtered under various argon discharge conditions. For this purpose, rig (2) was used so that (i) effects investigated were as near as possible to those that might occur in a real industrial process, (ii) the motorised rotating substrate feedthrough could be utilised to minimise the effects of local variations in filament distance from the samples under thermionic triode conditions, and (iii) the water cooled deposition chamber would permit long runs without potential overheating problems. The cylinders were mounted horizontally from a vertical rod fitted to the substrate feedthrough so that the assembly rotated about the central axis of the deposition chamber. The total surface area of the assembly was increased to about 3600 cm^2 by fitting a large flat plate to the rod near the top of the chamber. This provided a more realistic representation of the sample areas that would be encountered in commercial ion plating and increased the cathode current to levels which were appropriate for the rig instrumentation. Table 4.1 gives details of the cylindrical samples and their positions in the chamber.

To provide some indication of sample temperature during the sputtering process, a thermocouple mounted to a mild steel block of comparable dimensions to samples A2 and B2 was utilised. The block was positioned approximately mid-way between samples A and B. The main purpose of temperature monitoring in this experiment was to ensure that excessive

SAMPLE DESIGNATION	SAMPLE DIAMETER (cms)	HEIGHT ABOVE CHAMBER BASE (cms)	DISTANCE BELOW FLAT PLATE (cms)	LENGTH OF SAMPLE EXPOSED TO PLASMA (cms)
A1	0.3	23	37	9.5
A2	1.6	23	37	7
B1	0.3	48	12	9.5
B2	1.6	48	12	7

Table 4.1 Details of the cylindrical samples used and their positions in the deposition chamber.

heating of the jig assembly would not occur, as this may have damaged the substrate feedthrough.

The two main problems incurred with using rig (2) for this work were that (i) plasma bias supplies gave unacceptable waveform characteristics and (ii) the ion gauge to be used for chamber pressure measurement was uncalibrated. To overcome the waveform problem, all bias supplies used were run at maximum output, as discussed in Section 2.3.3. Thus diode discharges were run at 3 kV and thermionic triodes had to be operated with sample and filament biases of 200 V. The ion gauge was temporarily removed and fitted to the chamber of rig (1) to facilitate calibration against the Baratron capacitance-manometer, over an argon pressure range of 1 to 40 mTorr. This calibration was periodically checked during the experimental work so that any drift occurring in the ion gauge measurements could be compensated for.

Previous experience with the circular flat plate cathode, used to investigate the Child-Langmuir equation in Section 3.3.2, had indicated that grit blasting the cathode surface prior to use resulted in gradual current density changes with time under otherwise constant plasma conditions. This

could be attributed to a number of factors, including the gradual etching of asperities on the grit blasted surface during sputtering. As an alternative to grit blasting, the samples and other parts of the jig assembly were abraded with fine carborundum paper, prior to washing in acetone. In addition, the assembly was sputtered under 20 mTorr, 3 kV diode conditions for four hours to pretreat (etch) the surfaces so that they would be less likely to change during the actual experimental runs.

A series of trial runs were performed to evaluate the process parameters required for (i) adequate sputter weight loss and (ii) maintaining a thermocouple temperature of less than 500°C. This preliminary work and the constraints on plasma bias supply settings mentioned earlier, led to four experimental runs being performed. The run details are shown in Table 4.2.

RUN	DISCHARGE TYPE	ARGON PRESSURE (mTorr)	SAMPLE BIAS (Volts)	FILAMENT BIAS (Volts)	FILAMENT EMISSION (Amps)
S1	DIODE	20	3000	0	0
S2	THERMIONIC TRIODE	5	200	200	10
S3	THERMIONIC TRIODE	20	200	200	4
S4	DIODE	20	3000	0	0

Table 4.2 Run parameters used to study geometrical effects of plasma bombardment uniformity (Run S4 is a repeat of Run S1).

The run procedure was as follows:

(i) Weigh samples on microbalance and fit to jig assembly

(ii) Pump down to less than 10^{-5} Torr then set argon pressure

(iii) Sputter samples for two hours with jig assembly rotating at 3 revs/min

(iv) Allow samples to cool to less than 100°C and vent

(v) Remove samples and weigh.

The filaments used for thermionic triode sputtering, were made from 0.5 mm diameter tungsten wire, positioned in the form of a flat loop (mean diameter = 20 cms), approximately 6 cms above the chamber base. They were renewed prior to each triode run.

4.2.3 Results and Comments

The current densities, thermocouple temperatures and weight losses are summarised in Table 4.3. The mean and standard deviation values for current density and temperature were calculated from results taken at ten minute intervals during each sputtering run. The random errors in the sputter weight loss data were estimated to be less than ± 1%, based on microbalance measurement errors.

The following observations can be made from Table 4.3:

(i) The standard deviations for current density and temperature are significantly larger under thermionic triode conditions when compared with the diode results. Under diode conditions, the temperature and current density became relatively stable after about five minutes sputtering time, which can be attributed to the small thermal masses of the components involved. However, the triode runs showed a gradual increase in current density with run time and the temperature was also found to increase in a similar manner due to the increasing power density at the samples, hence the larger standard deviations. The reason for this effect might be attributed to a physical change in the

RUN	DISCHARGE TYPE	SAMPLE BIAS (Volts)	THERMOCOUPLE TEMPERATURE (^{o}C)		CURRENT DENSITY (mA cm^{-2})		SPUTTER WEIGHT LOSS/AREA (mg cm^{-2}) SMALL DIAM. CYLINDERS		LARGE DIAM. CYLINDERS	
			MEAN	S.D.	MEAN	S.D.	A1	B1	A2	B2
S1	20 mTorr DIODE	3000	455.3	28.2	0.0814	0.0048	1.7768	2.1501	0.4150	0.3772
S2	5 mTorr TRIODE	200	425.4	78.3	0.5035	0.1174	3.1205	1.2691	1.7537	0.5656
S3	20 mTorr TRIODE	200	384.5	76.8	0.4641	0.1373	4.0837	1.3886	2.5350	0.4824
S4	20 mTorr DIODE	3000	467.0	46.7	0.0767	0.0047	2.3404	1.7335	0.5985	0.5204

Table 4.3 SUMMARY OF RESULTS FROM THE CYLINDER SPUTTERING EXPERIMENT (S.D. = STANDARD DEVIATION).

filament characteristics. The triode runs were performed at an apparently constant filament emission. However, the presence of a positive ion space charge sheath around the filaments (as they were negatively biased) would have caused them to be subject to ion bombardment. The measured emission would have therefore had an unknown contribution from this ion current in addition to the actual electron emission effect. If the relative proportion of current due to ion bombardment had decreased with time, then the actual electron emission would have increased, causing greater plasma intensification and higher current density at the sample surfaces. A possible reason for the change in ion bombardment relative to true electron emission is detailed in Section 4.3.3.2.

(ii) There is a significant reduction in sputter weight loss with increased sample height in the chamber under triode conditions (compare A1 with B1 and A2 with B2 in Runs S2 and S3). This effect is not so evident under the diode conditions. Clearly, this must be due to spatial non-uniformity of the plasma and it is indicative of a potential disadvantage in the use of thermionic triode discharges.

(iii) The weight loss per unit area is greater for the smaller cylinders in all runs but the discrepancy is largest under diode conditions. This can be attributed to the sheath size effects as illustrated in Figure 4.2.

With regard to (iii), Table 4.4 shows the power density ratios between the large and small cylinders predicted from Equation 4.4. Although the sheath thicknesses were unknown, they were calculated from the sample bias and mean current density data, using the Child-Langmuir equation (Equation 3.6). Also shown, for comparison, are the equivalent sputter weight loss ratios calculated from the data in Table 4.3.

RUN	PREDICTED L (cms)	BOMBARDMENT EFFECTS- SMALL/LARGE CYLINDER RATIO PREDICTED (EQN 4.4)	SPUTTER WEIGHT LOSS RESULTS A	B	MEAN OF A & B
S1	4.179	4.637	4.282	5.701	4.991
S2	0.220	1.936	1.779	2.244	2.012
S3	0.230	1.966	1.611	2.879	2.245
S4	4.303	4.654	3.911	3.331	3.621

Table 4.4 Comparison between predicted power density and measured sputter weight loss.

The main observation which can be made from Table 4.4 is that the predicted power density ratios are comparable to the sputter weight loss ratios. As Runs S1 and S4 were performed under virtually identical conditions, these results may be combined. This gives mean ratios of 4.306 for sputter weight loss and 4.646 for power density. As the standard error on the former result is ± 0.504, this data shows that preferential sputtering effects on smaller sample radii can be predicted under diode conditions. The thermionic triode results (Runs S2 and S3) also show good agreement between theory and practice; predicted values being between the weight loss results of samples at positions A and B in each case. The higher weight loss ratios for samples at position B in these triode runs might be attributed to spatial non-uniformity of the plasma. A lower plasma density at a greater height in the chamber would produce a smaller current density at the sample surface. This would not only reduce the amount of material sputtered (see comment (ii) referring to Table 4.3) but also

increase the sheath thickness, for a given bias, in accordance with the Child-Langmuir equation. A larger sheath thickness for samples at position B would clearly increase the sputter weight loss ratio between small and large cylinders, as observed in Table 4.4.

There are a number of factors in this experiment which could make the good agreement between predicted and measured results (arguably) fortuitous. These will be discussed in Section 4.4.1.

4.3 PLASMA SPATIAL UNIFORMITY EFFECTS

4.3.1 Background

The previous SWL experiment using cylinders was, in addition to investigating geometrical phenomena, an evaluation of the technique for studying the effects of plasma uniformity. The results indicated that plasma density decreases with sample height in the chamber when a thermionic triode discharge is used. As the ionisation enhancing source (filaments) was positioned near the chamber base, it may be inferred that plasma density decreases with increasing distance from the filaments. The primary objective of this experiment was to investigate this effect.

4.3.2 Experimental

Figure 4.3a shows the experimental arrangement inside the chamber of rig (2). Four mild steel blocks, each 19.0 x 4.0 x 2.3 cms were mounted on the vertical rod positioned centrally in the chamber. Each block supported three mild steel samples at one end. The samples, with dimensions 3.80 x 1.25 x 0.30 cms, were flush mounted in three different orientations. The total surface area of the jig assembly was about 1390 cm^2. Table 4.5 gives details of sample orientation and position in the chamber.

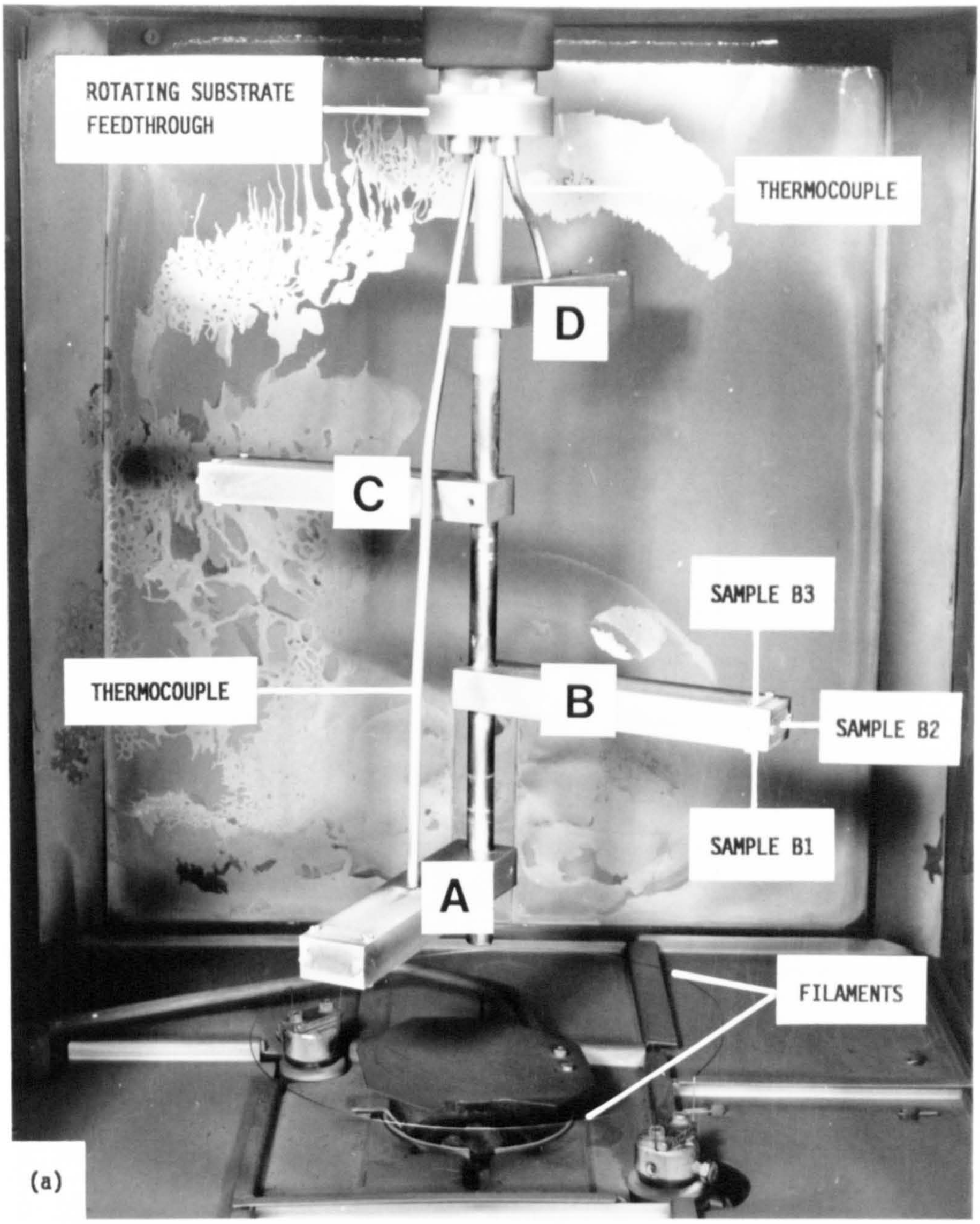

Figure 4.3 (a) Experimental arrangement for SWL investigations of plasma spatial uniformity.

(b) Close-up view of chamber base, showing the circular anode plate used in Run S10.

SAMPLE DESIG-NATION	ORIENTATION	RADIAL POSITION (cms)	HEIGHT ABOVE CHAMBER BASE (± 0.5 cms)	DISTANCE BELOW CHAMBER TOP (± 0.5 cms)
A1	DOWNWARDS	17.0	14.8	51.6
A2	SIDEWAYS	18.0	16.0	50.4
A3	UPWARDS	17.0	17.1	49.3
B1	DOWNWARDS	17.0	25.8	40.6
B2	SIDEWAYS	18.0	27.0	39.4
B3	UPWARDS	17.0	28.2	38.2
C1	DOWNWARDS	17.0	36.8	29.6
C2	SIDEWAYS	18.0	38.0	28.4
C3	UPWARDS	17.0	39.1	27.3
D1	DOWNWARDS	17.0	47.8	18.6
D2	SIDEWAYS	18.0	49.0	17.4
D3	UPWARDS	17.0	50.1	16.3

Table 4.5 Details of sample orientation and position in the deposition chamber.

The temperature of blocks A and D were each monitored by means of thermocouple wires fitted into a close tolerance hole drilled to the centre of the block. The wires were protected from plasma bombardment by steel tubing, as shown in Figure 4.3a. The block and sample surfaces were milled to a high quality surface finish, as an alternative to grit blasting, for

reasons outlined in Section 4.2.2. The etch pre-treatment and general run procedures were similar to those used in the cylinder sputtering work. However, to improve the accuracy of sample current measurement under diode conditions, where current instrumentation was insensitive (ref 14), a digital multimeter was used to monitor voltage drop across the panel meter shunt. The multimeter-shunt arrangement had previously been calibrated against known current values. Sputtering times for these runs were either 1, $1\frac{1}{2}$, or 4 hours.

Three types of discharge arrangement were studied; these were (i) diode, (ii) thermionic triode, and (iii) a configuration which may be termed a "positive plasma triode". In the case of (ii) and (iii), the filament arrangement shown in Figure 4.3 was used. Tungsten wire, 0.7 mm diameter, was used and it was positioned in the form of a flat loop with a diameter of 29 ± 0.5 cms at a height of 6.5 ± 0.5 cms above the chamber base. The arrangement used in (iii) differed from the more conventional set-up of (ii) in that the jig assembly was earthed and the plasma was made positive with respect to earth by using the crucible bias supply. As reported in Chapter 3, a positively biased electrode (anode) in the discharge will raise the plasma potential. This type of configuration was studied to see whether increased secondary electron emission effects from the chamber walls (by virtue of the elevated plasma potential) might partially offset the non uniform effects imparted by the filaments. The value of the plasma potential will be close to the anode bias provided the anode area is sufficiently large; a very small anode may produce a plasma potential lower, by an amount equal to the ionisation potential of the gas (15.8 volts in this case), as discussed in Section 3.2.2.2. To ensure the plasma potential would be similar to the anode bias, the anode area was increased by fitting a mild steel plate (32 cms diameter) to the crucible as shown in Figure

4.3b. To monitor the current from the earthed jig assembly, a 0 to 5A ammeter (previously calibrated) was connected in series between the substrate feedthrough and earth. The run details for all three discharge arrangements are shown in Table 4.6.

RUN	DISCHARGE TYPE	SPUTTERING TIME (Hours)	ARGON PRESS. (mTorr)	SAMPLE BIAS (Volts)	FIL. BIAS (Volts)	FIL. EMISS. (Amps)
S5	DIODE	4	24	3000	0	0
S6	THERMIONIC TRIODE	1	6	200	200	10
S7	THERMIONIC TRIODE	$1\frac{1}{2}$	6	200	200	10
S8	THERMIONIC TRIODE	4	6	200	200	10
S9	THERMIONIC TRIODE	$1\frac{1}{2}$	12.2	200	200	7
S10	POS. PLASMA TRIODE	$1\frac{1}{2}$	6	0*	200	10

Table 4.6 Run parameters used to study the effects of plasma spatial uniformity. * anode bias was ~ 75 volts above earth.

4.3.3 Results and Comments

4.3.3.1 Diode discharge (Run S5).

Figure 4.4 shows the SWL results as a function of height above the chamber base. Two main observations can be made from this data, (i) weight loss reaches a maximum value near the centre of the jig assembly for all sample orientations, and (ii) samples (1) and (3) show comparable weight losses but (2) gives values about 1.3 times higher.

The increase in weight loss near the centre suggests that sample current densities were higher in the middle than at the top or bottom. This in turn means that there must have been more ions available to diffuse into

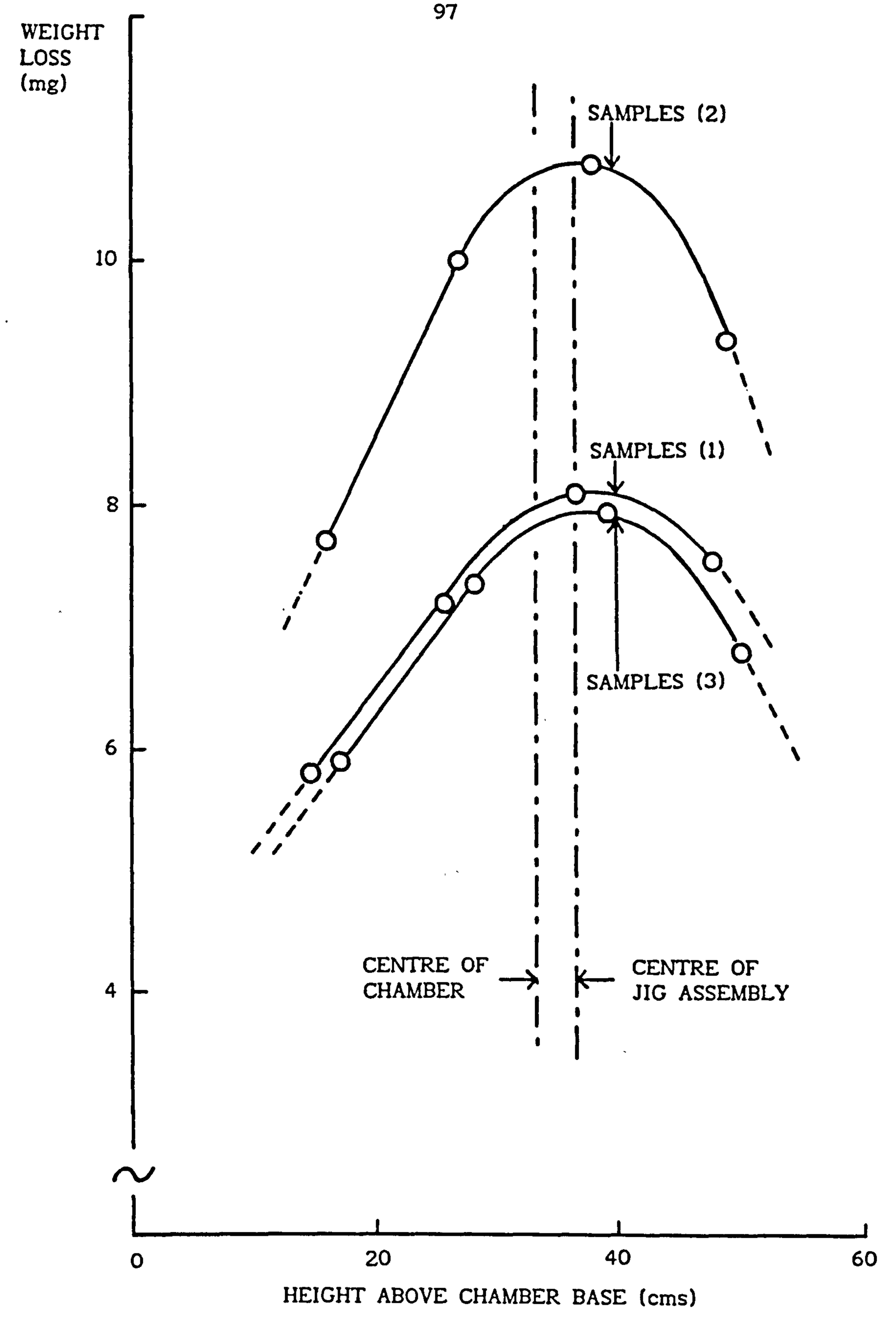

Figure 4.4 Weight loss measurements from a 3 kV, 24 mTorr diode discharge. Sputtering time was 4 hours (Run S5).

the sheath, implying that the plasma density was greater in the middle. Under diode conditions, the discharge is primarily sustained by electron emission from the cathode (jig assembly) as discussed in Chapter 3. Therefore, gas atoms situated near the centre of the jig assembly will be subjected to the effects of electrons emitted from a large proportion of the jig area. Conversely, the gas nearer to one end of the jig will tend to be subjected to electron bombardment from a more localised region and this may explain the changes in plasma density.

The greater weight loss observed with samples (2) could be due to sheath effects. Using the sample voltage and mean current density values; Equation 3.6 predicts the sheath thickness to be 3.4 cms. Figure 4.5 (drawn to scale) illustrates how sample (2) would receive a greater ion flux, as area B at the sheath-plasma boundary is greater than A. The effect is synonymous with the cylinder experiment in Section 4.2. However, in practice, the sheath would tend to be thinner at the corners as explained in Section 3.5.2.4, which might increase the influence of sheath curvature in this situation.

Figure 4.6 shows how the measured current and temperatures changed with time during the run. The temperature rise was considerably slower than that observed in the previous cylinder sputtering experiments and this can be attributed to the larger "thermal mass" of the blocks used in this arrangement. Initially, block D (at the top of the chamber) is slightly cooler than block A but as the temperatures approach steady state conditions, D becomes relatively warmer by about 30°C. As the jig feedthrough was water cooled, then the heat transfer from D to the feedthrough would have been higher than A initially because of the shorter conducting path. However, the heat conducted through the central rod from blocks A, B and C will have increased as the assembly approached steady

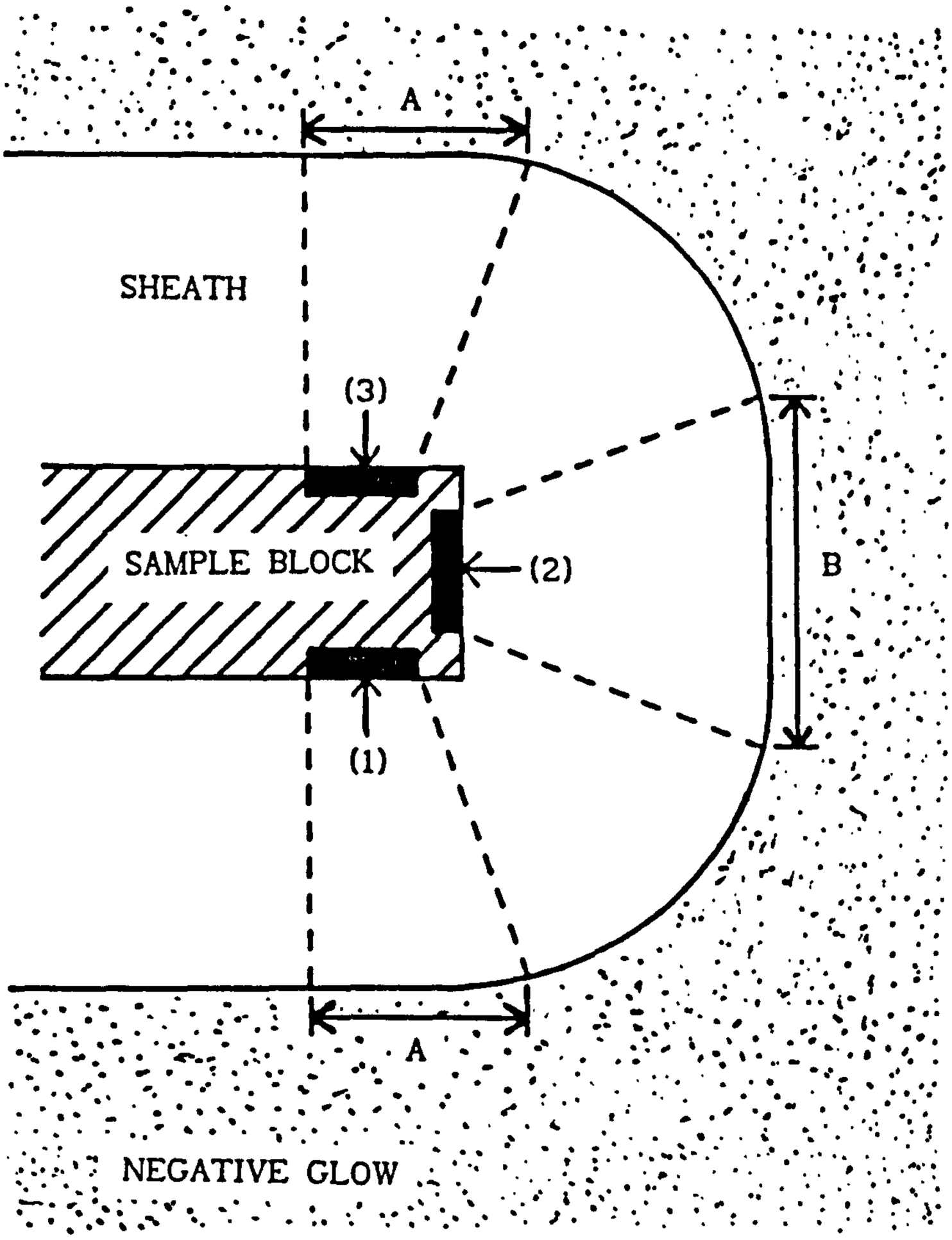

Figure 4.5 Scale illustration of how sheath effects could have produced greater sputter weight losses in samples (2) during Run S5.

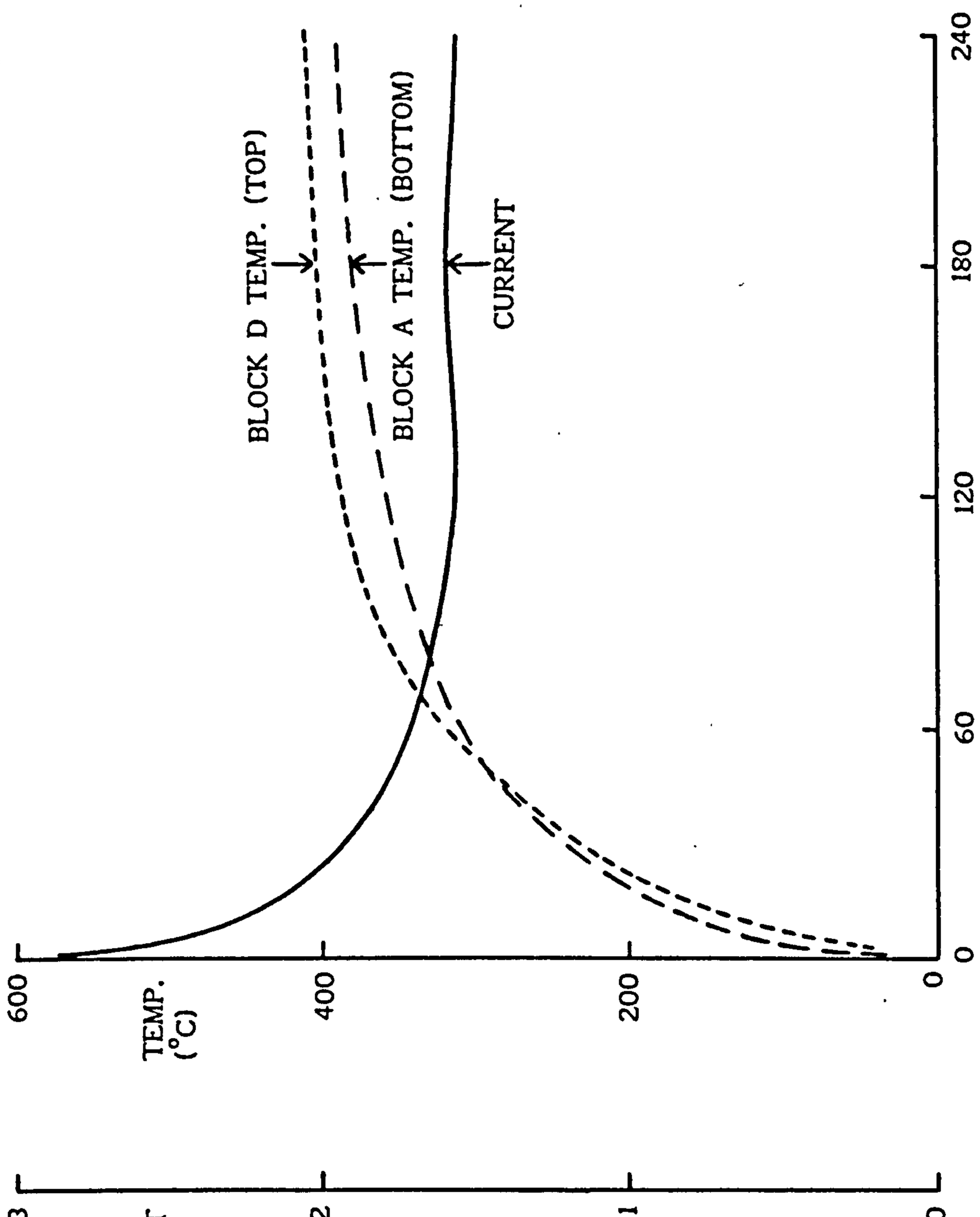

Figure 4.6 Jig assembly current and temperatures attained during Run S5.

state conditions and some of this energy would be conducted to D, raising the temperature slightly.

A more intriguing observation from Figure 4.6 is the decrease in current with time. This could be attributed to (i) surface changes altering the secondary electron emission coefficient, or (ii) some influence of bulk temperatures. It would be convenient to suggest that surface changes might be the cause, as secondary electron emission from the cathode is known to be very sensitive to changes in surface roughness and contamination effects. This is unlikely to be the reason though, because firstly the jig assembly had been subjected to many hours of sputter etching prior to this run so the surface roughness would not have changed. Secondly, the cylindrical SWL experiments reported in Section 4.2 gave steady current and temperature readings after about 5 minutes sputtering time under diode conditions. As both sets of SWL experiments were performed under comparable conditions, then contamination effects in this run would have been eradicated within the first 5 minutes of sputtering time. In fact, the rapid steady state conditions achieved in the cylindrical SWL diode runs can be attributed to the relatively smaller thermal masses used; had the temperature rise been slower, the time required to reach a steady current density might have been longer. The suggestion is, therefore, that increasing bulk temperature reduces the sample current density under diode conditions. Westwood and Boynton (ref 41) also noticed similar effects and they suggested that it may be due to a decrease in gas number density in the discharge and a consequent decrease in current, as the temperature of the system rises. As pressure was maintained at a steady level with the discharge running during the SWL experiments, but the argon flow rate into the chamber was generally observed to decrease slightly with run time, this explanation seems to be reasonable.

4.3.3.2 Thermionic triode discharges (Runs S6 to S9).

Figure 4.7 shows some of the weight loss results from Runs S6 to S8 as a function of height above the filaments on a semi-logarithmic plot. The main observation from Figure 4.7 is that the results from the 1 hour and $1\frac{1}{2}$ hour runs give linear relationships (ie, an exponential function) whereas those from the 4 hour run indicate a more complex function.

The reason for the non-exponential relationship of the 4 hour run can be attributed to contamination effects from the tungsten filaments. It was noticed that the jig assembly and samples appeared progressively darker nearer to the filaments and sample A1 in particular had a "sooty" appearance. The EDAX trace of sample A1 from Run S8 in Figure 4.8 confirms this explanation. Table 4.7 shows the measured diameters of the filaments after exposure to different process conditions.

PROCESS	MEAN DIAMETER (mm)	STD. DEVIATION (mm)
Unused	0.691	0.008
$1\frac{1}{2}$ hour heating in vacuum	0.690	0.007
$1\frac{1}{2}$ hour triode discharge (Run S7)	0.640	0.006
4 hour triode discharge (Run S8)	0.553	0.006

Table 4.7 Mean filament diameters, measured at four points in each case, after exposure to different process conditions.

The data shows a significant reduction in filament diameter when used in a discharge, but heating the filaments under vacuum conditions (at the same current) has no effect. This suggests that sputtering of the filaments by the plasma, rather than evaporation, has caused the tungsten

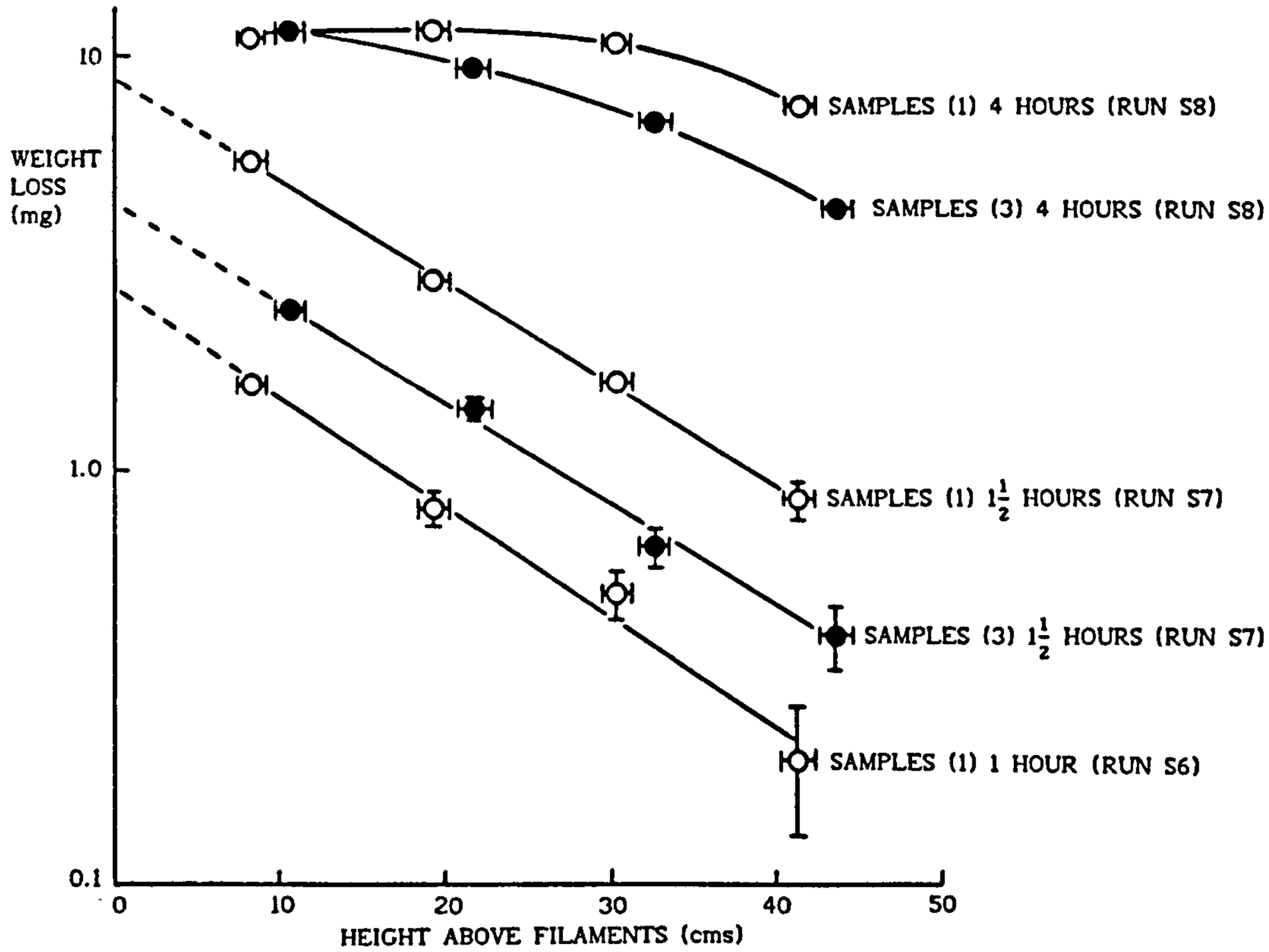

Figure 4.7 Weight loss results as a function of height above the filaments for thermionic triode discharges run for 1, $1\frac{1}{2}$ and 4 hours. Note: weight losses from samples (3) in Run S6 were too small to be measured with sufficient accuracy.

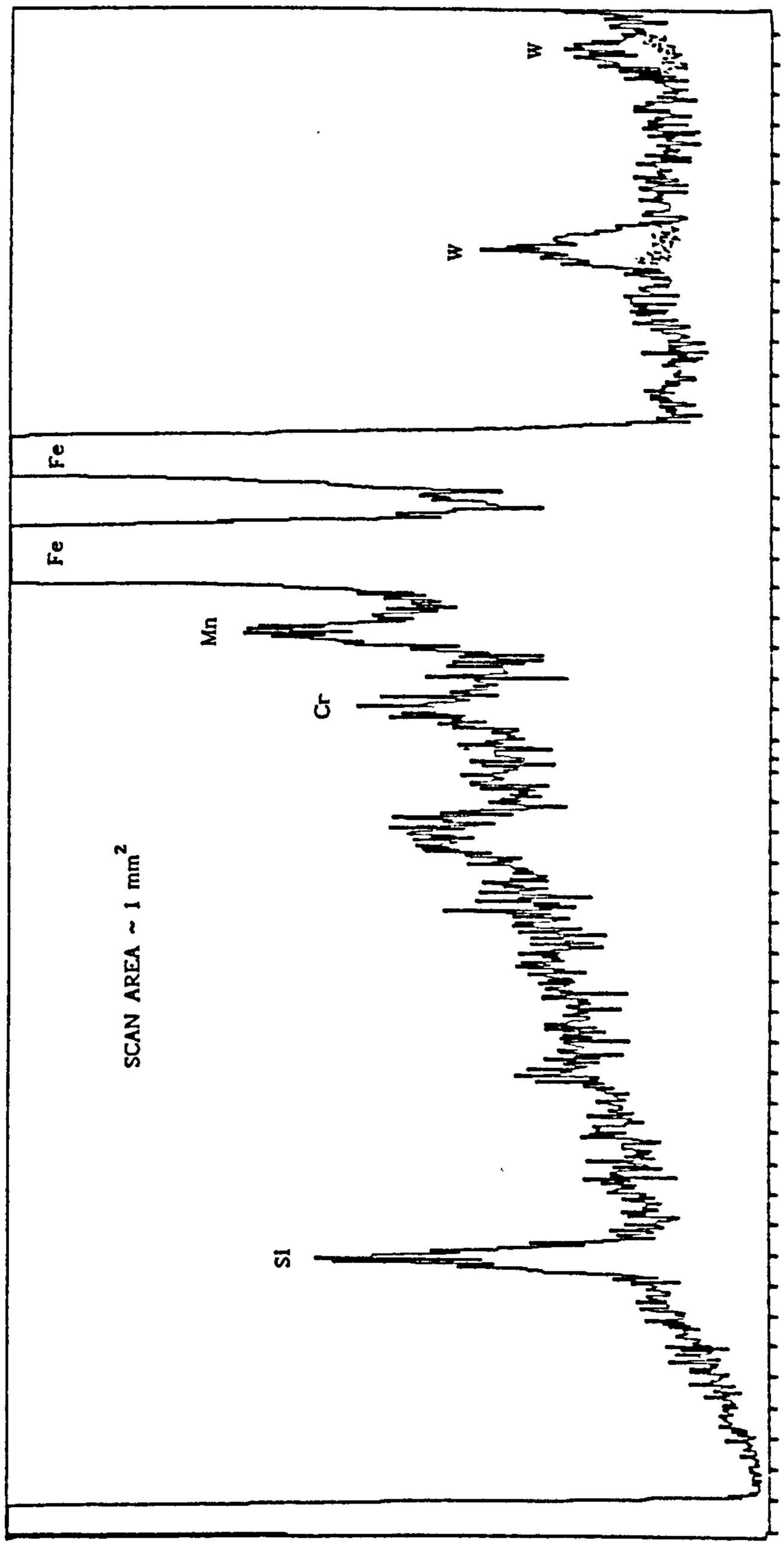

Figure 4.8 EDAX (Energy Dispersive Analysis by X-rays) trace of sample A1 from Run S8, showing tungsten peaks on the face bombarded by the discharge. Broken line represents trace from the rear face, which had not been exposed to the discharge.

contamination. Thus samples during longer SWL runs were being sputter coated with tungsten; the effect being greater on samples nearer to the filaments. It is interesting to note that the effect of sputter emission from the filaments could not have been constant. If it had been constant, the curvature in the SWL data from Run S8 would have also been apparent in Runs S6 and S7 in Figure 4.7. Figure 4.9 shows scanning electron micrographs of the filaments (a) in unused condition, (b) after exposure to 1 hour bombardment (from Run S6) and (c) after exposure to 4 hours bombardment (from Run S8). Clearly, the grain boundaries, which have become elongated during the wire drawing process, have opened up with exposure time. This creates a more faceted surface which changes the filament characteristics in two ways:

(i) The surface area of the filament increases with exposure to the plasma. The measured emission current, maintained at a constant level during each run, would have actually been a measure of the ion current arriving at the filament surfaces in addition to the true electron emission current. As shown in Section 4.2, the ion current density will depend on the area of the sheath/plasma boundary and not (in this case) the filament area. However, the total electron thermionic emission rate will increase as the actual surface area of the filament increases. This means that the proportion of true electron emission will increase relative to the ion current for a constant measured emission value. Therefore the intensity of plasma enhancement should increase with time and, from this effect, the sample current must also increase. Figure 4.10 confirms this effect. After the first 10 minutes, where contamination is being removed, the sample current rises gradually to a steady level at about 100 minutes. Unlike the diode discharge, where sample current depends on gas number density

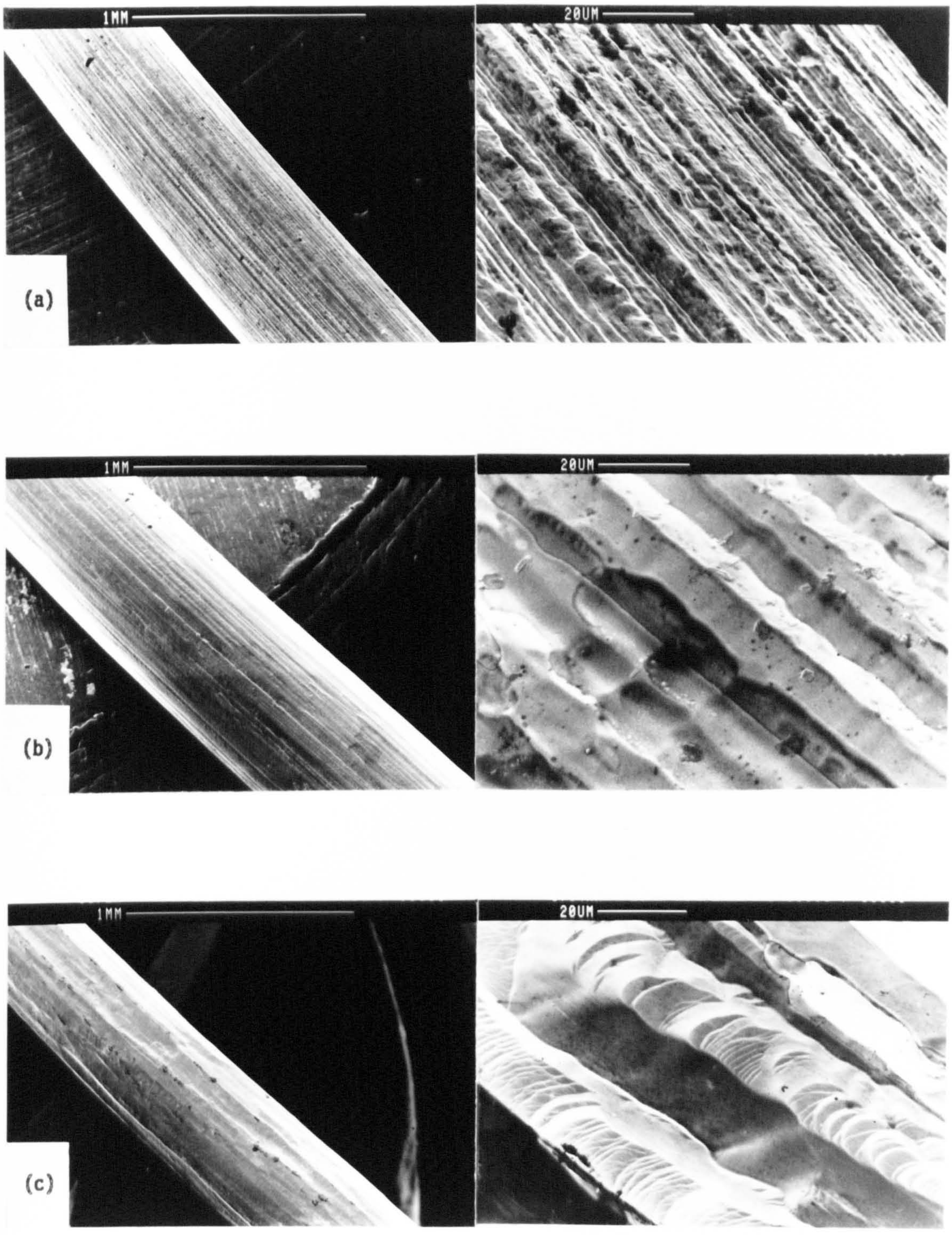

Figure 4.9 Scanning electron micrographs of the tungsten wire used as filaments in the SWL experiments, (a) in unused condition, (b) after exposure to 1 hour bombardment and (c) after exposure to 4 hours bombardment.

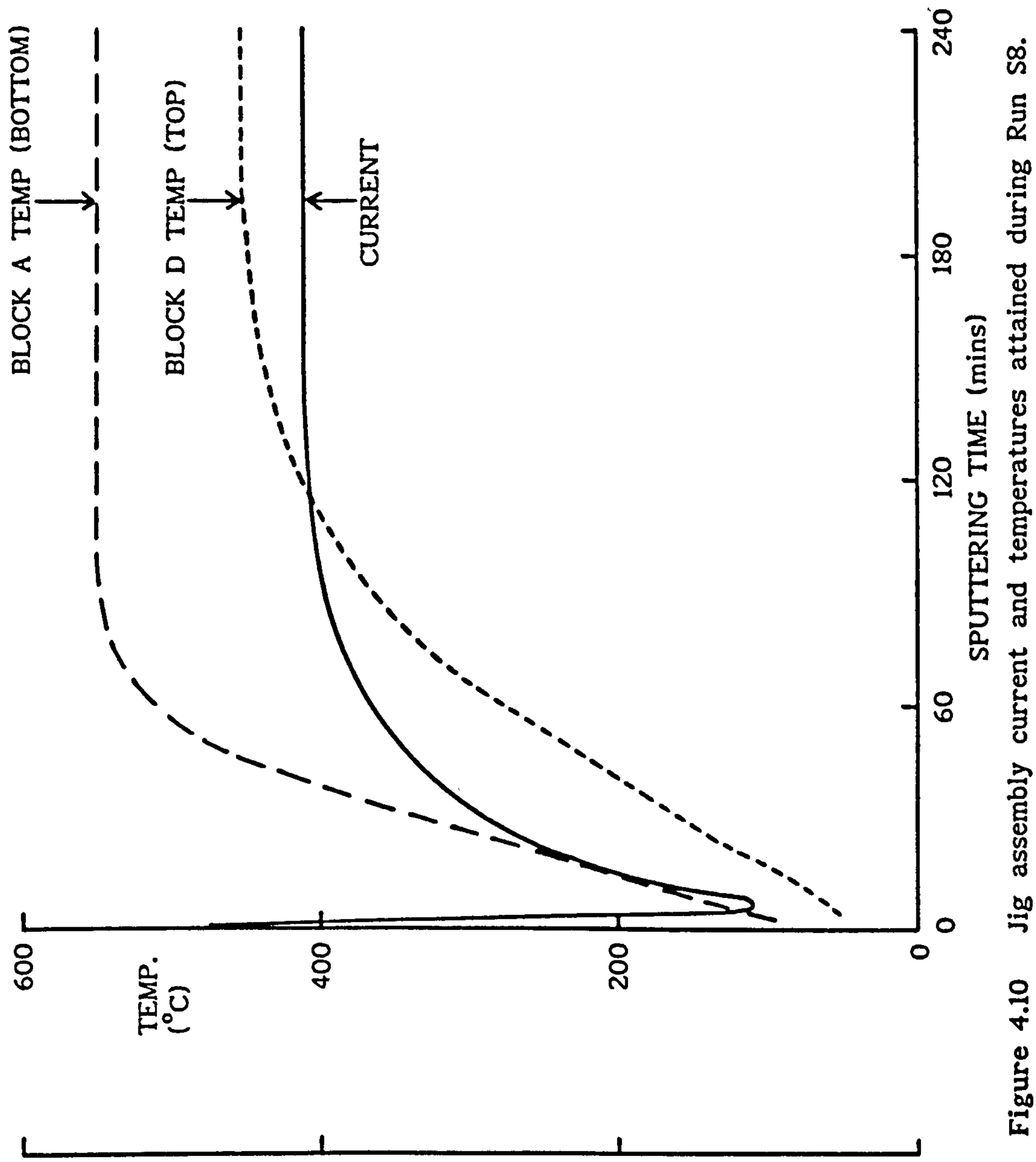

Figure 4.10 Jig assembly current and temperatures attained during Run S8. Runs S6 and S7 gave similar characteristics within their respective process times.

(Section 4.3.3.1) the thermionic triode depends primarily on electron emission from the filaments, so that this latter effect dominates any contribution that gas rarification may have on the current-time characteristic.

(ii) As the filament surface becomes more faceted with time, the probability of bombarding ions and high energy neutrals striking the surfaces at oblique angles must also increase. It is well known that sputter yield (per incident particle) is heavily dependent on the angle of incidence of the bombarding particles and yield tends to increase at more oblique angles of incidence (eg ref 26). Thus, for a given bombardment rate, the amount of sputtered tungsten might be expected to increase with filament exposure time in the discharge. This in turn could explain why the influence of tungsten contamination is considerably greater in Run S8, compared with Runs S6 and S7. However, as noted in (i) above, the ion bombardment rate is also thought to decrease with time and this would tend to offset the increased sputter yield. The only solution to this anomaly is to suggest that sputter yield increases more rapidly than the decrease in bombardment.

The exponential relationships for the 1 hour and $1\frac{1}{2}$ hour runs in Figure 4.7 clearly show that plasma density decreases with height above the filaments. This is also borne out by the lower temperature of block D (top of chamber) compared with that of block A in Figure 4.10. Complete plots of SWL data from Runs S7 and S9 are shown in Figure 4.11. The data from all three sample orientations in both runs give apparently linear relationships on the semi-logarithmic plots, indicating that the weight loss falls off exponentially with distance from the filaments. Table 4.8 summarises the linear regression parameters for exponential fits to the data; the mean

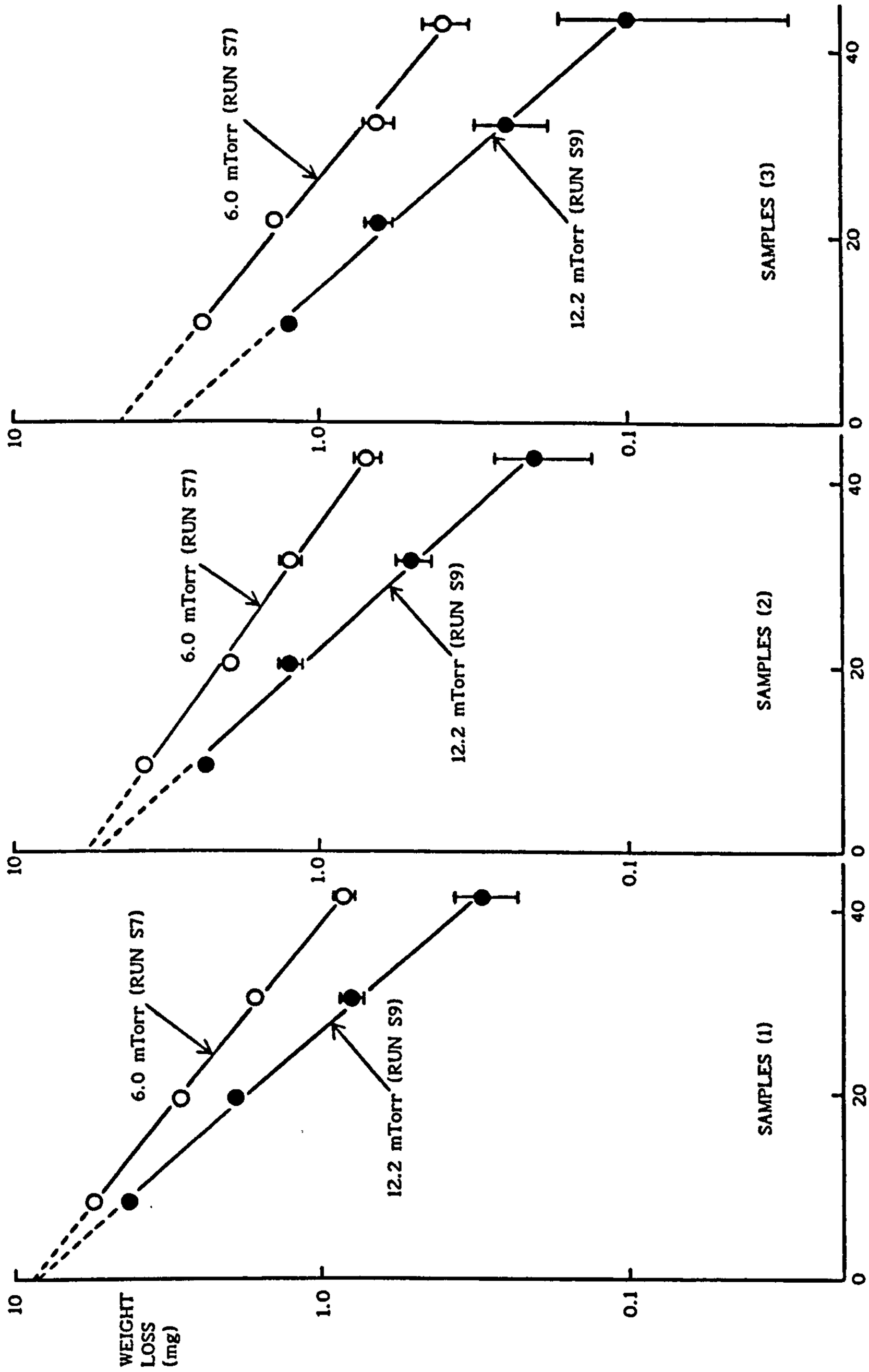

Figure 4.11 Weight loss results as a function of height above the filaments for thermionic triode discharges run for $1\frac{1}{2}$ hours at argon pressures of 6.0 and 12.2 mTorr (Runs S7 and S9).

current density and temperatures for both runs are given in Table 4.9.

	RUN S7 (6.0 mTorr)			RUN S9 (12.2 mTorr)		
	h (cms)	m_o (mg)	CORR. COEFF.	h (cms)	m_o (mg)	CORR. COEFF.
SAMPLES (1)	17.891	8.660	0.9993	12.525	8.520	0.9988
SAMPLES (2)	20.222	5.734	0.9978	13.240	5.246	0.9965
SAMPLES (3)	17.895	4.402	0.9962	12.883	3.010	0.9966

Table 4.8 Summary of the curve fitting parameters to the equation $m_s = m_o \exp(-x/h)$ where m_s = sputter weight loss at some distance x from the filaments, data from Runs S7 and S9.

	RUN S7 (6.0 mTorr)		RUN S9 (12.2 mTorr)	
	MEAN	STD. DEVIATION	MEAN	STD. DEVIATION
T_A (°C)	453.3	117.1	420.8	131.0
T_D (°C)	237.2	99.5	204.4	96.3
J ($mAcm^{-2}$)	1.286	0.333	1.298	0.552

Table 4.9 Mean and standard deviation values for current density (J) and temperatures of the lower and upper blocks A(T_A) and D(T_D). Results were calculated from readings taken every 10 minutes.

The following observations can be made from the data:

(i) The high correlation coefficients in Table 4.8 are indicative of a good fit to the exponential function and the parameter h may be

considered as an effective mean free path for the sputter weight loss process. The values of h for samples (1) and (3) are almost identical in each run. However, h is slightly larger for samples (2), and although sheath dimensions will have been considerably smaller than under diode conditions (see Figure 4.5), sheath geometry might explain this difference. It is interesting to see that h decreases as the argon gas pressure increases, for all three sample orientations. This would suggest that the process is governed by collision-limited phenomena, such as the creation of ions by electron impact with atoms. Clearly, the primary source of electrons in these discharges are the filaments. The filaments, negatively biased at 200 volts, emit electrons which accelerate across the surrounding ion sheath; thus electrons with nominal energies of 200 eV are ejected into the discharge. Using published collision cross section data (eg, from ref 16) and assuming the gas temperature was 300 K, the mean free path for electron impact ionisation for 200 eV electrons is 21.3 cms at 6 mTorr and 10.5 cms at 12.2 mTorr, using Equation 3.1. These figures are comparable to the data for h in Table 4.8 and this suggests that impact ionisation by electrons emitted from the filaments is the dominant mechanism that influences plasma spatial uniformity in thermionic triode discharges.

(ii) Table 4.9 shows that the mean current density and therefore power density, is similar for both runs. However, the sputter weight losses are consistently lower in Run S9, as shown in Figure 4.11 and by the m_o values in Table 4.8. This can be explained by the fact that although the average sheath thickness, L, in both runs would have been similar, (due to the same sample bias and current density) the mean free path for charge exchange, λ_c, will be different. In Run S9,

where the pressure was higher, λ_c would have been about half that of Run S7, due to the gas number density difference. The ratio, L/λ_c, governs the energy distribution of the bombarding ions and high energy neutrals, as discussed in Chapter 3. Therefore the bombarding species in Run S9 will have had a lower average energy. As sputter yield increases with energy over the range of interest here, the weight losses obtained are lower for Run S9. The slightly lower temperatures for Run S9 may also be indicative of this effect.

(iii) Within each run, the weight losses are highest for samples (1), intermediate for samples (2) and lowest for samples (3). This suggests that phenomena which result in surface bombardment have a preferred spatial orientation in thermionically supported discharges. Consider the following: The discharge is primarily sustained by electrons emitted from the filament which collide with atoms to create ions. These ions diffuse into some part of the sheath around the jig assembly and accelerate to bombard the samples directly and indirectly by the creation of high energy neutrals. Under the conditions observed here, the ion diffusion rate into the sheath must have been highest for those ions moving in an upwards direction and lowest for those moving downwards. The weak field in the pre-sheath region is responsible for drawing ions into the sheath, but it can be appreciated that the density of ions in the negative glow and any initial velocity (kinetic energy) in some preferred direction will also have some influence. Although ion density must clearly fall off with distance from the filaments, the regression curves in Figure 4.11 show that at some fixed height (ie, fixed ion density), bombardment is highest for the sample (1) direction and lowest for the sample (3) direction. Therefore, the effect must be a consequence of the ions

having a preferred motion in an upwards direction. Thus, ions moving upwards would have to change direction to diffuse into the sheath region around samples (2) or samples (3). Therefore of the ions moving upwards, only those with velocities (energies) sufficiently low to be attracted by the influence of the pre-sheath region in directions other than upwards are likely to contribute to the bombardment of samples (2) and (3). The cause of this preferential upwards motion by the ions must be due to electron emission effects from the filaments. As the filaments were situated at the base of the chamber, then the emitted electrons which influence the discharge would have been those moving upwards through the chamber volume. The flow of relatively high energy electrons through the discharge must create some electric field distribution which the ions may tend to counteract by also moving upwards. This anisotropic plasma phenomenon might be considered to be comparable to ambipolar diffusion; the latter process has been described for simplified situations in most of the standard texts on plasmas and glow discharges.

4.3.3.3 Positive plasma triode discharges

The results from Run S10 were significantly affected by contamination problems. Most of the samples, particularly samples (2) and (3), appeared to be dark grey or black after the run. As the jig assembly and chamber walls were subjected to similar bombardment effects, the source of contamination was probably material sputtered off the latter. In many cases, the contamination produced negative weight loss values, making a detailed interpretation of results impossible. However, the weight losses of samples A1, B1 and D1 were found to be 0.80, 0.40 and 0.15 mg respectively. This fall off rate with height above the filaments is

comparable to the results for samples (1) from Run S7 (Figures 4.7 and 4.11). It indicates that any benefits in terms of improved plasma uniformity, attributable to increased effects of electron emission from the walls, may not be significant.

Table 4.10 summarises the sample temperature and current density results for Run S10, the results for Run S7 are also given for comparison. It is interesting to see that although the mean value for T_A is similar for both runs, T_D is higher in Run S10, possibly indicating an improvement in plasma uniformity.

	RUN S10 (6.0 mTorr)		RUN S7 (6.0 mTorr)	
	MEAN	STD. DEVIATION	MEAN	STD. DEVIATION
T_A (°C)	446.6	140.4	453.3	117.1
T_D (°C)	339.4	133.5	237.2	99.5
J ($mAcm^{-2}$)	1.899	0.350	1.286	0.333

Table 4.10 Temperature and current density data from the positive plasma triode (Run S10) compared with a more conventional triode discharge (Run S7).

Although contamination problems have prevented a detailed investigation, the results suggest that raising the plasma potential in a thermionic triode discharge may reduce the effects of non-uniform plasma density but the improvement is likely to be small.

4.4 SPUTTER WEIGHT LOSS EXPERIMENTS - DISCUSSION

4.4.1 Cylinder Experiments

It has been assumed in the cylinder SWL experiments that weight loss is proportional to power density at the substrate surface; the latter being evaluated from simple considerations of cylindrical geometry and sheath thicknesses (see Table 4.4). Clearly, this is an over-simplification. For example, (i) the Child-Langmuir equation used was developed for flat plate geometries, (ii) the cylinders, particularly samples (2), were not very long in relation to their diameters thus sheath distortion from end effects may have been significant, and (iii) there may have been a substantial temperature difference between the smaller and larger diameter cylinders as the former had lower heat capacity (due to less mass), and were subjected to greater bombardment effects.

In the case of (i) a version of the Child-Langmuir equation for cylindrical geometry does exist, as reported in Section 3.5.2.4, but sheath thickness would have to be predicted by some iterative method. However, the form of the equation is similar to the relationship representing flat plate geometry. As ratios (rather than absolute values) were studied, this discrepancy is minimised. Similarly, sheath distortion due to end effects and temperature differences (which may have changed the sputtering yield) will have been minimised to some extent by considering only relative changes.

Although the factors outlined above will have had some influence in these results, the experiments have shown that the basic relationship between predicted sheath thickness and power density (as represented by the Child-Langmuir equation) correlates with sputter weight loss measurements, when geometrical effects are considered. This means that the Child-Langmuir equation may be used to evaluate the likely problems of preferential plasma

bombardment on substrate components which may have complex geometries or on batches of components which have mixed sizes. The experiments have also shown that enhancing the discharge provides a means of removing these potential problems by making the sheath thickness smaller.

4.4.2 Plasma Spatial Uniformity Experiments

4.4.2.1 Uniformity in thermionic triodes

One of the main results of the plasma uniformity experiments has been to show that sputter weight loss appears to decrease exponentially with height above the filaments in a thermionic triode discharge. The estimated mean free paths for ionisation by electrons emitted from the filaments are comparable to the values for h in Table 4.8, which might imply that this mechanism has the dominant influence. There are, however, other effects which may also influence the weight loss results. These are:

(i) The filament geometry used is effectively a ring source. Therefore, even without collision phenomena occurring, the flux density of electrons emitted from the filaments would decrease with height. (Characteristics of vapour emitting ring sources are described in ref 26).

(ii) The collision cross section for 200 eV electrons being elastically scattered in argon is about 3×10^{-16} cm^2 and this is comparable to the value for electron impact ionisation, which is about 2.5×10^{-16} cm^2 (eg, ref 16). Thus filament electrons would have had almost equal probabilities for creating ions or being elastically scattered.

(iii) The electron impact ionisation process creates an additional electron which may also be capable of causing further ionisation. In more general terms, these additional electrons contribute to the secondary and ultimate electron groups.

(iv) The sheath thickness around the samples will increase with height. This is due to the decreasing current density for a fixed sample bias, in accordance with the Child-Langmuir equation. Thus, the ion energy distribution will change, such that the average energy of the impinging ions (and high energy neutrals) will decrease with height, further reducing sputtering yield.

(v) Electrons emitted from the walls and, in particular, from the jig assembly may also create ions.

(vi) Each electron emitted from the filaments can create more than one ion.

(vii) High energy photons can create ions in the negative glow, in addition to those produced by electron impact.

Although points (i), (ii) and (iv) may tend to increase the rate of fall off of weight loss with height, (vi) might offset these effects. Point (vii) might be insignificant, if the role of photo-ionisation in a thermionic triode discharge is assumed to be negligible, as in the case of the simple diode layout (Section 3.2.3). It is difficult to ascertain the influence of (iii) and (v) or whether even the proposed diffusion of ions up the chamber (anisotropic plasma effects) and ionisation of metastables may have an effect on the spatial distribution of weight loss results. The situation is complicated by collision phenomena being energy dependent and by difficulties in evaluating the role of different energy groups of electrons in various parts of the chamber.

In spite of these problems, it is clear that the fall off in weight loss with distance from the filaments shows that electron emission from the latter must be the dominant influence on plasma uniformity. The fact that the fall off rate increases with increasing pressure (see Figure 4.11) suggests that the availability of electrons from the filament to create ionisation at greater heights, is primarily limited by collision phenomena,

rather than some of the other points raised above, eg ring source effects. As the main collision phenomena are likely to be electron elastic scattering and electron impact ionisation, the reasoning is simplified. Although the elastic scattering cross section for the filament electrons is comparatively large, their relatively high energies (about 200 eV) result in very small deflection angles; typically less than 20° (ref 67). The mean free paths for this process are about 17 cms and 8.5 cms at 6 mTorr and 12 mTorr argon pressure respectively. Over the distances considered in the chamber (less than 50 cms), it can be seen that the small number of path lengths and low deflection angles associated with filament electron scattering is unlikely to significantly influence the spatial distribution of ions created by electron impact. Therefore, if this is the case, impact ionisation by relatively unscattered filament electrons must be the dominant influential mechanism. Other influences which have been considered to be of second order importance here may become significant, however, if higher pressures, larger distances or even different filament or jig geometries are studied.

For practical ion plating systems, where thermionic enhancement is used, the decrease in bombardment from the plasma with thermionic emitter distance could result in reduced coating densification at greater distances. To some extent though, this effect will be offset by a fall off in deposition rate provided the thermionic emitter is positioned close to the vapour source. This is due to the fact that the vapour flux density also falls off with distance (see Chapter 6), so the ratio between plasma bombardment and vapour arrival rates at sample surfaces will be less likely to change with height above the vapour source and emitter. As demonstrated in the results of Figure 4.11, the rate of fall off in bombardment from the plasma can be reduced by using a lower discharge pressure, as this increases the mean free path length for electron impact ionisation. Changing the

thermionic emitter bias, to reduce the ionisation collision cross section, should also have a similar effect.

4.4.2.2 Plasma anisotropy in thermionic triodes

It was inferred from the lower weight losses on samples (2) and (3) (relative to samples (1)), in the thermionic triode experiments, that the ions must drift upwards. This upwards motion is unlikely to be caused by gas flow effects in the chamber, because the gas was admitted through the top and pumped out from the chamber base. The probable reason, as already suggested in Section 4.3.3.2, must be an electric field effect from electrons emitted by the filaments.

With the exception of rather idealised explanations of ambipolar diffusion behaviour in the published literature, there appears to be little, if any, information which relates to anisotropic phenomena in thermionic triode discharges. The effect is important for two reasons. Firstly, the applicability of the Child-Langmuir equation has to be questioned, because it is assumed that the ions enter the sheath region with zero energy. Clearly, this is not the case if the ions have some finite initial velocity. A more comprehensive version of the equation exists to account for situations where this cannot be assumed (Equation 3.7) though knowledge of the ion temperature is required, making its use impractical. However, the simplified equation has been tested under similar thermionic triode conditions in Chapter 3, and good agreement has been found between predicted and measured sheath thicknesses. Therefore, at least for practical purposes, the simplified version of the Child-Langmuir equation may still be considered applicable. The second effect relates to practical thermionically enhanced ion plating systems. The observed anisotropy, if it occurs generally, means that samples facing away from the thermionic emitter

will receive relatively less bombardment from the plasma. If the vapour flux incidence rate does not change with sample orientation, then coatings deposited on samples not facing the emitter are likely to be less dense and therefore possibly inferior. However, the vapour arrival rate will tend to be lower on surfaces remote from the source, (see Chapter 6). Therefore, if the thermionic emitter is positioned close to the vapour source, the two effects will offset each other to some extent, as with the spatial uniformity behaviour discussed in Section 4.4.2.1. This means that the plasma bombardment : vapour arrival ratio will be less likely to change with sample orientation.

4.4.2.3 Tungsten filament contamination

The observed contamination of samples due to tungsten sputtered from the filaments needs to be considered in terms of an actual thermionically supported ion plating process. The results from these experiments indicate that this form of contamination is only likely to become significant during longer coating runs (more than $1\frac{1}{2}$ hours). As most runs tend to be shorter than this (at present), then it may be assumed to be of little consequence, provided the filaments are regularly renewed. Longer runs may become more common in the future though; for example, in the production of thick coatings or when a continuous coating process may be used, where some form of load lock system is employed to ion plate successive batches of components.

There are a number of possible solutions to this potential problem. One of the simplest methods might be to reduce the filament bias but increase the temperature (electron emission rate) to maintain the required discharge enhancement. As the sputter yield decreases with decreased ion energy (by virtue of the lower bias), the amount of tungsten produced should

be less, provided that the sputter yield does not significantly increase with temperature.

If the filaments are positioned near to the vapour source, they may become coated which would thus eliminate the problem. Clearly, this depends upon the melting point of the vapour in relation to the filament temperature. Optical pyrometer measurements of filament temperature, carried out at various times during the course of this work, have given readings of 2000 - 2400 K, which is higher than the melting points of many evaporant materials (titanium melts at about 2000 K). Therefore any benefits derived from vapour deposition are likely to be minimal.

Other solutions might include changing the filament geometry to reduce sputtering. For example, the filament wire could be bunched or coiled so that the distance between adjacent turns was within the sheath dimensions. This would reduce the surface area of the sheath relative to the surface area of the wire, thus decreasing bombardment for a given electron emission rate. More elaborate solutions, such as a grid surrounding the filaments to trap the ions may be effective, but the electron emission will be reduced as the grid will also tend to either collect or repel electrons back depending on whether the grid is at a positive or negative potential with respect to the wire.

4.4.2.4 Positive plasma triodes

Although the results from Run S10 were subject to contamination problems, they show that any potential improvements in plasma bombardment uniformity are likely to be small. This observation is also supported by the data from enhancing discharges with only a positively biased electrode, reported in Chapter 3; the increased effects of electron emission from the walls being considerably weaker than the contribution from thermionic

emission.

The effect resulting in the contamination problem, which is believed to be material sputtered from the chamber walls, is also likely to occur in an actual ion plating system, using a similar arrangement. Whether it is a contamination problem in the latter case becomes questionable, because the chamber walls will be ion plated under conditions comparable to the actual samples. The coating deposited on the walls will be sputtered and possibly be re-deposited on the samples. However, although the wall deposit may have different stoichiometric properties (due to the vapour flux distribution), it is unlikely to have a detrimental effect on sample coatings provided that they are chemically similar. In fact, the mechanism may even be beneficial in terms of improving coating thickness uniformity in the process.

One of the main benefits of ion plating with this type of arrangement is that the substrates would be earthed with the deposition chamber. This would eliminate the need for substrate feedthroughs and thermocouples (used for measuring substrate temperatures) to be electrically isolated. It is apparent though, that further investigations are required to establish the potential merits of ion plating earthed samples in this type of discharge.

4.5 SUMMARY

The justification for investigating discharge characteristics by sputter weight loss (SWL) measurements, rather than by other means (eg, Langmuir probes), has been explained. The main advantage of SWL is that it provides a direct indication of discharge effects at the sample surface; these effects being representative of those which occur under ion plating conditions. Two SWL experiments were performed so that the influence of both sample geometry and plasma spatial density could be investigated.

The first experiment utilised mild steel cylindrical samples of two different diameters and these were sputtered under argon diode and thermionic triode conditions. It was found that the sputter weight loss ratio between small and large diameter cylinders gave good agreement with the power density ratio under all conditions. The power density ratios were calculated from sheath thickness predictions using the Child-Langmuir equation (simple flat cathode version) and geometrical considerations. These results have shown that the Child-Langmuir equation may be used to evaluate the potential difficulties associated with preferential bombardment, on substrate components with complex geometries, or on batches of mixed sized components. The experiment has also verified that enhancing the discharge (eg, by thermionic support) provides a means of removing these potential difficulties, by making the sheath thickness smaller.

The second experiment was primarily concerned with the influence of plasma spatial density effects on the sample surface. This utilised four mild steel blocks mounted at different heights above the chamber base. Samples for SWL measurements were mounted in various orientations on each block. Runs were performed under various argon diode and thermionic triode conditions. The diode results showed increased bombardment effects nearer to the centre of the jig assembly, which could be attributed to greater plasma intensification in the central region of the chamber. This increased plasma density probably arose from the greater availability of electrons emitted from the surfaces of the jig assembly. The thermionic triode results gave an exponential fall off in weight loss with distance from the thermionic emitter (filaments) for all sample orientations. It is proposed that this was primarily due to impact ionisation effects from electrons emitted by the filaments; this being the primary source of ionisation in these discharges. The insertion of an additional anode to elevate the

plasma potential, thereby increasing electron emission from the chamber walls, did not appear to provide any substantial improvement in plasma spatial uniformity under thermionic triode conditions. Samples facing the thermionic emitter exhibited greater weight losses than those in more remote orientations and this has been attributed to the electrons emitted by the filaments causing anisotropic effects in the plasma. The effects of non uniform plasma density and anisotropy in thermionic triode discharges are potential drawbacks to this method of enhancement. However, it is suggested that these effects will be offset to some extent, if the thermionic emitter and vapour source are positioned close to each other in ion·plating systems. In addition, plasma spatial uniformity could be improved by increasing the mean free path length for electron impact ionisation. This could be achieved by decreasing the discharge pressure or changing the thermionic emitter bias.

The current density and temperature under diode conditions became constant within a very short time in the cylinder experiment, though a much slower temperature rise was observed in the spatial uniformity experiment, due to the larger masses of the blocks used. The current density was observed to decrease as temperature increased in the latter experiment when a diode discharge was used and this has been attributed to gas rarification at constant pressure due to system heating. However, under thermionic triode conditions, both experiments showed that current density and temperature gradually increased with time. Although these runs were performed at an apparently constant filament emission, the ion current to the filaments would have made an unknown contribution to the measured emission. It is suggested that the proportion of actual electron emission increased with time and this caused greater discharge enhancement which resulted in the rise in current density and temperature under the conditions used. Scanning

electron micrographs of the filaments have shown that the grain boundaries open up with usage, producing a more faceted surface, which might be expected to increase the proportion of electrons emitted.

Longer run times in thermionic triode discharges (greater than $1\frac{1}{2}$ hours) resulted in samples becoming contaminated by tungsten sputtered off the filaments. A possible reason for the contamination to become more significant during longer runs is thought to be increased sputter yield. The yield (per bombarding particle) might be expected to increase if the grain boundaries open up, as observed on the micrographs of the filaments, and cause more bombardments to occur at oblique angles of incidence. This phenomenon may need careful consideration, particularly if longer ion plating runs are required.

5. ION PLATING DISCHARGES - OPTICAL EMISSION SPECTROSCOPY AND FURTHER INVESTIGATIONS OF THE CATHODE SHEATH.

5.1 INTRODUCTION

Although SWL experiments can provide direct information on the influence of discharge parameters at the sample surface, the technique is limited to interpretation of weight loss data. This chapter reports on further experimental work with discharges, where optical emission spectroscopy (OES) is the primary investigative technique.

There is a considerable amount of literature published on OES techniques in plasma processing. Most of the information refers to end point detection and diagnostics in plasma etching of semiconductors and other integrated circuit materials for the electronics industry (eg, refs 68, 69). Other papers report on OES based monitoring and control systems for diode type sputter deposition processes (eg, refs 70, 71) and thermionic triode ion plating systems (ref 72). The final group of publications provide data on the characterisation of sputter deposition discharges, using OES, sometimes in conjunction with other investigative techniques such as Langmuir probes. Examples include; spatial distribution of various excited species (refs, 73 - 76), nitrogen rotational temperature (ref 77), plasma electron temperature (refs 78, 79) and particle density of a particular species (ref 80). OES will not provide direct information on particle bombardment at the sample surface, and virtually all of the published OES work relates to studying the negative glow rather than elsewhere. However, it is a non-intrusive technique which is capable of providing spatially resolved information. Therefore it could be utilised to study the cathode sheath in addition to the negative glow.

The aim of the investigations presented here, is to provide

information on discharges which is either complementary to or in addition to the findings of Chapters 3 and 4. To achieve these aims required (i) OES equipment which was capable of providing spatially resolved information from the discharge, including the cathode sheath region, (ii) a systematic investigation of many discharges, ranging from simple argon diodes to those which occur during ion plating, and (iii) additional sheath thickness studies which were not performed in Chapter 3 (eg, during evaporation). The data could then be used to address specific areas of interest which relate to both fundamental and practical aspects of discharges used in ion plating. These include electron temperature determination, discharge intensity variations, dissociative charge transfer in nitrogenous discharges, tungsten filament contamination and the role of the metal species.

5.2 OES EQUIPMENT

5.2.1 Description

The OES apparatus used in this work comprised a Bentham Instruments M300EA monochromator coupled to a quartz fibre optic cable. The cable, nominally 1 m in length, had a 4 mm diameter receiving area and was shrouded by a flexible steel hose. The monochromator had a focal length of 30 cms and a 1200 lines mm^{-1} diffraction grating. The entrance and exit slit widths were adjustable for selecting optimum sensitivity and wavelength resolution. A built in stepper motor permitted motorised scanning of the spectral range and this was controlled by an externally connected drive unit (Bentham SMD3B). The motor drive unit provided scanning speeds from 1 to 400 steps/second, in increasing or decreasing wavelength steps, 1 step corresponding to 0.075 nm. Wavelength location was indicated by a

mechanical counter on the monochromator.

A Bentham 231 housing, with DH2 side window photomultiplier tube was fitted to the monochromator exit slit assembly for light output detection. The photomultiplier was powered by an external high voltage stabilised DC supply set to 1200 volts. To prevent the photomultiplier output giving a non-linear response to light intensity, the signal was fed into a pre-amplifier (Thorn-EMI Model A1) powered by an external low voltage stabilised supply. This provided four selectable conversion gains in decades, from 1 mV to 1 V per μA. The pre-amplified signal was then fed into a chart recorder (Graphtec Multicorder type MC6850, supplied by Environmental Equipments Ltd).

5.2.2 Evaluation

In order to use the OES system for experimental work, it was necessary to evaluate its performance in terms of (i) the maximum scanning speed it could be operated, without equipment response times influencing the results, (ii) the wavelength resolution as a function of entrance and exit slit widths, and (iii) the stability of the system in response to a steady light source input.

The limiting factor in the rate that a spectrum could be scanned, was the writing speed of the chart recorder. If a selected scan rate was too fast, then the more intense peaks in the spectral output would be attenuated in the chart recorder response, in relation to peaks of lower intensity. Clearly, this non-linear response would be undesirable. To ascertain the maximum permissible scan rate for linear response, the output from a He-Ne laser was set up to give (through the monochromator system) a nominal 90% deflection on the chart recorder. The 632.8 nm peak was alternately scanned at 1 step/sec and at successively faster speeds. The peak heights and

widths (full width half maximum) were then measured. This set of tests was repeated on three different occasions for statistical validity. Figure 5.1 shows the peak height as a function of scan speed, relative to the height at the lowest speed, of 1 step/sec. Also shown is the width of the peak in nm. Both curves begin to show some dependence on scan speed above 10 steps/sec. As these tests represent a "worst case" situation, they show that 10 steps/sec should provide a linear response under virtually all possible conditions and this speed was used for all the experimental work.

The wavelength resolution was also evaluated with repeated scans of the laser line at different monochromator slit widths. These results are shown in Figure 5.2 in terms of line width dependence on slit widths. Although these results do not provide resolution data in absolute terms, they at least give some indication as to how well-resolved adjacent peaks in spectral data are likely to be, for different slit widths.

System stability testing required a light source which would give a stable output intensity. This was achieved by using a low voltage incandescent light bulb powered by a stabilised supply. The bulb was subjected to a 1 hour burn-in period prior to the test and the bulb current was monitored (for a set voltage) to check stability. The bulb output was monitored at 600 nm with the monochromator system, and an intensity/time plot from the chart recorder was obtained over a four hour period from the system being switched on. It was found that after one hour (which would normally be allowed for equipment warming up), the drift in level was less than 3% over a 3 hour period. In any 10 minute period after the one hour warm up, the change in level varied between 0 and 0.8%.

Based on manufacturer's data, the approximate wavelength ranges of the relevant monochromator system components were:

Monochromator - 300 to 750 nm (peak response at about 500 nm)

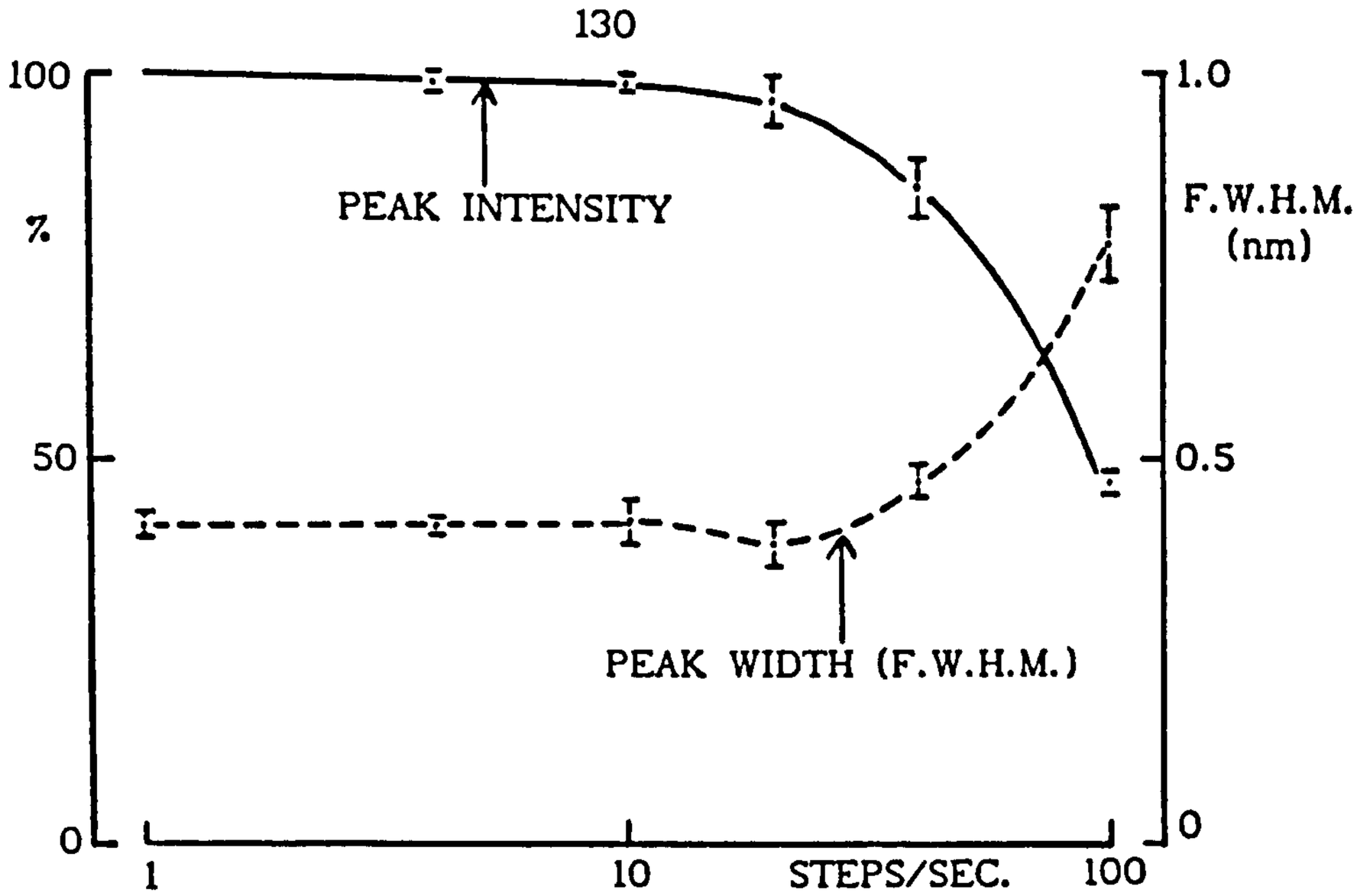

Figure 5.1 Scanning speed tests on the OES system, using the output from a He-Ne laser. Note that peak height and width show some dependence on scan speed above 10 steps/sec. Error bars are standard deviation values.

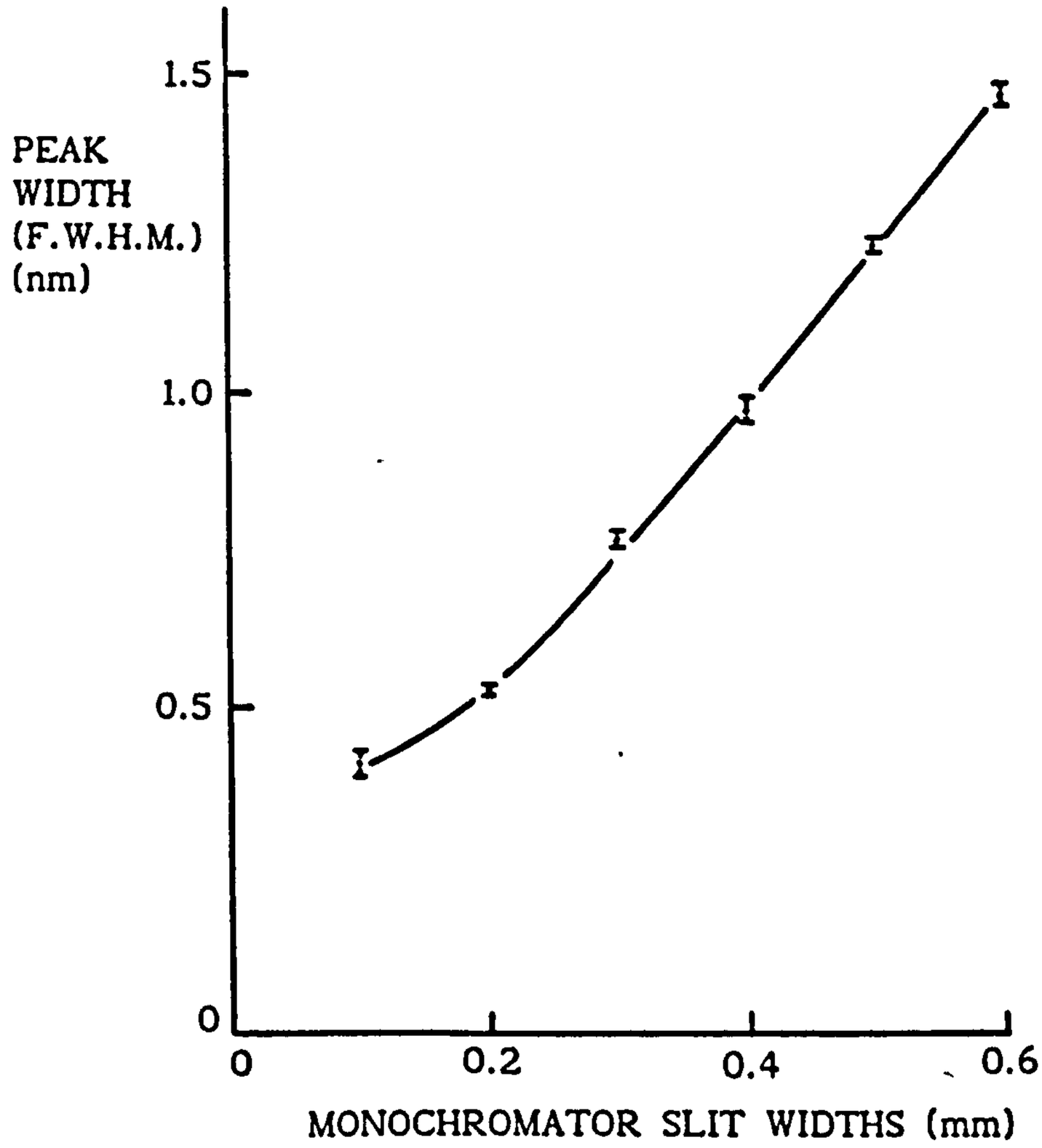

Figure 5.2 Line width dependence on monochromator slit widths (entrance and exit slit widths equal), scan speed = 1 step/sec, output from a He-Ne laser. Error bars are standard deviation values.

Photomultiplier - 200 to 800 nm (peak response at about 400 nm).

Fibre optic cable - 200 to 850 nm.

Therefore, the useful range of the system was from about 300 to 800 nm. As most of the useful spectral information is also to be found within this region, it was decided that spectral scans should be performed over this range. With a maximum scanning rate of 10 steps/sec, it would take approximately 11 minutes to perform a 300 to 800 nm scan and the stability would be better than 0.8%.

5.3 EXPERIMENTAL

Rig (1) was used for this work, so that (i) a wide range of bias levels could be employed, without the problems associated with power supply fluctuations incurred with rig (2), (ii) the Baratron capacitance-manometer installed gave pressure readings which were independent of the nature of the gas (unlike the ion gauge in rig (2)), thus readings from different gas mixtures would be more accurate, and (iii) the large viewport facilitated observation of the discharge during the experiments. Figure 5.3 shows the OES equipment connected to the rig. The fibre optic cable was fed through one of the standard 25 mm chamber feedthrough ports by means of a reducer screwed into the former. Due to the construction of the flexible steel covering on the fibre cable, it was not possible to make a vacuum tight seal between the cable and the reducer. The problem was resolved by sealing the monochromator end of the cable by means of an "O" ring within an aluminium adaptor. A flexible polythene tube, around the cable, provided the vacuum tight connection between the reducer and adaptor.

Figure 5.4 shows the arrangement inside the deposition chamber, as seen from the opposite side to the main viewport. The fibre optic cable was supported by a bush fitted to the end of a rod; the rod being part of a

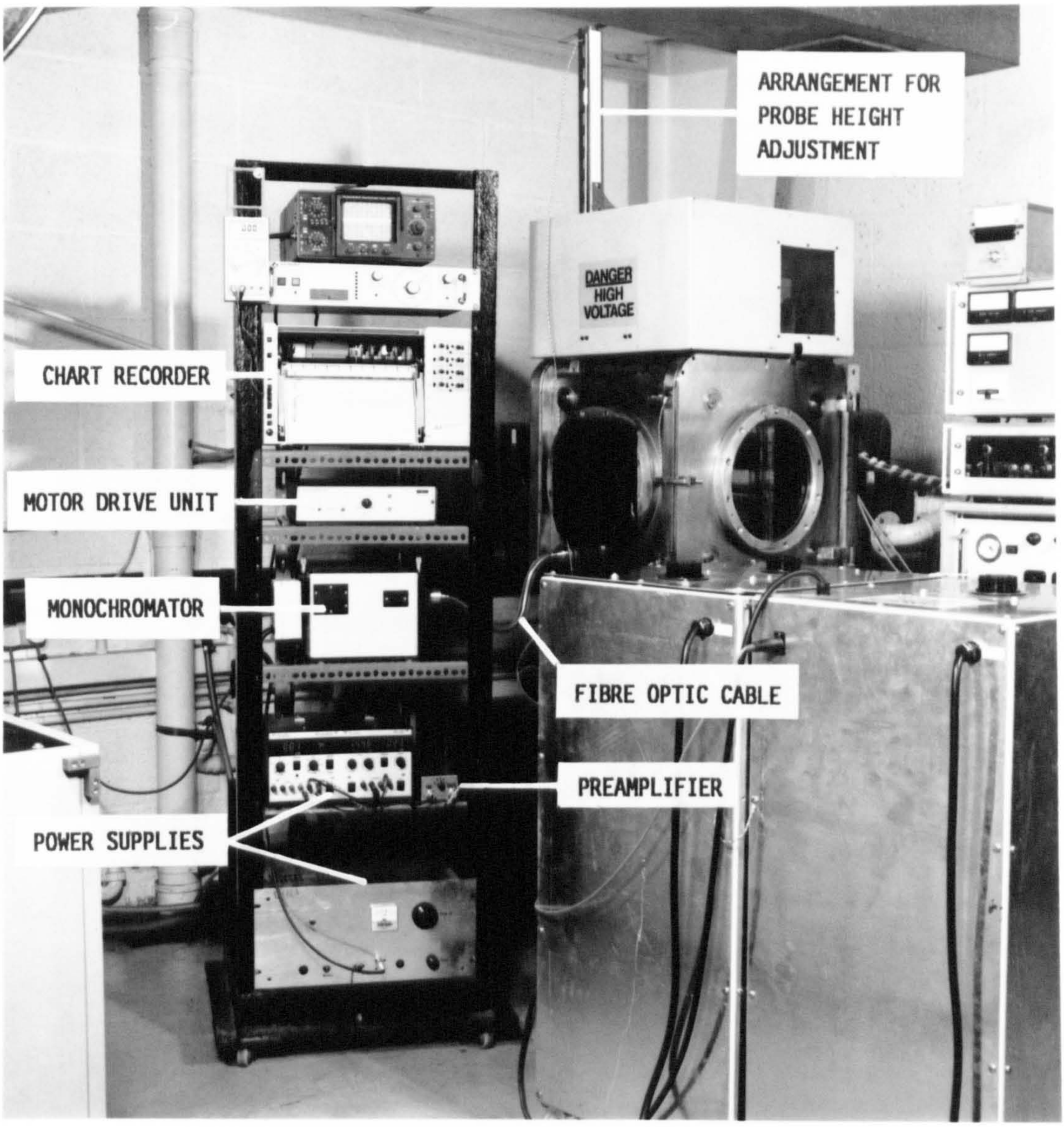

Figure 5.3 Optical emission spectroscopy equipment connected to rig (1).

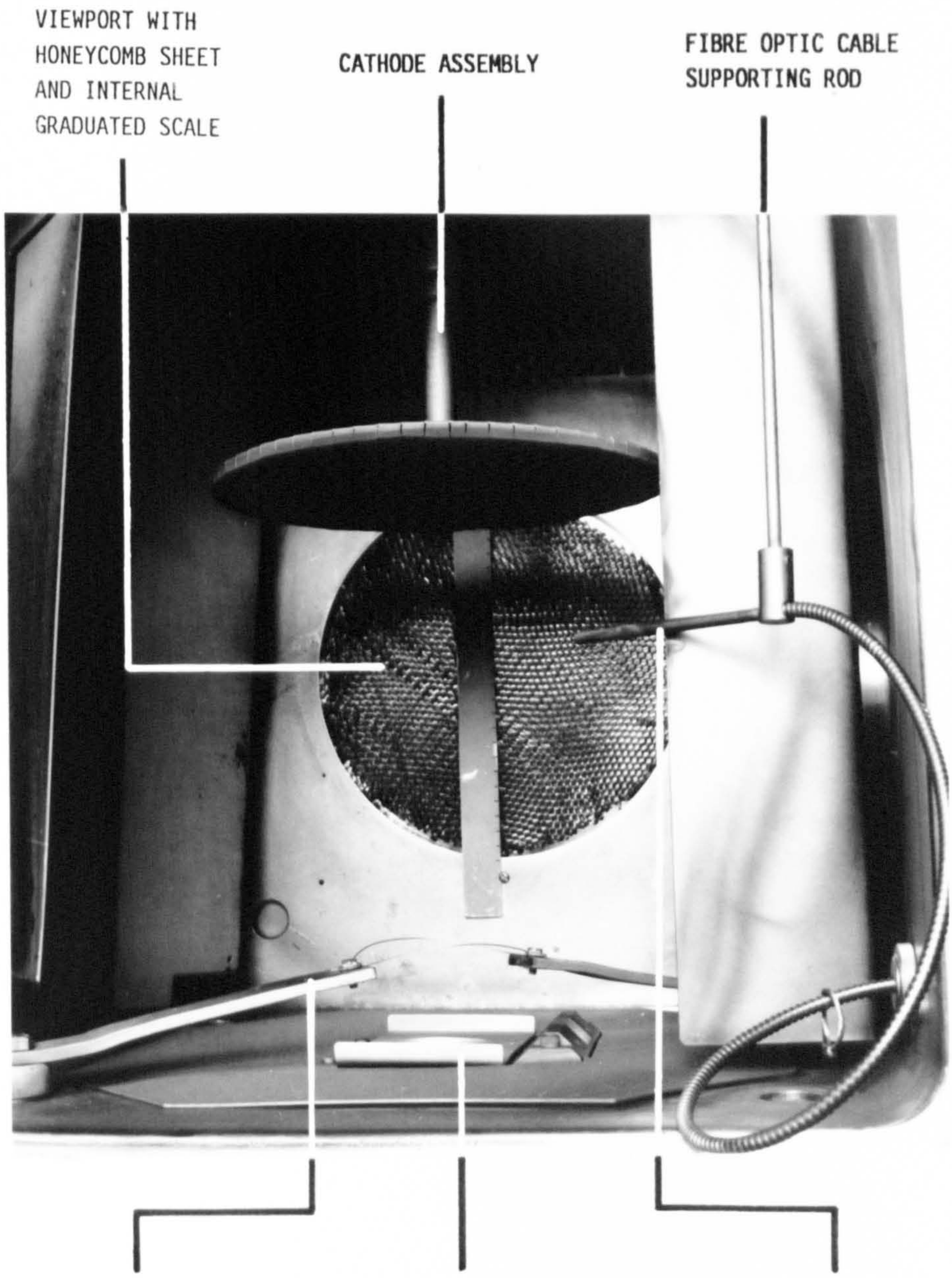

Figure 5.4 Arrangement inside the deposition chamber of rig (1) for OES and cathode sheath thickness studies.

push-pull feedthrough fitted in the top of the chamber. A stainless steel collimator tube, 12 cms long with an internal diameter of 0.55 cms was fitted to the cable end. This improved the definition of spatial resolution and prevented contamination of the cable end occurring from exposure to sputtered and evaporated species. The cathode was identical to that used for sheath thickness measurements in Chapter 3, being a 24.6 cm diameter mild steel disc, shielded so that only the lower face was subjected to bombardment from the discharge and evaporated species. The chamber shielding plate, adjacent to the fibre optic probe assembly, was modified so that the edge of the shielding performed as a guide for the collimator tube. The probe arrangement therefore permitted free movement in the vertical direction but allowed a fixed lateral position to be maintained; ie, the probe always pointed towards the central axis of the cathode. The probe was earthed with the supporting rod outside the chamber and a graduated scale, fitted above the chamber enclosure (as shown in Figure 5.3), facilitated accurate adjustment of the probe-cathode distance.

Figure 5.4 shows the filament assembly near the base of the chamber, used for thermionic triode discharges. Tungsten wire, 0.5 mm diameter, was used and this was positioned in the form of a horizontal loop with a diameter of 9.5 cms, at a height of 5 cms above the chamber base (cathode to base distance was 30 cms). Also shown is the viewport with the graduated steel strip for measuring sheath thickness, as used for the work reported in Section 3.3.2. For this work, however, a 2 cm thick metal sheet with a honeycomb structure was fitted into the viewport recess. This material, performing as a stack of collimator tubes, prevented the viewport window being coated; thus allowing discharge phenomena such as the sheath thickness to be observed during evaporation of the source material.

Table 5.1 gives details of the discharges studied. As described in

DISCHARGE TYPE	NUMBER OF RUNS	DISCHARGE PARAMETERS - RANGES USED					
		PRESSURE (mTorr)			CATHODE BIAS (Volts)	CATHODE CURRENT DENS. (mA cm^{-2})	FILAMENT BIAS (Volts)
		ARGON	NITROGEN	TOTAL			
ARGON DIODE	25	30 - 90	0	30 - 90	1k - 2k	0.04 - 0.31	0
ARGON TRIODE	16	4.5 - 15	0	4.5-15	100-500	0.10 - 0.55	20 - 150
NITROGEN DIODE	21	0	30 - 90	30 - 90	1k - 2k	0.05 - 0.24	0
NITROGEN TRIODE	18	0	1 - 40	1 - 40	200 -2k	0.08 - 0.30	35 - 150
ARGON/NITROGEN DIODE	13	21 - 48	2 - 29	50	2k	0.10 - 0.13	0
ARGON/NITROGEN TRIODE	6	5 - 9	1 - 5	10	200 -2k	0.16 - 0.18	100
TITANIUM/ARGON TRIODE	4	5	0	5	2k	0.33	100
TITANIUM/ARGON/NITROGEN TRIODE	2	4.5	0.5	5	2k	0.33	100

TABLE 5.1 DISCHARGES STUDIED IN THE OES EXPERIMENTS. ALL TRIODE DISCHARGES WERE THERMIONIC.

Section 3.3.2.2, a series of argon discharge-pump down cycles were performed prior to every period when experimental runs were to be made, to minimise the influence of contamination effects. Discharges containing mixtures of argon and nitrogen were set up as follows:

(i) Admit nitrogen into the chamber at the required partial pressure.

(ii) Monitor nitrogen pressure for 5 minutes (without further adjustment to flow rate) to ensure that there is no significant drift, taking pressure readings every minute.

(iii) Admit argon into the chamber to the required total pressure.

(iv) Perform run. Adjust argon flow rate, to compensate for any drift in total pressure, if necessary.

(v) After run, switch off argon flow and monitor nitrogen pressure for five minutes, taking pressure readings every minute.

(vi) If the nitrogen pressure monitored in (v) does not compare with (ii), discard the run and repeat the procedure from (i).

Prior to experimental work where the source material (titanium) was to be evaporated, all surfaces within the chamber were coated with titanium. Hence the characteristics of the cathode and other surfaces (in terms of, for example, secondary electron emission and sputtered species) would not be expected to change during these runs. EB gun power was maintained at a constant level during titanium evaporation (6 kV, 200 mA beam current) and gas flow (argon only or argon with nitrogen) was not adjusted, but pressure was monitored immediately before and after evaporation, to check for any drift. The source material was weighed before and after each run to enable the average evaporation rate to be estimated.

Each run in column 2 in Table 5.1 refers to one or more spectral scans (300-800 nm) performed at a particular cathode to probe distance for a given set of discharge conditions. Although only one scan per run might be

considered to be sufficient, the discharges containing nitrogen or titanium (by evaporation) gave spectral peak intensities which varied considerably. This necessitated performing repeat scans at different sensitivity settings on the monochromator system. The entrance and exit slit widths were set at 0.2 mm throughout the experimental work and sensitivity was altered either by changing the pre-amplifier gain (in decades) or the chart recorder range. An oscilloscope connected in parallel with the pre-amplifier output enabled the signal to be checked for possible overloading.

In general, the discharges were monitored at three cathode to probe distances. These were (i) in the middle of the sheath region, (ii) at the edge of the negative glow, and (iii) 10 cms from the cathode. Although (iii) depended on the sheath thickness for its relative position in the negative glow, the results could be regarded as being representative of the body of the negative glow region. Some discharges however, were monitored at additional positions, depending on requirements. Further details of the discharges studied are given, where appropriate, in the following sections.

5.4 ANALYSIS

To avoid confusion, the results are presented and interpreted in terms of specifically addressed subject areas, rather than attempting to show results in relation to different types of discharge. Thus any relevant background information is also included in the following sections.

5.4.1 Electron Temperature in Discharges Containing Argon

5.4.1.1 Background

As outlined in Chapter 3, the electron temperature is a fundamental plasma parameter. For discharges where the electron density and temperature is sufficiently low, "Corona equilibrium" is assumed to exist. Here,

excitation is said to occur by electron impact only (ie, no photo-excitation) and de-excitation takes place through spontaneous decay (refs 78, 81). An equation applicable to Corona equilibrium conditions, for estimating electron temperature from OES data, has been given by Hope et al (ref 78):

$$I^+/I^\circ = C\, T_e^{0.75} \exp\left[-(E_g + E_1 - E_p)/T_e\right] \qquad (5.1)$$

where I^+ = spectral line intensity from a singly charged ion, I° = spectral line intensity from an atom, C = a constant, T_e = electron temperature (in units of energy), E_g = ionisation potential of the atom, E_1 and E_p = ion and atom excitation energies from ground state, respectively. Although C is unknown, it was evaluated in ref 78 by comparison with results for T_e from Langmuir probe measurements in the same discharge. The discharge studied was argon, generated in an RF system with two parallel electrodes. As the electron densities and temperatures were found to be in the order of 10^{10} cm^{-3} and 1 to 10 eV, the authors assumed Corona equilibrium conditions were applicable. These values are also comparable to DC discharge conditions, typical charge carrier density values being 10^9 to 10^{11} cm^{-3} (refs 23, 42, 64) and effective electron temperatures of a few eV (see Section 3.2.2.1). Therefore, Equation 5.1 could be used to evaluate T_e from the discharges in this work.

In ref 78, C was found to be 0.62 $eV^{-0.75}$, using the Ar^+ peak at 480.6 nm and Ar° peak at 750.3 nm. Knowing that $(E_g + E_1)$ = 34.90 eV and E_p = 13.42 eV for these transitions allows T_e to be calculated from Equation 5.1 (by iteration) for this work using the same argon peaks. A second equation, given by Felts and Lopata (ref 79) may have also been used to evaluate T_e. However, it is comparable in form to Equation 5.1 and as the authors had not

evaluated the constants for use in argon discharges, the equation was not investigated here.

5.4.1.2 Results and comments

Figure 5.5 shows calculated T_e results as a function of argon pressure for diode discharges. There is only a slight increase in T_e with increasing pressure, and the difference between results taken at the negative glow edge and in the body of the glow (10 cms from the cathode) is negligible. The values of T_e in absolute terms appear to be higher than expected. As discussed in Section 3.2.2.1, the "effective" electron temperature in these discharges is quoted as being about 2 eV. The results are certainly higher than the published DC diode values obtained from Langmuir probe data (0.3 to 0.5 eV, refs 42, 61, 64) although the latter are generally considered to be the temperature of the ultimate electron group. However, as the constant C in Equation 5.1 was also evaluated from Langmuir probe measurements in ref 78, then values lower than ~ 2 eV might be expected in Figure 5.5. There are, however, a number of possible reasons for the discrepancy, due to the different experimental conditions used between this work and those of ref 78. For example, in ref 78 RF discharges were investigated, which may have had significantly different electron energy distribution characteristics. Also, differences in electrode and discharge chamber geometries, whether the chamber was electrically conductive, the sampling volume of the discharge and spectral response of the monochromator system may have had some effect.

Figure 5.6 shows the axial dependence of T_e for argon diode and thermionic triode discharges. Although the diode T_e results are virtually independent of distance, the triode data shows a slight fall off in temperature with increasing distance from the thermionic emitter. This effect and the overall rise in T_e under triode conditions is probably due to

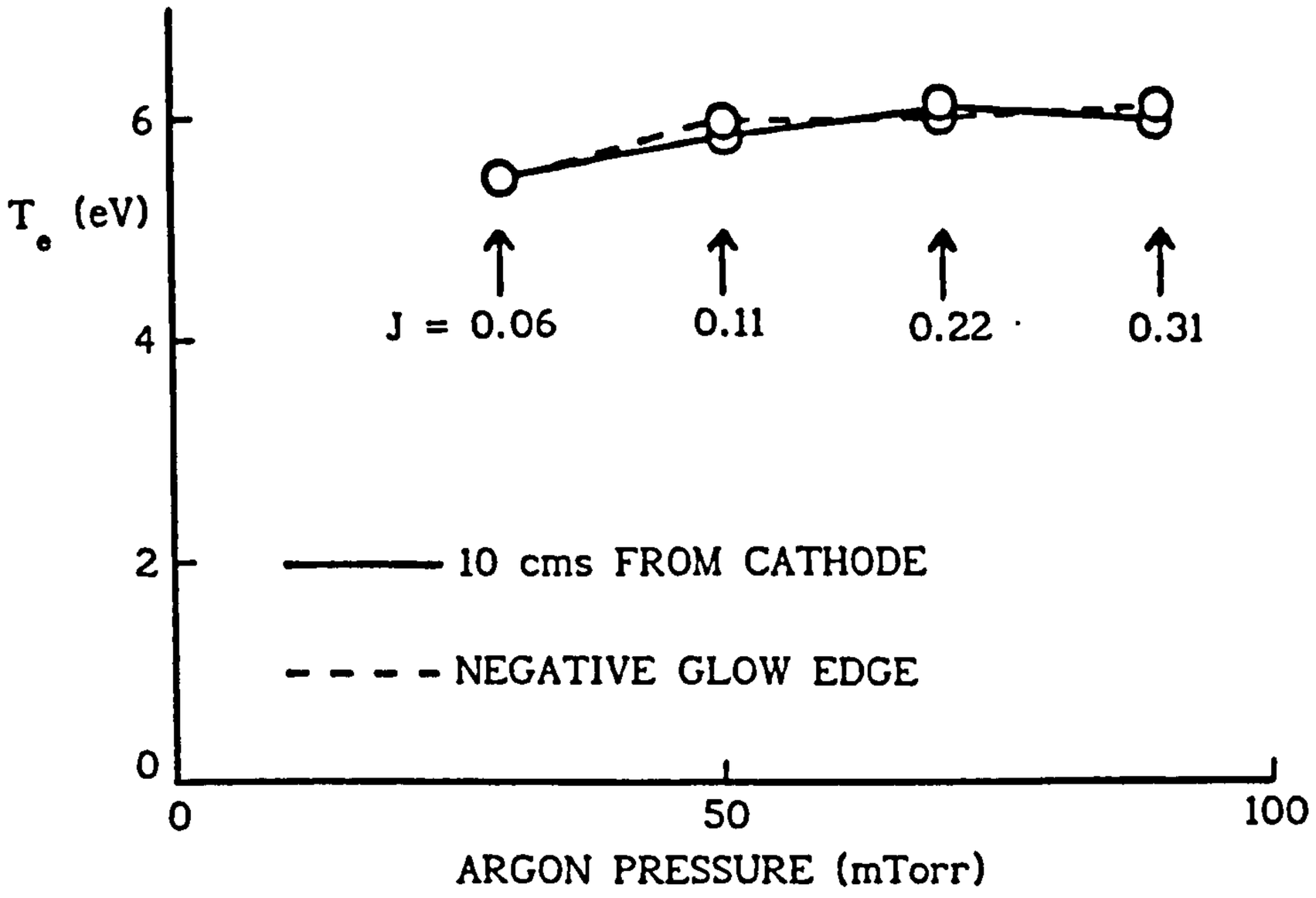

Figure 5.5 Calculated T_e values from Equation 5.1 for argon diode discharges at 2 kV. J = cathode current density (mA cm^{-2}).

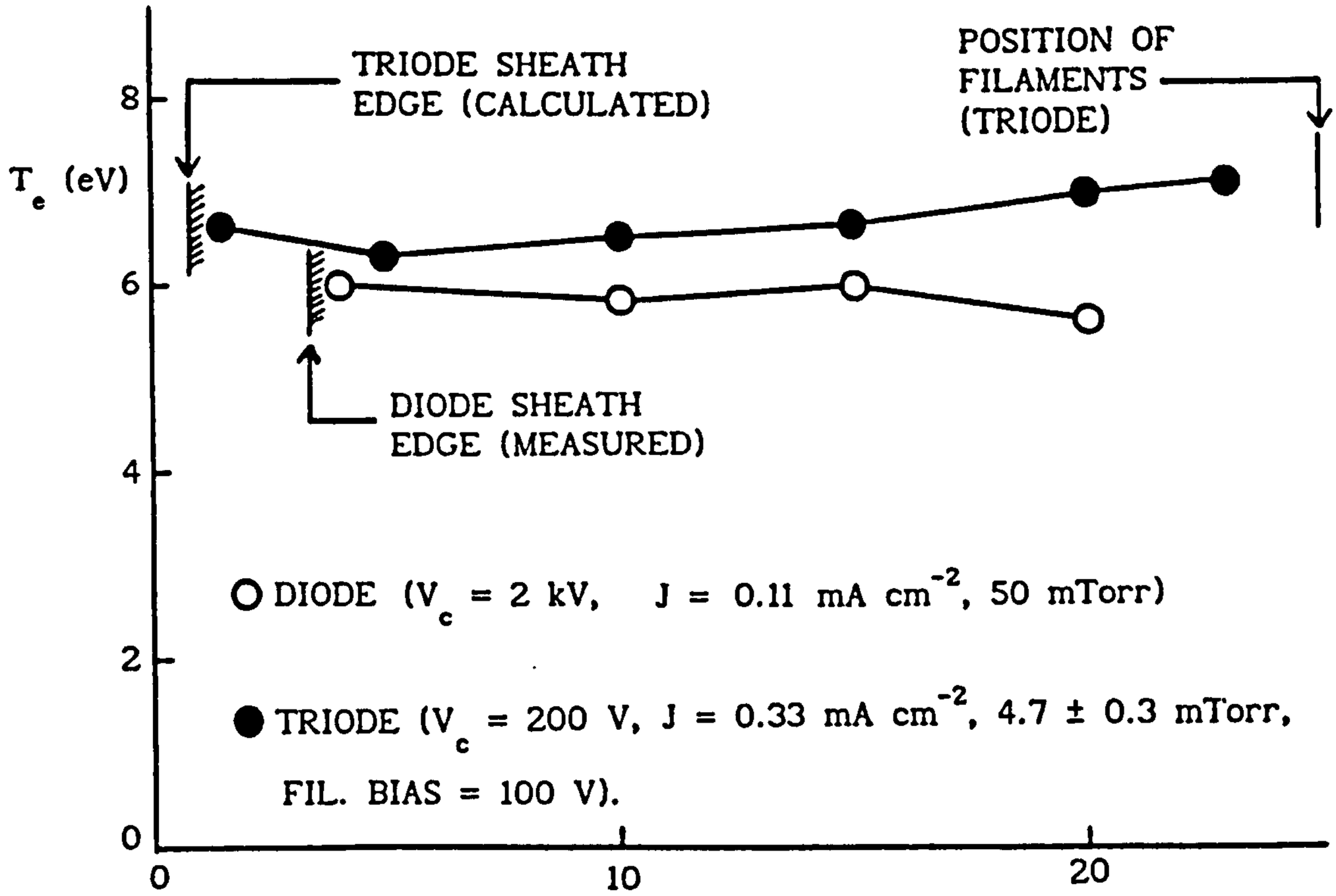

Figure 5.6 Calculated T_e values from Equation 5.1 for argon diode and thermionic triode discharges.

the influence of the relatively high energy electrons emitted by the filaments, altering the electron energy distribution.

Figure 5.7 shows that T_e in the body of the negative glow decreases slightly as the partial pressure of nitrogen in an argon-nitrogen diode

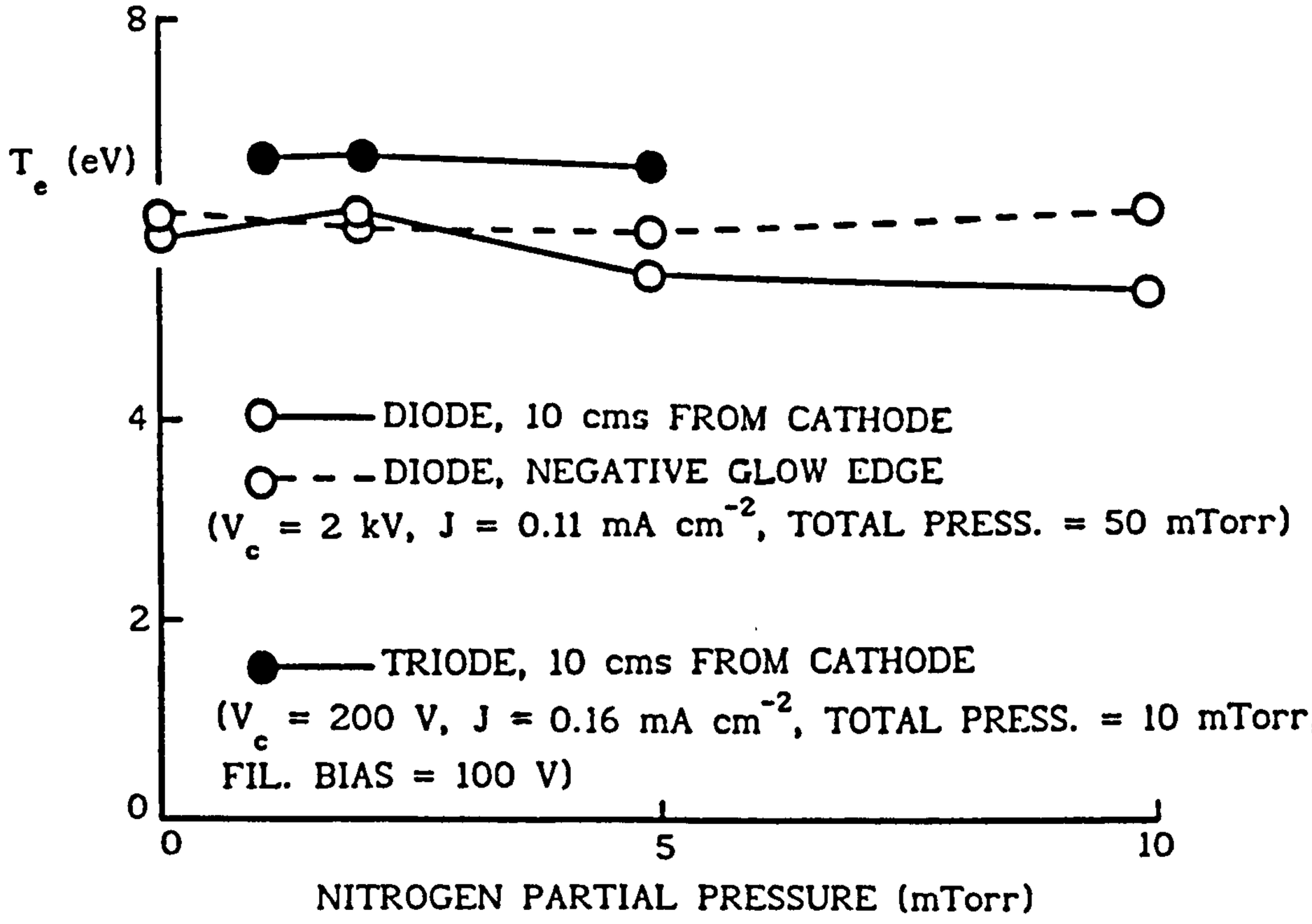

Figure 5.7 Calculated T_e values from Equation 5.1 for argon-nitrogen mixtures under diode and thermionic triode conditions.

increases. Lemperiere et al (ref 24) also found a decrease in T_e for the ultimate electron group, from Langmuir probe studies, when the proportion of nitrogen was increased in an Ar-N_2 diode discharge. They attributed the reduction to electron energy losses resulting from excitation of rotation and vibration levels in the nitrogen molecule (which can be compared with the comments on Table 3.9 in Section 3.5.2.2). It is interesting to note, however, that T_e appears to be virtually independent of nitrogen partial

pressure in Figure 5.7 at the negative glow edge of the diode discharges. This also seems to be true for the body of the negative glow under triode conditions. Although this is not so readily explainable, Bell et al (ref 82) found that T_e actually increased with nitrogen partial pressure in a DC magnetron Ar–N_2 discharge under certain pressure conditions and they suggested this was due to a reduction in the total electron collision cross section (though the reason is not clear). Thus the results in Figure 5.7 may be influenced by both effects.

Probably the most interesting observation in T_e evaluations from the OES results were those obtained during titanium evaporation. Table 5.2 summarises the results.

RUN	PRESSURE (mTorr)		MEAN EVAP. RATE (g/min)	T_e (eV)
	ARGON	NITROGEN		
E100	4.7 ± 0.3	0	0	6.50
E101	4.7 ± 0.3	0	0.107	12.07
E102	4.8 ± 0.2	0	0	6.73
E103	4.8 ± 0.2	0	0.068	11.25
E104	4.5	0.5	0	6.80
E105	4.5	0.4 ± 0.1	0.068	10.78

Table 5.2 Electron temperatures calculated from Equation 5.1, with and without Ti evaporation through Ar and Ar–N_2 thermionic triode discharges. Probe position = 10 cms from cathode; cathode bias and current density = 2 kV, 0.333 mA cm^{-2}, filament bias = 100 V. Errors quoted in the pressure data represent the maximum uncertainty due to drift.

It is clear that T_e almost doubled in value during evaporation. The cathode voltage and current density were maintained at a constant value for all the runs in Table 5.2 by adjusting the filament emission. These moderate changes in filament emission would not be expected to change T_e significantly. Prior to Run E100, titanium evaporation had been carried out in the chamber so that the only material sputtered into the discharge would be titanium, (as reported in Section 5.3). These precautions meant that either the EB gun or the presence of metal vapour in the discharges were the cause of the increase in T_e. Hurley (ref 83) also found that by using a shielded Langmuir probe, T_e almost doubled during titanium evaporation in an RF argon discharge. A possible explanation offered in ref 83 to account for this is that the energy exchange between evaporating surface atoms of the melt raises the gas temperature and therefore reduces its number density. This in turn means that energetic electrons make a smaller number of collisions with the gas atoms and instead tend to lose more energy in wall collisions. This causes an increase in electron temperature (presumably to compensate for the increased charge loss to the walls). There may however, be other reasons for the increase in T_e during evaporation. For example, as discussed in Chapter 3, Penning ionisation mechanisms are known to be significant. During evaporation, the argon metastable ionising collisions with titanium vapour will produce electrons which carry most of the surplus energy (ref 67). As the metastable energy is 11.56 eV and the titanium ionisation potential is 6.83 eV, the resulting electron energy, of about 4.7 eV, could distort the electron energy distribution, effectively increasing T_e. Another possibility is that if a large proportion of the charge is carried by the vapour (due to Penning ionisation, for example), there may be an increased charge loss to the walls arising from the more directional

motion of the vapour in contrast to the random motion of the gas, as mentioned in Section 3.5.2.1; thus T_e may increase to compensate for this loss.

Although electron temperature determination using Equation 5.1 gives uncertain results in absolute terms, the general changes in T_e with different discharge conditions appear to concur with published observations from Langmuir probe data.

5.4.2 Argon Line Intensities with Distance From the Cathode

5.4.2.1 Background

The spatial dependence of sputter weight loss data in Chapter 4 was primarily attributed to the availability of high energy electrons, either from the jig assembly (diode conditions) or the filaments (thermionic triode conditions). As these electrons would also lead to photon emission arising from de-excitation, the spatial variation in line intensities have been investigated for comparison with the sputter weight loss results.

5.4.2.2 Results and comments

Figure 5.8 is a semi-logarithmic plot of argon neutral and ion line intensities as a function of distance from the cathode, within the negative glow region. The following observations can be made:

(i) For equivalent emission lines, the triode intensities are significantly higher than those from the diode. This can be attributed to the greater electron density in the former, which increases the probability of excitation (and subsequent de-excitation). Also, the collision cross section for excitation generally decreases with increasing electron energy (ref 73) so that the high energy electrons in the diode (nominally 2 keV) will have

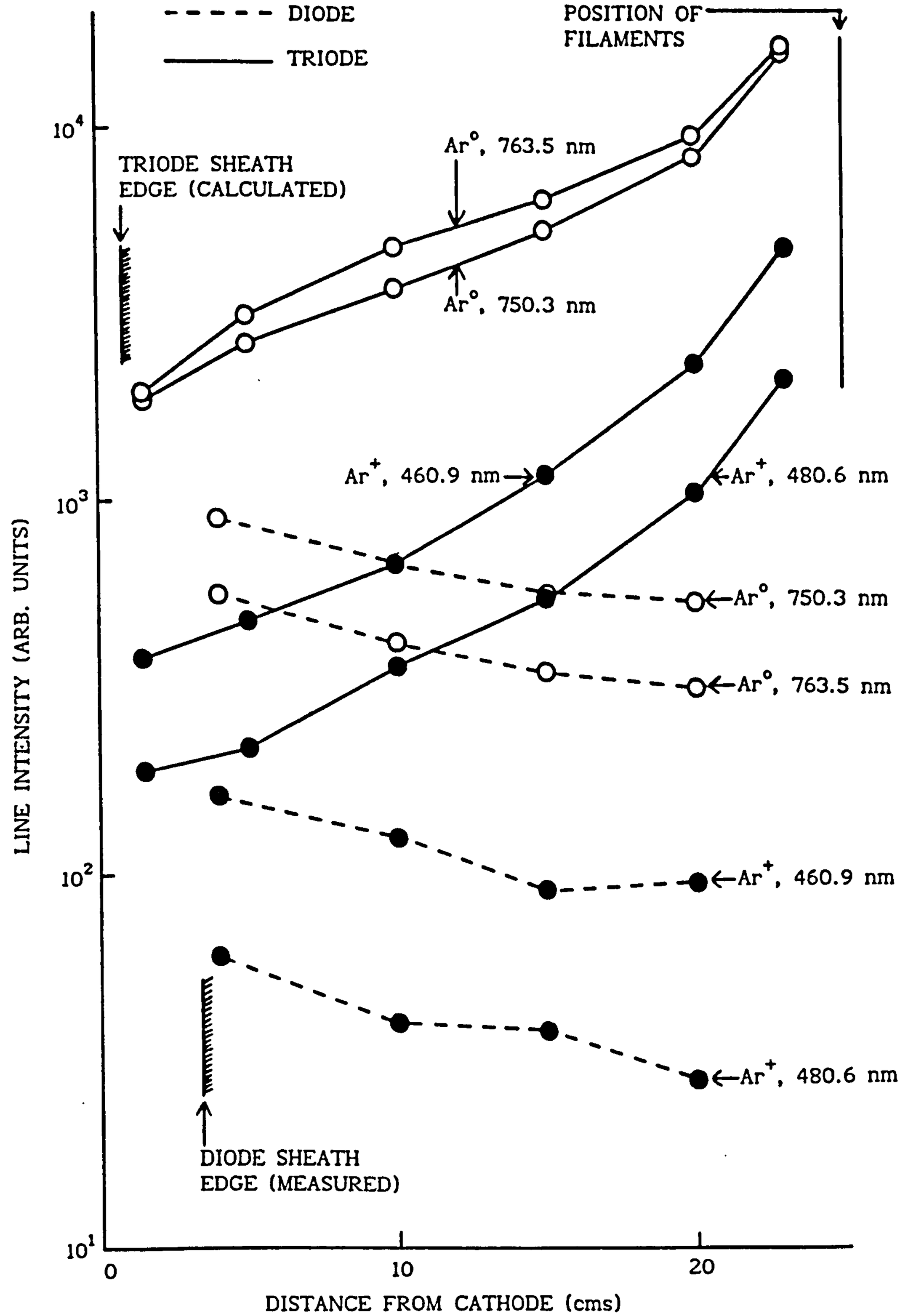

Figure 5.8 Plots of spectral line intensities as a function of distance from the cathode for argon diode and thermionic triode discharges. See Table 5.3 for the discharge conditions used.

less probability of causing excitation than the (nominally 100 eV) electrons emitted by the filaments in the triode.

(ii) The intensities fall off with distance from the primary electron emitter. For the diode, this is secondary electron emission from the cathode surface. Under triode conditions, however, it is clear that thermionic emission from the filaments has the most influential effect.

In general, the curves in Figure 5.8 may be considered to be almost linear, ie, the intensities approximate to an exponential fall off with distance from the primary electron emitter. Table 5.3 summarises the linear regression parameters for exponential fits to the data. Also shown are the effective collision cross sections, calculated from the mean free path h, and pressure data.

Although the linear regressions are only approximate, it is interesting to compare the σ_h values with published collision cross section data. For the argon neutral lines, the probability of excitation and subsequent de-excitation will depend on (i) availability of neutral atoms, (ii) availability of electrons and (iii) the electron impact excitation cross section. If the number density of neutrals is assumed to be constant throughout the chamber and if progressive rarification of electron flux density due to, for example, ring source effects (as discussed in Section 4.4.2.1) can be regarded as insignificant, then the availability of electrons from the primary emitting source will mainly depend on the elastic scattering cross section. Therefore, the rate of line intensity fall-off with distance can be attributed to the collision cross section values for electron elastic scattering and impact excitation, at least to a first order approximation. As there are no energy losses associated with the former process and the losses are relatively small for the latter, cross sections

DISCHARGE TYPE	ARGON LINE (nm)	CORR. COEFF.	I_o	h (cms)	σ_h (cms^2)
DIODE	750.3 Ar^o	0.9616	979.5	30.05	2.07×10^{-17}
V_c = 2 kV	763.5 Ar^o	0.9833	634.2	26.61	2.34×10^{-17}
J = 0.11 mA cm^{-2}	480.6 Ar^+	0.9712	68.87	22.52	2.76×10^{-17}
50 mTorr	460.9 Ar^+	0.9214	181.9	27.03	2.30×10^{-17}
TRIODE	750.3 Ar^o	-0.9850	1572	11.13	5.94×10^{-16}
V_c = 200 V	763.5 Ar^o	-0.9900	1833	11.35	5.83×10^{-16}
V_{fil} = 100 V	480.6 Ar^+	-0.9789	134.0	9.28	7.12×10^{-16}
J = 0.33 mA cm^{-2}	460.9 Ar^+	-0.9786	267.1	8.89	7.43×10^{-16}
4.7 ± 0.3 mTorr					

Table 5.3 Summary of the curve fitting parameters to the equation $I = I_o \exp(-x/h)$ from data in Figure 5.8, where x = distance from the cathode, σ_h = effective collision cross section calculated from h and argon pressure (assuming gas temperature = 300 K).

for the initial electron energies (2 keV for the diode and 100 eV for the triode) would be the most appropriate to consider. From the available published data, the excitation cross sections for argon lines at 750.3 nm and 763.5 nm have maximum values of 6.6×10^{-18} cm^2 and 1.8×10^{-17} cm^2 respectively, at about 20 eV electron energy (ref 16). At the higher electron energies considered here, they will be significantly less than these values. In contrast, the elastic scattering cross section is comparatively large, being about 6×10^{-16} cm^2 at 100 eV and 8×10^{-17} cm^2 at 2 keV (ref 16). Therefore, the σ_h results in Table 5.3 might be expected

to agree with the scattering cross section values. Under triode conditions, the σ_h results show excellent agreement with the 100 eV value, which suggests that elastic scattering of high energy electrons is the primary mechanism responsible for line intensity fall off with emitter distance. The agreement is not quite as favourable for the diode results. This is probably due to the greater influence of other electrons in the discharge such as those emitted from the chamber walls and the more energetic electrons from the secondary and ultimate groups. The background radiation from these contributions might be expected to increase h and thus decrease σ_h.

The ion lines also follow a similar trend to the neutrals, though the situation is more difficult to analyse as the ionisation process has also to be accounted for. The collision cross section for electron impact ionisation is about 5×10^{-17} cm^2 at 2 keV and 3×10^{-16} cm^2 at 100 eV (ref 16); these values being comparable to those for electron scattering. Thus σ_h for the ion lines in Table 5.3 should be larger than the values for the corresponding neutral lines, as ionisation and scattering events, arising from collisions by electrons from the primary emitter, will both contribute to the fall off in intensity. To some extent, this hypothesis is verified in Table 5.3 because the triode ion line data for σ_h is larger than for the corresponding neutrals. This difference is not apparent in the diode data, though in addition to the influence of electrons from other sources, the low intensities and subsequently worse signal to noise ratios may have influenced the shapes of these curves.

As a final comment, Petitjean et al (ref 25) also found a quasi-exponential relationship for the N_2^+ (391.4 nm) line with distance from the cathode in a nitrogen diode discharge. Although no explanation for the relationship is offered in ref 25, the result is at least supportive of the

observations from this work.

5.4.3 Dissociative Charge Transfer in Nitrogenous Discharges

5.4.3.1 Background

Observations discussed in Chapter 3 suggested that dissociative charge transfer mechanisms in the cathode fall region of nitrogen discharges may have a significant influence on the nature of the species arriving at the cathode. As previously reported, the following process is thought to occur:

$$N_2^+ \text{ (FAST)} + N_2 \longrightarrow N_2^{+*} \text{ (SLOW)} + N_2$$

$$N_2^{+*} \longrightarrow N^+ + N$$

Thus although N_2^+ is known to be predominant in the negative glow, the proportion of N^+ could increase due to this collision process occurring within the sheath. Comparison of measured sheath thickness data with predictions from the Child-Langmuir equation suggested that N^+ ions, rather than N_2^+ ions were the dominant charged species arriving at the cathode under diode conditions. Although no sheath thickness data was obtained for nitrogen thermionic triode discharges, it may be inferred that N_2^+ could be predominant under triode conditions, as the number of collisions within the sheath reduces with increased ionisation enhancement at lower discharge pressures.

To investigate this phenomenon further, the spectral line intensity ratios of nitrogen atomic and molecular emissions from nitrogenous discharges were studied. Table 5.4 gives the details.

The 746.8 nm and 337.1 nm peaks were found to be the most suitable for study in terms of signal to noise ratio. Unfortunately, these peaks could not be used for discharges containing argon as they became obscured by argon emission lines. Thus peaks at 493.5 nm and 380.4 nm had to be used for this purpose. The original intention was to study emissions from ion peaks but

N^+ emissions were found to be too low for reliable determination.

SPECIES	WAVELENGTH (nm)	EXCITATION THRESHOLD (eV)	TYPE OF DISCHARGE INVESTIGATED
N°	746.8	12.0	PURE NITROGEN
N_2°	337.1	11.1	PURE NITROGEN
N°	493.5	13.2	NITROGEN + ARGON
N_2°	380.4	11.1	NITROGEN + ARGON

Table 5.4 Details of the nitrogen peaks studied, data from refs 25 and 84.

Coburn and Chen (ref 80) have described a method of determining the relative quantity of a plasma species by comparing its spectral line intensity with that of a species of known quantity. The principle is as follows: For species x and y,

$$I_x \propto n_x \eta_x \quad \text{and} \quad I_y \propto n_y \eta_y$$

where I, n and η is the line intensity, ground state density and the excitation efficiency respectively, for each species. If the excitation threshold of the radiative level for each species is similar, then the excitation efficiency ratio can be assumed to be constant. Thus,

$$n_x/n_y = K\, I_x/I_y \qquad (5.2)$$

where K is a constant independent of discharge parameters. This technique has been used to study nitrogen in nitrogen-hydrogen discharges (ref 25) and fluorine in plasma etching discharges (ref 80). As the excitation thresholds of the N° and N_2° lines selected in this work are similar, the

method could be used to estimate the actual change in proportion of atomic nitrogen to molecular nitrogen under different conditions.

5.4.3.2 Results and comments

Figure 5.9 shows the N°/N_2° intensity ratios as a function of pressure in pure nitrogen diode discharges. The ratio is considerably greater in the sheath region than in the negative glow and this supports the hypothesis proposed in Chapter 3. The ratio in the sheath does not change significantly with pressure, as under diode conditions, the sheath thickness and mean free path for dissociative charge transfer are both (approximately) inversely proportional to pressure. Thus the average number of collisions within the sheath remains roughly constant. There is a slight increase in the intensity ratio at the edge and in the body of the negative glow as pressure is reduced. This is probably due to some of the nitrogen atomic species formed in the sheath diffusing back into the glow region; clearly as the gas number density reduces, the effect must become more prominent. At 50 mTorr, the intensity ratio is about 40 times higher in the middle of the sheath compared with the negative glow edge. If Equation 5.2 is assumed to be applicable, this means that the proportion of nitrogen atoms has increased by 40 fold.

Figure 5.10 shows how the intensity ratio changes with distance from the cathode in a nitrogen diode discharge. The horizontal error bars represent the spatial resolution limits of the fibre optic probe. The results clearly show an increase in the proportion of nitrogen atoms in the sheath nearer to the cathode, due to the rising probability of a molecule undergoing a dissociative charge transfer collision with distance travelled. It is interesting to note that in the middle of the sheath, the intensity ratio is only about 14 times higher than at the glow edge, which is

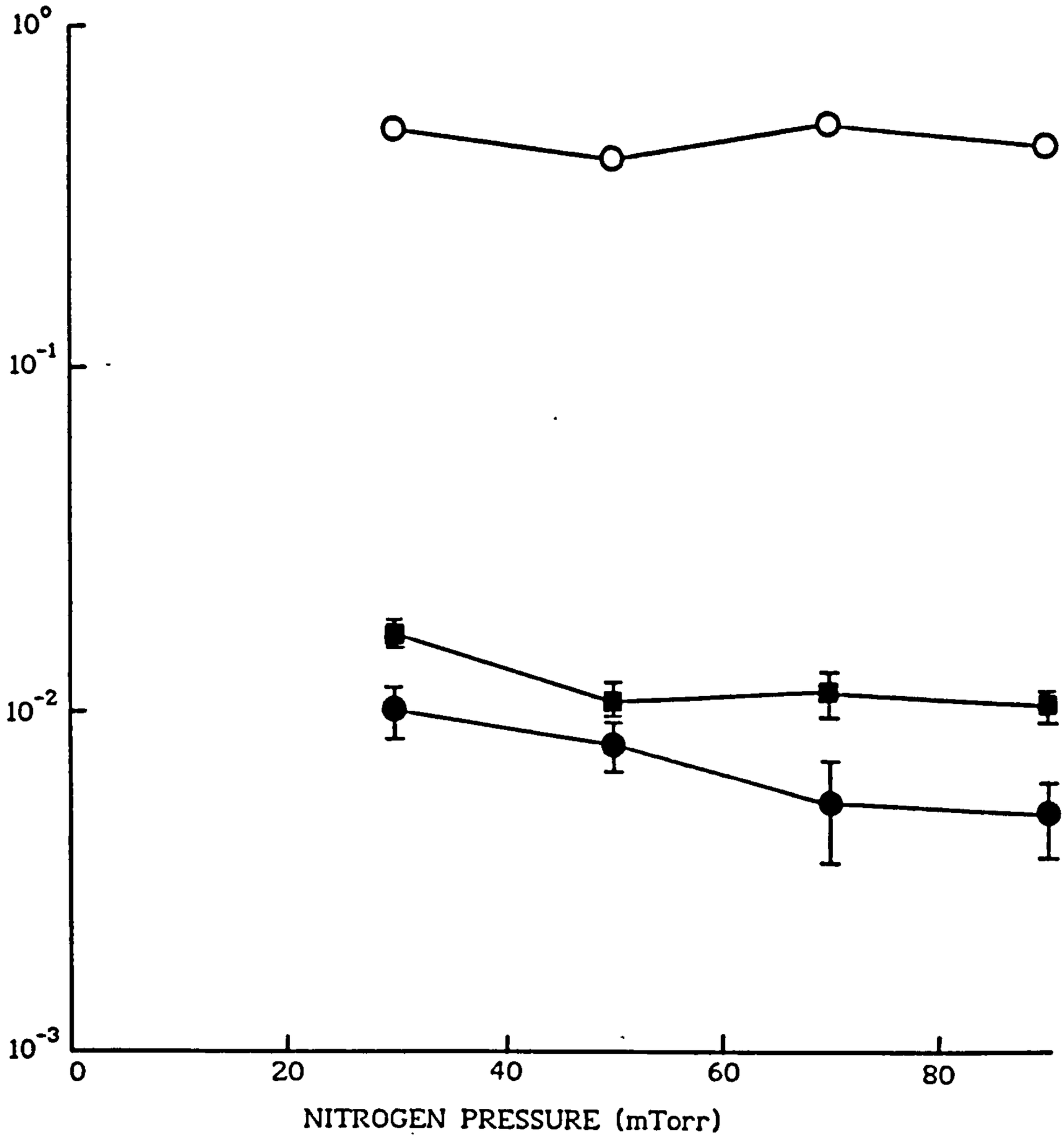

Figure 5.9 N°/N_2° intensity ratios as a function of pressure in pure nitrogen diode discharges, V_c = 2 kV, J = 0.07 to 0.24 mA cm^{-2}

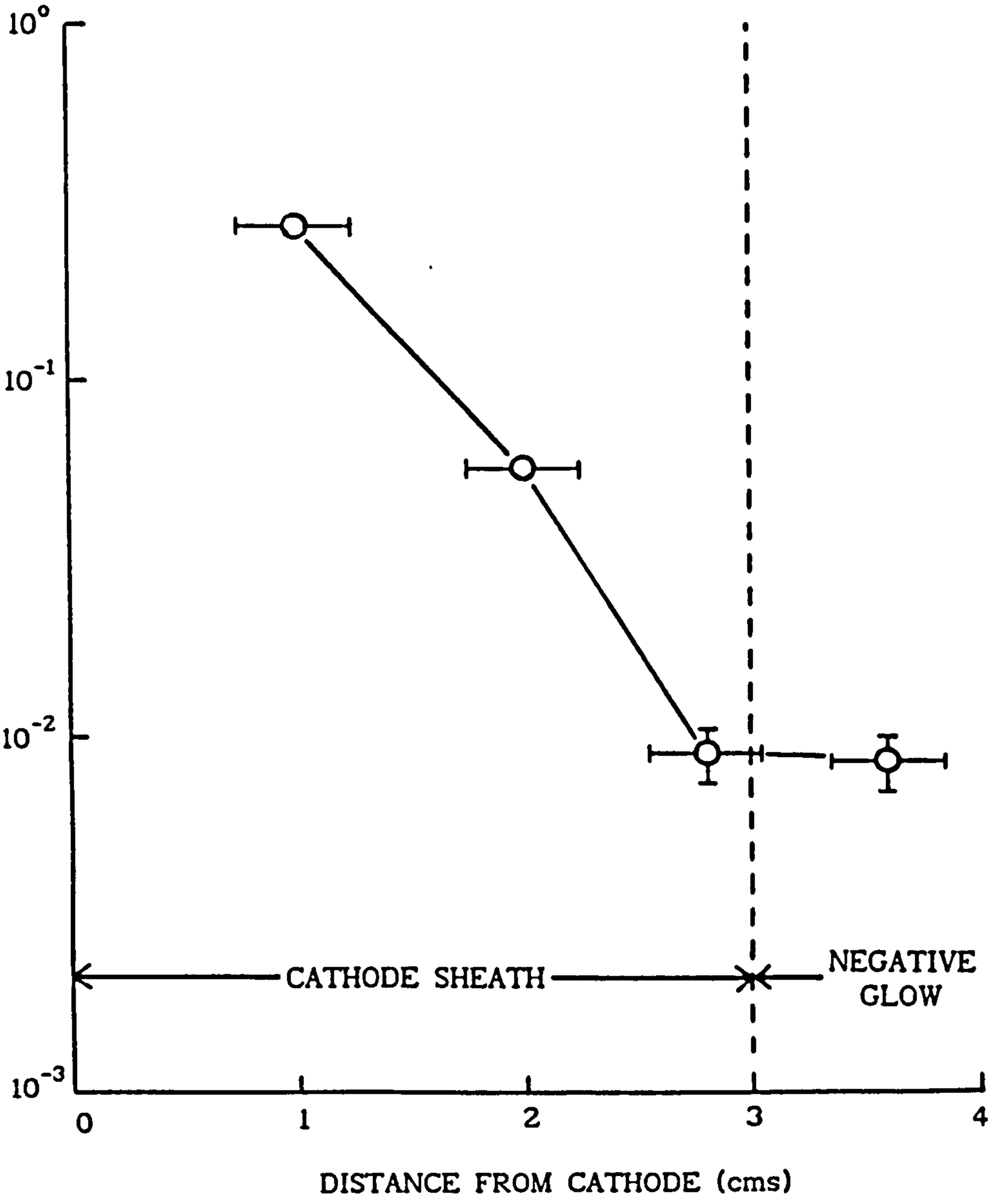

Figure 5.10 N°/N_2° intensity ratios as a function of distance from the cathode in a pure nitrogen diode discharge, V_c = 1 kV, J = 0.05 mA cm^{-2}, 50 mTorr.

significantly less than the results from Figure 5.9 at the same pressure. A possible explanation for this is that the cathode voltage for the data in Figure 5.10 was 1 kV instead of 2 kV, thus the average energy of ions accelerating across the sheath would have been lower. Data for the dissociative charge transfer collision cross section (ref 85) shows it to rise from about 1.5 x 10^{-16} cm^2 at 600 eV to about 7 x 10^{-16} cm^2 at 2 keV N_2^+ ion energy. It may be inferred that a reduced average ion energy decreases the cross section and consequently, less nitrogen atoms are produced.

Figure 5.11 shows how the intensity ratio changes under pure nitrogen thermionic triode conditions. For these results, the cathode voltage and current density were maintained at a constant value whilst the pressure was decreased from 40 mTorr to 1 mTorr by adjusting the filament emission. The large cathode bias used (2 kV), enabled a thick sheath to be maintained during these investigations. Also shown is data from a diode discharge at the same cathode voltage and current density. The data is therefore dependent only on one externally controllable parameter, namely pressure. The results show that the proportion of nitrogen atoms increases in the negative glow as pressure is reduced and this can be attributed to diffusion from the sheath region as previously discussed. The most interesting observation however, is that the proportion of nitrogen atoms decreases in the sheath as pressure is reduced and this supports the suggestion that the dominant ionic species arriving at the cathode in low pressure enhanced discharges will be N_2^+. During the course of these measurements, the sheath thickness was found to be about 3 cms under the 70 mTorr diode conditions but reduced to about 2.5 cms under 5 mTorr thermionic triode conditions, even though the cathode bias and current density were constant. This is indicative of the charge to mass ratio changing in the Child-Langmuir

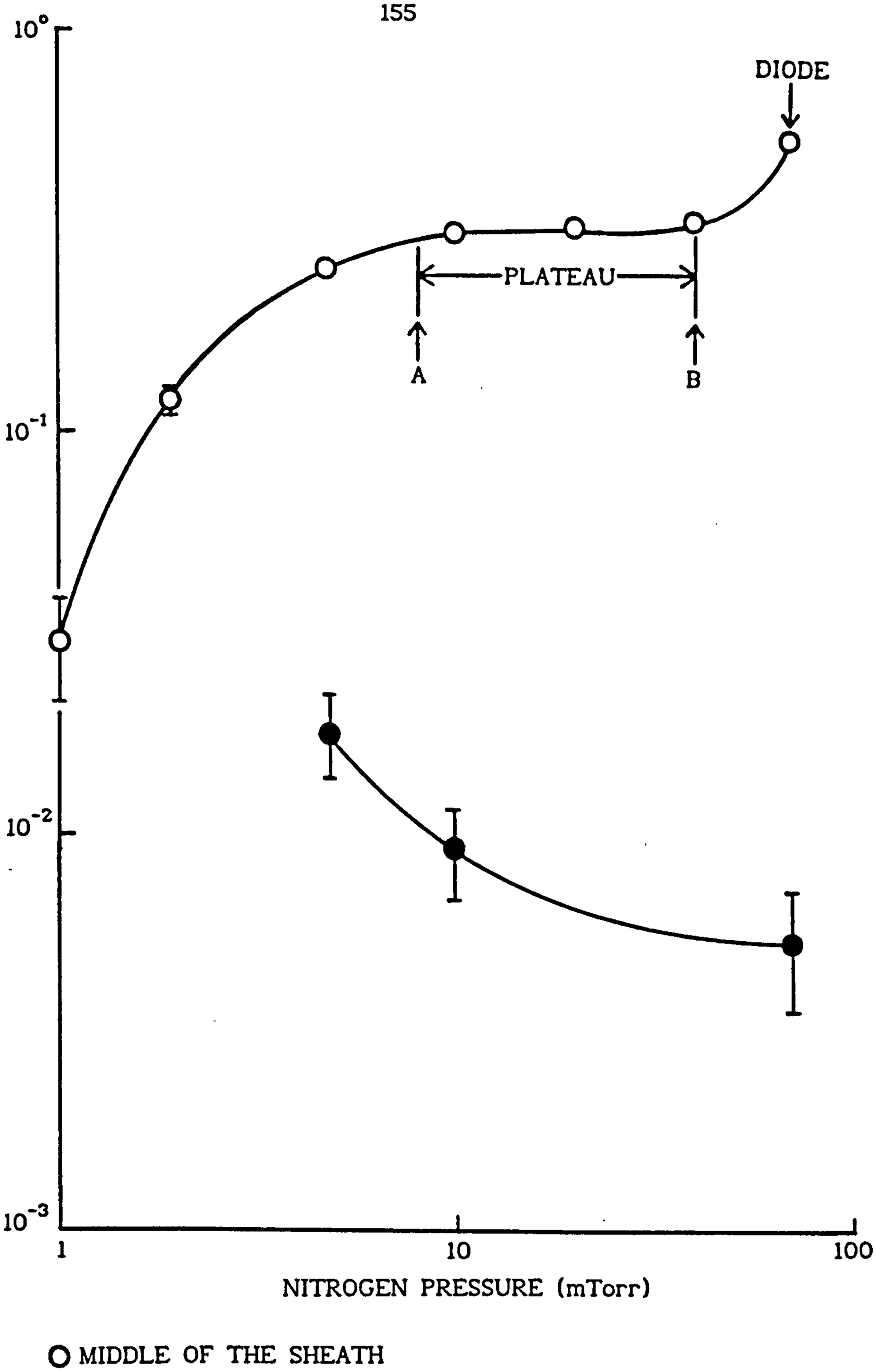

Figure 5.11 N°/N_2° intensity ratios as a function of pressure in pure nitrogen diode and thermionic triode discharges, V_c = 2 kV, J = 0.18 mA cm^{-2}, fil. bias = 100 V.

equation (Equation 3.6), which under the same voltage and current density conditions predicts sheath thicknesses of 2.68 cms for N^+ ions and 2.25 cms for N_2^+ ions. This gives a theoretical reduction in thickness of 84%, compared with the measured reduction of about 83%, which also supports the likelihood of nitrogen molecular ions being predominant in low pressure enhanced discharges. Although this comparison with the Child-Langmuir equation indicates that virtually all the ions arriving at the cathode at 70 mTorr are N^+ and at 5 mTorr the dominant species is N_2^+, the curve from the sheath region in Figure 5.11 shows that the reduction in nitrogen atoms between the same pressures is only a factor of about 2, assuming Equation 5.2 is applicable. This would appear to be a discrepancy; however, it must be stressed that the OES data was taken at the mid point in the sheath and not at the cathode surface. Therefore the actual proportion of nitrogen atomic species arriving at the cathode will have been considerably greater than the values inferred from Figure 5.11.

Another feature which can be observed in Figure 5.11 is a plateau region between about 8 to 40 mTorr in the sheath data. This may be due to the energy dependence of the dissociative charge transfer collision cross section, as previously discussed. As the pressure decreases, there will be fewer collisions in the sheath and therefore, the average energy gained by ion acceleration will increase. As the cross section increases with energy, there will be proportionally more dissociative charge transfer collisions at "A" and fewer at "B" in Figure 5.11 which tends to offset the pressure effect and produces the plateau.

Figure 5.12 is identical in form to the previous figure, but shows the sheath data evaluated from the other N° and N_2° peaks detailed in Table 5.4. These peaks permitted the investigation of nitrogen-argon discharge mixtures. Although there is more scatter in this data compared with that of

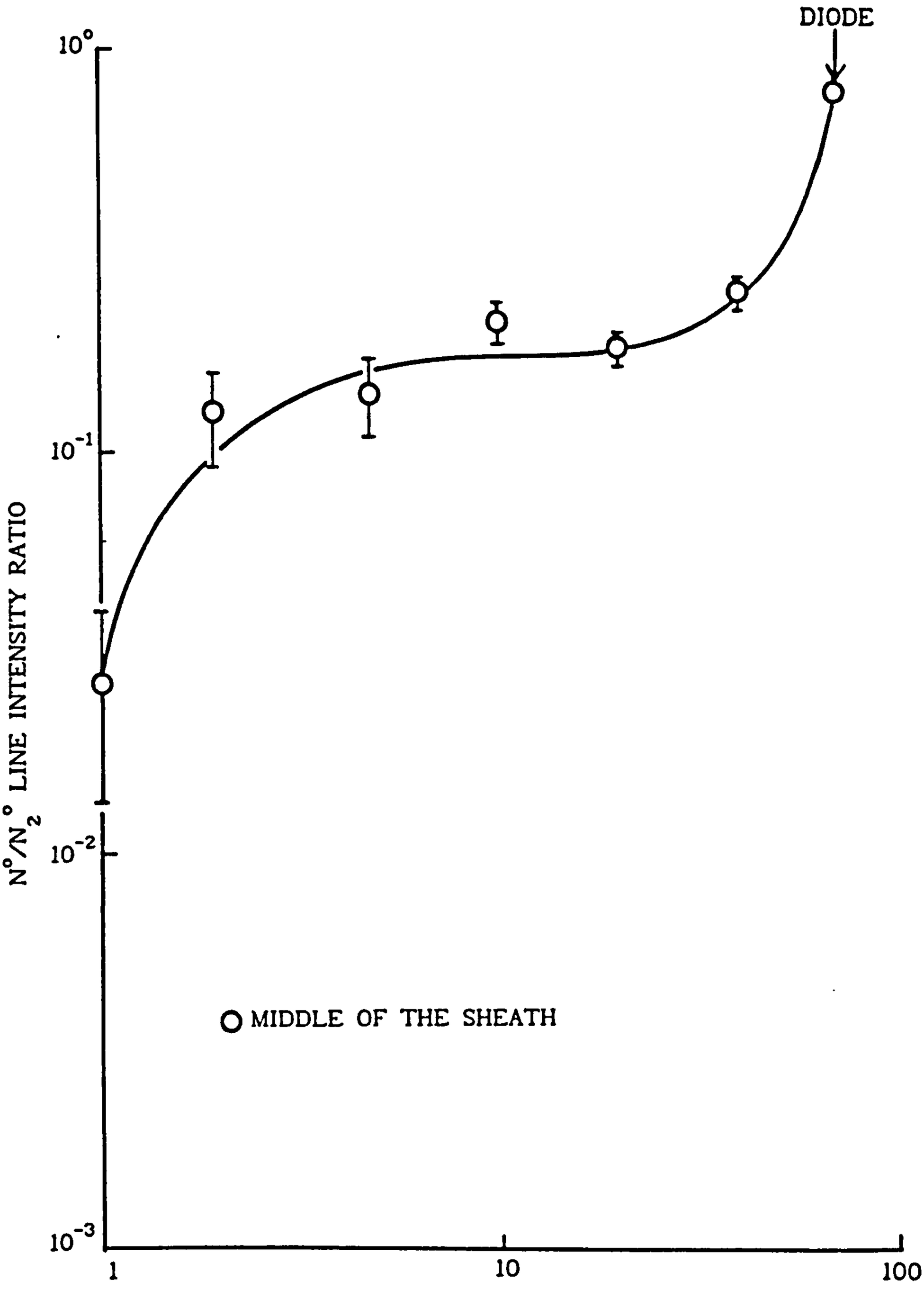

Figure 5.12 N°/N_2° intensity ratios, plotted in the same form as Figure 5.11 (same discharge conditions), using the alternative nitrogen peaks detailed in Table 5.4. These peaks permit the investigation of nitrogen-argon discharge mixtures.

Figure 5.11, the general characteristic of the curve is comparable to the former.

Figure 5.13 shows how the intensity ratios change with nitrogen partial pressure in diode discharges containing argon. Considering the sheath data, the ratio decreases as the proportion of nitrogen in the discharge decreases, due to reduced probability of dissociative charge transfer collisions. However, there appears to be no plateau. This can be explained by the fact that under these conditions, the total discharge pressure was constant (50 mTorr). Thus the total collision rate in the sheath (for all types of collision) and hence the average N_2^+ ion energy between collisions would not have changed significantly with nitrogen partial pressure. Therefore, the effects of collision cross section energy dependence are not apparent.

There appears to be a slight increase in the proportion of atomic nitrogen when argon is introduced into the discharge in Figure 5.13. This is most readily observable in the peaks at 25 mTorr, as compared with pure nitrogen at 50 mTorr, for the negative glow data. Also, at 2 mTorr nitrogen partial pressure, there appears to be more nitrogen atomic species in the negative glow than in the sheath. Clearly, this is indicative of an additional process which dissociates nitrogen; one which involves argon. Possible reactions are:

$$Ar^+ + N_2 \longrightarrow N^+ + N + Ar$$

$$Ar^{2+} + N_2 \longrightarrow N^+ + N + Ar^+$$

In both reactions, the (excited) N_2^{+*} is formed as an intermediate process. It is uncertain which of these reactions are predominantly responsible as available published data on dissociative reactions are difficult to compare. The Ar^+ reaction has a threshold at about 20 eV and a value of 5×10^{-17} cm^2 at 40 eV (eg ref 86). This threshold value is comparable to that for

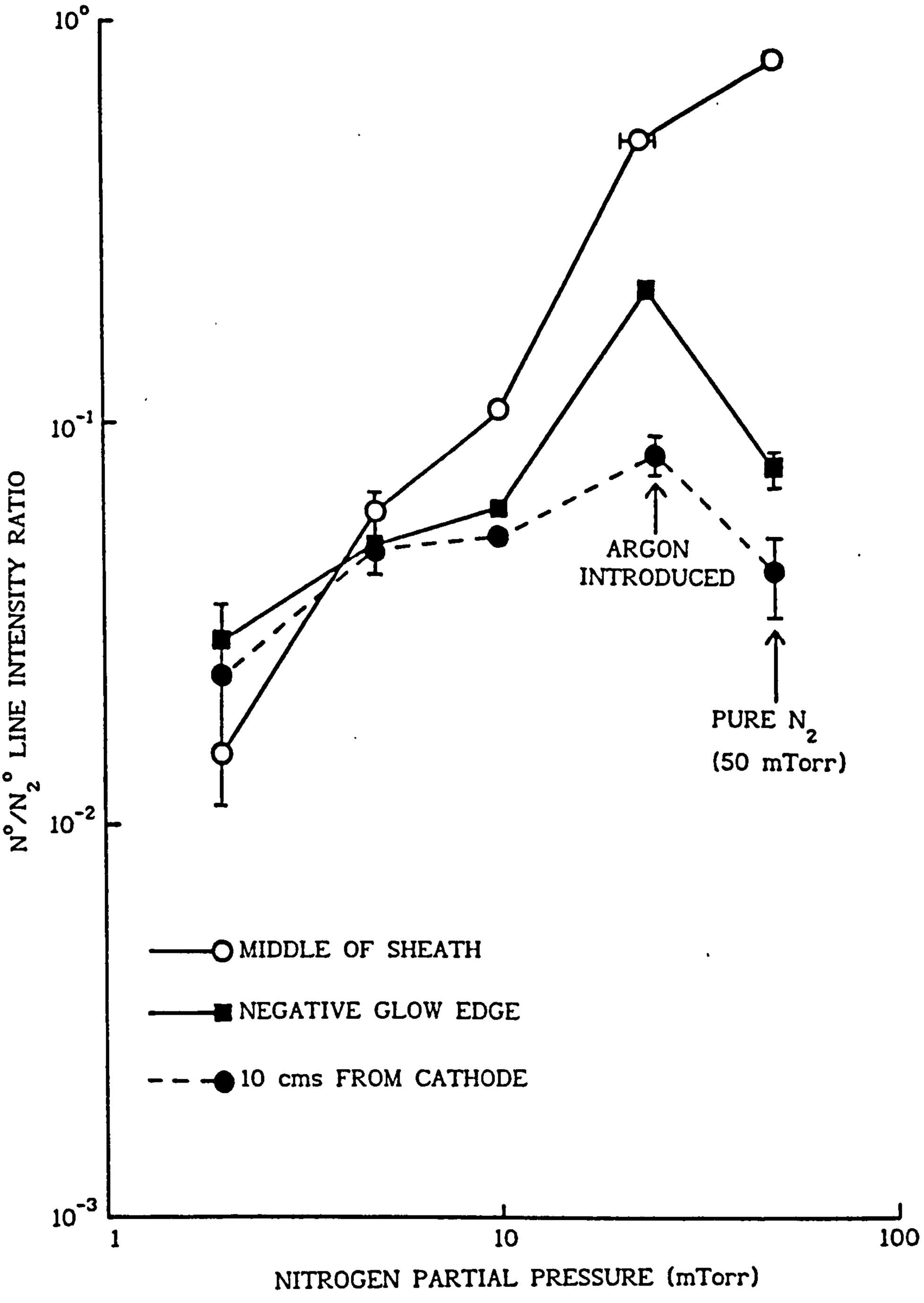

Figure 5.13 N°/N_2° intensity ratios as a function of nitrogen partial pressure in diode discharges containing nitrogen + argon. The total pressure was maintained constant at 50 mTorr. V_c = 2 kV, J = 0.10 to 0.13 mA cm^{-2}.

dissociative charge transfer involving nitrogen only (~ 24 eV, ref 87) though the cross section value is smaller, the latter being about 1 x 10^{-16} cm^2 at 40 eV (ref 88). However, in ref 89, where glow discharge mass spectroscopy investigations of DC diode nitrogen-argon discharges were performed, the authors believed that the Ar^{2+} reaction could be significant, the rate constant for this being high (ref 90), even though the number density of Ar^{2+} ions in the discharge can be expected to be low. Although no data can be found for the energy threshold of the Ar^{2+} reaction, if it is very low, this could explain the increased presence of nitrogen atomic species in the (low ion energy) negative glow region as shown in Figure 5.13.

Figure 5.14 shows the N°/N_2° intensity ratios as a function of nitrogen partial pressure in the sheath region of low pressure (10 mTorr) nitrogen-argon thermionic triode discharges. The cathode voltage and current density were maintained at a constant value for these discharges, as described earlier for the pure nitrogen triode data. The intensity ratio (and therefore the proportion of nitrogen atomic species) appears to be largely unaffected by nitrogen partial pressure, in contrast with the equivalent data for pure nitrogen triodes taken from Figure 5.12. Clearly, this is due to the additional influence of argon on the former, as described in relation to Figure 5.13.

The data presented in this section supports the inferences made in Chapter 3 concerning the effects of dissociative charge transfer of nitrogen in the cathode fall region. In addition, the influence of argon on nitrogen dissociation appears to become significant, particularly in low pressure thermionic triode discharges where the proportion of nitrogen present is low.

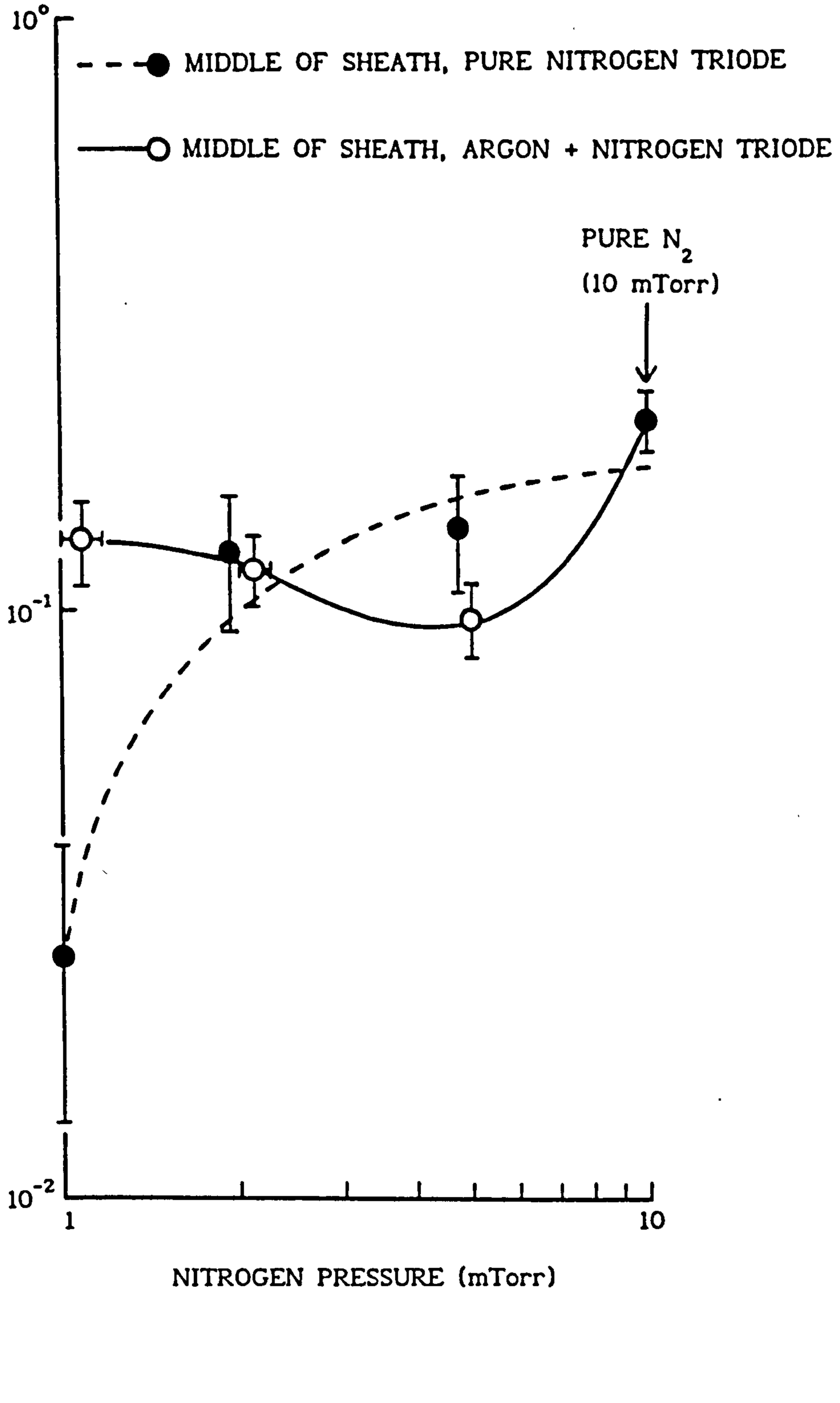

Figure 5.14 N°/N_2° intensity ratios as a function of nitrogen pressure in thermionic triode discharges containing pure nitrogen (data from Figure 5.12) and nitrogen + argon mixtures (total pressure maintained constant at 10 mTorr). For all discharges, conditions were: V_c = 2kV, J = 0.18 mA cm^{-2}, fil. bias = 100 V

5.4.4 Tungsten Filament Contamination Effects

5.4.4.1 Background

As discussed in Section 4.4.2.3, potential contamination problems arising from tungsten being sputtered from filaments might be reduced by decreasing the filament bias in triode discharges. This was investigated by analysing OES data from a series of argon thermionic triode discharges, by maintaining constant pressure, cathode voltage and current density. The fibre optic probe was positioned at 10 cms from the cathode. The filaments had been used for about 4 hours prior to this investigation. Filament bias was increased from 20 volts to 150 volts whilst reducing thermionic emission to maintain a constant degree of enhancement. Only one tungsten emission line (W° at 522.47 nm, ref 91) was found to be suitable for analysis in the OES data. Unfortunately, contamination effects in discharges containing nitrogen could not be investigated as this peak was obscured by nitrogen emission lines. Alternative peaks were either too weak or were obscured by other emission lines. Although the absolute line intensity could be studied, variations in the tungsten emission intensity which were not due to changes in the amount of sputtered tungsten in the discharge might be significant, such as excitation probability changes with energy and intensity of electrons emitted by the filaments. To alleviate this, the tungsten peak required ratioing with another species which could be assumed to be of constant number density in the discharge yet has similar excitation probability characteristics. As the cathode bias and current density was constant, the sputtering rate of iron into the discharge must have also been constant. Two Fe° peaks were selected, one at 371.99 nm, the other at 374.60 nm; these having excitation energy thresholds of 3.3 eV and 3.4 eV respectively (ref 91). Although no data could be found for the excitation threshold of the tungsten peak, other W° peaks have values in the range 3.2

to 3.4 eV (ref 91). Thus it may be assumed that the selected tungsten and iron peaks have similar excitation thresholds.

5.4.4.2 Results and comments

The results are shown in Figure 5.15. The intensity ratio for both plots (using each Fe line) decreases as filament bias is reduced. The ratio at 20 volts is about 70% of the value at 150 volts for each curve. If Equation 5.2 is assumed to be applicable, this means that the amount of tungsten in the discharge is reduced to ~70%. Therefore, although it appears that contamination might be reduced by using a lower filament bias, the effect is likely to be small. As the sputtering threshold for tungsten in argon is 33 eV (eg, ref 16), a large reduction in the presence of tungsten in the discharge might be expected to occur below 50 volts bias. Clearly, this does not occur in Figure 5.15. The probable explanation is that the sputtering threshold for the (hot) filaments was lower than the quoted value; the likelihood being that the latter figure was determined from tungsten at considerably lower temperatures. Unfortunately, there appears to be no published data available to verify this, though sputtering yield generally increases with target temperature for most materials (eg, refs 16, 86) and it might be inferred that sputtering energy threshold will also decrease.

5.4.5 Sheath Thickness Measurements During Titanium Evaporation

5.4.5.1 Background

As discussed in Section 5.3, the honeycomb material in the chamber viewport permitted observation of the cathode fall region during evaporation of titanium into the discharges. Sheath thicknesses could therefore be measured with and without the presence of titanium evaporation (Runs E100 to

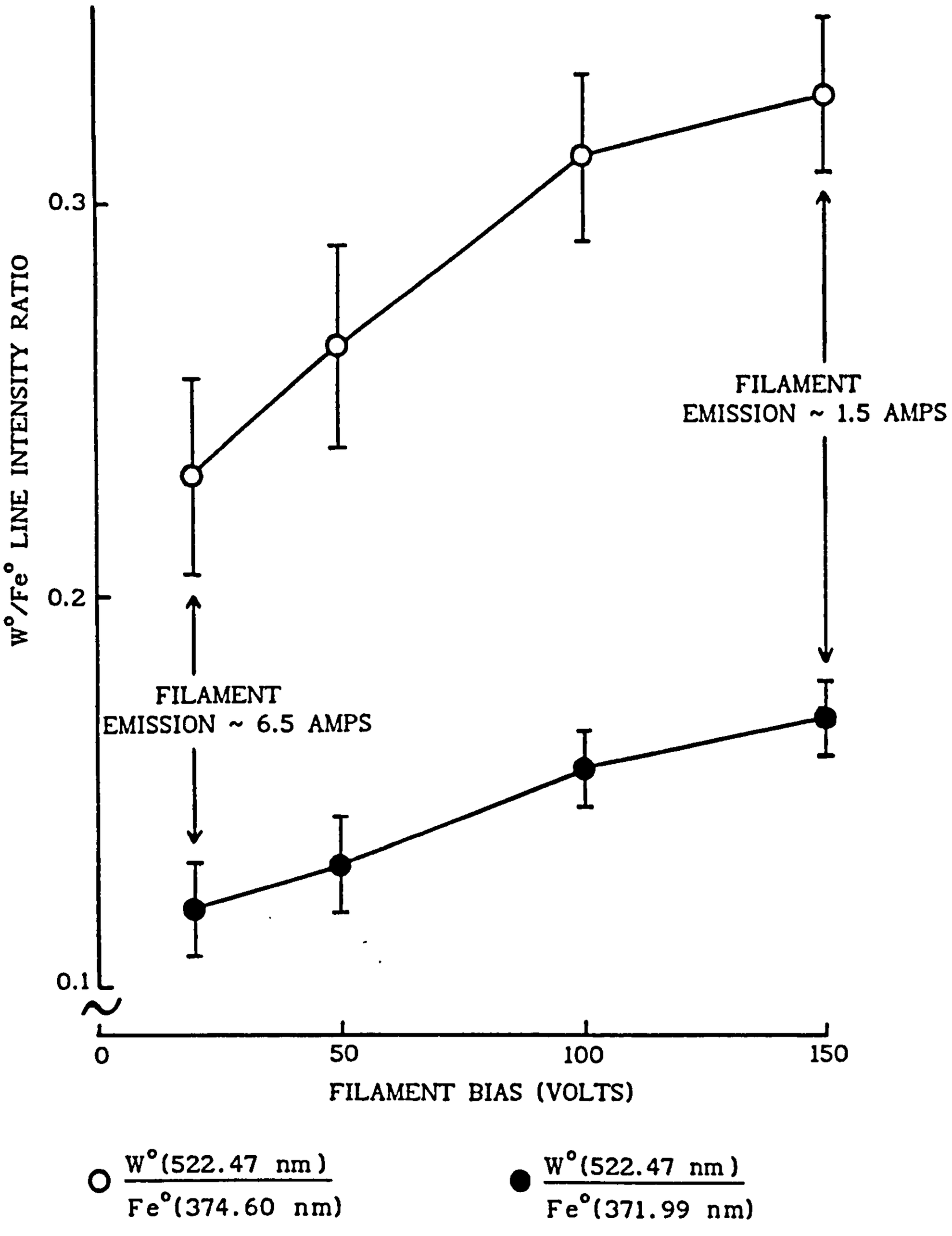

Figure 5.15 Tungsten/iron spectral line intensity ratios as a function of filament bias under pure argon thermionic triode conditions, V_c = 200 V, J = 0.33 mA cm^{-2}, 4.9 ± 0.1 mTorr.

E105), the process parameters being given in Table 5.2. As explained in Section 5.3, the interior of the chamber was coated with titanium prior to Run E100 and cathode voltage, current density and gas pressure were maintained at constant values during this series of runs. Although there is a possibility that the voltage drop across the sheath may have changed during evaporation (due to, for example, increased electron temperature) this will have probably been insignificant in comparison with the magnitude of the applied cathode bias (2 kV), as will be discussed in Section 5.5.1. Thus, if sheath voltage and current density is constant and the Child-Langmuir equation is assumed to be applicable when evaporation is performed, then any change in sheath thickness with the onset of evaporation must be due to a change in the charge to mass ratio of the ionic species arriving at the cathode. Thus, from the equation, the sheath thickness is given by:

$$L = (4 \varepsilon_o / 9J)^{1/2} \ (2q / m_i)^{1/4} \ V_c^{3/4} \qquad (3.6)$$

with V_c and J constant, then:

$$(L_{Ar} / L_E)^4 = (q / m_i)_{Ar} / (q / m_i)_E \qquad (5.3)$$

where subscripts E and Ar represent the parameters under argon discharge conditions with and without evaporation respectively. During evaporation, if N is the fraction of ions arriving at the substrate which are metal (Ti), then

$$(q / m_i)_E = N(q / m_i)_{Ti} + (1 - N) (q / m_i)_{Ar} \qquad (5.4)$$

Therefore, from Equations 4.7 and 4.8,

$$(q / m_i)_{Ti} = [(q / m_i)_{Ar} / N] [(L_E / L_{Ar})^4 - 1 + N] \qquad (5.5)$$

If $(q/m_i)_{Ar}$ is assumed to be 1/40 (ie the only argon ionic species being Ar^+), then the charge to mass ratio for the titanium species $(q/m_i)_{Ti}$ can be evaluated as a function of N from Equation 5.5 knowing the sheath thickness ratio (L_E/L_{Ar}).

5.4.5.2 Results and comments

It was found that the sheath thickness appeared to reduce from 1.8 cms (no evaporation) to 0.8 cms during evaporation, for all the runs. The addition of 10% nitrogen to the discharge (Runs E104, E105) did not significantly affect the results. The negative glow region was bright bluish-green whilst the sheath was dark blue during evaporation.

Figure 5.16 is a plot of Equation 5.5 using the value for (L_E/L_{Ar}) from the results above. The equation predicts that below some critical value, N_c, the titanium ions are negatively charged. If the equation is valid below N_c, the results would suggest that these ions could modify the (positive ion) sheath by, for example, recombination processes. At $N = N_c$, a large proportion of the ion current (~ 96%) is predicted to be transported by titanium neutrals, and clearly this result is invalid. Above N_c, the titanium ions become positively charged. It is highly improbable that the effective charge carried by titanium ions is negative. This is because Penning ionisation, for example, is known to be a primary mechanism for ionising metal species and this creates positive ions only (see Section 3.5.2.1). Therefore, it would appear that the validity of Equation 5.5 is restricted to values for N greater than N_c.

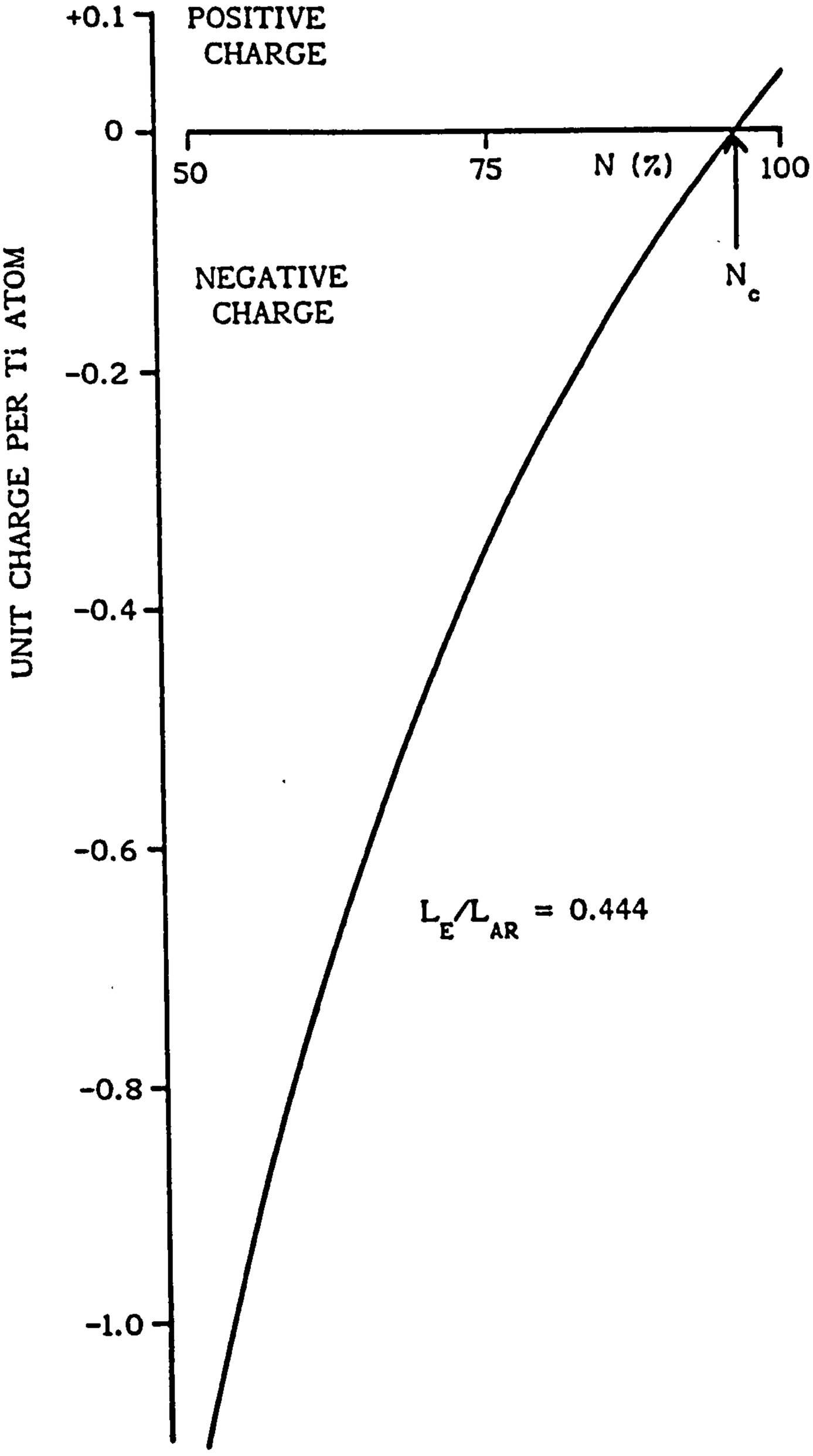

Figure 5.16 Plot of Equation 5.5 using the experimentally determined L_E/L_{Ar} value. N = fraction of ions arriving at the substrate which are titanium.

Figure 5.17 shows the results plotted in terms of titanium atoms per (positive) unit charge for values of N greater than N_c. The broken curves represent the upper and lower limits of possible spread in the results, arising from the estimated error (± 0.1 cms) in the sheath thickness measurements. The range of these limits is large due to the influence of the fourth power term on the sheath thickness ratio in Equation 5.5. However the results indicate that:

(i) At least some of the titanium arrives at the cathode in the form of ionised atomic clusters, the indication being that they consist of a minimum of tens of atoms per unit charge.

(ii) The titanium contributes to at least 90% of the ion current density at the substrate.

The suggestion that clusters form in ion plating is, to some extent, supported by evidence provided in the literature. Metal evaporation in the presence of a low pressure inert gas (gas evaporation) has been reported in a number of papers (eg, refs 92-98) as a means of producing aggregates in the gas phase. Metal atoms effused from the source lose their energy by collisions with gas atoms. This vapour cooling can lead to homogeneous nucleation, the critical diameter for spontaneously formed embryonic particles being the order of atomic dimensions once the vapour has cooled by a few hundred degrees (ref 96). Aggregate size increases with gas pressure (refs 92, 95, 96, 98), gas atomic mass (refs 94, 96, 97, 98) and metal vapour pressure (refs 96, 98). These experiments produced particle sizes in the range 50Å to 2000Å, containing 10^3 to 10^8 atoms. Metal microclusters are reported in refs 97 and 98 which contained less than a few hundred atoms when produced in helium gas. However, the gas pressures used in refs 92 to 98 (0.5 to 250 Torr) were considerably higher than those used under typical ion plating conditions. Therefore, cluster sizes might be expected to be

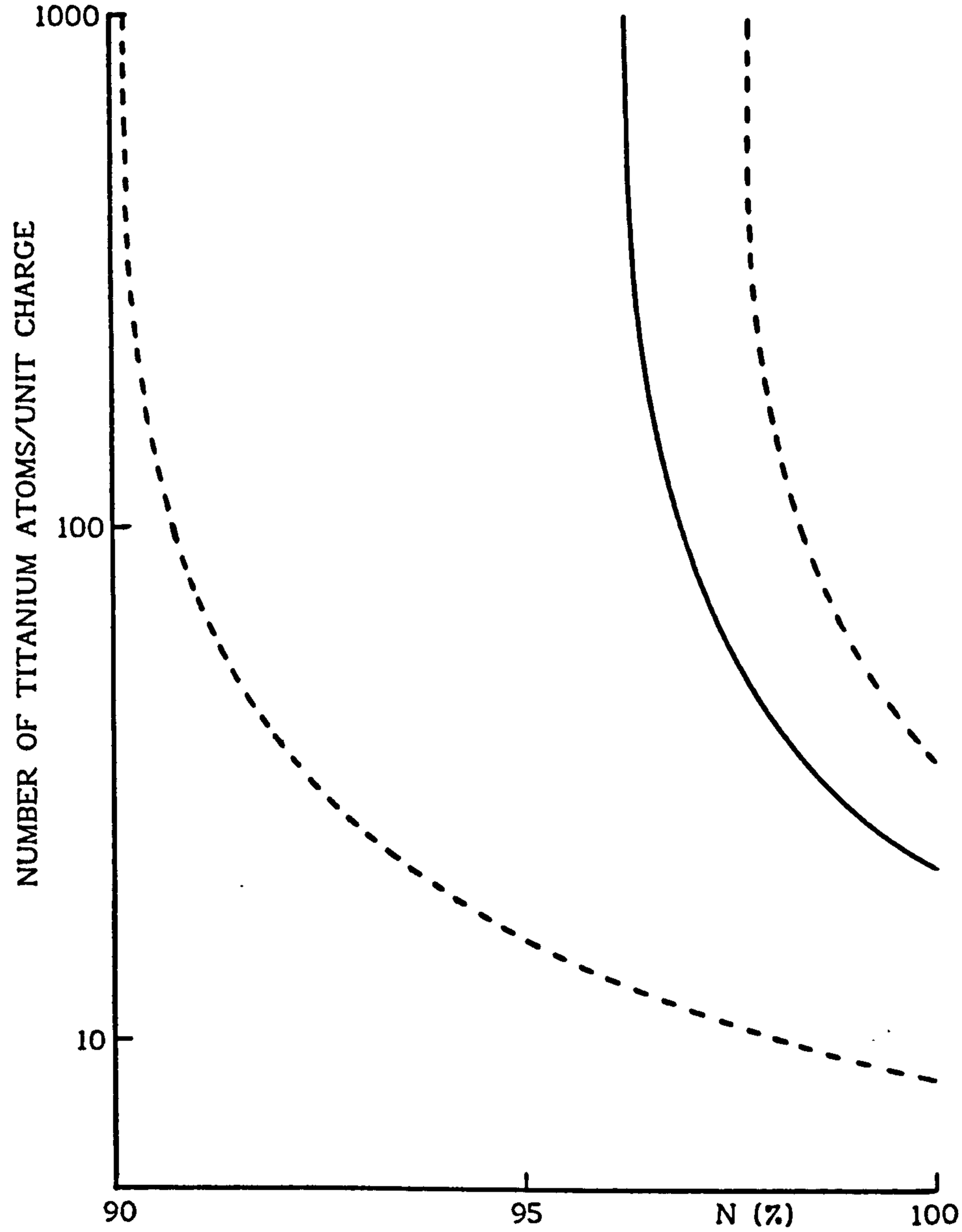

Figure 5.17 Plot of Equation 5.5 using the experimentally determined L_E/L_{Ar} value, for the region where titanium ions are positively charged. Broken curves represent the upper and lower limits of possible spread in the results due to the estimated ± 0.1 cm error in sheath thickness measurements.

smaller in the latter case. An extrapolation of the data in ref 96, for gas evaporation of aluminium in argon, indicates that at about 5 mTorr argon pressure, clusters containing a few thousand atoms could be produced. As the average gas temperature in ion plating is little more than the ambient (room) temperature, this extrapolated result should be representative of the cluster sizes that might be obtained here; the value at least concurs with the data in Figure 5.17.

There are, however, other phenomena which can be expected to occur due to the presence of a glow discharge. One such effect might be fragmentation of large clusters into smaller ones, due to either energetic electron impact or multiple ionisation. Pfau et al (ref 99) found that frequent fragmentation events occurred in antimony clusters for electron ionising energies exceeding 35 eV. Electrons emitted from substrates and sources of ionisation enhancement would exceed this level of energy in most ion plating configurations. The large proportion of ion current transported to the substrate by metal ions, as shown in Figure 5.17, may be attributed to the effects of Penning ionisation. This also supports the suggestion made in Section 3.5.2.1, that the metal could become ionised in preference to the argon. Multiple ionisation of the clusters is also likely to occur, due to preferential ionisation by Penning mechanisms. This in turn may lead to fragmentation of smaller clusters within the particle size distribution, if the Coulomb repulsive energy exceeds the binding energy of a surface atom in the cluster (refs 100, 101).

Finally, as reported in Section 3.5.2.1, the generally observed reduction in substrate current density during metal evaporation could be explained, if the charge to mass ratio of the metal ions were smaller than that of the argon ions. The likelihood of metal cluster formation supports this suggestion, if it is assumed that cathode sheath thickness does not

change appreciably (unlike the controlled conditions used in this work) when metal is evaporated in practical ion plating systems.

5.5 DISCUSSIONS

5.5.1 Electron Temperature in Ion Plating

Although some doubt exists over the absolute accuracy of the T_e results, the observations from the relative changes in T_e generally concur with those of other workers. Perhaps the most interesting result is the apparent doubling in T_e during titanium evaporation through the discharge. The fact that this observation agrees with findings published elsewhere (albeit under different conditions) gives credence to this result. Whatever the reason for the large increase in T_e during evaporation, the main concern has to be how relevant this result might be in relation to practical ion plating systems.

With reference to Chapter 3, probably the main practical effect of changes in T_e can be restricted to the influence on sheath voltages. If an electrically isolated substrate is used in an ion plating system, then it will develop a negative potential, V_f, with respect to the plasma potential V_p, so that no current is drawn:

$$V_p - V_f = (kT_e / 2e) \ln (m_i / 2.3\ m_e) \qquad (3.2)$$

Thus $V_p - V_f$ will roughly double in magnitude during evaporation. Usually however, the substrate is negatively biased by external means and the applied voltage is assumed to be equal to the potential drop across the substrate (cathode) sheath. As already discussed in Section 3.2.2.2, there will be a small potential in addition to the applied substrate bias. This additional potential will be positive with respect to an anode, if the anode

is large. Its value will never exceed that of $(V_p - V_f)$ as some electron current will be drawn to balance the cathode ion current. Therefore, Equation (3.2) represents an extreme use where the anode is infinitely large in comparison with the cathode. For a large earthed anode then, where a typical value of T_e might be 2 eV, the plasma potential with respect to earth will be less than 10 volts but during evaporation, this limit could increase to 20 volts.

One of the assumptions made when using the Child-Langmuir equation is that the applied voltage is equal to the sheath potential. Increasing T_e will therefore make this assumption less valid. Clearly though, as the increase is likely to be less than 10 volts during evaporation, the effect will be minimal when applied voltages are in the order of 100 to 1000 volts. Thus calculations performed for evaluating metal cluster size in Section 5.4.5 will not be significantly affected.

Another phenomenon arising from increased plasma potential relative to an earthed anodic chamber, might be to improve plasma uniformity, due to the greater potential drop across the anode sheath. Electrons emitted from the chamber walls would accelerate to higher energies and possibly create more ions. However, as the increase in anode sheath voltage will be small, this effect will probably be insignificant.

It is therefore apparent that changes in electron temperature, unless they are manyfold, are unlikely to be of any significant consequence in relation to the practical aspects of ion plating. Nevertheless, further investigations of how T_e changes with, for example, different evaporation rates and evaporant materials, may provide a better insight into the processes occurring in ion plating. This could be performed with an OES system (as demonstrated here) which had previously been directly calibrated with Langmuir probe data in discharges without evaporation taking place.

5.5.2 Dissociative Charge Transfer of Nitrogen

The data in Section 5.4.3 appears to support the suggestion that dissociative charge transfer in the cathode sheath of a nitrogen discharge may have a significant influence on the nature of the species arriving at the cathode. However, other mechanisms could also occur, such as electron impact dissociation,

$$e + N_2 \longrightarrow N + N + e$$

and electron impact dissociative ionisation,

$$e + N_2 \longrightarrow N + N^+ + 2e$$

According to ref 102, the collision cross section for these processes combined, rises to a maximum of about 2×10^{-16} cm^2 at 100 eV and then decreases with increasing electron energy. In fact, the shape and size of the cross section is comparable to non-dissociative electron impact ionisation of nitrogen (~ 2.6×10^{-16} cm^2 at 100 eV). Therefore, we might expect as many nitrogen atomic ions and neutrals as there are molecular ions in the negative glow. However, this is still a very small proportion in relation to the total gas number density, so that even if the values are correct in ref 102 (their estimated errors are large), the amount of nitrogen atomic species generated in the negative glow should be very low. This concurs with the OES data in this work.

The proportion of N^+ ions relative to N_2^+ ions entering the cathode sheath must also be considered. Data given in ref 86 shows that the probability of electron impact dissociative ionisation is about 10 to 20% of

that for non-dissociative electron impact ionisation for electron energies of up to 1 keV. Also, the threshold for creating N^+ is higher than for N_2^+ (about 28 eV compared with 14.5 eV). Therefore, the proportion of N^+ entering the sheath from the negative glow should be considerably less than 10% of the N_2^+ current. This again seems to concur with the OES data in this work; the N/N_2 ratio in the sheath being typically more than 10 times the value in the negative glow.

As the cross sections for electron impact dissociation mechanisms and creation of N_2^+ are similar, we would not expect the former to be a significant process in the sheath region. The conclusion is, therefore, that dissociation by charge transfer rather than by electron impact appears to be the dominant dissociative mechanism occurring in these discharges. Some caution must be exercised however, in assuming that Equation 5.2 can be rigidly applied for assessing the actual change in proportion of N to N_2 species from the OES data. Although not reported by Coburn et al in ref 80, the shape of the (energy dependent) excitation cross section, in addition to the excitation threshold, should be similar for both species under consideration, as pointed out in ref 25. This effect may not be too important in the negative glow region where electron energies are generally low so that most excitation collisions occur near the threshold. Unfortunately, in the sheath region, average electron energies will be considerably higher so that differences in the shapes of the excitation cross sections may be more significant. In spite of this, it is clear that the OES results support the inferences arising from Child-Langmuir equation predictions.

Although the results show strong evidence for nitrogen atomic rather than molecular ions being the dominant ionic species arriving at the cathode under certain conditions, we can expect that the resulting molecular neutrals

formed by dissociative charge transfer will carry most of the kinetic energy from the collision process. Symmetrical charge transfer collisions, ie:

$$N_2^+ \text{ (FAST)} + N_2 \text{ (SLOW)} \longrightarrow N_2^+ \text{ (SLOW)} + N_2 \text{ (FAST)}$$

have a collision cross section value which is typically 10 times larger than that for dissociative charge transfer (ref 85). Thus, in pure nitrogen diode discharges, most of the energy will be transported by molecular neutrals, produced by symmetrical and dissociative charge transfer collisions in the cathode sheath. Under enhanced discharge conditions, fewer collisions will occur and most of the energy may then be transported by molecular ions. Although the situation becomes more complex when a significant proportion of the gas in the discharge is argon, the main point is that nitrogen molecular species are likely to transport most of the energy to the cathode, in preference to atomic species, regardless of the discharge conditions used. Therefore, the importance of nitrogen dissociative charge transfer mechanisms in ion plating (and other plasma processes such as nitriding) has to be questioned. Even if nitrogen atomic species were considered to be beneficial to coating formation or nitridation (by virtue of their smaller mass), the molecular form would have a high probability of dissociating at the surface under all discharge conditions, requiring only about 9.7 eV to do so (ref 102). Thus bombardment by N^+ ions may not necessarily provide any significant benefits.

The tentative conclusion which can be drawn from these considerations is that under practical ion plating conditions, nitrogen dissociative charge transfer mechanisms in the sheath may not have an important role. Perhaps the most significant result of this part of the work is to emphasise that the nature of the species existing in the negative glow is not necessarily

the same as the species arriving at the cathode.

5.5.3 Results Which Relate to the Sputter Weight Loss Experiments

The OES work on axial line intensity dependence in Section 5.4.2, can be compared with the SWL results from thermionic triode discharges in Chapter 4. The sputter weight loss fall off was found to correlate with the probability of impact ionisation by filament electrons with distance from the emitter. Ring source and electron scattering effects were considered to have an insignificant contribution to the results. Conversely, the OES results were found to correlate well with the probability of filament electrons becoming scattered. Clearly, ionisation processes would have been irrelevant as some of the data studied was from neutral species. As de-excitation was the mechanism studied in the OES work, other excitation processes such as photo-excitation may have been contributory, though if Corona equilibrium is assumed (see Section 5.4.1.1) they would not be expected to occur. The fact that line intensities were found to fall off with distance from the primary electron emitter in both diode and triode discharges, suggests that the availability of emitted electrons to create excitation directly or indirectly was the principle factor. Unlike the SWL work, OES results were taken from a relatively narrow region along the central axis of the discharge. Thus, although electron scattering angles would have been small (as discussed in Section 4.4.2.1), the influence of scattering will have been much more significant in the OES data. It is apparent therefore, that the SWL and OES studies are based on different physical phenomena occurring in the discharge. However, both studies are linked by the fact that they show (i) electrons from the primary emitter dominate the discharge characteristics and (ii) their influence approximates to an exponential fall off with distance from the emitter.

The OES work on tungsten emission in Section 5.4.4 supports the evidence for contamination problems observed in the SWL work on thermionic triode discharges. Additional comment, though, is required on the applicability of Equation 5.2 to the data. Although the excitation thresholds for the tungsten and iron lines might be similar, the shapes of their energy dependent cross sections could be significantly different. Fortunately, as discussed in Section 5.5.2, the studies were made in the negative glow region, where most of the excitation collisions would occur near the threshold. Therefore, the indication that the amount of tungsten in the discharge only decreases by about 30% as filament bias is reduced to 20 volts is probably reliable.

5.5.4 Metal Clusters in Ion Plating

The likely presence of gas phase metal cluster formation in ion plating, as suggested in Section 5.4.5, gives rise to some important implications. For example, if the average energy of ions arriving at the substrate is in the order of 100 eV, then the energy per metal atom transported to the substrate will be considerably lower. For example, a cluster containing 1000 atoms would have only ~ 0.1 eV per atom. However, the ionic (and high energy neutral) gas species such as argon and reactive gases will still bombard the coating surface during deposition with energies of, typically, 100 eV per atom. The gas species will redistribute the material by, for example, sputtering the growing layer. Whether this sputtered material returns to the substrate in a predominantly monatomic form or is captured by the arriving clusters is uncertain. Therefore, the effects of cluster formation on the properties of the growing coating are unclear.

Conventional ion plating theories presuppose that the metal vapour is

atomic in nature (eg, ref 103). There has been little or no comment in the literature about the possibility that the metal may arrive at the substrate in the form of clusters. Only two independent references (refs 104, 105) have been found which mention aggregate formation in ion plating. Both suggest that if clusters do form, they will become negatively charged (as any isolated body immersed in a plasma would) and be repelled from the substrate. Although this might be expected to occur, only those clusters which are large enough to behave as a bulk material rather than a group of atoms are likely to be affected. The number of atoms required by a metal cluster, to attain the properties associated with the bulk phase seems to be difficult to ascertain. The question might be comparable to asking how large a cluster has to be before its ionisation potential becomes the work function. Various results on measurements of ionisation potential as a function of cluster size have been reported (refs 106, 107) but there appears to be no sharp transition to the work function of the bulk metal. Instead, the ionisation potential decreases asymptotically towards the work function value and the size at which a cluster attains the work function does not appear to have been determined. By analogy then, it could be inferred that clusters would have to be large, possibly considerably more than 1000's of atoms in size, to sustain a negative charge build-up from the plasma.

Although research into clusters in other branches of science seems to have been growing rapidly in recent years, there are still many fundamental questions which need to be answered. This makes the role of clusters in ion plating difficult to analyse. Clearly, further investigations of the ion plating process are required to understand the phenomenon and its role in coating formation.

5.6 SUMMARY

Optical emission spectroscopy (OES) investigations and further sheath thickness measurements have been performed to provide information on various aspects of ion plating discharges. The OES apparatus used enabled spatially resolved spectral data to be produced so that the cathode sheath and negative glow regions could be investigated. Diode and thermionic triode discharges were studied, using argon, nitrogen and argon-nitrogen mixtures. Evaporation of titanium in discharges was also investigated. Electron temperature, spatial distribution of line intensities, tungsten filament contamination effects, nitrogen dissociation, and cathode sheath thickness changes with titanium evaporation were the main areas of study.

Electron temperature, T_e, was evaluated from OES data using an equation from the published literature. T_e was found to be slightly higher under argon thermionic triode conditions when compared with results obtained from diode discharges. This is attributed to the influence of the high energy electrons injected into the discharge from the thermionic emitter. A slight decrease in T_e was observed when nitrogen was introduced into the argon discharges under certain conditions. This may have been due to electron energy losses caused by excitation of nitrogen molecules. When titanium was evaporated in thermionic triode discharges, T_e was found to double in value. Possible explanations for this include (i) increased charge loss to the chamber walls by electrons due to rarefication of the gas above the vapour source, (ii) increased charge loss to the walls by the vapour, due to the vapour being highly ionised and more directional than the gas, and (iii) distortion of the electron energy distribution in the discharge due to electrons created from Penning ionisation collisions. It is suggested that these changes in T_e may not be of any significant consequence in relation to the practical aspects of ion plating.

Studies of ion and neutral line intensities from argon diode and thermionic triode discharges have shown that triode intensities are considerably greater. This can be attributed to the greater electron density and increased excitation probability in the latter case. Line intensities were found to fall off with distance from the primary electron emitter, approximating to an exponential decay. Curve fits to the data yielded effective collision cross section values which were close to those for elastic scattering of electrons from the primary emitter. These results, as with those reported in Chapter 4, show that electrons from the primary emitter dominate the discharge characteristics and their influence can be represented by exponential decay functions.

Investigations in Chapter 4, have shown that potential contamination problems could occur in discharges where tungsten filaments are employed as thermionic emitters, due to sputter removal of tungsten. OES studies of tungsten emission in argon thermionic triode discharges have indicated that lowering the filament bias (but increasing the filament temperature to obtain the same degree of discharge enhancement) would reduce the amount of tungsten sputtered into the discharge. Unfortunately, the actual reduction in tungsten is estimated to be small, even when the filament bias is drastically reduced.

Sheath thickness measurements on nitrogen diode discharges reported in Chapter 3, suggested that although N_2^+ might be the dominant ionic species arriving at the cathode under enhanced discharge conditions, this could change to N^+ when diode configurations are used. The proposed mechanism was N_2^+ undergoing dissociative charge transfer collisions in the cathode sheath to become N^+. Results from OES monitoring of atomic and molecular nitrogen line intensities in the sheath and negative glow regions supports this hypothesis. It was found that the N/N_2 intensity ratio was very low in the

negative glow but considerably higher in the sheath region of pure nitrogen diode discharges. This ratio decreased in the sheath region as the amount of thermionic enhancement was increased and the discharge pressure was reduced so that fewer collisions would occur. Further sheath thickness measurements also indicated that N_2^+ would be the dominant ionic species in enhanced discharges. In addition to dissociative charge transfer, other dissociation mechanisms such as those due to electron impact can occur but their influence appears to be less significant. The addition of argon into the nitrogen discharges indicated that dissociative charge exchange involving argon could occur; the influence being strongest in very low pressure triode discharges with a relatively large proportion of argon present. Although nitrogen dissociative charge transfer has been shown to be significant under certain discharge conditions, its importance in terms of practical ion plating (and other processes such as plasma nitriding) is questionable. This is because (i) nitrogen molecular species are likely to transport most of the energy to the cathode in preference to the atomic species, irrespective of discharge conditions, and (ii) the energy required for nitrogen molecules to dissociate at the cathode surface is comparatively low, making this alternative dissociation mechanism likely in all discharge configurations.

A comparison of sheath thickness measurements taken with and without the presence of titanium evaporation in thermionic triode discharges has indicated that the charge to mass ratio of the titanium ions is very small and that at least 90% of the ion current at the cathode is transported by the metal species. The conclusion is that at least some of the titanium arrives at the cathode in the form of ionised atomic clusters, consisting of a minimum of 10's of atoms per unit charge and Penning ionisation causes the metal to become highly ionised. The suggestion that metal clusters form

under ion plating conditions is supported to some extent, by gas evaporation experiments reported in the published literature; the likely mechanism being homogeneous nucleation occurring in the discharge. The significance of metal clusters in ion plating is difficult to analyse and further investigations would be required to understand its possible role in coating formation.

6. GAS SCATTERING PHENOMENA AND COATING THICKNESS UNIFORMITY

6.1 BACKGROUND

Chapters 3, 4 and 5 have highlighted the role of ionisation mechanisms in ion plating and outlined some of the general principles which influence the optimisation of glow discharges in these systems. There are however, other mechanisms of potentially equal importance. These govern evaporant flux transportation between the vapour source and substrate, thus influencing coating thickness uniformity. One of the great virtues of ion plating is that it produces coatings of good thickness uniformity. This was once attributed to evaporant ions following "electric lines of force" around the sample (ref 108). Subsequent work (refs 109, 110) has shown the "throwing power" to be primarily dependent upon deposition chamber pressure, ie, the effect is due to gas scattering of the evaporant material rather than ionisation effects.

The most frequently quoted rules for predicting thickness uniformity are those derived from the Cosine law (ref 26). They consist of equations which predict the coating thickness distribution on a flat horizontal surface positioned above an idealised source (eg, point, disk or ring sources). In practice these equations have limited use because (i) most real sources have sidewalls which can cause "beaming" of the flux (electron beam evaporation of certain materials can cause "drilling", resulting in similar effects), (ii) temperature variation can occur over the surface of a real source, affecting the emission characteristics, and (iii) intermolecular collisions within the evaporant flux causes scattering at practical evaporation rates. Modifications to the Cosine law concept have

been used to reduce the discrepancies between theory and practice (eg refs 109, 111, 112), though they are inappropriate for typical ion plating conditions where gas scattering is predominant.

Monte-Carlo modelling of simple ion plating (ref 113) and sputtering systems (eg, refs 114, 115) has predicted thickness distributions which, in many cases, were comparable to experimental measurements. However, the Monte-Carlo technique has certain drawbacks. Powerful computing facilities are required and calculation times are generally very long. For example, the calculations performed in ref 115 ranged from 7 minutes to 8 hours. Also, these models are applicable only to specific situations; there is no generally accepted universal treatment.

A need exists for a relatively simple mathematical model which is applicable to all ion plating systems where gas scattering is the primary influence on coating thickness uniformity. To date, the only attempt made to produce a simple universal model has been the following empirical relationship (refs, 116, 117):

$$R = 0.202U_R - 0.606 \qquad (6.1)$$

and

$$U_R = [62.8/A^{1/2}] - [10^{-3}\ Ps^3/A] \quad (\text{for } P \geq 10 \text{ mTorr}) \qquad (6.2)$$

The model represents thickness uniformity for a horizontally mounted substrate positioned centrally above a vapour source, where R = uniformity parameter expressed in terms of the front to back thickness ratio ("front" being the substrate surface facing the source), A = substrate area facing the source (in cm^2), s is the source to substrate distance (in cms) and P is the argon pressure (in mTorr). This model was based on limited data and other variables were suggested in refs 116 and 117, such as deposition and

sputtering rates, which may also influence R values. Further testing of the model (ref 11) gave only partial verification; data available at that time were found to follow the expression:

$$R = R_o - 2 \times 10^{-4}\ Ps^3/A \quad (P \geq 10\ mTorr) \tag{6.3}$$

where R_o = parameter, characteristic of a particular system.

Subsequent trials on Equation (6.3) using data from this work (to be described later) has shown that the Ps^3/A relationship only holds over a very restricted range. A new model is therefore required which needs to be based on a more theoretical argument and have a wider range of applicability.

6.2 THICKNESS UNIFORMITY MODEL - ANALYSIS

Figure 6.1 illustrates schematically, the principal considerations of the new model. The evaporant flux emerges from the melt pool, consisting of atoms or molecules, with energies near to the melting temperature. For most evaporant materials, this initial thermal energy will be between 5 and 10 times that of the ambient scattering medium (low pressure inert gas). For example, titanium atoms will have initial energies in the order of 0.17 eV (1 eV ~ 11600 K, Ti melts at ~ 2000 K) compared with the ambient gas energy of 0.025 eV (290 K). Therefore, the initial flux energy will be about 7 times greater than the ambient gas. These figures should also be applicable to evaporation in a glow discharge plasma as the neutrals will be near to room temperature and the ions (of which there are relatively few, even in an enhanced discharge) will be at about 500 K (Section 3.2.2.1). The vapour emerges from the molten pool and will generally move in an upwards direction (due to initial interaction with the pool surface) with this initial energy.

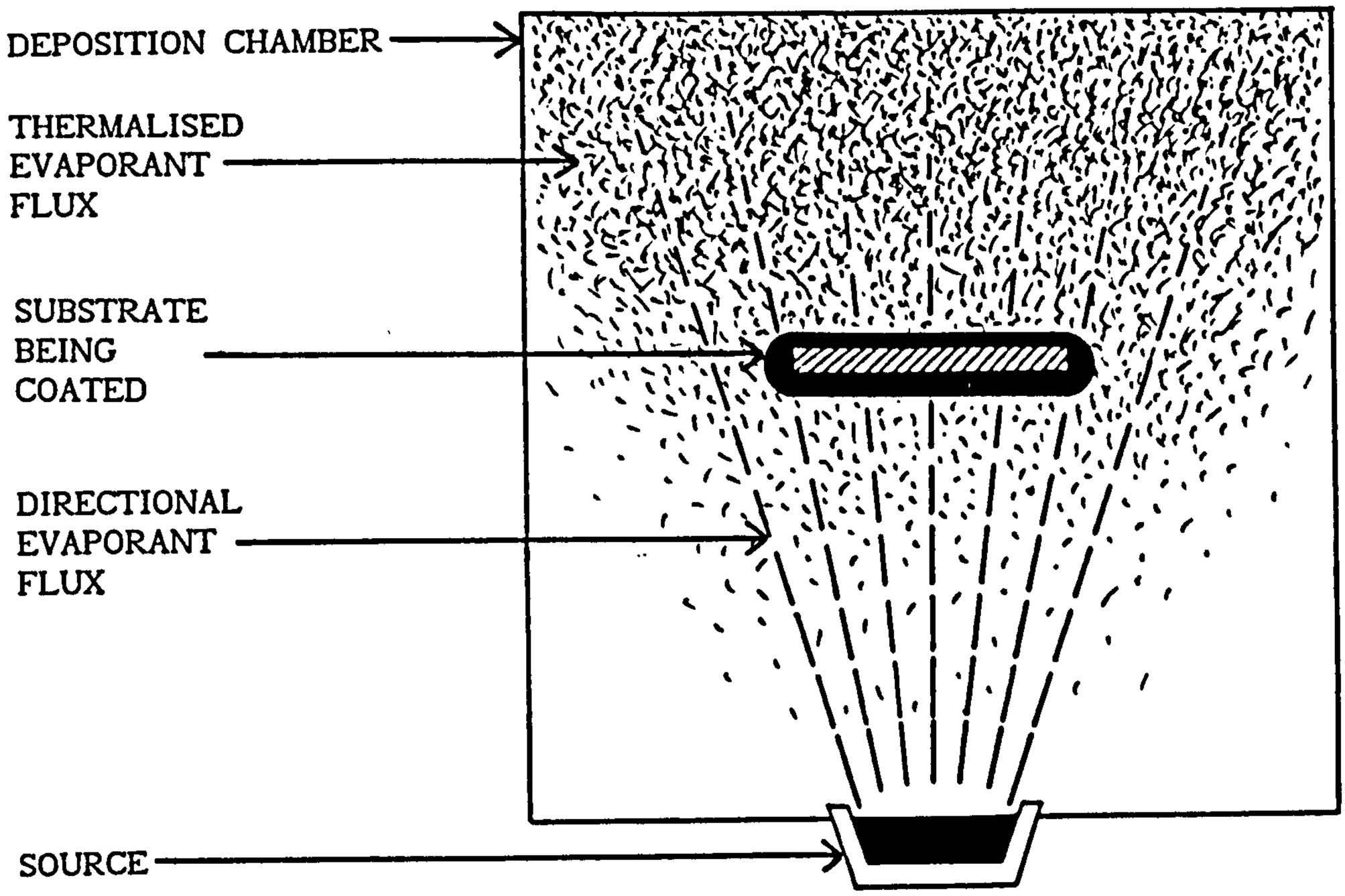

Figure 6.1 Illustration showing the principal considerations of the coating thickness uniformity model.

Collisions with the ambient gas atoms occur and at each interaction, the vapour will lose some of its energy. After a number of collisions, the vapour energy will have decreased to that of the ambient gas; ie, the vapour is thermalised.

The evaporant flux can thus be considered to have only two components, (i) the non-thermalised vapour, which is assumed to move in an upwards direction only ("directional" in Figure 6.1) and (ii) the thermalised vapour, which has been scattered to the point of thermal equilibrium with the ambient gas and therefore has no preferential direction of motion. Therefore, only the thermalised component can make a contribution to coating the back face of a flat horizontally mounted substrate.

Figure 6.2 illustrates the approach of the model in more detail. As front and back thicknesses on thin flat horizontal substrates are being considered, then the vapour flux motions can be resolved into only two directions, ie, upwards and downwards. From consideration of simple collision probability principles, the proportion of non-thermalised flux must decrease exponentially with distance from the source, thus the thermalised component must correspondingly increase as a (1 - exponential) function. Hence substrates positioned further from the source will have improved thickness uniformity as the proportion of thermalised vapour increases. It should be noted that progressive dilution of the total vapour flux with increasing distance will also occur. This will decrease the coating thickness in absolute terms for samples positioned further from the source, as shown by the coated substrate illustrations in Figure 6.2. It is assumed that the chamber dimensions are large compared with the substrates so that the walls have no influence on vapour flux motion. Representing the argument mathematically:

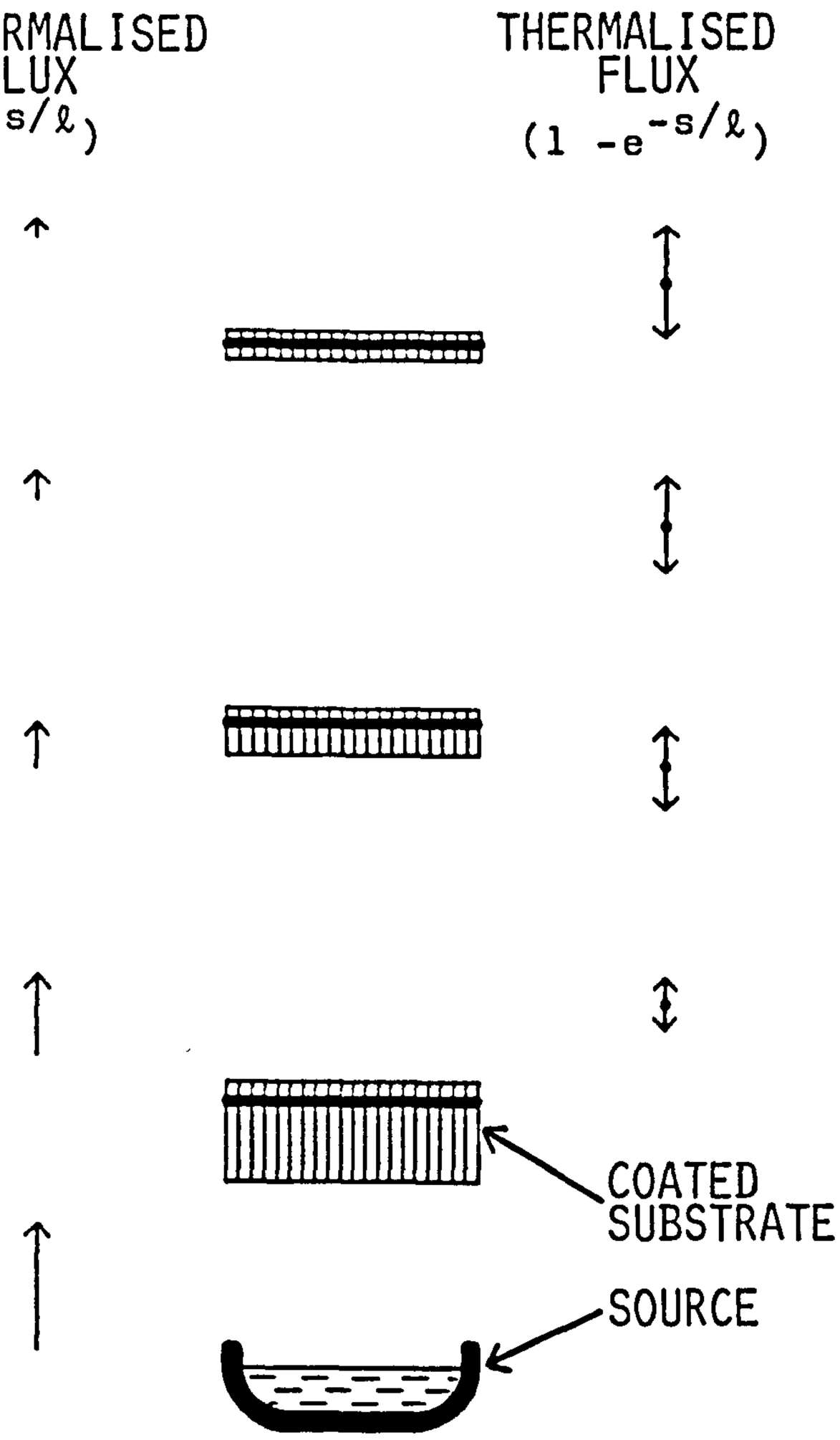

Figure 6.2 Schematic showing how the relative proportions of non-thermalised and thermalised vapour fluxes influence the coating thickness uniformity of thin flat substrates as a function of source to substrate distance.

$$\text{Non-thermalised flux moving upwards} = \psi e^{-s/\ell} \tag{6.4}$$

where s = source to substrate distance, ℓ = associated mean free path, and ψ = a function of s to account for the progressive dilution of the vapour flux.

$$\therefore \text{ Vapour scattered out and thermalised} = \psi\,(1-e^{-s/\ell}) \tag{6.5}$$

As the thermalised vapour has no preferential direction, then on average, half of this component must be moving upwards and the other half moves downwards, ie

$$\text{Thermalised component moving upwards} = \frac{1}{2}\,\psi\,(1-e^{-s/\ell}) \tag{6.6}$$

$$\therefore \text{ Total vapour moving upwards} = \psi\, e^{-s/\ell} + \frac{1}{2}\,\psi\,(1-e^{-s/\ell})$$

$$= \frac{1}{2}\,\psi\,(1+e^{-s/\ell}) \tag{6.7}$$

$$\text{The total vapour moving downwards} = \frac{1}{2}\,\psi\,(1-e^{-s/\ell}) \tag{6.8}$$

Assuming that the front to back thickness ratio, R, is dependent only upon vapour flux arrival rates, then dividing Equation (6.7) by (6.8) gives:

$$R = \frac{1 + e^{-s/\ell}}{1 - e^{-s/\ell}} = \coth\,(s/2\ell) \tag{6.9}$$

Equation 6.9 is thus a simple model equating thickness uniformity with source to substrate distance and an associated mean free path. Transposing this equation gives:

$$\ell = \frac{s}{-\ell n\left[\frac{R-1}{R+1}\right]} \qquad (6.10)$$

Equation 6.10 allows the model to be empirically validated from measurements of R at various s values. Plots of s versus $-\ell n[(R-1)/(R+1)]$ should yield linear relationships with gradients equal to ℓ.

6.3 MODEL VALIDITY TESTS - EXPERIMENTAL

6.3.1 Coating Deposition

Coating trials using rig (1) were performed to test the model under various conditions. The main benefit from using rig (1) for this work, was in the use of the capacitance-manometer for accurate pressure measurement. Usually, four samples were coated in each run, the samples being thin flat plates mounted at various heights above the source. The jig supporting the samples was a vertically mounted rod, positioned centrally above the source. The samples were fitted in horizontal slots cut into the rod so that masking effects caused by supporting the samples were minimised. Also, the samples were positioned about the rod axis to prevent one sample occluding the directional vapour to another sample.

The substrate materials used were either copper or glass, the choice of material depending on the type of coating produced. For example, a colour difference between coating and substrate was preferable to facilitate ball crater thickness measurements (as described in the following section); very smooth substrate materials such as glass enabled sub-micron thickness coatings to be measured with reasonable accuracy. The copper samples were ground and polished on successively finer grades of carborundum paper, down to 800 grit size, to make them suitably smooth for coating thickness

measurements. Generally, the coating procedure was as follows:

(i) Clean substrates with acetone, mount on jig

(ii) Weigh source material, prepare rig for run, pump down

(iii) Sputter clean for about 20 minutes

(iv) Set up ambient gas (argon) pressure and monitor for 5 minutes, taking pressure readings every minute.

(v) Evaporate under gas evaporation (no discharge) or ion plating conditions for about 20 minutes with no gas flow adjustment.

(vi) After evaporation, monitor ambient gas pressure for 5 minutes, taking pressure readings every minute. These readings and those from (iv) were used to estimate the mean and standard deviation values of ambient gas pressure during coating.

(vii) Allow samples to cool, vent chamber, remove samples and weigh the source material to evaluate the amount evaporated.

At the time that these runs were performed, rig (1) was set up for RF ion plating work on another project. Thus all discharges used for sputter cleaning and ion plating utilised the RF facility, in the work reported here. As the primary interests in this chapter were to investigate the influence of gas scattering phenomena, it is of little consequence. Details of the RF facility are given in ref 11.

6.3.2 Coating Thickness Measurement

There are a number of relatively simple methods for evaluating coating thickness, such as (a) using a mask during coating and measuring the resulting step thickness with a profilometer; (b) weighing the sample before and after deposition to evaluate the mass deposited, thickness being estimated knowing the sample area and coating material density; (c) measuring thickness directly from the cross section of a fractured sample on

a scanning electron microscope. None of these methods are particularly accurate. Method (a) requires a well fitting mask to obtain a good step profile and etching of the sample surface during the sputter cleaning stage will make the measured thickness smaller than the true thickness. Field effects around the mask during ion plating can also cause localised changes in coating thickness. Method (b) requires an accurate determination of the film density. In practice, the density will be less than the bulk value and it will depend upon the process parameters used. As with (a), material loss during sputter cleaning may also cause some error. Method (c) suffers from uncertainties in the viewing angle and, to a lesser extent, magnification errors.

An accurate, reliable technique was required to measure coating thickness over a wide range (< 1 to 100 μm), where systematic errors would be negligible and random errors could be readily estimated. The ball cratering method was therefore used. This involves eroding a small crater through the coating surface and into the substrate using a spinning steel ball. The crater dimensions are then measured to give the coating thickness. Although ball cratering has been used for obtaining Auger depth profiles (eg ref 118), the technique was only recently investigated in any detail for thickness determination (ref 119). Further evaluations of the method (ref 11) have shown that there is good agreement between this technique and thickness measurements from electron microscopy, over the range studied (1 - 100 μm).

Figure 6.3 shows the principle of the ball crater method. The ball is driven by a rotating shaft and a low viscosity abrasive solution aids smooth running and rapid erosion of the sample surface. Measuring the crater geometry x and y yields the coating thickness, t, from the equation:

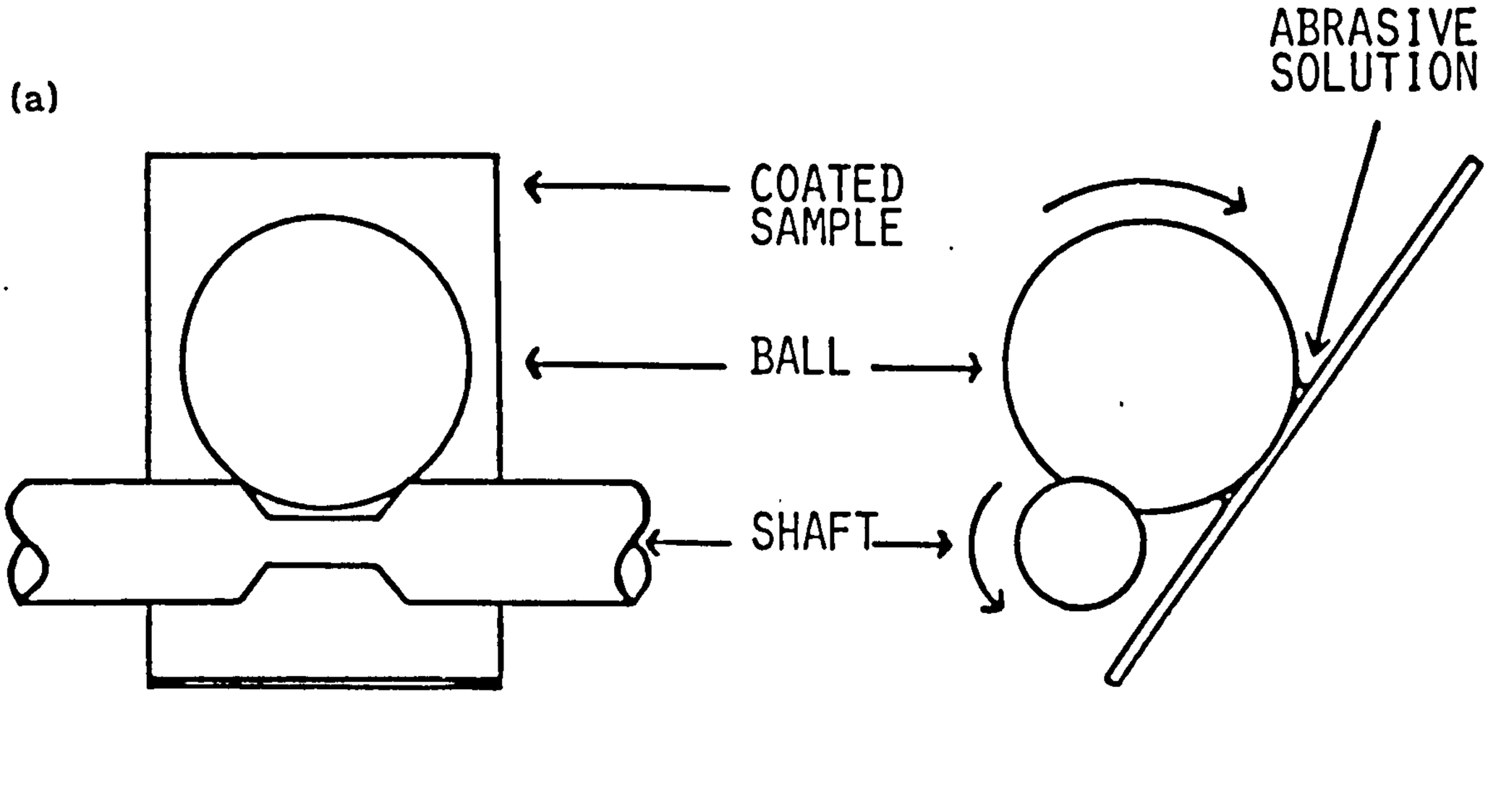

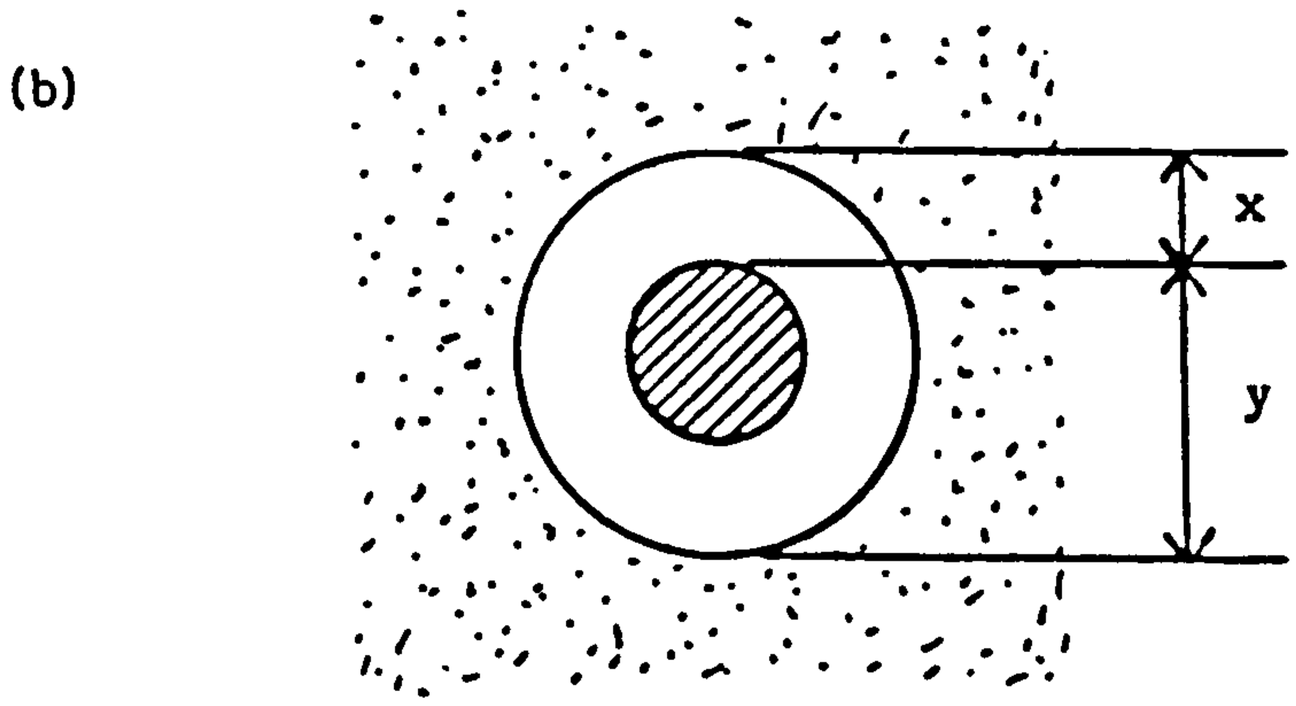

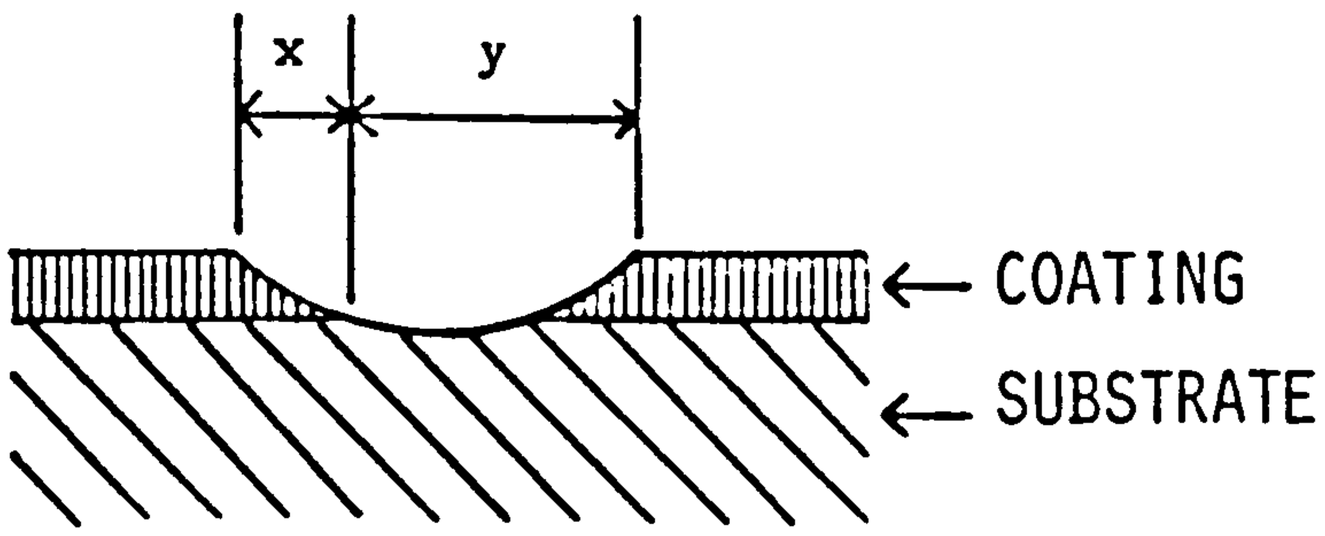

Figure 6.3 (a) Principle of the ball crater method for measuring coating thickness. (b) Plan and cross section of resulting crater. (after ref 11).

$$t = xy/D \qquad (6.11)$$

where D is the ball diameter. The ball cratering machine used in this work had a variable speed motor driven shaft. A 2.54 cm diameter steel ball was used and this was driven at speeds of 100 to 500 revs/minute. The abrasive solution consisted of 1 μm diamond particles in a kerosene base. Erosion times varied between a few seconds to tens of minutes, depending on coating thickness and wear characteristics. The sample was then washed with acetone to remove debris. A Shinko Profilometer with x100 magnification was used as a travelling microscope to measure crater geometry. A minimum of four determinations of thickness were made on each crater (measurements taken in four orientations) to evaluate the mean and standard error (std. deviation/(no. of data points)$^{1/2}$). In most cases, more than one crater on each face was required and up to 12 craters were made, if (i) the coating was very thin and thus more difficult to measure, (ii) the front to back thickness ratio, R, was near to unity (because an error in R becomes greatly magnified in the log function in Equation 6.10 as R approaches unity), (iii) the crater quality or symmetry was poor, due to poor coating adherence or irregular sample surfaces. In all cases however, thickness was measured at or very close to the centre of each sample face.

6.4 MODEL VALIDITY TESTS - RESULTS AND OBSERVATIONS

6.4.1 Thickness Uniformity with Source to Substrate Distance

6.4.1.1 Ambient gas pressure and ionisation conditions

Figure 6.4 shows plots of s versus $-\ell n$ [(R-1)/(R+1)] for 3 x 3 x 0.1 cm copper substrates coated with titanium. Four samples per run were coated by gas evaporation, under different argon pressures (Figs 6.4 a-c) and also

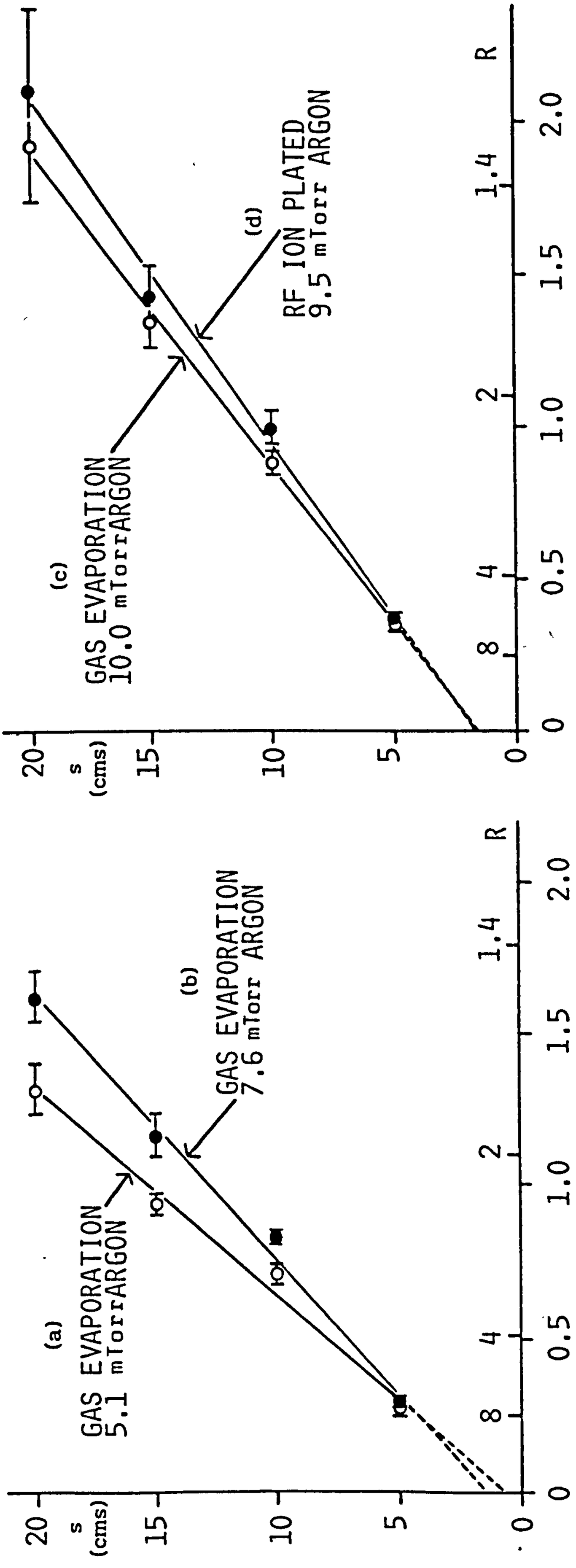

Validity tests on the thickness uniformity model; plots (a) to (d) are from Runs U1 to U4 respectively. The error bars are derived from the standard errors in the original coating thickness data.

Figure 6.4

under ion plating conditions (Fig 6.4d). The solid lines are least square fits to the data and linearity is good in all cases, indicating that Equation 6.10 is valid and the thickness uniformity model is verified for these conditions. The relevant data is given in Table 6.1.

RUN	PROCESS DETAILS				EQN. 6.10 - LIN.REG.		
	ARGON PRESS. (mTorr)		MEAN EVAP. RATE(g/min)	TYPE[2]	CORR. COEFF.	INT. (cms)	ℓ (cms)
	MEAN	S.D.[1]					
U1	5.13	0.11	0.188	G.E.	0.9942	+0.51	14.84
U2	7.58	0.13	0.180	G.E.	0.9964	+1.42	11.42
U3	9.99	0.32	0.143	G.E.	0.9992	+1.63	9.67
U4	9.48	0.57	0.130	I.P.	0.9968	+1.73	8.82

(1) S.D. = standard deviation of the argon gas pressure from readings taken immediately before and after the deposition process. Provides a measure of the drift in ambient gas pressure during deposition.

(2) G.E. = gas evaporation. I.P. = ion plated (RF discharge).

Table 6.1 Validity tests on the thickness uniformity model, using 3 x 3 x 0.1 cm substrates under different process conditions.

The following observations can be made from these results:

(i) Extrapolation of the regression line to the y-axis gives a positive intercept in all cases. The intercept value increases from 0.5 to 1.7 cms with increasing ambient gas pressure. This could be a "virtual source" effect, first reported by Smith (ref 120), who attributed the

phenomenon to being caused by a "viscous cloud" above the source from the relatively high local density of evaporant material. Thus, even under vacuum evaporation conditions (no ambient gas), mutual scattering of the evaporant flux can occur which raises the location from where the vapour appears to originate. The results in Figure 6.4 and Table 6.1 suggest that the virtual source height is also influenced by ambient gas pressure.

(ii) Figures 6.4 a-c show that increasing the ambient gas pressure decreases the gradient value for otherwise similar experimental conditions. This means that the associated mean free path, ℓ, is reduced as pressure is increased, which concurs with the general principles of simple collision theory.

(iii) Figure 6.4d shows a smaller gradient value than 6.4c, indicating a slight improvement in thickness uniformity for the ion plated coatings when compared with those produced by gas evaporation under similar conditions.

The additional influences of bombardment from the discharge on front to back thickness ratios will be discussed in Section 6.5.1.1.

6.4.1.2 Substrate area and aspect ratio

Table 6.2 summarises the process parameters and results obtained from Equation 6.10 for 0.1 cm thick copper substrates, gas evaporated with titanium (argon pressure ~ 10 mTorr). Four identical substrates were used in each run, mounted at 5, 10, 15 and 20 cms above the source, as in the previous section. Figure 6.5 shows plots of s versus $-\ell n[(R-1)/(R+1)]$ for these runs.

The model assumes that front to back thickness ratio is independent of substrate area, provided the area is small compared with deposition chamber

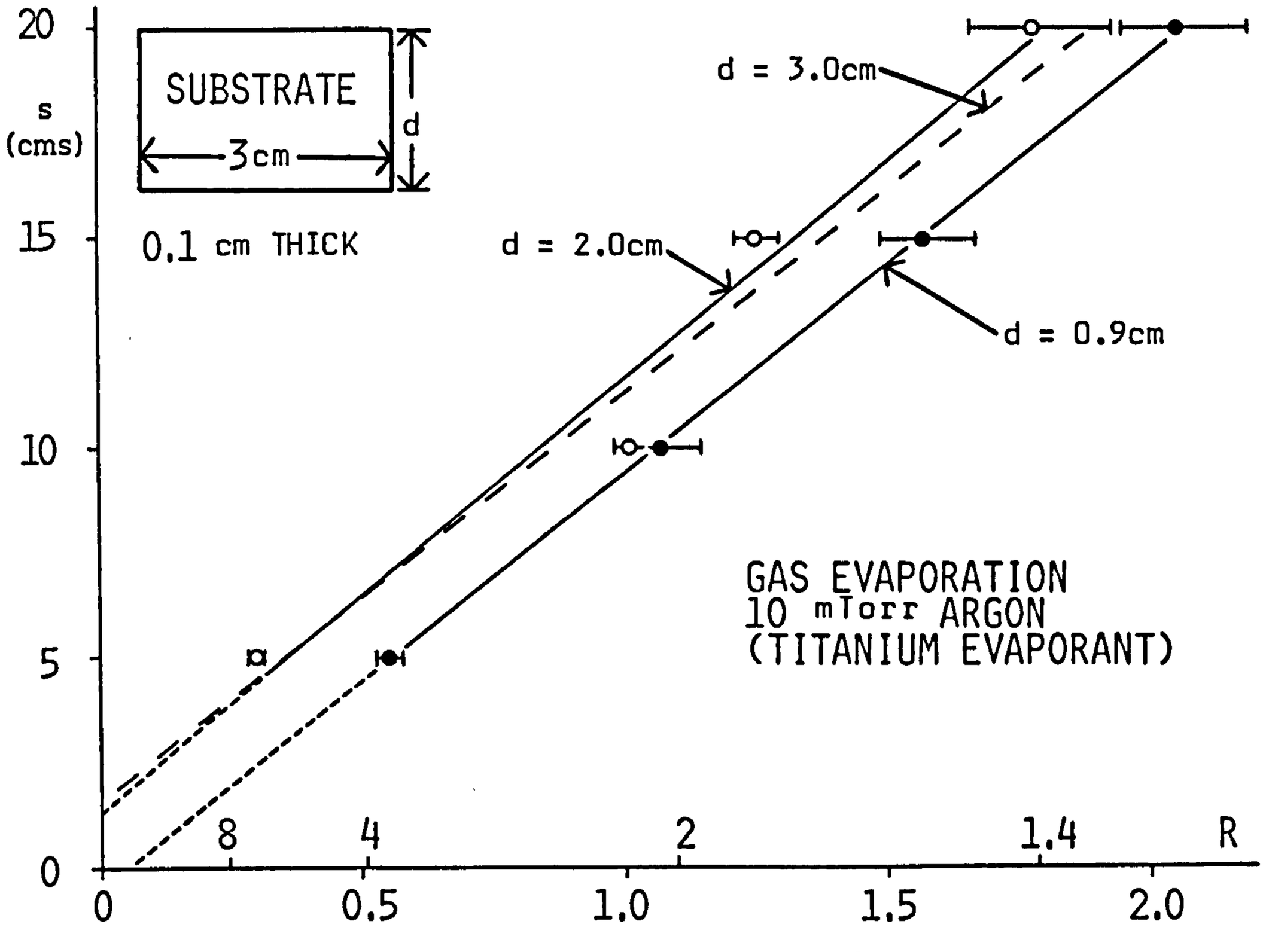

Figure 6.5 Validity tests on the thickness uniformity model for substrates of different width, d: Run U3, d = 3 cms; Run U5, d = 2 cms; Run U6, d = 0.9 cms. Data points for Run U3 have been omitted for clarity.

dimensions. The results in Table 6.2 and Figure 6.5 appear to confirm this

RUN	SUBSTRATE		PROCESS DETAILS			EQN 6.10 -LIN.REG.		
	DIMENSIONS (cms)	ASPECT RATIO	ARGON PRESS. (mTorr) MEAN	S.D.	MEAN EVAP. RATE (g/min)	CORR. COEFF	INT (cms)	ℓ (cms)
U3	3 x 3	1.0	9.99	0.32	0.143	0.9992	+1.63	9.67
U5	3 x 2	1.5	10.19	0.25	0.140	0.9836	+1.29	10.32
U6	3 x 0.9	3.3	10.44	0.31	0.113	0.9999	-0.61	9.98

Table 6.2 Validity tests on the thickness uniformity model for small substrates of different areas and rectangular aspect ratios.

assumption, in that (i) the correlation coefficients are high, indicating that Equation 6.10 is valid and (ii) the gradient, ℓ, in all three runs is similar. The intercept values for Runs U3 and U5 are comparable within the limits of repeatability, though Run U6 shows a negative intercept. This negative value might imply that either there was no virtual source effect or significant burrowing of the melt had occurred. Inspection of the melt after this run showed no burrowing effects and although the slightly lower evaporation rate in this run may have had some influence, the absence of a virtual source is unlikely when the results from other runs are considered. Aternatively the result may be indicative of the model breaking down when substrates with very small dimensions are used and this is discussed in Section 6.5.1.3.

6.4.1.3 Evaporant material

Figure 6.6 shows plots of the model validity test for three different source materials under gas evaporation at about 10 mTorr argon pressure.

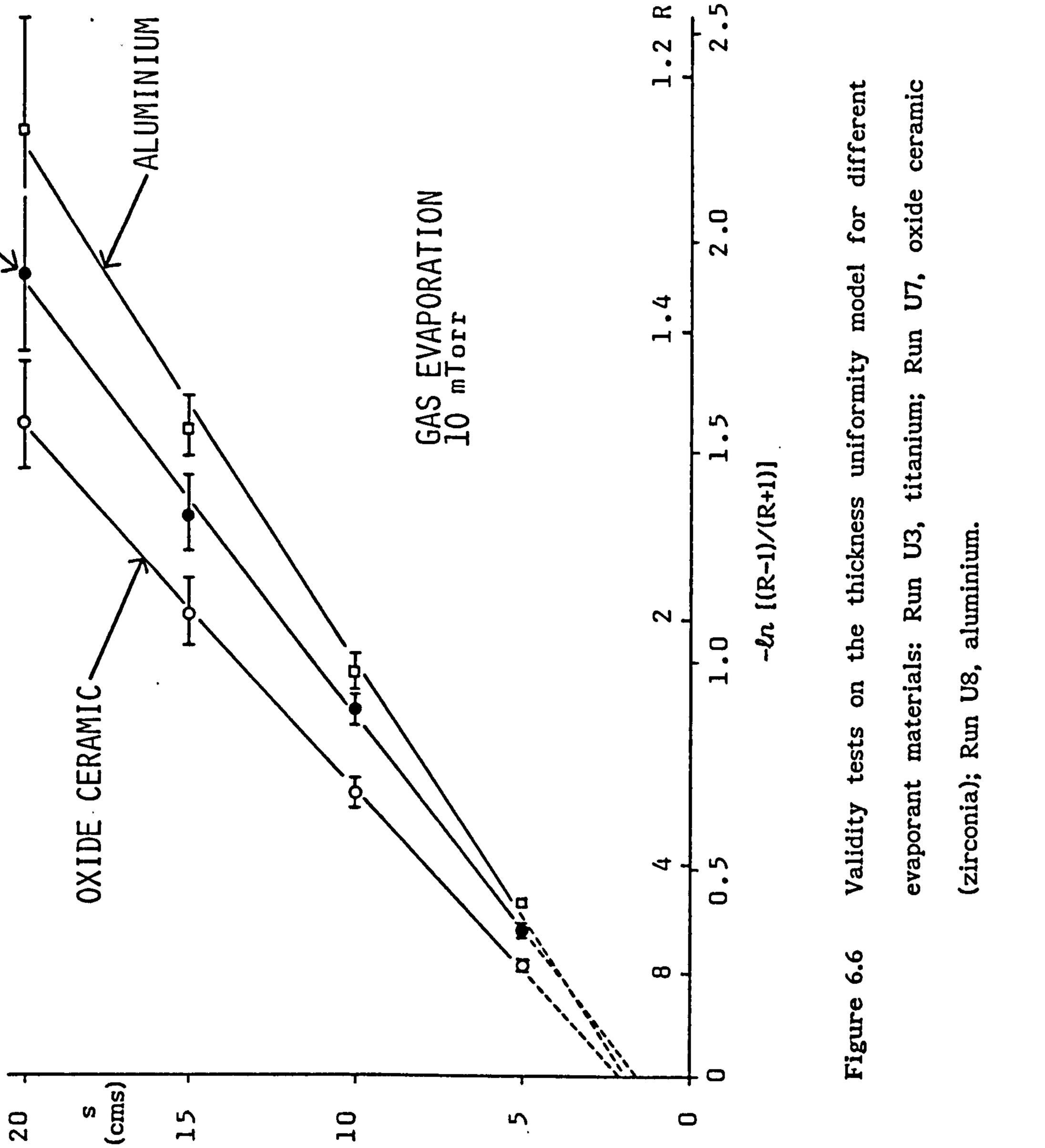

Figure 6.6 Validity tests on the thickness uniformity model for different evaporant materials: Run U3, titanium; Run U7, oxide ceramic (zirconia); Run U8, aluminium.

The substrates were 3 x 3 x 0.1 cm copper samples and Table 6.3 gives the relevant data. Linearity in all three runs is good, indicating that the model is valid for different source materials, including compounds such as zirconia, where dissociation of the material is to be expected ($ZrO + O_2$) in the vapour phase (eg, ref 26).

RUN	PROCESS DETAILS				EQN.6.10 - LIN. REG.		
	ARGON PRESS. (mTorr)		MEAN EVAP.	SOURCE	CORR.	INT.	ℓ
	MEAN	S.D.	RATE(g/min)	MATERIAL	COEFF.	(cms)	(cms)
U3	9.99	0.32	0.143	TITANIUM	0.9992	+1.63	9.67
U7	9.95	0.15	0.026	ZIRCONIA	0.9998	+2.08	11.50
U8	9.97	0.05	0.050	ALUMINIUM	0.9983	+1.88	8.15

Table 6.3 Validity tests on the thickness uniformity model for 3 x 3 x 0.1 cm substrates using different source materials.

It is interesting to note that (i) the gradient, ℓ, increases as the atomic or molecular weight of the source material is increased and (ii) materials other than titanium exhibit virtual source effects.

6.4.1.4 Evaporation rate

Figure 6.7 and Table 6.4 gives results for gas evaporation of aluminium at 10 mTorr argon pressure for two different evaporation rates. The larger source to substrate distances used in Run U9 (up to 35 cms) produced thinner coatings with front to back thickness ratios nearer to unity. This tended to increase the errors in evaluating the coating

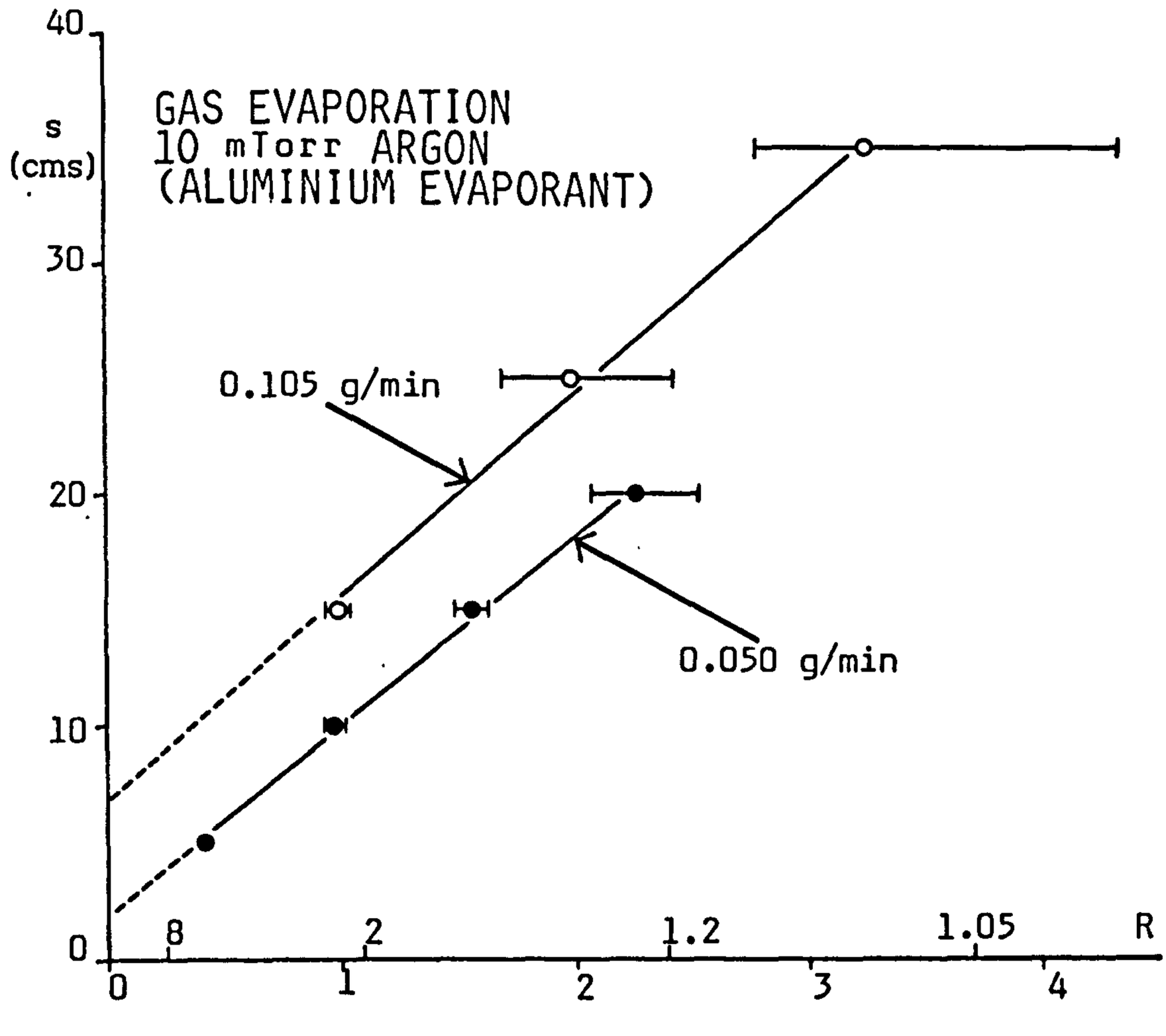

Figure 6.7 Validity tests on the thickness uniformity model for evaporation at different rates: Run U8, 0.050 g/min; Run U9, 0.105 g/min.

thicknesses, as shown by the larger error bars in Figure 6.7. The problem was reduced to some extent by using glass microscope slides as substrates, their smooth surfaces facilitating sub micron thickness measurement, as reported in Section 6.3.1.

RUN	SUBSTRATE MATERIAL AND DIMENSIONS (cms)	PROCESS DETAILS			EQN. 6.10 - LIN. REG.		
		ARGON PRESS. (mTorr)		MEAN EVAP. RATE (g/min)	CORR. COEFF.	INT (cms)	ℓ (cms)
		MEAN	S.D.				
U8	COPPER, 3x3x0.1	9.97	0.05	0.050	0.9983	+1.88	8.15
U9	GLASS, 7.5x2.6x0.1	10.35	0.38	0.105	0.9974	+6.78	8.81

Table 6.4 Validity tests on the thickness uniformity model for gas evaporation of aluminium at different evaporation rates.

The results show that although ℓ does not change significantly, the virtual source height appears to increase as evaporation rate is increased. Clearly, this is due to the viscous cloud above the source becoming larger at the higher rate. The data also shows that the model is valid for source to substrate distances greater than the maximum value of 20 cms used in runs preceding Run U9.

6.4.2 Variation of the Mean Free Path, ℓ, With Argon Pressure

6.4.2.1 Results from this work

If the gradient, ℓ, determined from Equation 6.10 is a mean free path length, then ℓ should be inversely proportional to the number density or pressure of the ambient gas. Therefore a plot of argon pressure versus $1/\ell$

should yield a linear relationship. Figure 6.8 shows the values for ℓ and argon pressure plotted in this form from Runs U1, U2 and U3 (data in Table 6.1). Although there are only three data points, the uncertainties in the ℓ values are sufficiently small (as they are results of regression analyses) to indicate that the relationship in Figure 6.8 is linear. It is interesting to note that the linear regression of this data (denoted by the solid line) gives a significant negative intercept value. This implies that finite, rather than infinite, front to back thickness ratio values would have resulted, if a run with no ambient gas present had been performed. The most probable explanation for this effect can be attributed to collisions between evaporant flux particles which thus creates a mutual scattering effect. Clearly, this phenomenon must be related to the evaporant flux density, thus very low evaporation rates and/or large source areas may not exhibit this effect. It must also be synonymous with the virtual source phenomenon reported earlier.

From the thickness uniformity model analysis in Section 6.2, the mean free path, ℓ, should be a measure of the distance travelled by an evaporant flux particle before becoming thermalised. Therefore, the gradient of the data from the titanium gas evaporation runs in Figure 6.8 should correspond to the pressure-distance product of thermalisation at 300 K (ambient gas temperature) for titanium atoms initially at about 2000 K (Ti melting point). Precise data on thermalisation distances of energetic particles in ambient gases does not appear to be available, particularly over the range of interest in this work. However, a Monte-Carlo computer model of the thermalisation of energetic atoms in sputtering processes has been published by Somekh (ref 121), Data from his model permits the evaluation of the pressure distance product for 2000 K argon atoms becoming thermalised in ambient argon at 300 K. As the atomic masses of argon and titanium are 40

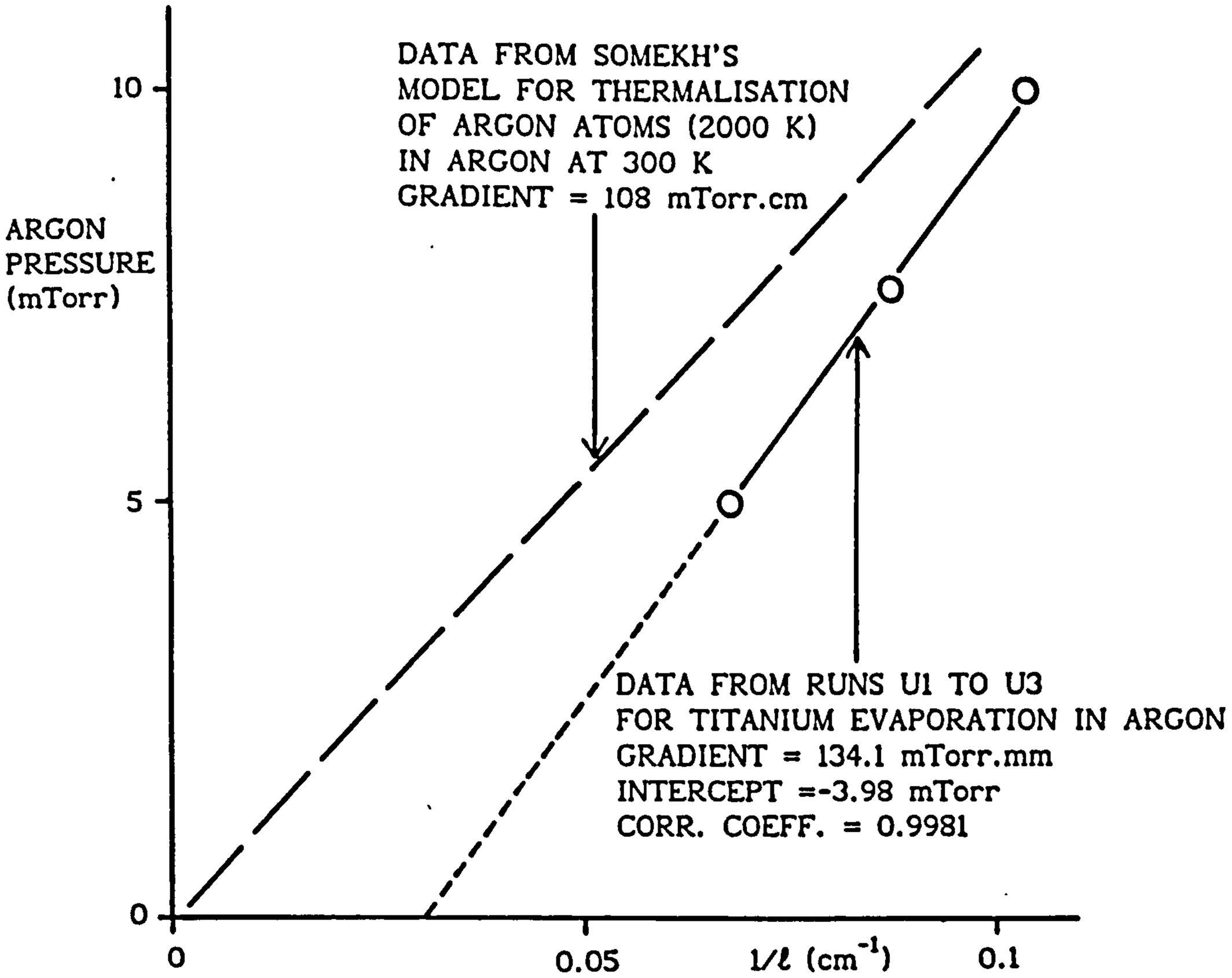

Figure 6.8 Plot showing a linear relationship between argon pressure and $1/\ell$ for data from Runs U1 to U3. Also shown (dashed line) is thermalisation mean free path data evaluated from Somekh's model (ref 121). Note the comparable gradients.

and 48, then the results for argon in argon from ref 121 should be similar to the titanium in argon data from this work. The dashed line in Figure 6.8 shows the argon data evaluated from Somekh's model and the gradient is in fact comparable to the regression line from the titanium results. This provides some evidence that ℓ is primarily associated with the mean free path for thermalisation.

6.4.2.2 Results evaluated from published data

No suitable data has been found from published sources to test the validity of Equation 6.10 in terms of results for R as a function of s. There are however, published results from which front to back thickness ratios can be obtained at fixed source to substrate distances for different argon pressures. Knowing the distance s and the ratio R enables ℓ to be predicted from Equation 6.10. Thus plots of argon pressure versus $1/\ell$ should yield linear relationships if the thickness uniformity model is valid. This analysis is only approximate however, because virtual source effects cannot be evaluated. Predictions for ℓ from Equation 6.10 will thus be larger, particularly at small s values. Figure 6.9 shows data evaluated from published sources in this form and Table 6.5 provides further information, including relevant data from this work (Runs U1 to U3), for comparison.

The following observations can be made from Figure 6.9 and Table 6.5:

(i) All four plots show no systematic deviations from linearity, though significant scattering about the regression lines is apparent. The scatter can be attributed to random experimental errors which are unknown, except for the data from refs 116 and 117. Systematic errors could also have a significant effect on the gradient and intercept values obtained from published data. These include, argon gas pressure measurements, coating thickness measurement, source to

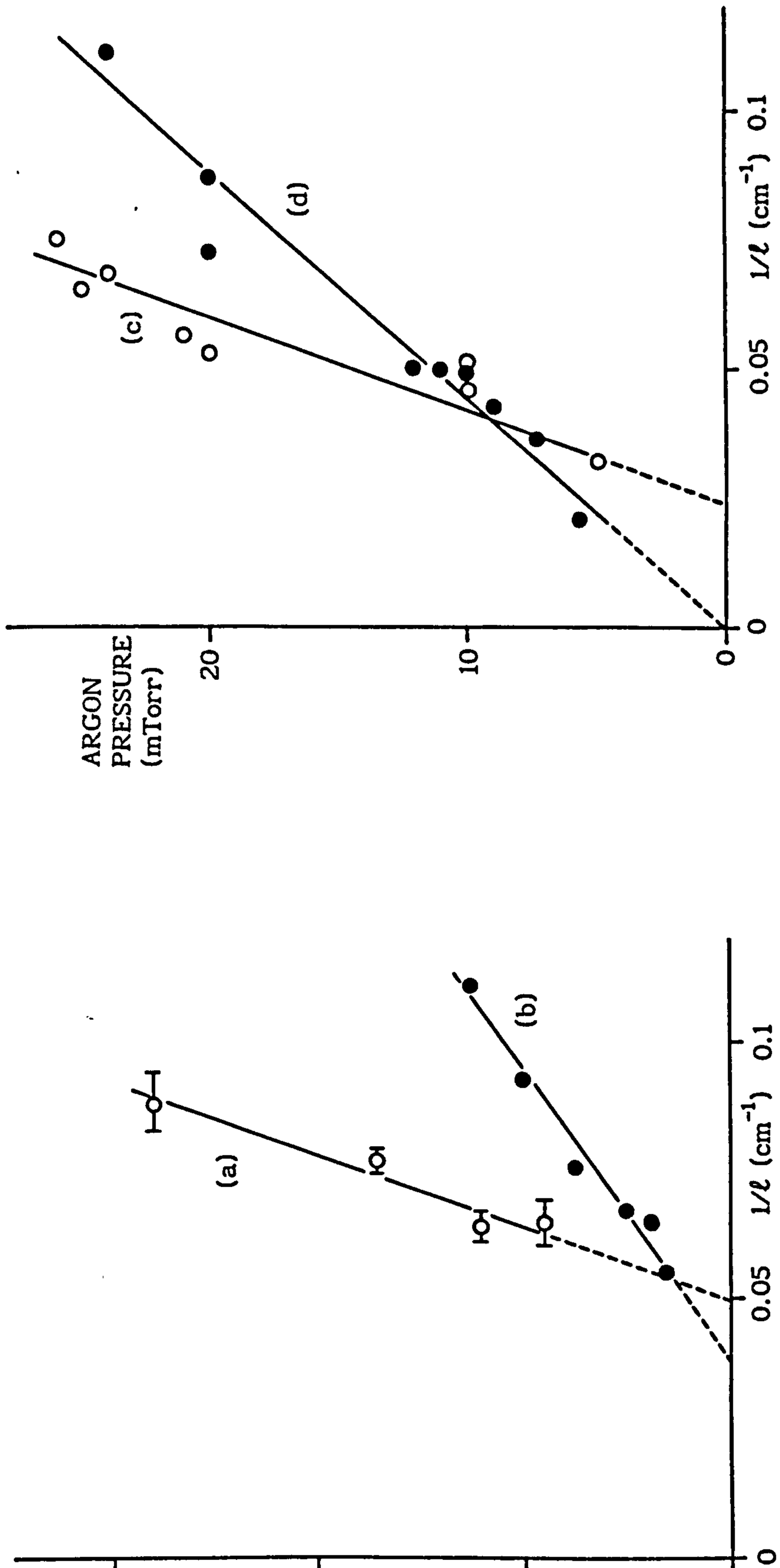

Figure 6.9 Plots showing linear relationships between argon pressure and $1/\ell$ using data from published sources in the thickness uniformity model: (a), from refs 116 and 117; (b) from ref 122; (c) from ref 123 (cylindrical substrates); (d) from refs 103 and 123.

REF	SUBSTRATE DIMENSIONS (cms)	PROCESS DETAILS EVAPORATION SOURCE	SOURCE MATERIAL	s (cms)	TYPE	ARGON PRESS. vs 1/ℓ LIN.REG. CORR. COEFF.	INTERCEPT (mTorr)	GRADIENT (mTorr.cms)
THIS WORK	3x3x0.1	EB GUN	TITANIUM	5 to 20	G.E.	0.9981	-3.98	134.1
116, 117	3x3x0.012	RESISTIVE	ALUMINIUM	10.0	I.P.	0.9729	-71.86	143.6
122	4x4x0.2	EB GUN	?	15.2	I.P.	0.9845	-13.70	355.7
103, 123	5.08x1.78x0.11	EB GUN	GOLD	16.5	I.P.	0.9712	-0.03	227.6
123*	1.91dia.,2.28Len.	EB GUN	GOLD	16.5	I.P.	0.9217	-12.82	546.2

ALL ION PLATED RUNS WERE UNDER DC DIODE CONDITIONS

* CYLINDRICAL SUBSTRATE, ORIENTATION UNKNOWN

TABLE 6.5 DETAILS OF THE TESTS PERFORMED TO INVESTIGATE THE SUGGESTED LINEAR RELATIONSHIP BETWEEN ARGON PRESSURE AND 1/ℓ .

substrate distance and virtual source effects, possible shadowing effects due to substrate jigging arrangements, and also ionisation conditions (as discussed in Section 6.5.1.1.). Notwithstanding these factors, the relationships show a reasonable degree of linearity, which gives further evidence that the model is universally applicable.

(ii) The results from refs 116 and 117 (Figure 6.9 (a)) show a particularly steep gradient and large negative intercept value. The steep gradient may have resulted from any of the systematic error sources listed above. In more specific terms, the relatively short source to substrate distance (10 cms) and unknown virtual source effects coupled with large cathode sheath thicknesses (which would be expected in DC diode ion plating), may have played a significant role in reducing the change in ℓ with argon pressure. If the large negative intercept can be attributed entirely to evaporant flux mutual scattering effects, then the evaporation rate for this particular run must have been unusually high in relation to the other results in Table 6.5. However, this may have been the case, because resistive evaporation was used. A charge of about 0.4 g was evaporated within one minute (ref 116) so that the lowest evaporation rate would have been ~ 0.4 g/min. This is 2 to 3 times greater than rates for titanium used in this work (Table 6.1). In practice though, effective evaporation rates from the work in refs 116 and 117 may have been considerably higher with that type of source, ie, approaching what is commonly termed as "flash evaporation" conditions.

(iii) Curves (c) and (d) in Figure 6.9 show different slopes and intercepts for similar runs; the only known difference between these runs is that cylindrical, rather than thin flat substrates, were used for the data in (c). It may be assumed from the intercept value in Figure 6.9 (d)

that mutual scattering effects from the evaporant flux were extremely low. These results therefore show that substrate geometries which do not approximate to thin flat plates will alter the characteristics predicted by the thickness uniformity model.

6.5 DISCUSSIONS AND FURTHER DEVELOPMENTS

6.5.1 Uncertainties and Limitations in the Thickness Uniformity Model

6.5.1.1 Ionisation effects

The model described in this chapter has been derived with the assumption that front to back coating thickness ratios are dependent only on the directionally resolved motions of thermalised and non-thermalised vapour fluxes. However, it is clear that the presence of a glow discharge can significantly change the characteristics of a depositing coating. Figure 6.10 highlights two of the main effects which could influence the resulting thickness ratio under ion plating conditions, in comparison with gas evaporation.

Figure 6.10b shows how uniformity could be made worse; the coating flux arrival rate on the back surface is less than that at the front, whereas the bombardment rate from the plasma could be assumed to be similar at both surfaces under certain discharge conditions. The net result is that the ratio between plasma bombardment and vapour flux incidence rates is greater on the back than on the front face. This results in a proportionally greater sputter removal rate and increased coating densification on the back, making R larger than under gas evaporation conditions. This effect has been observed between RF ion plated and gas evaporated coatings for experimental thermal barrier applications (refs 11, 12).

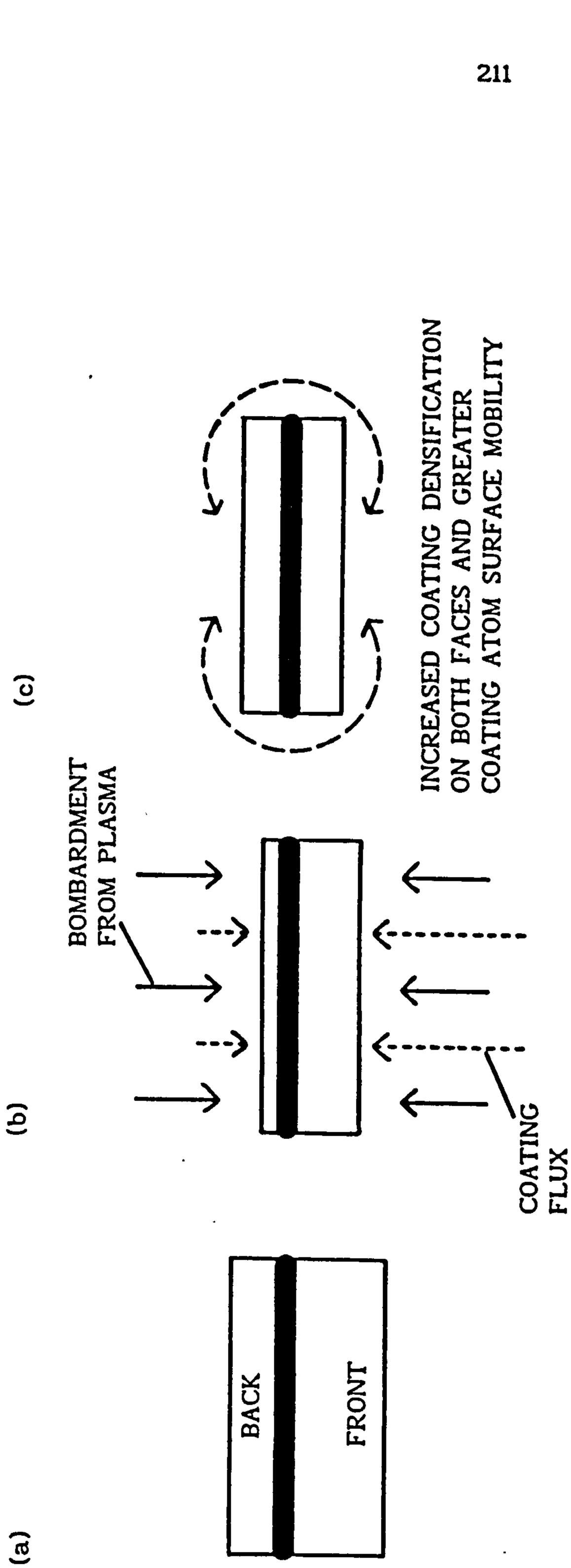

Figure 6.10 Influence of ionisation effects on the front to back coating thickness ratio, R:

(a) Gas evaporation, $R = R_z$

(b) Ion Plating, $R > R_z$ (worse uniformity)

(c) Ion Plating, $R < R_z$ (better uniformity)

Figure 6.10c shows how thickness uniformity could be improved. Here, the plasma bombardment significantly enhances coating densification on both faces and atom surface mobility is increased to a point where coating material may be transferred from one face to the other. Thus R becomes smaller than under gas evaporation conditions.

In a real ion plating environment, all of the effects described above are likely to occur and whether R is increased or decreased due to the presence of a discharge will obviously depend on which factors are predominant. It is apparent from Figure 6.4 c-d that the RF ion plated results in this work (Run U4) indicate that the effects illustrated in Figure 6.10c have been dominant here. Although the model has not been investigated with DC thermionic triode discharges, the observed exponential fall off in bombardment effects with distance and anisotropic phenomena reported in Chapter 4 will also have some influence. However, as suggested in Section 4.4.2, positioning the thermionic emitter close to the vapour source would tend to reduce potential variations in the ratio between plasma bombardment and vapour arrival rates. Thus under these conditions, R might be expected to be closer to the gas evaporation values in comparison with other discharge configurations.

Another phenomenon which may influence the front to back coating thickness ratio is the size of the cathode sheath region surrounding the sample. When the vapour flux reaches the plasma-sheath boundary, the proportion of vapour which is ionised will accelerate across the sheath with energies far greater than those assumed in the model. Thus, scattering phenomena based on thermalisation effects outlined in the model are inappropriate within the sheath region; the vapour ions and any resulting high energy neutrals from charge exchange and other interactions will tend to follow straight paths to the substrate. If the vapour flux is metal,

then most of the arriving coating material is likely to be ionised, as reported in Chapters 3 and 5, making the effects described above more probable. Such influences may only become significant however, if the sheath thickness is large compared with the substrate or the source to substrate distance; eg, the result of argon pressure versus $1/\ell$ in Figure 6.9a, as discussed in Section 6.4.2.2. Modern ion plating systems with enhanced discharges, where sheath thicknesses are in the order of a few millimeters are unlikely to exhibit deviations from the model arising from this effect.

6.5.1.2 Composition of the vapour flux and thermalisation distances

The comparable pressure-distance products for thermalisation shown in Figure 6.8 for argon neutrals in argon (Somekh's predictions) and titanium atoms in argon (this work) appears to support the model and inferences about the nature of the predicted mean free path, ℓ. However, some comment is required in relation to (i) the reliability of data from published thermalisation distance models, and (ii) the possibility that atomic clusters form in the vapour phase (Chapter 5).

With regard to (i), Somekh's model (ref 121) was used for comparative purposes here, as it was the only work which contained data that could be used to evaluate thermalisation distances for atoms of appropriate atomic mass with very low initial energy. The data was extracted from Somekh's predictions of the variation in energy with distance for high energy argon neutrals in argon gas at 500 K, corrected to 300 K. Although this correction was made as Somekh stated in his paper, the assumptions and possible errors in this adjustment are not known. Also, the result is based on argon neutrals rather than metal (titanium) atoms and although the mass numbers (40 and 48) are comparable, there may be different interaction

mechanisms between metal-argon collisions and argon-argon collisions. Again this is an unknown effect; Somekh's predictions for metal atoms thermalised in argon do not cover the energy range of interest here (less than 2000 K). However, his results for chromium (mass 52) initially at 10^5 K gives a pressure-distance product of about 280 mTorr.cms for a final energy of 10^3 K and for argon (mass 40), this is 330 mTorr.cms over the same energy range; the ambient argon gas being at 500 K in both cases. This shows that thermalisation distances for metal atoms and inert gas atoms of comparable masses might be similar.

The overall reliability of Somekh's model should also be questioned. Other models have been published and it is interesting to compare them in general terms. Westwood's predictions (ref 124), which predate Somekh's model, give considerably shorter thermalisation distances than the latter, though this has been attributed to Westwood using an energy independent (and therefore less appropriate) scattering cross section (ref 121). Predictions given by Abril et al, which are the most recent, are comparable to Somekh's model for sputtered metal (tungsten) in argon (ref 125) though their results for energetic argon neutrals in argon (ref 126) predict distances which are significantly smaller. No explanation for this discrepancy is offered in ref 126 even though the difference is acknowledged. It may be inferred from ref 125 however, that the discrepancy could be attributed to the functions which describe the rate of change of particle energy with distance at low energies in the two models. The dependence of thermalisation distance on atomic (or molecular) mass also appears to be uncertain. Westwood's model predicts increased thermalisation distances as the atomic mass of the flux increases, yet Somekh's model predicts the opposite effect. This discrepancy may be due to assumptions made about the two basic parameters which govern thermalisation distance. The first parameter is the mean free path between

collisions, λ_s. Both models show this to decrease with increasing atomic mass of the flux due to the corresponding increase in collision cross sectional area. The second parameter is the number of collisions required to thermalise the energetic flux atoms, η_s. In Westwood's model, η_s increases as the flux atomic mass increases for atoms moving normal to the source. As thermalisation distance = $\eta_s.\lambda_s$, it can be seen that this product may increase or decrease with atomic mass, depending on whether η_s changes more rapidly than λ_s as a function of mass. Somekh's model gives no information on the dependence of η_s with atomic mass though it must be assumed in this case that η_s increases less than λ_s or actually decreases with increasing mass. Although both models give thermalisation results in terms of distance travelled normal to the source, the discrepancies in the dependence of η_s on atomic mass might be attributed to factors such as the assumptions made for the initial energy and angular distribution of the flux.

The observation that thermalisation distance increases with flux atomic or molecular mass (Table 6.3 and Figure 6.6), from the thickness uniformity model, appears to support the trend given by Westwood's model. However, these results are only representative of a single argon pressure (10 mTorr). As Figure 6.8 shows, for example, the gas evaporation of titanium gives a negative intercept value, which has been attributed to vapour pressure effects (Section 6.4.2.1), is likely to change with different evaporant materials. The thermalisation pressure-distance product, which is the gradient in Figure 6.8, cannot be determined from a result for ℓ obtained at a single argon pressure, without knowing the intercept value. Therefore, further values of ℓ at other argon pressures would be required for aluminium and zirconia pressure-distance products to be evaluated.

In addition to the comments above, the possibility that the evaporant material forms atomic clusters in the vapour phase must also be considered. The fraction of energy lost per collision, β, is given by (eg, ref 73):

$$\beta = 8/3 \frac{m_s m_g}{(m_s + m_g)^2} \left[1 - \frac{T_g}{T_s} \right] \qquad (6.12)$$

where m_s = mass of an energetic flux particle at temperature T_s and m_g = mass of an ambient gas atom (argon) at temperature T_g. Equation 6.12 shows how β depends on particle mass. For a 50 atom titanium cluster, about 15 times less energy would be lost in a collision with an argon atom, when compared with the energy lost in a similar collision involving a single titanium atom. However, the 50 atom cluster would also be nearly 14 times larger than a single atom in cross sectional area (as area $\propto$ volume$^{2/3}$ for a sphere), causing a corresponding increase in collision probability. Thus thermalisation distances might not be expected to change significantly for small clusters, if Equation 6.12 is assumed to be applicable. However, when a 500 atom cluster is considered, almost 150 times less energy would be lost in a collision, compared with only a 63 fold increase in cross sectional area. Therefore, the presence of larger clusters could significantly increase the values for ℓ obtained from the thickness uniformity model. Clearly, the use of Equation 6.12 in this situation has to be questionable, as other factors may also be important. These are the factors which influence the disagreement between the models of Somekh and Westwood, on the dependence of thermalisation distance with mass, discussed earlier.

The points discussed in this section seem to indicate that the agreement between data derived from Somekh's model and the titanium gas evaporation results in Figure 6.8 could be fortuitous. The most significant reasons for this are that, firstly, the more recent model of Abril et al

(ref 126) gives shorter thermalisation distances for energetic argon than Somekh's model. If the results of the former are correct, then the gradient from Somekh's data in Figure 6.8 will be too large. Secondly, the possibility of the titanium flux being in the form of atomic clusters would also tend to make the gradient from the gas evaporation data in Figure 6.8 larger than if the material were single atoms, if Equation 6.12 is assumed to be applicable. Therefore, the two effects tend to offset each other, giving an erroneous agreement.

6.5.1.3 Geometrical effects

The coating thickness uniformity model assumes that (a) there are no masking effects from substrate supports or neighbouring substrates, (b) samples are horizontally mounted centrally above the source so that the vertical source to substrate distance is equivalent to the actual distance (ie, no angular corrections), (c) substrates are thin and (d) substrate area has no effect on results, provided the dimensions are small with respect to the deposition chamber. Although the criteria for (a) and (c) have been satisfied to within reasonable practical limitations, some comments on (b) and (d) are required.

The substrate mounting geometry used in this work resulted in sample centres (where coating thicknesses were measured) being slightly offset from the central vertical axis. This offset, for Runs U1 to U8 was about 1.5 cms. As samples were positioned at vertical distances of 5 to 20 cms above the source, the actual distances between source and substrate centres would have therefore been 5.22 to 20.06 cms. The errors incurred from this effect are therefore insignificant compared with other sources of error, such as changes in the actual source height during evaporation. For Run U9 though, where glass microscope slides were used, the offset was about 3.7 cms.

However, samples were positioned further away from the source, at 15 to 35 cms, giving actual distances of 15.46 to 35.20 cms. Again, even the 0.5 cms error in the sample closest to the source is small.

The results reported in Section 6.4.1.2 show that ℓ is not significantly changed for small samples which have different areas and aspect ratios. This is reasonable, considering that ℓ is primarily related to the mean free path for thermalisation. The predicted negative virtual source height in Run U6 (Table 6.2 and Figure 6.5) appears to be a significant effect and it is difficult to explain. The negative value means that although ℓ is unaffected, the values of R in Run U6 are lower than those in Runs U3 and U5; ie, thickness uniformity is improved. This could be an indication of the model breaking down for very small substrate dimensions (width = 9 mm in this case), as other effects not accounted for in the model, could become significant. It is also interesting to note the results of Upadhye et al (ref 127) for thickness uniformity on a small glass rod (3 mm diameter) in a sputtering system (7.6 cms diameter source). Interpreting their results in terms of front to back thickness ratios shows no significant change with source to substrate distance, until the substrate is very close to the deposition chamber wall (Table 6.6).

Therefore, as with Run U6, the results in Table 6.6 show a deviation from the model; the disagreement being more extreme in the latter case. Although the cylindrical substrate geometry used in ref 127 is not ideal for data interpretation, the reasons behind the discrepancies from this set of results and those from Run U6 may have similar explanations. The following reasons are put forward to explain these observations:

(i) The range of coating atom mobility on the surface is comparable to small substrate dimensions so that material depositing on one face may have a high probability of transferring to the other face (a similar

argument to that shown in Figure 6.10c).

SOURCE TO SUBSTRATE DISTANCE (cms)	FRONT TO BACK THICKNESS RATIO
15.2	1.244
22.9	1.325
25.4	1.253
27.4	1.302
29.2	1.718

Table 6.6 Thickness uniformity results from ref 127 (20 mTorr pressure) showing no significant change in thickness ratio until the distance is close to the source to chamber wall distance (30.5 cms).

(ii) The influence of collisions between the coating flux and ambient gas atoms near to the substrate surface become more significant as substrate dimensions are reduced. Thus coating atoms which may have been on a trajectory to hit (for example) the front face of a large substrate would continue for a small substrate and subsequently re-scatter to possibly hit the back face or eventually deposit on the chamber walls. The effect is shown schematically in Figure 6.11.

(iii) If the source emitting area is large compared with the substrate area, then the probability of non-thermalised vapour influencing the measured thickness of the back face coating could become significant, particularly if the substrate has a spherical or cylindrical geometry as shown schematically in Figure 6.12.

Reason (i) is unlikely, because the coatings discussed here were not ion-plated. Thus energies at the surface under consideration here, would be far too low for this effect to be significant. Reason (ii) is more

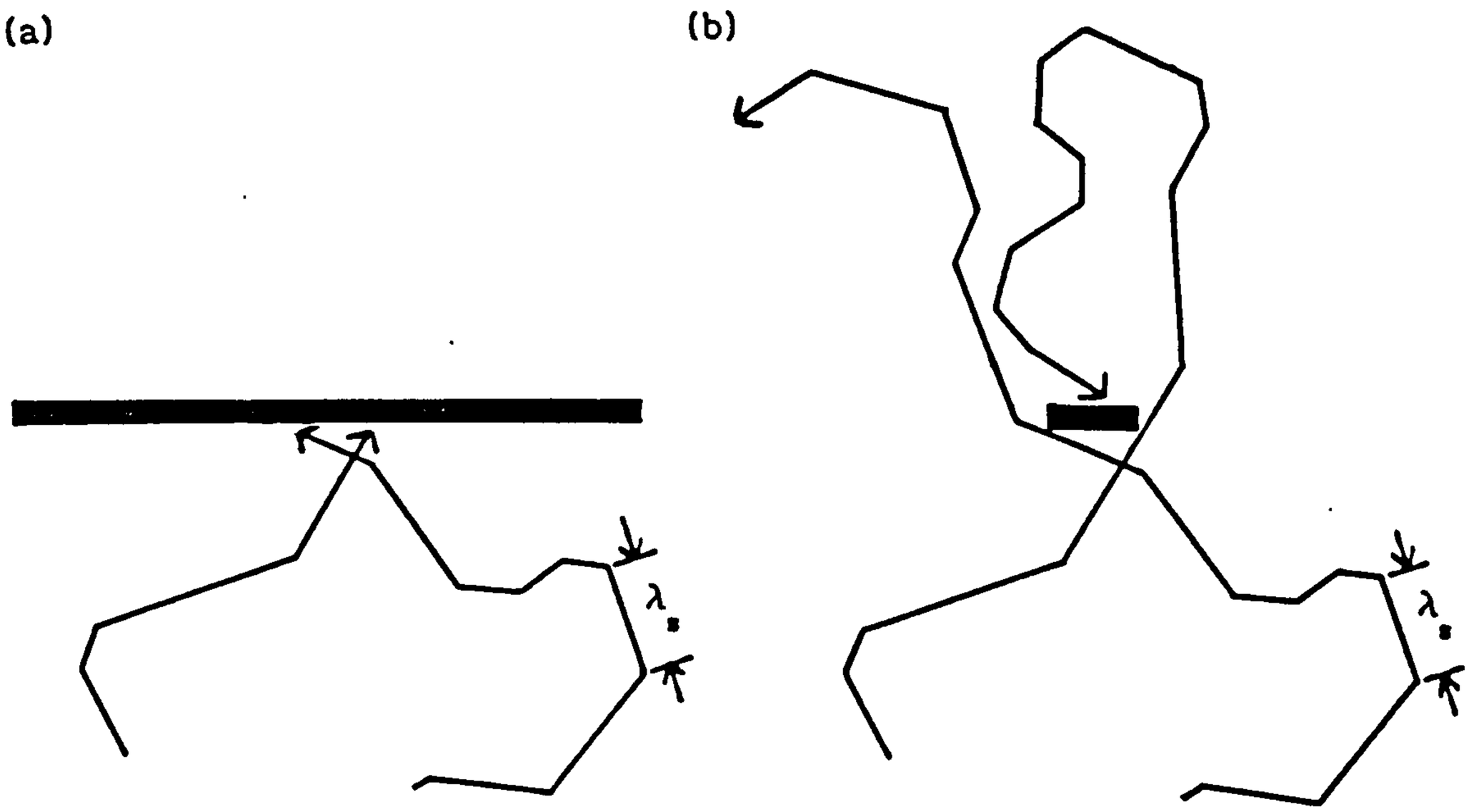

Figure 6.11 (a) Possible trajectories of two coating atoms (non-thermalised) striking the front face of a substrate.

(b) Identical situation, but substrate dimensions are now comparable to the collision mean free path, λ_s. In this case, the atoms become thermalised and strike the back face or the chamber walls.

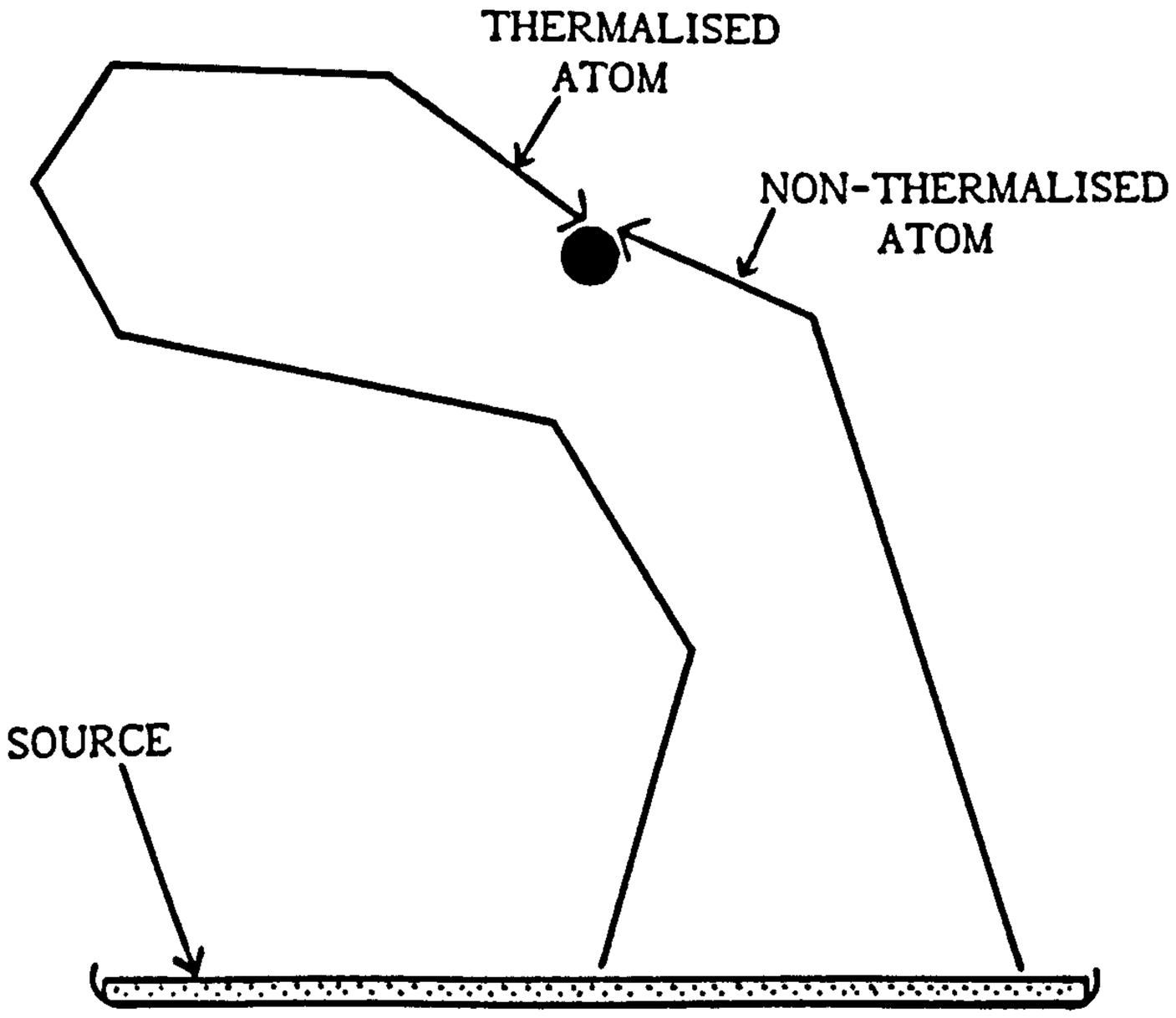

Figure 6.12 Possible trajectories of coating atoms from an extended source striking a small cylindrical or spherical substrate, showing how a non-thermalised atom may strike the "back" face.

realistic, particularly if the mean free path between individual collisions is comparable to the substrate dimensions. From Westwood's calculations (ref 124), this mean free path, λ_s, for a coating atom (atomic mass ~ 50) in argon at 10 mTorr is about 6 mm, thus supporting this view. However, the likely presence of atomic clusters would make λ_s smaller and deflection angles at each collision would be reduced. Nevertheless, the argument suggests that as substrate dimensions approach λ_s, the influence of the non-thermalised (or directional) evaporant flux on front to back thickness ratio could decrease. This in turn means that thickness uniformity under these circumstances is improved, as observed in Run U6. Reason (iii), though a less probable contribution to the effects observed in Run U6, could be significant for the data from ref 127. In general, sputtering systems are likely to be more susceptible to the effects of (iii) due to the relatively large source areas used. The phenomenon will probably only be significant though, for very small substrates which approximate to spherical or cylindrical geometries.

6.5.2 Absolute Thickness Fall Off Rates and Virtual Source Effects

So far, only coating uniformity in terms of front to back thickness ratios has been discussed. Another important aspect in ion plating is the fall off in deposition rate with distance from the vapour source, ie: thickness uniformity, in absolute terms, as a function of source to substrate distance. The measured front face thicknesses from Runs U1 to U9 can be used to investigate these effects.

6.5.2.1 An empirical power law for front face thickness data

The simplest idealised situation that could represent thickness fall off with source to substrate distance would be to consider the vapour source

as a point, emitting vapour radially in straight lines in all directions. Coating thicknesses on the front faces of flat substrates positioned tangentially to the source would be directly dependent upon the local vapour flux density. In turn, the flux density would be inversely proportional to the square of the distance from the source under such conditions. Thus in the simplest case, coating thickness would be expected to follow an inverse square law with source to substrate distance.

From the above argument, it follows that thickness rates in practical situations may follow an inverse power law, ie:

$$t_f = Bs^{-n} \qquad (6.13)$$

where t_f = front face thickness of a flat plate sample mounted centrally above the vapour source, B = constant of proportionality, s = source to substrate distance, and n = power index, which is 2 for an inverse square law. Thus:

$$\log t_f = -n \log s + \log B \qquad (6.14)$$

Knowing t_f and s, Equation 6.14 allows n and B to be evaluated by linear regression. Table 6.7 summarises the results of fitting Equation 6.14 to available data and Figure 6.13 shows some of the data graphically.

The following observations can be made from these results:

(i) The index, n, is affected by the ambient gas pressure (Runs U1 to U3). As pressure increases, n increases from near inverse square law conditions to a value of about 2.4 at 10 mTorr (Runs U3, U5 and U6). This can be attributed to ambient gas atoms scattering out the directional or semi-directional vapour flux; clearly this effect will

increase as argon pressure is increased.

(ii) The index is influenced by the nature of the evaporant material (compare Runs U3, U7 and U8) and evaporation rate-virtual source height differences; compare Run U8 (virtual source height = 1.88 cms, evaporation rate = 0.050 g/min) with Run U9 (virtual source height = 6.78 cms, evaporation rate = 0.105 g/min). This can be attributed to differing scattering cross sections (material) and vapour flux densities (evaporation rate and virtual source effects).

RUN	PROCESS DETAILS			EQN. 6.14 - LIN. REG.		
	SOURCE MATERIAL	MEAN ARGON PRESSURE (mTorr)	TYPE	B (μm)	n	CORR. COEFF.
U1	TITANIUM	5.13	G.E.	3279	2.095	-0.9976
U2	TITANIUM	7.58	G.E.	3710	2.246	-0.9939
U3	TITANIUM	9.99	G.E.	3375	2.401	-0.9999
U5	TITANIUM	10.19	G.E.	3659	2.389	-0.9985
U6	TITANIUM	10.44	G.E.	3604	2.353	-0.9934
U7	ZIRCONIA	9.95	G.E.	8562	3.091	-0.9963
U8	ALUMINIUM	9.97	G.E.	3234	2.709	-0.9981
U9	ALUMINIUM	10.35	G.E.	39921	3.297	-0.9962
U4	TITANIUM	9.48	I.P.	8900	2.799	-0.9940

Table 6.7 Linear regression results for front face thickness data using Equation 6.14. B is the predicted thickness that would have been achieved at s = 1 cm.

(iii) The index is increased from 2.4 (Run U3) to 2.8 (Run U4), when coatings are ion plated. This can be explained by considering how the plasma bombardment density and vapour flux density vary with

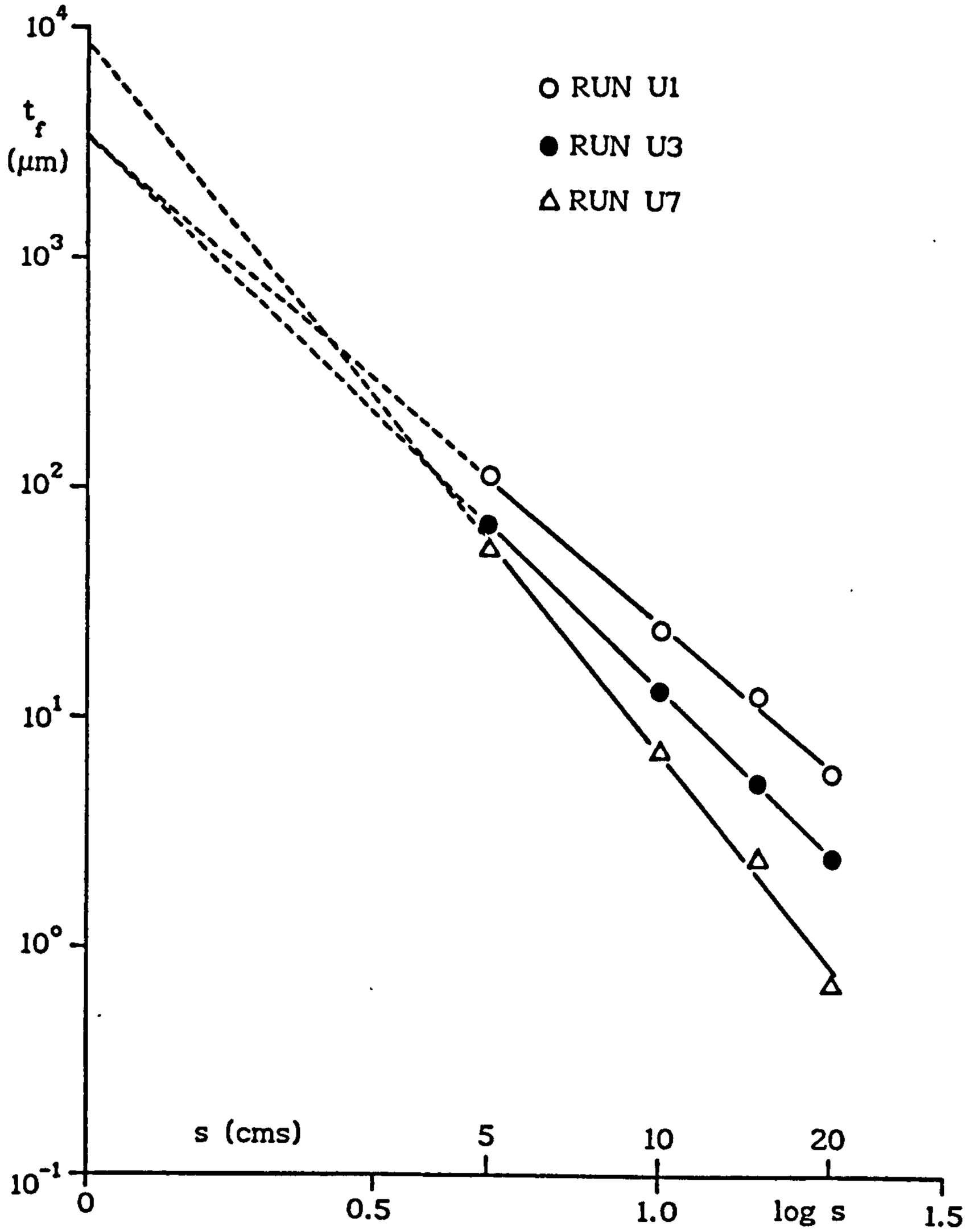

Figure 6.13 Some logarithmic linear regression results showing a power law relationship between front face coating thickness and source to substrate distance.

increasing source to substrate distance. The plasma density (being generated by RF rather than DC thermionic triode) is not likely to decrease with height in the chamber, whereas the vapour density falls off with distance from the source. The net result is that samples further away from the vapour source will receive a greater plasma bombardment to vapour flux incidence rate than of those nearer. Therefore, greater sputter removal and coating densification will occur on the more remote samples, producing relatively thinner coatings, which is reflected in the increased value of n.

6.5.2.2 Investigation of the ψ function

The high correlation coefficients in Table 6.7 shows that Equation 6.13 fits well to data from all the process conditions investigated. It is apparent though, that Equations 6.13 and 6.7 (from Section 6.2) must be related, the latter representing the total vapour moving upwards during the coating process. Thus,

$$t_f = Bs^{-n} \propto \frac{1}{2} \psi \, (1+e^{-s/\ell})$$

Now ψ is a function of s to account for the progressive dilution of vapour flux, which would occur even if no gas scattering were present. This means that if the vapour source could be considered as a point emitter, then ψ would actually be an inverse square law function of s. Thus,

$$\psi \propto s^{-m} \qquad (6.15)$$

where m = 2 for a point source. Substituting Equation 6.15 into 6.7 gives,

$$t_f \propto \frac{1}{2} s^{-m} (1 + e^{-s/\ell})$$

$$\therefore \quad t_f = \frac{C}{2} s^{-m} (1 + e^{-s/\ell}) \qquad (6.16)$$

where C = constant of proportionality. Therefore, Equations 6.13 and 6.16 are equivalent, though the latter is a more "exact" expression as vapour flux dilution and gas scattering effects are separated. This means that the value of index m should be independent of ambient gas pressure in gas evaporation, unlike index n in Equation 6.13. Transposing Equation 6.16 gives,

$$\frac{2t_f}{(1 + e^{-s/\ell})} = C s^{-m}$$

$$\therefore \quad \log \left(\frac{2t_f}{1 + e^{-s/\ell}} \right) = -m \log s + \log C \qquad (6.18)$$

As t_f, s and ℓ are known from the runs performed in this work, then a linear regression of log $[2t_f/(1+e^{-s/\ell})]$ versus log s should verify the relationship and yield a gradient value of -m. However, there is an uncertainty, the virtual source effect. The virtual source height is known for each run and to assume that all the vapour originates from this position is justified. Thus, Equation 6.17 becomes,

$$\log \left(\frac{2t_f}{1 + e^{-(s-h)/\ell}} \right) = m \log (s-h) + \log C \qquad (6.18)$$

where h = virtual source height. Table 6.8 summarises the results of fitting Equation 6.18 to data from all runs performed under gas evaporation conditions except Run U6. This run has been excluded due to the negative

value of virtual source height obtained (see Sections 4.4.1.2 and 4.5.1.3). Also shown in Table 6.8 is an estimation of the actual vapour source radius.

RUN	PROCESS			EQN 6.18-LIN REG		
	SOURCE MATERIAL	VIRTUAL SOURCE HEIGHT h(cms)	REAL SOURCE RADIUS r(cms)	h/r	m	CORR. COEFF.
U1	TITANIUM	0.51	2.2	0.232	1.763	-0.9969
U2	TITANIUM	1.42	2.2	0.647	1.657	-0.9901
U3	TITANIUM	1.63	2.2	0.739	1.722	-0.9990
U5	TITANIUM	1.29	2.2	0.587	1.804	-0.9968
U7	ZIRCONIA	2.08	0.3	6.930	2.074	-0.9900
U8	ALUMINIUM	1.88	1.8	1.075	1.878	-0.9931
U9	ALUMINIUM	6.78	1.8	3.877	1.996	-0.9870

Table 6.8 Linear regression results for front face thickness data using Equation 6.18. The real source radius was estimated from the solidified melt pool after each run.

The results show the correlation coefficients to be slightly lower than those evaluated for the simple power law (Equation 6.14) in Table 6.7. This can be attributed to the more complex analysis and contributory errors arising from uncertainties in the values of h and ℓ. However, the most significant feature is that the index, m, is influenced by the height of the virtual source in relation to the size of the real source. This is shown graphically in Figure 6.14. Allowing for some degree of uncertainty, Figure 6.14 shows that as the h/r ratio increases, m attains a value of about 2 when h/r is greater than unity. This implies that provided the virtual

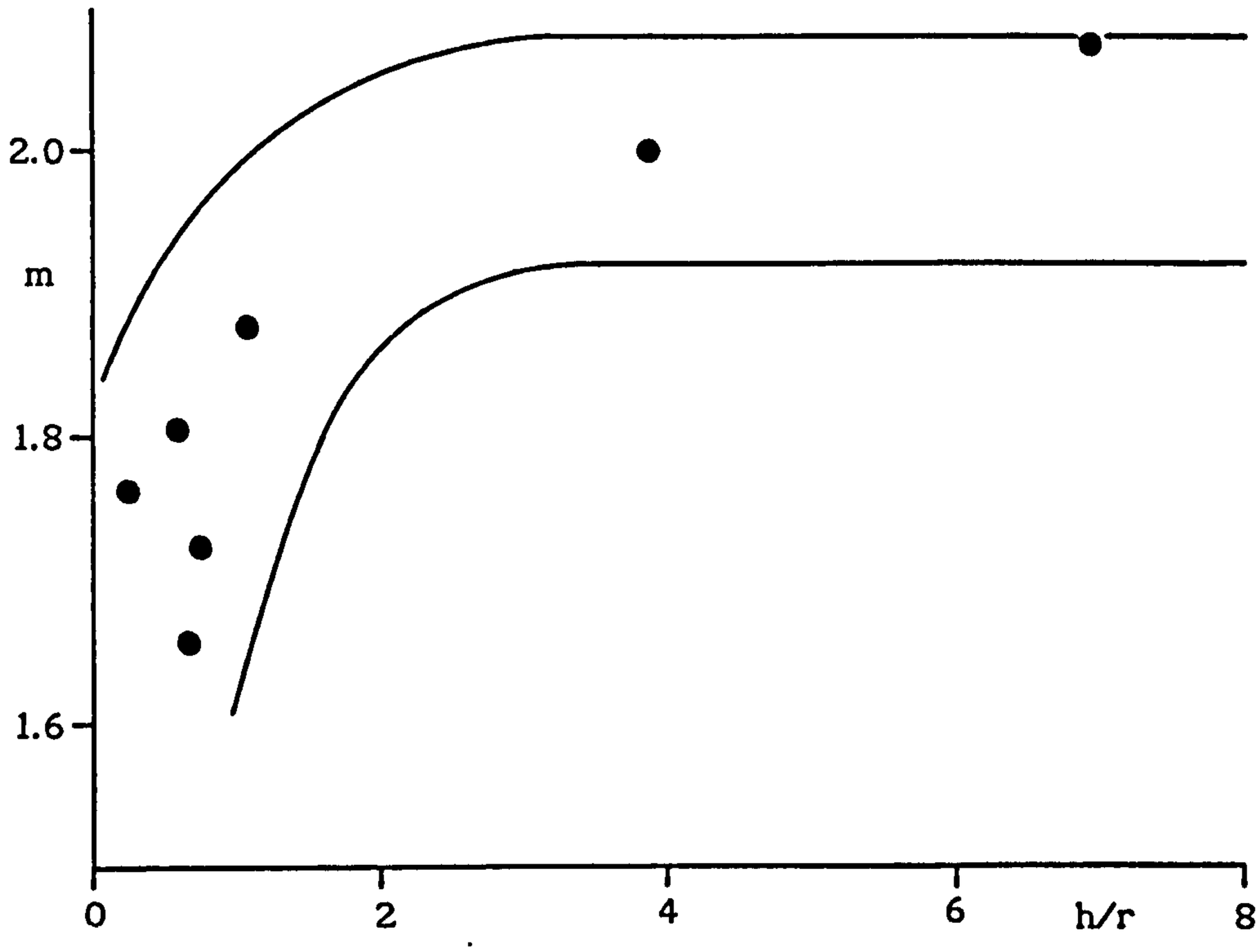

Figure 6.14 Plot of power law index, m, from Equation 6.18 as a function of the ratio between virtual source height and real source radius, h/r. Note that m ~ 2 when h/r is greater than unity.

source height is large compared with the real source dimensions, then the ψ function becomes an inverse square law; the vapour originating from a point at height h above the real source.

When h/r is less than unity, the situation becomes more complex. The "effective" vapour source is no longer a single point emitter, though it may approximate to a disc source. Consider the following:

From ref 26, the coating thickness, t_f, resulting from a disc source is

$$t_f \propto \frac{1}{r_d^2} \cdot \frac{(r_d/s)^2}{1 + (r_d/s)^2}$$

Simplifying,

$$\therefore t_f \propto \frac{1}{s^2 + r_d^2} \qquad (6.19)$$

where s = source to substrate distance and r_d = disc source radius. A typical value for the index m, when h/r is less than unity, is about 1.75 (Runs U1 to U5 in Table 6.8). If the effective source approximates to a disc source for these runs, then,

$$s^{-1.75} \propto \frac{1}{s^2 + r_d^2} \qquad (6.20)$$

Table 6.9 shows the results of testing Equation 6.20 by performing linear regressions between $s^{-1.75}$ and $(s^2 + r_d^2)^{-1}$ for different values of r_d.

The optimum fit for Equation 6.20 occurs when the effective source radius is about 2.2 cms. This figure concurs with the estimated radius of the real source in Table 6.8 for Runs U1 to U5.

EFFECTIVE SOURCE RADIUS r_d, (cms)	CORRELATION COEFFICIENT
1.0	0.999747
1.5	0.999880
2.0	0.999981
2.2	0.999997
2.5	0.999977
3.0	0.999789

Table 6.9 Linear regression test of Equation 6.20, using s = 5, 10, 15 and 20 cms for each r_d value tested.

Although the analysis here is not a rigorous mathematical treatment (eg, it is assumed that s ~ s-h in Equation 6.20), there is sufficient evidence to suggest that as h/r decreases, the effective source characteristics change from a point emitter to those of the real source. Therefore, when h/r is greater than unity, the ψ function follows an inverse square law with source to substrate distance; for smaller h/r values, the ψ function approximates to an inverse power law with an index of between 1.6 to 1.8.

6.5.2.3 Further comments on the virtual source phenomenon

In recent years, there appears to have been little comment on virtual sources in the published literature. Quantitative data on the height, size and shapes of virtual sources is rare. A pinhole camera technique employed

by Graper, (ref 111) during EB evaporation of aluminium, gave virtual source heights of 0.1 to 0.6 cms above the crucible. These are generally lower than the values obtained in this work (0.5 to 6.8 cms in Table 6.8) though the evaporation rates used in ref 111 are not known. It can be inferred from Reiley's calculations (ref 112) that he obtained a virtual source height of 1 to 2 cms above the melt pool during EB evaporation of copper at an evaporation rate of about 11 g/min. Although the virtual source height from ref 112 is comparable to those of this work, the evaporation rate and therefore the vapour density must have been considerably greater in the former case. The work reported in refs 111 and 112 were performed under vacuum evaporation conditions. Thus, in addition to differences in EB gun characteristics (which would influence the molten pool size and resulting vapour density), the presence of argon in the runs performed here, could have increased the virtual source height by enhancing the scattering occurring within the viscous region above the real source. To some extent, this suggestion is supported by the observed increase in virtual source height with increased argon pressure (Figure 6.4 a-c).

The likelihood of the vapour being in the form of atomic clusters requires some comment here. As reported in Section 5.4.5.2, the clusters are probably formed by gas phase (homogeneous) nucleation. Clearly, the probability of this occurring must be greatest in regions where the vapour density is highest. Therefore, we might expect a large proportion of the clusters to be formed in the virtual source region.

6.5.3 Predictions and Extensions To The Thickness Uniformity Model

6.5.3.1 Predictions from the basic model

Figure 6.15 shows the model, represented by Equation 6.9, in graphical form. Thus, for a given thermalisation mean free path, ℓ, and source to

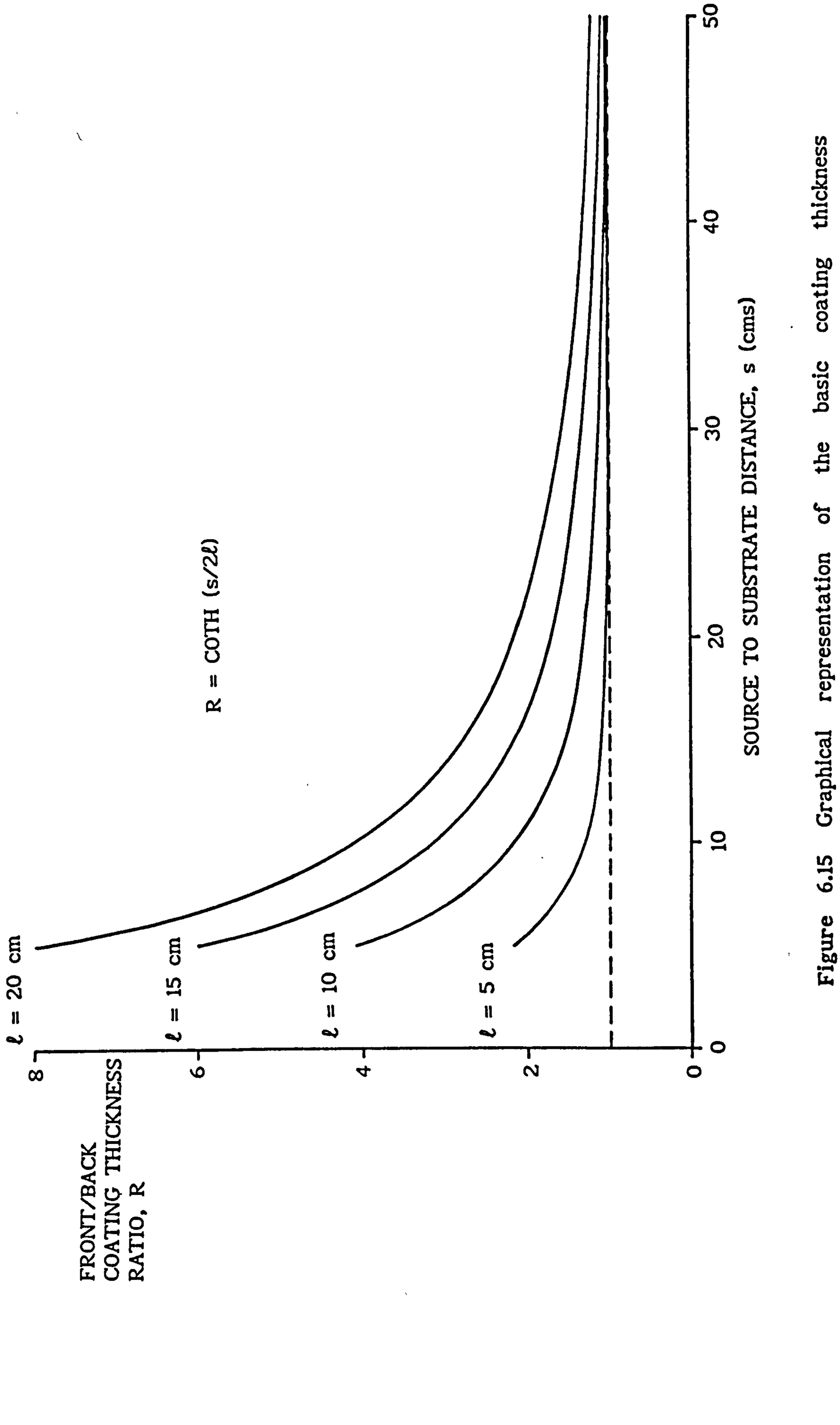

Figure 6.15 Graphical representation of the basic coating uniformity model.

substrate distance, the front to back coating thickness ratio, R, may be evaluated. Typical ℓ values from this work and those derived from published data are generally between 10 to 15 cms, under both ion plating and gas evaporation conditions. To improve uniformity (by reducing R), ℓ could be decreased by increasing the ambient gas pressure. However, as reported in Section 1.3, this could be detrimental to the coating properties and, in the case of ion plating, the intensity of bombardment from the discharge might have to be increased to counteract this effect. Increasing the bombardment may create other problems, such as unwanted heating of the substrates. If the vapour forms atomic clusters, then ℓ may also be decreased if cluster size could be reduced (Section 6.5.1.2). As a large proportion of the clusters might be expected to form in the virtual source region, then it may be possible to significantly reduce or even eliminate the virtual source effect by using very low evaporation rates. Unfortunately, the rates required to achieve this could be too low for practical coating purposes. Uniformity may also be improved by increasing the source to substrate distance, though the coating thickness in absolute terms will be reduced, as reported in Section 6.5.2.

Clearly, there will always be a penalty to be paid for improving coating thickness uniformity by increasing the effects of gas scattering. The model also shows that, at least in theory, a value of R being equal to unity cannot be achieved for the situations studied here.

6.5.3.2 Extensions to the basic model

Figure 6.16 shows three different source-substrate configurations which could be modelled by applying the concepts reported in this chapter.

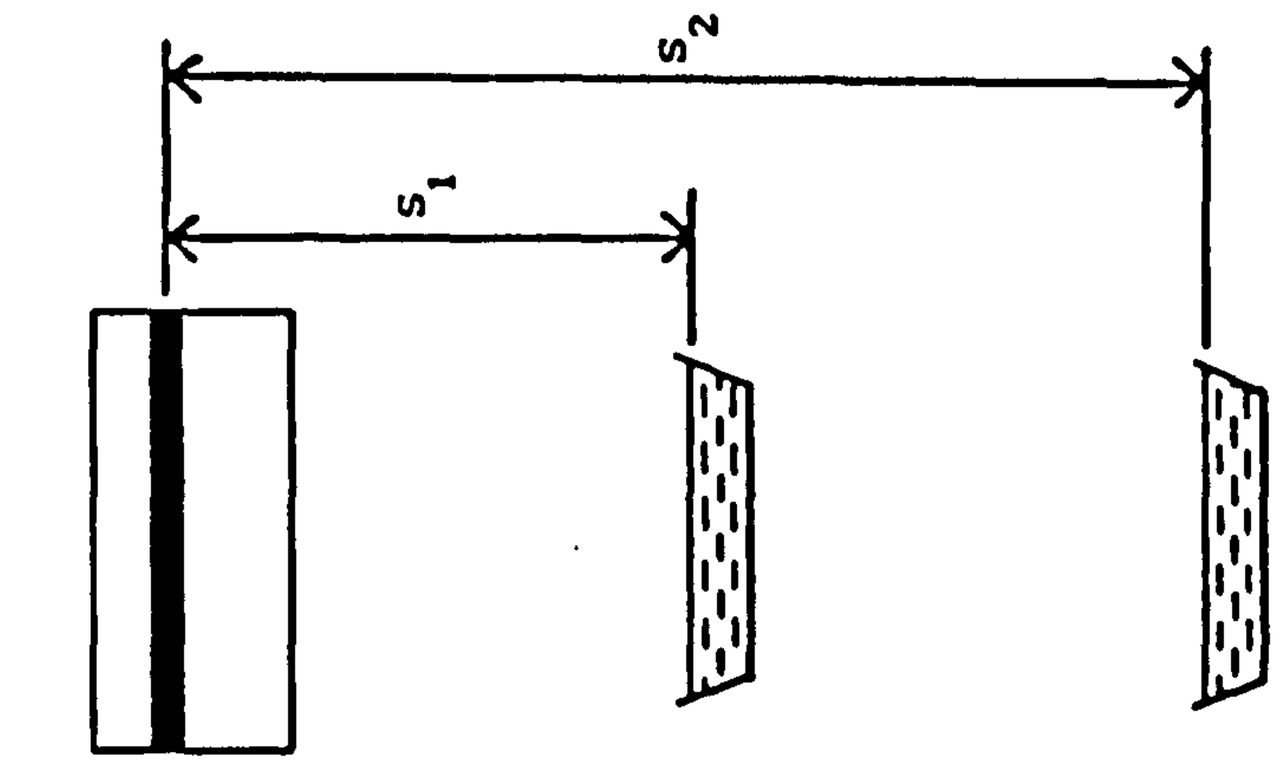

Figure 6.16 Examples of some source–substrate configurations which can be represented by extending the basic thickness uniformity model: (a) substrate not mounted horizontally; (b) thick substrate and (c) two vapour sources.

(i) Angled Substrate (Figure 6.16a):

Non-thermalised flux moving upwards = $\psi e^{-s/\ell}$ (6.4)

∴ Non-thermalised flux moving in direction "a" = $\psi e^{-s/\ell} \cos\theta$ (6.21)

Thermalised vapour has no preferential direction.

∴ Thermalised vapour in direction "a" or "b" = $\frac{1}{2} \psi(1-e^{-s/\ell})$ (6.22)

∴ Total vapour in direction "a" = Eqn 6.21 + Eqn 6.22

Total vapour in direction "b" = Eqn 6.22

As R is assumed to be dependent only on the vapour flux arrival rates, then

$$R = \frac{\text{Eqn 6.21 + Eqn 6.22}}{\text{Eqn 6.22}} = \frac{1 + e^{-s/\ell} (2 \cos \theta - 1)}{1 - e^{-s/\ell}} \qquad (6.23)$$

When $\theta = 0^\circ$, Equation 6.23 becomes $R = \coth (s/2\ell)$, which as we would expect, is the original model (Equation 6.9). For a vertically mounted substrate, $\theta = 90^\circ$, and Equation 6.23 predicts R to be unity. This is also to be expected, though obviously the terms "front" and "back" become inappropriate for this value of θ.

(ii) Thick substrate (Figure 6.16b):

Non-thermalised flux arriving at front face = $\psi_F \, e^{-s_F/\ell}$ (6.24)

Thermalised flux arriving at the front face = $\frac{1}{2} \psi_F \, (1 - e^{-s_F/\ell})$ (6.25)

Thermalised flux arriving at the back face = $\frac{1}{2} \psi_B \, (1 - e^{-s_B/\ell})$ (6.26)

where ψ_F and ψ_B are functions of s_F and s_B respectively, to account for progressive dilution of the vapour flux.

$$\therefore R = \frac{\text{Eqn 6.24 + Eqn 6.25}}{\text{Eqn 6.26}} = \frac{\psi_F \, (1 + e^{-s_F/\ell})}{\psi_B \, (1 - e^{-s_B/\ell})} \qquad (6.27)$$

As shown in Section 6.5.2.2,

$$\psi \propto s^{-m} \tag{6.15}$$

where m ~ 2 for a virtual source height larger than the real source radius and m ~ 1.75 for smaller virtual sources. Thus, Equation 6.27 becomes:

$$R = \frac{s_F^{-m}\,(1 + e^{-s_F/\ell})}{s_B^{-m}\,(1 - e^{-s_B/\ell})} \tag{6.28}$$

Table 6.10 shows some values for R as a function of substrate thickness, under otherwise identical process conditions, using Equation 6.28.

SUBSTRATE THICKNESS $(s_B - s_F)$ cms.	R
0	1.716
0.1	1.729
1.0	1.849
10	3.288
20	5.432

Table 6.10 Results for R, predicted from Equation 6.28, using the values; m = 2, ℓ = 15 cms, s_F = 20 cms.

The results show how thickness uniformity is made worse as substrate thickness is increased.

(iii) Two Vapour Sources (Figure 6.16c)

The sources are assumed to be identical and that the upper source does

not cause any shadowing of the lower source.

Total flux moving upwards from a single source = $\frac{1}{2}\psi\ (1 + e^{-s/\ell})$ (6.7)

∴ Total flux moving upwards from the sources at distances of s_1 and s_2

$$= \frac{1}{2}\psi_1\ (1 + e^{-s_1/\ell}) + \frac{1}{2}\psi_2\ (1 + e^{-s_2/\ell}) \quad (6.29)$$

where ψ_1 and ψ_2 are functions of s_1 and s_2 respectively, to account for progressive dilution of the vapour flux from both sources.

Total flux moving downwards from a single source = $\frac{1}{2}\psi\ (1 - e^{-s/\ell})$ (6.8)

∴ Total flux moving downwards, towards the back face from two vapour sources

$$= \frac{1}{2}\psi_1\ (1 - e^{-s_1/\ell}) + \frac{1}{2}\psi_2\ (1 - e^{-s_2/\ell}) \quad (6.30)$$

Dividing Equation 6.29 by Equation 6.28 and substituting the ψ functions for Equation 6.15, we get:

$$R = \frac{(s_1/s_2)^{-m}\ (1 + e^{-s_1/\ell}) + (1 + e^{-s_2/\ell})}{(s_1/s_2)^{-m}\ (1 - e^{-s_1/\ell}) + (1 - e^{-s_2/\ell})} \quad (6.31)$$

Equation 6.31 could be useful in situations where substrates are mounted on a carousel arrangement which passes them over two vapour sources in turn; the sources being at different heights to each other.

Although Equations 6.23, 6.28 and 6.31 have not been verified experimentally, these extensions to the basic thickness uniformity model demonstrate the potential for modelling situations which are less idealistic than the conditions studied in this work.

6.6 SUMMARY

A model which unifies coating thickness uniformity with source to substrate distance has been presented. The model is based on the assumption that uniformity, expressed in terms of the front to back coating thickness ratio, R, depends only on the relative proportions of thermalised and non-thermalised vapour fluxes arriving at the substrate. For a thin flat horizontally mounted substrate, positioned directly above a vapour source, the model is $R = \coth(s/2\ell)$, where s is the source to substrate distance and ℓ is an associated mean free path.

Coating trials were performed to test the validity of the model under various deposition process conditions. From gas evaporation runs (using argon as the ambient gas), the influences of the following variables were studied; (i) argon gas pressure, (ii) substrate size, (iii) source material, and (iv) evaporation rate. To evaluate the effects of plasma bombardment on the model, an ion plating run was also performed. Plots of s against a logarithmic function of measured R values yielded linear relationships for all the experimental runs investigated. This indicated that the model was valid and the resulting gradients allowed ℓ to be quantified. In general, these plots also exhibited positive value intercepts on the s axis and this has been interpreted as a virtual source phenomenon; the intercept value representing the height of the virtual source above the real source. The effect has also been reported in the published literature and it has been attributed to a "viscous cloud" being formed above the melt pool from the relatively high local vapour flux density. It is suggested that if the vapour nucleates into clusters, then a large proportion of these clusters would be expected to form in the virtual source region.

Using values of ℓ from this work and from published DC ion plating data, plots of argon pressure versus $1/\ell$ were found to give linear

relationships in all cases, which supports the universal applicability of the model. Large negative value intercepts on the argon pressure axis were generally obtained from these plots, indicating that finite R values would have been obtained, even if no ambient gas had been present. This has been attributed to mutual scattering, imparted by the vapour flux on itself, and it is therefore synonymous with the virtual source phenomenon.

Although the model was found to be valid under ion plating and gas evaporation conditions, it is suggested that the effects of bombardment from the discharge in the former case could change R, depending on the process conditions. The RF ion plating run performed in this work was found to give R values which were slightly lower than those obtained under equivalent gas evaporation conditions.

The product of argon pressure and ℓ, obtained from the titanium gas evaporation runs in this work, was found to be comparable to pressure-thermalisation distance data from a published model. Although this provides some evidence that ℓ is primarily associated with the mean free path for thermalisation, the agreement may be fortuitous. This is because a thermalisation distance model published more recently has indicated that the pressure-distance product from the previous published model could be too large. Also, the possibility of the titanium vapour being in the form of atomic clusters may have caused the resulting ℓ values from this work to be larger than if the flux had been individual atoms.

Using front face thickness data from the coating trials, the thickness in absolute terms was found to fit an empirical inverse power law with source to substrate distance. The power, being dependent on process conditions, was between 2 and 3.3 for the data studied. In general, the power was observed to increase (ie, the thickness decreased more rapidly with distance from the source) if the ambient gas pressure was increased. A

more detailed analysis of the front face thickness data has enabled the ψ function to be evaluated. This function represents the progressive dilution of the vapour flux with distance from the source, which would occur even if no gas scattering effects were present. For cases where the virtual source height was larger than the radius of the real source, ψ was found to be an inverse square law; ie, all the vapour appears to originate from the virtual source which behaves as a point emitter. For smaller virtual source heights, the power was observed to decrease from 2 to a value of 1.6 to 1.8. This has been attributed to the influences of the real source becoming more significant as virtual source height decreases.

Predictions from the basic front to back thickness ratio model show that uniformity may be improved, either by reducing ℓ or increasing the source to substrate distance. To reduce ℓ would require an increase in the ambient gas pressure, which may be detrimental to coating properties. Reducing ℓ by decreasing the size of clusters (should they be formed) might require impractically low evaporation rates. Increasing the distance from the source would reduce the coating thickness in absolute terms. Therefore, exploiting gas scattering phenomena to improve thickness uniformity requires consideration of other coating parameters which may be detrimentally influenced. By applying the concepts of the basic model and knowledge of the ψ function, front to back thickness ratio models have been derived for an angled substrate, a thick substrate and for two vapour sources. Although these models have not been experimentally verified, they demonstrate the potential for studying situations more complex than those considered in this work.

7. GENERAL SUMMARY

Although individual summaries have been given at the end of each chapter, the aim of this chapter is to pull together the main findings of Chapters 3 to 6. This means that the results can be considered in terms of their influences on ion plating process optimisation. Numbers in square brackets refer to the chapter where the work has been reported.

7.1 DISCHARGE ENHANCEMENT

As the suggested minimum recommended bombardment energy for ion plating is low (40 - 70 eV), and the attainment of higher energies may be less significant than increasing the bombardment intensity [3], the ability to enhance ion plating discharges at low substrate bias levels is of primary importance. By studying various argon discharge layouts [3], it has been shown that energetic gas bombardment of the cathode (substrate), in strongly enhanced discharges, is mainly from ions rather than high energy neutrals. Under these conditions, a large proportion of the bombarding ions have maximum energy; this energy being dependent on the voltage drop across the cathode sheath. Enhancement with a thermionic emitter can give excellent ion intensity and energy transportation characteristics at low substrate bias voltages. In addition, cathode sheath thickness can be considerably reduced with this type of arrangement, in accordance with the Child-Langmuir equation. This can minimise preferential bombardment of substrate corners, edges, etc [3] and improve bombardment uniformity on substrate components with complex geometries or on batches of mixed sized components [4].

There are, however, some potential drawbacks in using thermionically supported discharges. These are: (i) spatial non-uniformity of the plasma,

and (ii) tungsten filament contamination effects. With regards to (i), sputter weight loss experiments [4] have shown that weight loss falls off exponentially with distance from the thermionic emitter and this has been primarily attributed to the decrease in availability of electrons emitted by the filaments to create ions. These experiments have also shown that electrons from the filaments cause anisotropic effects in the plasma, reducing the influence of plasma bombardment on sample surfaces which are remote from the emitter. Plasma spatial non-uniformity was also observed in optical emission spectroscopy experiments [5]. Here, light intensities were found to decrease exponentially with distance from the primary electron emitter, giving further evidence that electrons from the main emitter (in diodes as well as thermionic triodes) dominate the discharge characteristics. In the case of (ii), longer sputter weight loss runs [4] resulted in samples becoming contaminated with tungsten sputtered from the filaments. This has been attributed to increased sputter yield arising from the gradual opening up of grain boundaries in the filament wire, with usage. Runs of up to $1\frac{1}{2}$ hours did not appear to be affected. Optical emission spectroscopy studies of tungsten emission in argon thermionic triode discharges [5] have indicated that filaments run at lower voltages but at higher temperatures (to maintain the same degree of discharge enhancement) would reduce the amount of tungsten sputtered into the discharge, though the improvement is likely to be small.

7.2 CHARACTERISTICS OF THE MAIN SPECIES PRESENT IN ION PLATING DISCHARGES

7.2.1 Argon Gas

Argon is generally used in ion plating as a buffer gas; ie, it has no chemical influence on the coating process but it is used to attain the

appropriate conditions for ion plating to be performed. In thermionically enhanced pure argon discharges, ionisation efficiencies of up to a few per cent can be achieved [3]. Under typical thermionic triode conditions, most of the energy transported to the substrate would be from ions (rather than high energy neutrals); the majority of ions being Ar^+ formed by electron impact ionisation of argon ground state atoms and metastables [3].

7.2.2 Reactive Gas (Nitrogen)

Nitrogen is a reactive gas which is commonly used in ion plating, to produce ceramic coatings such as titanium nitride. The energy transportation characteristics of pure nitrogen discharges are likely to be comparable to those of argon under similar conditions. However, the ionisation of nitrogen could be influenced by its preference for being excited and its possible interactions with the heated filaments used as electron emitters in thermionically supported discharges [3]. These effects may be detrimental to the generation of ions (electron impact being the main mechanism), particularly under thermionic triode conditions, and the overall ionisation efficiency for any discharge containing sufficient nitrogen could be reduced.

Cathode sheath thickness measurements [3,5] and optical emission spectroscopy investigations of the proportion of nitrogen atomic to molecular species in nitrogenous discharges [5] have shown that dissociative charge transfer mechanisms can have a significant influence on the nature of the species arriving at the cathode. Although N_2^+ is the main ionic species generated in the negative glow region of pure nitrogen discharges, the majority of ions arriving at the cathode could be N^+, due to dissociative charge transfer collisions in the cathode sheath. This is likely to occur in discharges where a large number of collisions would be expected to take

place in the sheath; eg, in a pure nitrogen diode layout. Enhancing these discharges has shown that the proportion of N^+ ions arriving at the cathode is decreased, as the sheath approaches collisionless conditions. Thus N_2^+ is likely to be the dominant ionic species arriving at the cathode in pure nitrogen thermionic triode discharges. The addition of argon into nitrogen discharges has indicated that dissociative charge exchange collisions involving argon could occur; the influence being strongest in very low pressure enhanced discharges with a relatively large proportion of argon present. The importance of nitrogen dissociation within the cathode sheath in terms of practical ion plating is questionable. This is because nitrogen molecular species (high energy neutrals or ions) are likely to transport most of the energy to the cathode in preference to the atomic species, irrespective of the discharge conditions used. Also, the energy required for dissociation of nitrogen molecules at the cathode surface is low in comparison with the average bombarding energy, making this alternative mechanism for dissociation highly probable in all discharge configurations [5].

7.2.3 Evaporant Material

Although the evaporant materials commonly used in ion plating are metals, other materials, such as ceramics, can also be directly evaporated. One of the primary interests in this work though, has been to gain a better understanding of the characteristics of metal species in discharges.

The proportion of metal which is ionised in an argon based plasma is probably high, due to Penning ionisation effects [3]. Cathode sheath thickness measurements with and without the presence of titanium evaporation in argon thermionic triode discharges have indicated that at least 90% of the ion current at the cathode is transported by the metal species. In

addition to this being supportive of Penning ionisation having an important role, the sheath thickness results have led to the conclusion that at least some of the titanium arrives at the substrate in the form of ionised atomic clusters, consisting of a minimum of 10's of atoms per unit charge [5].

A model which unifies coating thickness uniformity with source to substrate distance has predicted the existence of a virtual source phenomenon. This is believed to be a localised region of high vapour density, formed above the melt pool. Further investigations of the model have indicated that the virtual source approximates to a point emitter, its influence being dependent on process conditions such as evaporation rate, ambient gas pressure and its size relative to the dimensions of the real source [6]. It is believed that if clusters of the evaporant material are present, they are probably formed by gas phase (homogeneous) nucleation [5]. As the probability of this occurring must be greater in regions of high vapour density, a large proportion of the clusters could be expected to be formed in the virtual source region. The model has also quantified a parameter, ℓ, which is primarily associated with the mean free path for thermalisation. It is believed that the presence of clusters in the vapour during coating deposition could make ℓ longer which in turn would produce coatings of poorer thickness uniformity than if all the vapour were individual atoms [6].

The limited published data available suggests that the ion energy distribution of a metal arriving at the cathode of an argon discharge has a much greater high energy content than that of argon in the same discharge [3]. However, much of the information is from discharges where the metal was sputtered rather than evaporated. The lower vapour flux densities generally encountered with sputtering sources would be less likely to cause metal clusters to be formed. Even where ion energy distributions of

evaporated metals have been reported, mass discrimination in the detector systems used would have prevented the identification of large ionised atomic clusters. Although the energy distribution of the metal flux arriving at a substrate during ion plating might have a high energy content, the energy transported per individual atom in a cluster will be very low. For example, a 1000 atom cluster would only be equivalent to about 0.1 eV per atom, yet the energetic gas species present (argon and reactive gases) would be expected to have the order of 100 eV per atom during deposition [5].

Optical emission spectroscopy investigations have indicated that the electron temperature almost doubles when metal is evaporated into a discharge and this concurs with published data. This is possibly due to increased charge loss to the chamber walls, and/or distortion of the electron energy distribution due to Penning ionisation. Although this effect may increase the plasma potential slightly, it is suggested that this or any other related influences will not be significant in relation to the practical aspects of ion plating [5].

Although most of the work on evaporant materials has been concerned with metals, some comment on the direct evaporation of ceramics in ion plating is required here. The thickness uniformity model has indicated the presence of a virtual source during gas evaporation of zirconia [6]. Therefore, it would be reasonable to suggest that this material may also form clusters in the vapour phase, even though it is believed to partially dissociate into ZrO and free oxygen. In general, the possibility of ceramic based vapours containing clusters cannot be disregarded. The role of Penning ionisation with these materials is uncertain. The work on metals has indicated that this mechanism has a profound influence in ion plating discharges, though whether ceramic based vapours would become significantly ionised by the same means would clearly depend on the ionisation potentials

of the vapour species present.

7.3 SUBSTRATE BOMBARDMENT FROM THE GAS AND VAPOUR SPECIES

The following points, arising from the findings of this work, have to be considered in terms of their influences on coatings produced by thermionic triode ion plating:

(i) Thermionically enhanced discharges exhibit a decrease in plasma density with distance from the thermionic emitter [4,5]. The effect of bombardment from gas species at the substrate surface appears to fall off exponentially with distance from the electron source; the rate of decay being dependent on the mean free path for electron impact ionisation of the gas [4].

(ii) Thermionically enhanced discharges produce anisotropic behaviour, resulting in substrate surfaces which directly face the electron emitter, receiving greater bombardment from the gas than those in more remote orientations. This is thought to be due to the motion of ions in the plasma being influenced by local field effects from the energetic thermionically emitted electrons [4].

(iii) The vapour arrival rate at a substrate (from an EB evaporation source) decreases with distance from the source. For substrate surfaces facing the source, the fall off in coating thickness under gas evaporation conditions appears to follow an inverse power law with source to substrate distance; the power being typically between 2 and 3, depending on the process conditions. Increasing the gas pressure raises the power index [6].

(iv) The vapour arrival rate at substrate surfaces which are remote from the vapour source is less than that received by surfaces which directly face the source. Increasing the gas pressure or the source

to substrate distance improves the coating thickness distribution. For thin horizontally mounted substrates positioned directly above the vapour source, the front to back coating thickness ratio follows a hyperbolic function with source to substrate distance [6].

(v) A significant proportion of the metal vapour in an ion plating discharge will become ionised, mainly due to the action of argon metastables; ie, Penning ionisation [3]. Investigations with titanium evaporation in thermionic triode discharges has indicated that a minimum of 90% of the substrate ion current is carried by the metal and that at least some of the metal arrives as atomic clusters [5].

Clearly, to achieve ion plated coatings which have the same density and structure, irrespective of their position in the deposition chamber, the ratio between the rate of bombardment from the discharge and vapour arrival must be maintained as constant as possible throughout the deposition volume. For ion plating in thermionic triode discharges, it can be seen from points (i) and (iii) above, that positioning the electron emitter close to the vapour source provides a means of attaining a near constant ratio between energetic bombardment from the gas species and vapour incidence rates. Although the former decreases exponentially and the latter decreases as an inverse power law with source to substrate distance, adjusting the gas pressure and/or the thermionic emitter bias voltage will change the relative fall off rates. Thus over practical source to substrate distances, an acceptable balance could be obtained.

Points (ii) and (iv) can also be offset to some extent, by positioning the electron emitter close to the vapour source. Under these conditions, substrate surfaces not directly facing the source and emitter will receive less intense energetic gas bombardment in addition to a reduced vapour arrival rate.

Point (v) gives rise to some interesting implications. Some caution must be exercised in assuming that at least 90% of the substrate ion current is from metal ions. The result can only be considered as an indication, even for the conditions studied in this work, as it has not been directly proved. Nevertheless, in strongly enhanced discharges, most of the energy transported to the substrate is by ions [3]. If a large proportion of the ions are metal, then the energetic bombardment intensity will be comparable to the metal vapour arrival rate on all substrate surfaces. Thus, even if ion plating was performed in a discharge with uniform plasma density, the metal coating structure and density characteristics would not be expected to change significantly with local variations in vapour arrival rates. This means that at least in the case of ion plated metal coatings, the "self bombardment" by the depositing material indicates that the influence of energetic gas bombardment might be less important than originally considered. However, other effects require some comment here:

If at least some of the metal ions arrive as clusters, then the average energy per incident atom could be very low for these particles (~ 0.1 eV for a 1000 atom cluster). Conversely, the energetic gas species will bombard the growing layer with ~ 100 eV per atom. Therefore, even if most of the bombardment energy is transported by the metal species, the mechanisms which are thought to be beneficial in ion plating (atomic displacement, sputtering, etc) may be primarily influenced by high energy gas bombardment. Also, when a reactive gas such as nitrogen is used to produce ceramic coatings, the presence of high energy nitrogen bombardment might be important for properties such as coating stoichiometry and homogeneity.

Furthermore, the metal vapour becomes ionised by direct electron impact and, to a greater extent, by argon metastables. As metastables are

also created by electron impact, the probability of metal ionisation will depend on the availability of higher energy electrons in the discharge. Thus metal vapour ionisation must also depend on the intensity of discharge enhancement and, in the case of thermionic support, where the electron emitter is positioned. Ideally, the emitter should be situated close to the region of highest vapour density, to maximise the probability of the metal becoming ionised. Therefore, the emitter should be positioned near to the vapour source.

To summarise, the main points to be considered with regards to uniformity of bombardment and vapour arrival rates in thermionic triode ion plating, are:

(a) Although a large proportion of the energy transported to the substrate might be expected to be carried by the metal vapour, the influence of energetic gas bombardment is, nevertheless, likely to be significant. Therefore, it is important to maintain a constant ratio between energetic gas bombardment and vapour arrival rates.

(b) Positioning the thermionic emitter close to the vapour source provides a means of attaining a more constant ratio between energetic gas and vapour impingement rates. This arrangement will also maximise the probability of the metal vapour becoming ionised.

The points discussed in this section pertain to the evaporation of metals. However, it is probable that these inferences are also applicable to thermionic triode ion plating where ceramic materials are directly evaporated. As discussed in Section 7.2.3, some ceramic based vapours may not become Penning ionised. If this is so, then such vapours may not be highly ionised (unlike metals) and the significance of maintaining a constant ratio between energetic gas bombardment and vapour arrival rates becomes even more apparent.

7.4 PROCESS OPTIMISATION CONSIDERATIONS IN THERMIONIC TRIODE ION PLATING

Based on the findings of this work, and assuming that the thermionic emitter is positioned close to the vapour source, Table 7.1 outlines some of the problems that might be encountered when using thermionic triode ion plating. The last column lists possible solutions to these problems, though it is clear that optimising for one aspect of the process may be detrimental to another. Thus careful balancing of the process parameters is necessary, to obtain the most suitable conditions for producing coatings of uniform quality with the required characteristics.

7.5 ION PLATING BY ALTERNATIVE TECHNIQUES

Although the work has concentrated on the use of evaporation sources in thermionic triode discharges, many of the findings should be applicable to other methods of ion plating. For example, the fall-off in plasma bombardment and anisotropic behaviour of discharges might be observed in systems which employ unbalanced magnetron sputtering sources or arc sources. This can be attributed to electron emission from these sources producing non-uniform discharge enhancement effects which may be compared with the characteristics of a thermionic emitter. However, the presence of the magnetic fields, which are associated with these devices, may result in the decrease in plasma bombardment following a more complex relationship with distance than that obtained with thermionic emitters.

The coating thickness uniformity model and empirical power law for absolute thickness with source to substrate distance is also expected to be applicable to other ion plating methods. Thermalisation distances, which play an important role in determining the thickness uniformity arising from

CAUSE:	EFFECT:	SUGGESTED SOLUTIONS:
IONISATION EFFICIENCY TOO LOW	POOR COATING QUALITY (EG, LOW DENSITY, OPEN POROUS STRUCTURE)	DECREASE GAS PRESSURE. INCREASE SUBSTRATE CURRENT DENSITY.
SUBSTRATE (CATHODE) SHEATH TOO THICK	PREFERENTIAL BOMBARDMENT OF SUBSTRATE CORNERS, EDGES, ETC. PRODUCES LOCAL VARIATIONS IN COATING CHARACTERISTICS.	REDUCE SHEATH THICKNESS BY DECREASING THE BIAS OR INCREASING THE CURRENT DENSITY AT THE SUBSTRATE, IN ACCORDANCE WITH THE CHILD-LANGMUIR EQUATION.
FILAMENT MATERIAL USED AS THERMIONIC EMITTER IS SPUTTERED.	MAY CONTAMINATE COATINGS.	REPLACE FILAMENTS MORE FREQUENTLY TO REDUCE THE INFLUENCE OF GRAIN BOUNDARIES OPENING UP. DECREASE THERMIONIC EMITTER BIAS BUT INCREASE TEMPERATURE (TO MAINTAIN THE SAME DEGREE OF ENHANCEMENT) SO THAT SPUTTERING RATE IS REDUCED. CHANGE FILAMENT GEOMETRY TO REDUCE GAS BOMBARDMENT IN RELATION TO THE ELECTRON EMISSION RATE.
PLASMA DENSITY DECREASES TOO RAPIDLY WITH DISTANCE FROM THE THERMIONIC EMITTER.	REDUCED EFFECT FROM ENERGETIC GAS BOMBARDMENT COMPARED WITH THE VAPOUR ARRIVAL RATE AT LARGER SOURCE TO SUBSTRATE DISTANCES. MAY PRODUCE COATINGS WHICH VARY IN QUALITY WITH THEIR POSITION FROM THE SOURCE.	DECREASE USABLE RANGE IN DEPOSITION CHAMBER. INCREASE THE MEAN FREE PATH FOR ELECTRON IMPACT IONISATION, BY CHANGING THE THERMIONIC EMITTER BIAS (SO THAT ELECTRONS ARE EMITTED WITH AN ENERGY WHICH HAS A SMALLER COLLISION CROSS SECTION FOR IMPACT IONISATION) OR BY REDUCING THE GAS PRESSURE.
VAPOUR FLUX DENSITY DECREASES TOO RAPIDLY WITH DISTANCE FROM THE SOURCE.	COATINGS AT LARGER SOURCE TO SUBSTRATE DISTANCES ARE TOO THIN RELATIVE TO THOSE CLOSER TO THE SOURCE.	DECREASE USABLE RANGE IN DEPOSITION CHAMBER. DECREASE THE GAS PRESSURE TO REDUCE FALL-OFF.
INSUFFICIENT VAPOUR ARRIVING AT SUBSTRATE SURFACES REMOTE FROM THE SOURCE.	POOR COATING THICKNESS UNIFORMITY BETWEEN SUBSTRATE SURFACES IN DIFFERENT ORIENTATIONS.	INCREASE GAS PRESSURE TO REDUCE MEAN FREE PATH FOR VAPOUR THERMALISATION. INCREASE THE SOURCE TO SUBSTRATE DISTANCES USED. ROTATE SUBSTRATES DURING DEPOSITION.

TABLE 7.1 SOME OF THE PROBLEMS THAT MIGHT BE ENCOUNTERED IN THERMIONIC TRIODE ION PLATING, WITH SUGGESTED SOLUTIONS.

gas scatting effects, may not necessarily be comparable to those obtained with evaporation sources. In addition, the source area (relative to substrate size) and typical source to substrate distances used in other techniques could be widely different. For example, a sputtering source usually has a large vapour emission area. Thus non-thermalised vapour may deposit onto substrate surfaces remote from the source (an effect not accounted for in the model) and this will tend to improve thickness uniformity in terms of front to back thickness ratios. However, shorter source to substrate distances are generally used (when compared with evaporation sources) and this would be detrimental to uniformity. Sputtered vapour thermalisation distances will probably be longer because the material will leave the source with energies greater than those attained with conventional evaporation. Conversely, the large source area and lower vapour emission rates associated with sputtering will result in lower vapour densities and this may reduce the probability of clusters being formed. This may shorten the thermalisation distances, offsetting the previous effect.

Some of the inferences from this work, when applied to other types of ion plating processes, are obviously speculative. However, it is hoped that they will, where applicable, be eventually verified for other systems.

8. RECOMMENDATIONS FOR FUTURE WORK

The work has highlighted a number of phenomena occurring in ion plating which require further investigation. Also, some of the inferences made from experimental results may be considered to be rather speculative. This chapter outlines some suggestions for future work, which should yield further information on the mechanisms which influence the ion plating process and provide confirmation of the suggested explanations for observed phenomena.

8.1 FURTHER INVESTIGATIONS WITH TECHNIQUES USED IN THIS WORK

8.1.1 Sputter Weight Loss (SWL) Experiments

The exponential fall off in plasma bombardment and anisotropic behaviour, observed under thermionic triode discharge conditions in Chapter 4, requires further evaluation. Although the effects of discharge pressure on bombardment uniformity has been studied, the influence of bias voltage, and, in particular, the thermionic emitter bias, has not been evaluated. It is expected that SWL runs performed with different emitter bias voltages will show changes in the bombardment fall off rate with distance from the emitter. This can be attributed to the energy dependence of the collision cross section for impact ionisation of the emitted electrons, thus providing a means of changing bombardment density with distance, as suggested in Table 7.1. Runs with different emitter bias settings may also show that the influence of plasma anisotropy can be decreased by using electrons emitted at lower energies. This might occur through a reduced perturbation of the plasma.

SWL experiments could also be performed with discharges using other forms of enhancement such as magnetic fields, or with layouts which utilise

RF biasing. As with the thermionic triode results of this work, the data may provide a further insight into the potential benefits and problems that might be encountered with these discharges.

8.1.2 Optical Emission Spectroscopy (OES) Experiments

8.1.2.1 Equipment improvements

The spatial resolution of the monochromator system used in this work could be improved by simply reducing the diameter of the collimator tube attached to the end of the fibre optic cable. However, the sensitivity of the system may have to be increased, either by using larger monochromator slit widths (which would be detrimental to wavelength resolution) or increasing the signal amplification (which could reduce the signal to noise ratio). A well defined sampling volume of the discharge could be obtained by limiting the distance through which the fibre optic probe "sees into" the plasma. This might be achieved by fitting a light absorbing cavity at some distance from the end of the collimator tube, although problems associated with distortion of the plasma may be incurred. Alternatively, a quartz lens system, shielded from the discharge, could be fitted to the end of the fibre optic probe to improve spatial resolution/sampling volume definition.

The time required to perform a spectral scan in this work was quite long (~ 11 minutes). The limiting component in the system was the writing speed of the chart recorder used. The scan time could be reduced considerably, by recording spectral information electronically, by, for example, interfacing the monochromator system with a microcomputer.

8.1.2.2 Future work

The suggestions outlined in the section above would improve the experimental capabilities considerably. For example, improved spatial

resolution would allow the cathode sheath/negative glow boundary to be studied in more detail, so that OES could be used to determine sheath thickness. Faster spectral scan speeds would reduce the potential difficulties incurred with obtaining information from discharges that may be unstable.

Probably the most interesting aspect of future OES investigations would be to perform detailed studies of metal and ceramic based vapours in discharges. For example, the spatial distribution of various plasma species could be studied with and without the presence of evaporation. This could provide information on the characteristics of the virtual source phenomenon and the general vapour flux distribution under different process conditions. Estimations of electron temperature from the spectral data may show spatial variations and changes with, for example, evaporation rate. This information may give a better insight into the mechanisms occurring in the ion plating process.

OES monitoring of the plasma species as a function of time is also likely to yield useful information. For example, the tungsten emission intensity could be monitored from an argon thermionic triode discharge (which uses tungsten filaments) to evaluate how potential coating contamination problems change with time. The technique might be useful for investigating other thermionic emitter geometries or material designed to reduce this effect. Another possibility would be to monitor the emission intensities of species from evaporation, with time. The dissociated gas species from direct evaporation of a ceramic material might be found to change, relative to the other vapour species present, during the coating process. This could arise from gradual stoichiometric changes in the source material, due to preferential emission of one of its elements, for example. Such effects might produce inhomogeneous coatings.

8.1.3 Cathode Sheath Thickness Measurements

Sheath thickness measurements with gases other than argon or nitrogen, that are likely to be used in ion plating, could be compared with predictions from the Child-Langmuir equation. This may provide useful information on the nature of the ionic species arriving at the cathode.

Further work on comparing cathode sheath thicknesses with and without the presence of metal evaporation should yield more information on clusters and the proportion of cathode ion current which is transported by the metal species. Changes in the sheath thickness ratio (ie, thickness with evaporation/thickness without evaporation) at different evaporation rates, gas pressures and source to cathode (substrate) distances, may show revealing trends in the data, such as the dependence of cluster size on the amount of vapour present in the discharge. Measurements of sheath thickness ratios with different vapour source materials might also give more insight into cluster formation. The role of Penning ionisation could be investigated, by evaluating how the estimated proportion of current transported by metal ions changes, when conditions for Penning ionisation cannot occur. This could be achieved by comparing sheath thickness ratios from metal evaporation in argon discharges with results from discharges using an alternative gas which will not cause Penning ionisation of the metal vapour.

As a final comment, it would be interesting to measure the sheath thickness in a pure metal discharge; this being achieved by thermionic support during evaporation. By comparing with predictions from the Child-Langmuir equation, a unique value of the charge to mass ratio of the species arriving at the cathode could be obtained. This would indicate whether clusters are also formed without the presence of an ambient gas.

8.1.4 Gas Scattering and Thickness Uniformity Modelling

The basic coating thickness uniformity model ($R = \coth(s/2\ell)$) requires further validity tests. The model has not been tested under thermionic triode ion plating conditions, or in coating systems which employ vapour sources other than EB or resistive evaporation.

Extensions to the model, which have been proposed in this work, need to be experimentally verified. Further extensions to the model would obviously be useful; in particular, the development of expressions to represent the radial dependence of the vapour flux due to progressive dilution and gas scattering effects. The latter would be appropriate for representing the radial thickness distribution across large substrate areas or for substrates which are mounted off-axis from the vapour source.

Investigations in this work have shown that after accounting for gas scattering effects, the progressive dilution of the vapour flux with distance from the source follows an inverse square law, provided that the virtual source height is larger than the radius of the real source. Unfortunately, the data supporting this evidence is limited and rather scattered (see Figure 6.14). More results are required to substantiate this.

8.2 FURTHER INVESTIGATIONS WITH OTHER EXPERIMENTAL TECHNIQUES

In addition to the methods employed in this work, other investigative techniques should also be considered. One of the most informative methods of analysing the ion plating process, is to directly sample the species arriving at the substrate during coating deposition. This can be achieved by means of an energy resolving mass spectrometer system, mounted behind a cathode (substrate) to analyse the bombarding species through an aperture of

appropriate dimensions in the cathode. Although such systems have been used elsewhere (as reviewed in Chapter 3), the available published data is very limited. Also, these systems have used mass spectroscopy equipment which would have been incapable of detecting the presence of large atomic clusters. Future investigations would require mass detection over a much wider range, and one method of achieving this would be to employ a time-of-flight mass spectrometer. This would confirm whether clusters are present and, if they are, information could be provided on their size distribution and bombardment energy characteristics under different process conditions. Important information on the characteristics of the bombarding gas species (argon and reactive gases) during ion plating could also be obtained with this technique. Also, the effects of using various forms of discharge enhancement and different types of vapour sources could be evaluated. Unfortunately, the capital outlay and time required to make the technique operative may be prohibitive.

Alternative investigative techniques include Langmuir probes and conventional mass spectroscopy. These may be capable of providing further information, but it is likely to be very limited. Langmuir probes could be used to evaluate electron temperatures in simple discharges (ie, only argon gas present) to provide a means of calibrating electron temperature results from OES data. Electron temperature determination by OES from more complex discharges (eg, during evaporation) could then be evaluated in absolute terms. Conventional mass spectroscopy techniques, where the sampling orifice is located in one of the chamber walls, may provide useful information on how the amount of dissociated gas from a ceramic vapour source changes with time, and this could be correlated with simultaneous monitoring by OES (see Section 8.1.2.2).

Finally, investigations of a more practical nature might be

considered. Although it is believed that dissociative charge transfer collisions in the cathode sheath of nitrogenous discharges may not have any practical relevance, nitriding experiments may provide useful information. If the experiments are performed under thermionic triode discharge conditions, then substrate bias and current density (and therefore power) can be maintained constant. Hence, the effects of pressure and the additional influence of argon in the discharge could be investigated in terms of the hardness and case depth achieved. Any variation in these properties would be attributable to changes in the energy distribution of the bombarding species or dissociative charge transfer mechanisms. In addition to nitriding experiments, more investigations with the "positive plasma triode" layout discussed in Chapter 4 are required. The assessment of ion plated coatings, produced under these conditions, may show that the technique is worthy of further consideration.

9. CONCLUSIONS

The following conclusions, which pertain to the optimisation of ion plating systems, can be drawn from this work:

(i) Based on the energy requirements of mechanisms considered to be important in the ion plating process, it is suggested that the minimum bombardment energy at the substrate should be 40 to 70 eV. Increasing the energy above this range may be less important than increasing the ion intensity or ionisation efficiency.

(ii) From the cathode voltage, current density and pressure data, the performance of various argon discharge configurations can be compared in terms of bombardment intensity and energy transportation characteristics of species arriving at the cathode. This information can be used to indicate the relative merits of different discharge enhancement methods.

(iii) Discharge enhancement can considerably reduce cathode sheath thickness, in accordance with the free-fall version of the Child-Langmuir equation. Smaller sheath thicknesses will decrease preferential bombardment of substrate corners, edges, etc. Also, bombardment uniformity will be improved on substrates with complex geometries and batches of mixed sized components.

(iv) Discharges enhanced with a thermionic emitter (thermionic triode discharges) provide a means of obtaining very small cathode sheath

thicknesses and excellent bombardment energy - intensity characteristics at the substrate surface. However, the influence of bombardment decreases exponentially with distance from the thermionic emitter. Surfaces not directly facing the emitter may receive less bombardment due to anisotropic behaviour. If the thermionic emitter comprises tungsten filaments, the amount of sputtered tungsten in the discharge may become significant after a long period of filament exposure. This could result in coatings ion plated in such discharges becoming contaminated, unless preventative steps are taken.

(v) Although nitrogen discharges are believed to have comparable energy transportation characteristics (at the cathode) to argon, ionisation of nitrogen might be influenced by its preference for excitation and interactions with the filaments used as electron emitters in thermionic triode layouts. These effects could be detrimental to the generation of ions and the overall ionisation efficiency for any discharge containing sufficient nitrogen may be reduced. Under certain conditions, dissociative charge transfer collisions in the cathode sheath of nitrogenous discharges can result in most of the N_2^+ ions becoming N^+ ions before they arrive at the cathode. However, when high energy neutral transportation characteristics and dissociation mechanisms occurring at the cathode surface are considered, the importance of dissociative charge exchange collisions in ion plating is questionable.

(vi) When a metal is evaporated into a discharge containing argon, a large proportion of the vapour is likely to be ionised because of Penning ionisation effects. Experimental evidence indicates that at least 90%

of the ion current at the cathode is transported by the metal species in an argon thermionic triode discharge. Furthermore, at least some of the metal arrives in the form of ionised atomic clusters consisting of a minimum of 10's of atoms per unit charge, under these conditions. The clusters are believed to be formed by gas phase (homogeneous) nucleation and their presence may be detrimental to metal bombardment energy and coating thickness uniformity. The electron temperature can almost double in value during metal evaporation, though it is thought that this may not have any significant influence in relation to the practical aspects of ion plating.

(vii) The front to back coating thickness ratio, R, as a function of source to substrate distance, s, can be represented by the expression $R = \coth(s/2\ell)$, for thin flat substrates mounted directly above the vapour source. The mean free path, ℓ, is related to the thermalisation distance of the vapour species. This thickness uniformity model is derived from consideration of the relative proportions of thermalised and non-thermalised vapour fluxes which are present when evaporation takes place in the presence of a low pressure gas. The model may also be used for ion plating systems.

(viii) Evaluation of the thickness uniformity model, using experimental data, predicts the existence of a virtual source phenomenon. This is believed to be a localised region of high vapour density formed above the melt pool and its characteristics seem to approximate to those of a point emitter. The influence of the virtual source in the coating process depends on parameters such as evaporation rate, ambient gas pressure and its size in relation to the dimensions of the real

source. If clusters of vapour atoms are present, a large proportion of these could be expected to be formed in the virtual source region.

(ix) For substrate surfaces facing the source, coating thickness in absolute terms empirically follows an s^{-n} law with source to substrate distance, s. The power, n, is typically between 2 and 3, depending on process conditions.

(x) To achieve ion plated coatings with uniform characteristics, it is important to maintain a constant ratio between energetic gas bombardment and vapour arrival rates on all substrate surfaces. Under thermionic triode ion plating conditions, positioning the electron emitter close to the vapour source provides a means of attaining this, as the reduction in energetic gas bombardment on substrate surfaces further away from, or not facing the thermionic emitter will tend to be offset by a comparable reduction in vapour arrival rate from the source.

It is hoped that these findings will be useful to practitioners of ion plating and that it will encourage further research into this very complex field of coating technology.

REFERENCES

1. D M Mattox, *J Vac Sci Technol*, 10, 47, (1973).

2. B A Movchan, A V Demchishin, *Phys Met Metallog*, 28, 83, (1969).

3. D M Mattox, Sandia Corp. Monograph, RPT SC-R-65-852, (1965).

4. T M Walls, D D Hall, D G Teer, B L Delcea, *Thin Solid Films*, 54, 303, (1978).

5. B Berghaus, UK Patent Specification, 510993, (1938).

6. D M Mattox, *Electrochem Technol*, 95, 2, (1964).

7. A Matthews, *Surface Engineering*, 1, 93, (1985).

8. A Matthews, *J Vac Sci Technol*, A3, 2354, (1985).

9. G A Baum, Dow Chemical Co., RPT RFP-686 UC-25, Colorada, USA, (1967).

10. J A Thornton, *Ann Rev Mater Sci*, 7, 239, (1977).

11. K S Fancey, MSc Thesis, Hull University, (1986).

12. K S Fancey, A Matthews, *J Vac Sci Technol*, A4, 2656, (1986).

13. A Matthews, *Adv Mat Manuf Processes*, 3, 91, (1988).

14. K S Fancey, A Matthews, Report to Tecvac Ltd (Confidential), September, (1987).

15. J Beynon, The Conduction of Electricity Through Gases, Harrap, London, (1972).

16. B N Chapman, Glow Discharge Processes, Wiley, New York, (1980).

17. J E Greene, *J Vac Sci Technol*, 15, 1718, (1978).

18. N N Petrov, *Sov Phys Solid State*, 2, 865, (1962).

19. D B Medved, P Mahadevan, J K Layton, *Phys Rev*, 129, 2086, (1963).

20. L B Loeb, Fundamental Processes of Electrical Discharge in Gases, Wiley, New York, (1939).

21. R Papoular, Electrical Phenomena in Gases, ILIFFE, London, (1965).

22. P F Knewstubb, A W Tickner, *J Chem Phys*, 36, 684, (1962).

23. D J Ball, *J Appl Phys*, 43, 3047, (1972).

24. G Lemperiere, J M Poitevin, *Vacuum*, 37, 825, (1987).

25. L Petitjean, A Ricard, *J Phys D Appl Phys*, 17, 919, (1984).

26. L I Maissel, R Glang (Eds), Handbook of Thin Film Technology, McGraw-Hill, New York, (1970).

27. K G Emeleus, *J Phys D*, 14, 2179, (1981).

28. W D Davis, T A Vanderslice, *Phys Rev*, 131, 219, (1963).

29. J Rickards, *Vacuum*, 34, 559, (1984).

30. D G Armour, H Valizadeh, F A H Soliman, G Carter, *Vacuum*, 34, 295, (1984).

31. H Valizadeh, PhD Thesis, Salford University, (1982).

32. C G Crockett, *Vacuum*, 23, 11, (1973).

33. P Saulnier, A Debhi, J Machet, *Vacuum*, 34, 765, (1984).

34. J Machet, G Gadet, P Saulnier, J Guille, 8th Int Vac Conf, Cannes, France. F Abeles, M Croset (Eds). Pub. Societe Francaise Du Vide, (1980).

35. J E Houston, J E Uhl, Sandia Labs RPT, SC-RR-0122, (1971).

36. Z Wronski, *Vacuum*, 36, 329, (1986).

37. N A G Ahmed, *J Phys E*, 13, 1305, (1980).

38. F W Aston, H E Watson, *Proc Royal Soc*, A, 86, 168 (1912).

39. T C Tisone, P D Cruzan, *J Vac Sci Technol*, 12, 1058, (1975).

40. F F Chen in Plasma Diagnostic Techniques, R H Huddlestone, S L Leonard, (Eds), Academic Press, New York, (1965).

41. W D Westwood, R Boynton, *J Appl Phys*, 43, 2691, (1972).

42. G Lemperiere, J M Poitevin, C Fourrier, *J Phys D*, 11, 293, (1978).

43. A Gras-Marti, I Abril, J A Valles-Abarca, *Thin Solid Films*, 124, 59, (1985).

44. R Hegerberg, T Stefansson, M T Elford, *J Phys B*, 11, 133, (1978).

45. R Hegerberg, M T Elford, H R Skullerud, *J Phys B*, 15, 797, (1982).

46. J W Sheldon, *Phys Rev Lett*, 8, 64, (1962).

47. Y Yaneko, T Iwai, S Ohtani, K Okuno, N Kobayashi, S Tsurubuchi, M Kimura, H Tawara, *J Phys B*, 14, 881, (1981).

48. G Astner, A Barany, H Cederquist, H Danared, S Huldt, P Huelplund, A Johnson, H Knudsen, L Liljeby, K G Rensfelt, *J Phys B*, 17, L877, (1984).

49. T Takagi, *J Vac Sci Technol*, A2, 382, (1984).

50. G Carter, D G Armour, *Thin Solid Films*, 80, 13, (1981).

51. J S Colligon, *Vacuum*, 36, 413, (1986).

52. A Matthews, PhD Thesis, Salford University, (1980).

53. A Matthews, in W D Sproul, J E Green, J A Thornton (Eds), Proc Topical Symp Physics and Chemistry of Protective Coatings, American Vacuum Society, Series 2, American Institute of Physics Conf Proc, 149, AIP, New York, (1986).

54. J W Coburn, *Rev Sci Instr*, 41, 1219, (1970).

55. J W Coburn, E Kay, *App Phys Lett*, 18, 435, (1970).

56. J W Coburn, E Kay, *Solid State Technol*, Dec, 49, (1971).

57. B R Natarjaran, A H Eltoukhy, J E Greene, T L Barr, *Thin Solid Films*, 69, 201, (1980).

58. D K Bohme, J M Goodings, *J Appl Phys*, 37, 4261, (1966).

59. P F Little, A Von Engel, *Proc Roy Soc*, A, 224, 209, (1954).

60. B P Johansson, J E Sundgren, H T G Hentzell, S E Karlsson, *Thin Solid Films*, 111, 313, (1984).

61. E Eser, R E Ogilvie, K A Taylor, *Thin Solid Films*, 68, 381, (1980).

62. P M Chung, L Talbot, K J Touryan, Electric Probes in Stationary and Flowing Plasmas, Springer, New York, (1975).

63. T L Thomas, E L Battle, *J Appl Phys*, 41, 3428, (1970).

64. L Protin, G Fleury, C Vautier, *Vacuum*, 34, 791, (1984).

65. A Matthews, Proc Conf on Ion Assisted Surface Treatments, Techniques and Processes, Warwick, Sept 1982. The Metals Society, (1982).

66. A Matthews, D T Gethin, *Thin Solid Films*, 117, 261, (1984).

67. G Francis, Ionisation Phenomena in Gases, Butterworths, London, (1960).

68. W R Harshbarger, R A Porter, T A Miller, P Norton, *Appl Spectroscopy*, 31, 201, (1977).

69. B J Curtis, *Solid State Technol*, April, 129, (1980).

70. S Schiller, U Heisig, K Steinfelder, J Strumpfel, R Voigt, R Fendler, G Teschner, *Thin Solid Films*, 96, 235, (1982).

71. A G Spencer, R P Howson, Proc Int Congress on Optical Science and Engineering, Hamburg, F.R.G., Sept 1988, SPIE, (1988).

72. K Salmenoja, A S Korhonen, M S Sulonen, *J Vac Sci Technol*, A3, 2364, (1985).

73. J E Greene, F Sequeda-Osorio, *J Vac Sci Technol*, 10, 1144, (1973).

74. T Pech, J P Chabrerie, A Ricard, *J Vac Sci Technol*, A6, 2987, (1988).

75. W D Westwood, R J Boynton, *J Appl Phys*, 44, 2610, (1973).

76. W D Westwood, *J Appl Phys*, 44, 2619, (1973).

77. A Ricard, H Michel, P Jacquot, M Gantois, *Thin Solid Films* 124, 67, (1985).

78. D A Hope, T I Cox, V G I Deshmukh, *Vacuum*, 37, 275, (1987).

79. J Felts, E Lopata, *J Vac Sci Technol*, A6, 2051, (1988).

80. J W Coburn, M Chen, *J Appl Phys*, 51, 3134, (1980).

81. R W P McWhirter, in Plasma Diagnostic Techniques, R H Huddlestone, S L Leonard (Eds), Academic Press, London (1965).

82. B C Bell, D A Glocker, *J Vac Sci Technol*, A6, 2047, (1988).

83. R E Hurley, *Vacuum*, 34, 351, (1984).

84. S V Dresvin, Physics and Technology of Low Temperature Plasmas, Iowa State University Press/AMES, (1977).

85. W McGowan, L Kerwin, *Can J Phys*, 42, 2086, (1964).

86. S C Brown, Basic Data of Plasma Physics, M.I.T. Press, Cambridge, Mass, (1966).

87. W B Maier, R F Holland, *J Chem Phys*, 59, 4501, (1973).

88. W B Maier, *J Chem Phys*, 55, 2699, (1971).

89. J M Poitevin, G Lemperiere, *Thin Solid Films*, 120, 223, (1984).

90. F Howorka, *J Chem Phys*, 68, 804, (1978).

91. M.I.T. Wavelength Tables, Wiley, New York, (1939).

92. K Kimoto, Y Kamiya, M Nonoyama, R Uyeda, *Japan J Appl Phys*, 2, 702, (1963).

93. O Reifenschweiler, *Rev Sci Instrum*, 35, 456, (1964).

94. N Wada, *Japan J Appl Phys*, 7, 1287, (1968).

95. S Yatsuya, S Kasukabe, R Uyeda, *Japan J Appl Phys*, 12, 1675, (1973).

96. C G Granqvist, R A Buhrman, *J Appl Phys*, 47, 2200, (1976).

97. K Sattler, J Muhlbach, E Recknagel, *Phys Rev Lett*, 45, 821, (1980).

98. P Pfau, K Sattler, J Muhlbach, R Pflaum, E Recknagel, *J Phys F: Met Phys*, 12, 2131, (1982).

99. P Pfau, K Sattler, J Muhlbach, E Recknagel, *Phys Lett*, 91, 316, (1982).

100. K Sattler, J Muhlbach, O Echt, P Pfau, E Recknagel, *Phys Rev Lett*, 47, 160, (1981).

101. S Mukherjee, K H Bennemann, *Surf Sci*, 156, 580, (1985).

102. H F Winters, *J Chem Phys*, 44, 1472, (1966).

103. C T Wan, D L Chambers, D C Carmichael, *J Vac Sci Technol*, 8, VM99, (1971).

104. D M Mattox, Sandia Labs. RPT, SLA-73-0619, Albuquerque, (1973).

105. S Aisenberg, R W Chabot, *J Vac Sci Technol*, 10, 104, (1973).

106. S Sugano, Y Nishina, S Ohnishi (Eds), Proc 1st NEC Symp Hakone and Kawasaki, Japan 1986. Microclusters, 4, Springer Series in Materials Science, (1987).

107. G Benedek, T P Martin, G Pacchioni (Eds). Proc 13th Int School, Erice, Italy, 1987. Elemental and Molecular Clusters, 6, Springer Series in Materials Science, (1987).

108. T Spalvins, J S Przybyszewski, D H Buckley, NASA Tech Note: TN D-3707, (1966).

109. R J Hill (Ed), Physical Vapour Deposition, Airco Temescal, Berkeley, California, (1976).

110. K D Kennedy, G R Schuermann, H R Smith, *Res Dev*, Nov, (1971).

111. E B Graper, *J Vac Sci Technol*, 10, 100, (1973).

112. T C Reiley, PhD Thesis, Stanford University, USA, (1974).

113. A Bessaudou, F S Caluyo, J Machet, 6th Int Conf on Ion and Plasma Assisted Techniques, IPAT '87, Brighton, CEP Consultants, Edinburgh, (1987).

114. G Gonzalez-Diaz, I Martil, F Sanchez-Quesada, M Rodriguez-Vidal, *J Vac Sci Technol*, A1, 1394, (1983).

115. T Motohiro, *J Vac Sci Technol*, A4, 189, (1986).

116. K S Fancey, BSc Project RPT, Brunel University, (1982).

117. K S Fancey, J Beynon, *Vacuum*, 34, 591, (1984).

118. J M Walls, D D Hall, D E Sykes, *Surf Interface Anal*, 1, 204, (1979).

119. J Valli, J Palogarui, U Makela, VTT Research Notes, 435, Technical Research Centre of Finland, (1985).

120. H R Smith, Proc 12th Annual Tech Conf. Soc. Vacuum Coaters, Detroit, Pub Soc Vac Coaters, Cleveland, Ohio, (1969).

121. R E Somekh, *J Vac Sci Technol*, A2, 1285, (1984).

122. M El-Sherbiney, PhD Thesis, Salford University, (1974).

123. D L Chambers, D C Carmichael, *Res Dev*, 22, 32, (1971).

124. W D Westwood, *J Vac Sci Technol*, 15, 1, (1978).

125. I Abril, A Gras-Marti, J A Valles-Abarca, *J Vac Sci Technol*, A4, 1773, (1986).

126. I Abril, A Gras-Marti, J A Valles-Abarca, *Vacuum*, 37, 391, (1987).

127. R S Updadhye, M K Kong, E J Hsieh, *J Vac Sci Technol*, A6, 1891, (1988).

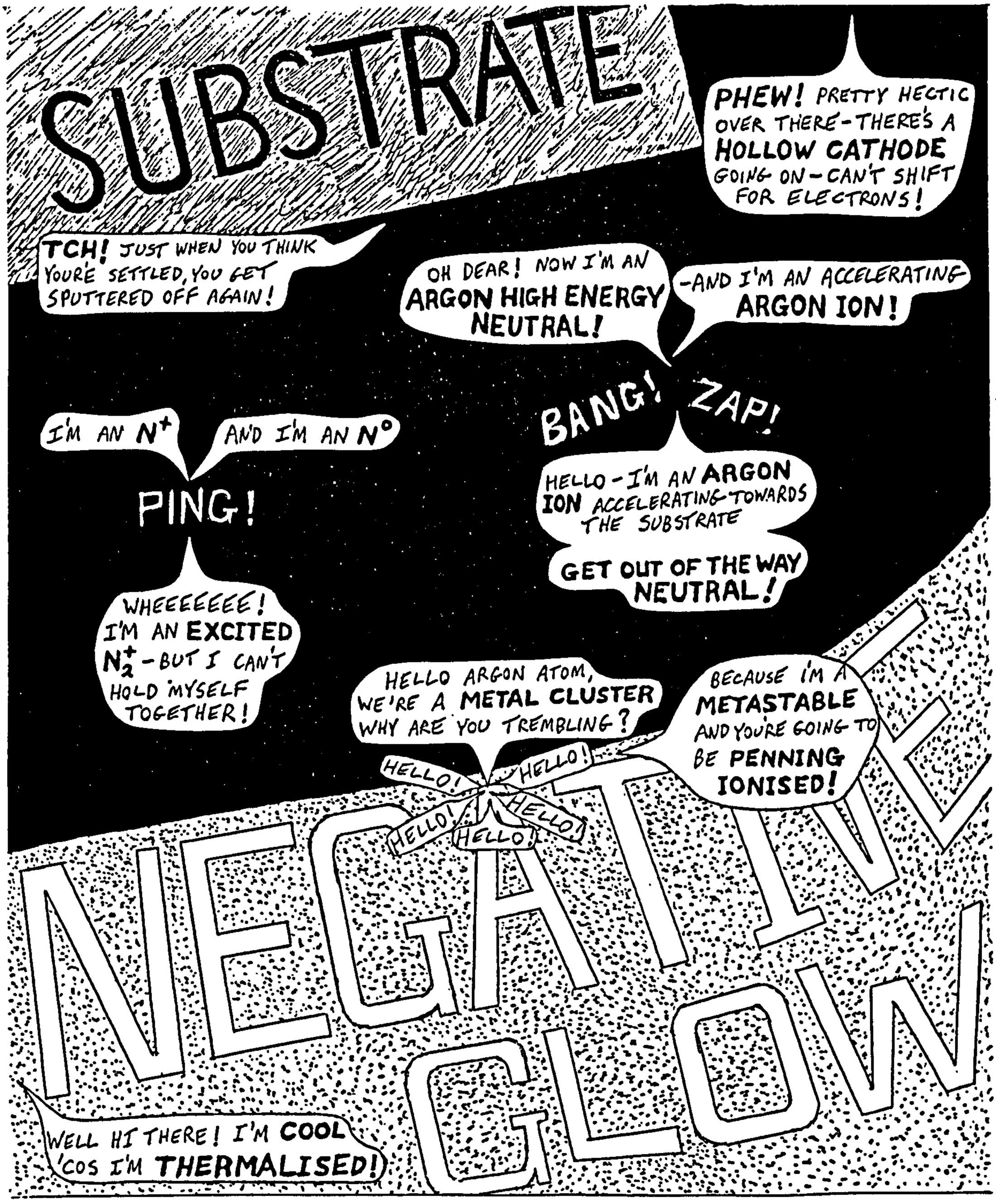
SUBSTRATE
PHEW! PRETTY HECTIC OVER THERE-THERE'S A HOLLOW CATHODE GOING ON-CAN'T SHIFT FOR ELECTRONS!
TCH! JUST WHEN YOU THINK YOU'RE SETTLED, YOU GET SPUTTERED OFF AGAIN!
OH DEAR! NOW I'M AN ARGON HIGH ENERGY NEUTRAL!
-AND I'M AN ACCELERATING ARGON ION!
BANG!
ZAP!
I'M AN N^+
AND I'M AN N°
PING!
HELLO - I'M AN ARGON ION ACCELERATING TOWARDS THE SUBSTRATE
GET OUT OF THE WAY NEUTRAL!
WHEEEEEEE! I'M AN EXCITED N_2^+ - BUT I CAN'T HOLD MYSELF TOGETHER!
HELLO ARGON ATOM, WE'RE A METAL CLUSTER WHY ARE YOU TREMBLING?
BECAUSE I'M A METASTABLE AND YOU'RE GOING TO BE PENNING IONISED!
HELLO!
HELLO!
HELLO!
HELLO!
HELLO!
NEGATIVE GLOW
WELL HI THERE! I'M COOL 'COS I'M THERMALISED!